

UNCLASSIFIED

AD 4 4 4 6 0 2

DEFENSE DOCUMENTATION CENTER

FOR

SCIENTIFIC AND TECHNICAL INFORMATION

CAMERON STATION, ALEXANDRIA, VIRGINIA



UNCLASSIFIED

NOTICE: When government or other drawings, specifications or other data are used for any purpose other than in connection with a definitely related government procurement operation, the U. S. Government thereby incurs no responsibility, nor any obligation whatsoever; and the fact that the Government may have formulated, furnished, or in any way supplied the said drawings, specifications, or other data is not to be regarded by implication or otherwise as in any manner licensing the holder or any other person or corporation, or conveying any rights or permission to manufacture, use or sell any patented invention that may in any way be related thereto.

444602

WL TDR-64-71, Vol I

WL
TDR
64-71
Vol I

COMPUTER CODES FOR SPACE RADIATION ENVIRONMENT AND SHIELDING

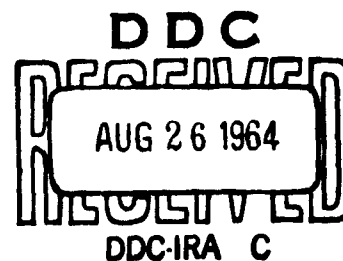
Volume I

August 1964

TECHNICAL DOCUMENTARY REPORT NO. WL TDR-64-71, Vol I



Research and Technology Division
AIR FORCE WEAPONS LABORATORY
Air Force Systems Command
Kirtland Air Force Base
New Mexico



Project No. 5101, Task No. 510118

(Prepared under Contract AF 29(601)-6061 by
The Boeing Company, Aero-Space Division,
Seattle, Washington.)

Research and Technology Division
Air Force Systems Command
AIR FORCE WEAPONS LABORATORY
Kirtland Air Force Base
New Mexico

When Government drawings, specifications, or other data are used for any purpose other than in connection with a definitely related Government procurement operation, the United States Government thereby incurs no responsibility nor any obligation whatsoever; and the fact that the Government may have formulated, furnished, or in any way supplied the said drawings, specifications, or other data, is not to be regarded by implication or otherwise as in any manner licensing the holder or any other person or corporation, or conveying any rights or permission to manufacture, use, or sell any patented invention that may in any way be related thereto.

This report is made available for study upon the understanding that the Government's proprietary interests in and relating thereto shall not be impaired. In case of apparent conflict between the Government's proprietary interests and those of others, notify the Staff Judge Advocate, Air Force Systems Command, Andrews AF Base, Washington 25, DC.

This report is published for the exchange and stimulation of ideas; it does not necessarily express the intent or policy of any higher headquarters.

DDC AVAILABILITY NOTICE

Qualified requesters may obtain copies of this report from DDC.

FOREWORD

This report is submitted to the Air Force Weapons Laboratory, Kirtland Air Force Base, New Mexico, in accordance with the requirements set forth in AF Contract AF 29(601)-6061 and SA No. 1 to AF Contract AF 29(601)-6014, as amended. This report is divided into two volumes. Volume I describes the theoretical development and numerical methods used in the generation of the computer codes. Volume II consists of seven independently bound sections, each of which treats the programming, coding, and operation of a specific computer code. They are prepared as an operator's manual.

Results of other work performed under these contracts, which consisted of application of existing codes to specific radiation analysis, have been previously transmitted to the Air Force Weapons Laboratory and are not included in this report.

The work has been done under the joint supervision of J. A. Barton and B. W. Mar within the Nuclear and Space Physics Section under the direction of G. L. Keister. The technical contributions were prepared by the following authors: Section 2, W. R. Doherty; Section 3, J. R. Benbrook, W. R. Doherty, W. R. Sheldon, and J. R. Thomas; Section 4, B. W. Mar and K. Moriyasu; Section 5, B. W. Mar; Section 6, M. C. Wilkinson; Section 7, B. W. Mar; Section 8, W. R. Doherty; and Appendix, K. Moriyasu.


ABSTRACT

The objective of this program is to develop mathematical representations and computer codes for determining the absorbed dose and the linear-energy-transfer spectrum at arbitrary points within a spacecraft on an arbitrary trajectory in space. The radiation environment, including spectral, angular and temporal dependence, was represented mathematically, and calculation of the flux and flux rate of each particle type was coded. Specifically, codes were devised to (1) determine the spacecraft trajectory; (2) convert the trajectory in geographic coordinates to magnetic coordinates B , L , and t and to equivalent magnetic dipole coordinates R , λ , and t ; (3) calculate the unit-flux dose or total dose of penetrating and secondary radiation at a dose point within the spacecraft; and (4) integrate the various subroutines and instruct a plotter to plot program output.

The computer program was devised for maximum growth capability and flexibility, but there are inevitable shortcomings in view of the rapid development of space research. Recommendations are made for further studies.

PUBLICATION REVIEW

This report has been reviewed and is approved.



DUANE A. ADAMS
1Lt USAF
Project Officer



IRVING J. RUSSELL
Colonel USAF
Chief, Biophysics Branch



PERRY L. HUIE
Colonel USAF
Chief, Research Division

CONTENTS

1.0	INTRODUCTION	1
2.0	SPACECRAFT TRAJECTORY	3
2.1	Approximate Trajectories	3
2.2	Point-by-Point Trajectories	7
2.3	Conversion to Magnetic Coordinates	7
2.4	Time-Saving Techniques	7
3.0	RADIATION ENVIRONMENT	11
3.1	Trapped Radiation	11
3.1.1	Omnidirectional Flux Maps	13
3.1.2	Spectral Dependence	22
3.1.3	Time Dependence	33
3.1.4	Angular Distributions	34
3.2	Untrapped Radiation	49
3.2.1	Solar Particle Events	49
3.2.2	Galactic Cosmic Radiation	55
4.0	VEHICLE ANALYSIS	59
5.0	ELECTRON SHIELDING	63
5.1	Monte Carlo Studies	63
5.1.1	Interactions	63
5.1.2	Modifications	66
5.1.3	Angular Distribution of Penetrating Electrons	66
5.1.4	Accuracy of Monte Carlo Calculation	77
5.2	Radiation Transport	81
5.2.1	Primary Electrons	81
5.2.2	Bremsstrahlung Shielding	97
6.0	PROTON SHIELDING	115
6.1	Interactions of Protons with Matter	115
6.1.1	Interactions with Electrons	115
6.1.2	Interactions with the Nucleus	118
6.2	Radiation Transport	121
6.2.1	Protons	121
6.2.2	Neutrons	124
6.2.3	Gammas	126
6.2.4	Geometrical Considerations	127

6.3	Dose Calculations	128
6.3.1	Energy Deposition	128
6.3.2	Linear Energy Transfer Spectrum	130
6.3.3	Semiconductor Damage	132
6.4	Results	132
6.4.1	Program Descriptions	132
6.4.2	Sample Calculations	134
6.4.3	Comparison with Oak Ridge Calculations	144
7.0	ANGULAR DISTRIBUTION OF INCIDENT RADIATION FLUXES AND THE EFFECTS OF VEHICLE ORIENTATION	147
8.0	PROGRAM INTEGRATION AND UTILIZATION	159
9.0	CONCLUSIONS AND RECOMMENDATIONS	163
9.1	Conclusions	163
9.1.1	Spacecraft Trajectories	163
9.1.2	Radiation Environment	163
9.1.3	Vehicle Analysis	163
9.1.4	Electron Shielding	163
9.1.5	Proton Shielding	164
9.1.6	Effects of Angular Distribution of Incident Radiation	164
9.2	Recommendations	164
	APPENDIX	167
	REFERENCES	173
	DISTRIBUTION	183

LIST OF FIGURES

1.	Orbit Geometry	6
2.	The geometry of the B - L coordinate system	12
3.	A B-L plot of the minimum altitude h_{\min}	14
4.	The Hess P-1 proton flux map	16
5.	The composite spectra of Hess and Vette	17
6.	The Vette high-energy proton map	18
7.	The electron flux map (November 1962)	19
8.	The electron spectrum proposed by Vette	20
9.	The Vette low-energy proton map	21
10.	The basic electron spectra used in the program	25
11.	The relative amplitudes of the first four basic electron spectra as determined from West's measured spectra	27
12.	The relative amplitudes of the last four basic electron spectra as determined from West's measured spectra	28
13.	The B dependence of the C_i 's at $L = 1.3$	29
14.	The basic proton spectra used in the program	31
15.	Parameters of the pitch angle distribution	36
16.	Equatorial pitch angle distributions for Hess P-1 proton map	37
17.	Equatorial pitch angle distributions for the high-energy proton map	38
18.	Equatorial pitch angle distributions for the low-energy proton map	39
19.	Equatorial electron pitch angle distributions	40
20.	Equatorial pitch angle distributions at $L = 3.5$ and $L = 5.0$ for the electron and low-energy proton maps	41

21.	Proton cutoff energies versus L	52
22.	Variation of vertical cutoff	54
23.	The time variations of cosmic radiation at Thule, Greenland, $\lambda_m = 88^\circ \text{ N}$	56
24.	Cosmic ray counting rate as measured by Explorer VII satellite (November 1959 to December 1960)	57
25.	Input data for improved vehicle analysis	60
26.	Energy loss in aluminum	65
27.	Average cosines for 1-Mev electrons incident at 0, 30, and 60 degrees on aluminum	69
28.	Diffusion lengths for 1-Mev electrons, normal incidence	72
29.	Diffusion lengths for 3-Mev electrons, normal incidence	73
30.	Diffusion lengths for 6-Mev electrons, normal incidence	74
31.	Angular distribution of 1-Mev electrons transmitted through 0.175 gm/cm^2 of aluminum, normal incidence	75
32.	Angular distribution of 1-Mev electrons transmitted through aluminum, normal incidence	76
33.	Normalizing factor f_0 for 1000 electron histories	78
34.	Comparison of single and multislab results	86
35.	Transmission factor as a function of thickness of aluminum for 1-Mev incident electrons	88
36.	Monte Carlo histograms for 1-Mev electrons incident on aluminum	89
37.	Transmission through mica of monoenergetic electrons of 0.2065 Mev	90
38.	Mathematical model for differential number spectrum	91
39.	LET spectrum of various radiation types	93

40.	Effects of incident angle on electron transmission	95
41.	LET spectrum of standard X-rays, flare produced protons, and neutron recoil protons from thermal fission	98
42.	Geometry of bremsstrahlung calculations	103
43.	Thick-target bremsstrahlung angular distribution	107
44.	Density of dislocation formation in silicon due to monoenergetic protons	133
45.	Freden-White spectrum--protons incident	135
46.	40-Mv solar event spectrum--protons incident	136
47.	100-Mv solar event spectrum--protons incident	137
48.	160-Mv solar event spectrum--protons incident	138
49.	Number-LET spectrum for 40-Mv solar event spectrum	139
50.	Number-LET spectrum for 100-Mv solar event spectrum	140
51.	Number-LET spectrum for 160-Mv solar event spectrum	141
52.	Energy-LET spectrum for 40-Mv solar event spectrum	142
53.	Differential energy spectrum for 100-Mv solar event spectrum	143
54.	Comparison of the results of Alsmiller with this study	145
55.	Definition of angles	147
56.	Coordinate system for angular distribution calculations	148
57.	Geometry for example studied	149
58.	Geometry for Case 2 and Case 3 examples of non-isotropic angular distribution	151

LIST OF TABLES

1.	Average and maximum average percentage differences of computed and interpolated magnetic coordinates	9
2.	Basic proton spectra adapted for Hess and Vette flux maps	32
3.	Monte Carlo diffusion lengths	68
4.	Theoretical and statistical errors for target increments. 1-Mev electrons normally incident on aluminum. Increment thickness 2.5×10^{-2} g/cm ²	82
5.	Multislabs electron number transmission	85
6.	Summary of special cases	105
7.	Comparison of bremsstrahlung results	109
8.	Bremsstrahlung transmission versus lead shell thickness for three specific body points	110
9.	Bremsstrahlung transmission versus iron shell thickness for three specific body points	111
10.	Bremsstrahlung transmission versus aluminum shell thickness for three specific body points	112
11.	Bremsstrahlung transmission versus beryllium shell thickness for three specific body points	113
12.	Shield configuration for study of proton angular distribution	152
13.	Dose transmission factor for Hess protons	153
14.	Fraction of free-space flux crossing a unit surface	155

INDEX OF PRINCIPAL SYMBOLS

SYMBOL	NAME	UNITS
A	atomic weight of absorber; flux tube cross sectional area	gm/mole cm^2
$A(h\nu)$	distribution function for angle as a function of photon energy	photons/degree
a	semimajor axis; screening length	km cm
a_0	Bohr radius	$5.29(10^{-9}) \text{ cm}$
B	magnetic induction; parameter in Bethe-Molière theory	gauss
B_i	buildup factor	
b	parameter in Bethe-Molière theory	
$C_i(i)$	amplitude of the i^{th} basic spectrum in the j^{th} measured spectrum	
c	speed of light	$3(10^{10}) \text{ cm/sec}$
c_K	K-shell correction factor	
D	radiation dose	rad
D_i	radiation dose from particles of type i	rad
$D(E)$	dislocation density	cm^{-2}
$DD(x)$	defect density	cm^{-3}
d	diffusion length	cm
E	eccentric anomaly; kinetic energy	radian Mev
e	electron charge	$4.8(10^{-10}) \text{ statcoulomb}$

F	omnidirectional particle flux; ratio of the number of particles crossing unit area of a surface to the omnidirectional flux	$\text{cm}^{-2} \text{sec}^{-1}$
F_i	relative standard deviation of the i^{th} spectrum	
$F_N(E, E')$	spectrum of neutrons produced by an incident proton of energy E	neutron/(Mev proton)
$F_p(E, E')$	spectrum of protons produced by an incident proton of energy E	proton/(Mev proton)
F_α	directional flux per steradian	$\text{cm}^{-2} \text{sec}^{-1} \text{ster}^{-1}$
$F_\gamma(E')$	spectrum of gammas produced by an incident proton	photon/(Mev proton)
$F(t)$	function which describes instantaneous flux-time dependence	
$F(x/X_o)$	distribution of the bremsstrahlung source	
f_B	fractional pitch-angle density at B	
f_o	normalizing factor	
f_i^H	basic spectral function of Hess P-1 protons	Mev^{-1}
f_i^V	basic spectral function of Vette high-energy protons	Mev^{-1}
$f_i(E)$	basic spectral function for electrons	Mev^{-1}
G_i	spectrum of protons for the i^{th} L shell	
$G_i(E)$	the i^{th} measured electron spectrum	Mev^{-1}
H	arbitrary division point between hard and soft collisions	Mev
h_a	apogee altitude	km
h_p	perigee altitude	km
\hbar	reduced Planck's constant	$1.054(10^{-27}) \text{ erg sec}$

I	mean ionization potential	Mev
$I(h\nu, E)$	energy radiated per unit energy interval by an incident electron of energy E	Mev/(Mev electron)
i	inclination angle	radian
J	omnidirectional flux	$\text{cm}^{-2} \text{sec}^{-1}$
J_0	isotropic flux	$\text{cm}^{-2} \text{sec}^{-1}$
J_2	second-harmonic gravitational coefficient	$1.0856(10^{-3})$
J'	modified second-harmonic gravitational coefficient	$1.632(10^{-3})$
$j(E)$	spectral function	Mev^{-1}
$j_0(t)$	instantaneous flux	$\text{cm}^{-2} \text{sec}^{-1}$
$K(E)$	range of electron	gm cm^{-2}
$K(h\nu)$	flux-to-dose conversion factor for photons of energy $h\nu$	$\text{rad}/(\text{proton cm}^{-2})$
$k_e = \sqrt{GM_e}$	a gravitational constant	$6.313(10^2)(\text{km})^{3/2} \text{sec}^{-1}$
L	McIlwain's magnetic shell parameter	earth radii
l	semilatus rectum;	km
	length of particle trajectory	cm
M	mean anomaly;	radian
	dipole moment of the earth	$8.1(10^{25}) \text{ gauss cm}^3$
m	mass	gm
m_0	electron rest mass	$0.511 \text{ Mev}/c^2$
N	number of particles in a flux tube of cross sectional area A_i	
	number density of atoms	cm^{-3}
N_0	Avogadro's number	$6.025(10^{23}) \text{ atoms/mole}$

N_N	number of neutrons per inelastic collision	
N_p	number of protons per inelastic collision	
n_o	number of electrons scattered through an angle greater than θ_{\max} by a single collision	
$n_B(\cos \alpha)$	trapped particle density per unit cosine α	cm^{-3}
$n(B)$	trapped particle density at B	cm^{-3}
P	anomalous period of orbit;	sec
	magnetic rigidity;	Mv
	momentum	Mev/c
P_o	average e-folding rigidity	Mv
$P_o(t)$	instantaneous e-folding rigidity	Mv
P_c	vertical cut-off rigidity	Mv
Q	energy imparted to an electron by a proton	Mev
Q_{\max}	maximum energy that can be imparted to an electron by a proton of energy E	Mev
R	invariant radius	mean earth radii
R_{eq}	equatorial earth radius	6378.2 km
R_e	mean radius of the earth	6371.2 km
$R(E)$	range of a proton of energy E	gm cm^{-2}
r	geocentric radius	km
r_o	classical electron radius	$2.82(10^{-13}) \text{ cm}$
S	path length	cm
S_i	number of particles of type i	
S_E	stopping power	$\text{Mev cm}^2 \text{ gm}^{-1}$
T	kinetic energy	Mev

T_{iN}	dose transmission factor for radiation of type i penetrating sector of type N	rad/particle
$T(E)$	fraction of incident electrons of energy E that are transmitted	
t	time	sec
t_o	initial time	sec
V	screened coulomb potential	statvolt
v	velocity	cm/sec
\bar{v}	average particle velocity	cm/sec
$W(E)$	average amount of energy radiated by an electron of energy E	Mev
X_o	radiation length	gm cm ⁻²
X_c	parameter in Bethe-Molière theory	gm cm ⁻²
x	thickness	gm cm ⁻²
Z	atomic number	
α	fine structure constant; pitch angle	1/137 degree
α_o	equatorial pitch angle	degree
α_1	a parameter of Bethe-Molière theory	cm sec ⁻²
β	ratio of velocity to the velocity of light; argument of perigee	radian
β_o	initial argument of perigee	radian
Γ	the gamma function	
γ	half-angle of Störmer cone	radian

δ	heading coefficient	
e	eccentricity	
θ	colatitude	radian
θ_o	initial colatitude	radian
θ_H	angular half width	degree
Λ_o	initial latitude	degree
$\Lambda^{(n)}$	the fraction of electrons penetrating section n which are incident on the dose point	
λ	latitude (invariant)	degree
μ	dimensionless magnetic moment	
$\mu_N(E)$	attenuation coefficient for neutrons of energy E	$\text{cm}^2 \text{ gm}^{-1}$
$\mu_p(E)$	attenuation coefficient for protons of energy E	$\text{cm}^2 \text{ gm}^{-1}$
$\mu_\gamma(h\nu)$	attenuation coefficient for gammas of energy $h\nu$	$\text{cm}^2 \text{ gm}^{-1}$
ν	frequency	sec^{-1}
$\psi(x) = \frac{\sqrt{x}}{\sqrt{\nu}} F(B \sqrt{x}, L)$	a function proportional to the omnidirectional flux	
$\psi'(x)$	derivative of ψ with respect to its argument	
ρ	density	gm cm^{-3}
σ	relative standard deviation	
σ_o	diffusion length	gm cm^{-2}
σ_{in}	inelastic cross section	cm^2
$\sigma(\theta)$	differential scattering cross section	$\text{cm}^2 \text{ ster}^{-1}$
τ_D	decay time	sec

τ_R	rise time	sec
ϕ	longitude	degree
ϕ_o	initial longitude	degree
$\phi_{BL}(\alpha)$	directional flux per unit cosine α	$\text{cm}^{-2} \text{sec}^{-1}$
$\phi_i(E)$	differential energy spectrum of particles of type i	$\text{cm}^{-2} \text{Mev}^{-1}$
χ	a function which determines the pitch angle distribution	
ψ	true anomaly	radian
Ω	solid angle;	steradian
	longitude of ascending node	radian
Ω_o	initial longitude of ascending node	radian
ω_e	earth's angular velocity	$7.292(10^{-5}) \text{radian/sec}$
ω_N	weighting factor	

1.0 INTRODUCTION

Prior to 1956, the radiation hazard to manned spaceflight was not apparent. The subsequent rapid increase in knowledge of solar particle events and the discovery of geomagnetically trapped particles in 1958 has led to the necessity of considering space radiation in the development of manned space systems. To meet the need for preliminary design information, digital computer programs were developed to predict the radiation fluxes and radiation doses encountered in space missions.

The first-generation programs computing space-radiation doses were developed to provide preliminary design information, but they were based on meager information about the radiation environment and on a simplified shielding analysis. However, these programs have provided a basis for the development of better programs, incorporating new environmental data and a more sophisticated shielding analysis.

The development of the second-generation computer program, containing additions and modifications to the original program developed by The Boeing Company, has been particularly concerned with the trajectory and environment codes and the radiation-transport codes.

Throughout the development of this new program, efforts have been made to provide maximum flexibility, growth potential, and minimum machine time compatible with detail and accuracy. To provide flexibility, the computer codes are so designed that the analyst has the option of using them independently. For example, the shielding codes may be used to determine the optimum vehicle structure and arrangement of internal equipment to provide maximum radiation shielding; the trajectory code may be used to select an orbit or trajectory incurring an acceptable radiation flux or flux rate; or a variety of B-L maps may be employed to determine the effect of the environmental model. To provide growth capability, the program can readily accept new experimental data on the radiation environment and on the interaction of radiation with matter. Several techniques have been employed to reduce the computer machine time, but the analyst has the option of increasing the accuracy of the flux calculation at the expense of increased machine time. With an understanding of the assumptions, limitations, optional modes, and ramifications of the routines, and with the exercise of good judgment, the program will provide valid, accurate, and economical solutions to space-radiation problems.

The succeeding sections include the theoretical development of the mathematical representations, a discussion of the reliability and validity of the assumptions that have been made, and an evaluation of the results obtained with these codes. The sequence of these sections is in parallel with the following general methods of determining the radiation fluxes and doses for space systems:

- 1) Calculation of the spacecraft trajectory in B, L, and t coordinates;
- 2) Devising a mathematical representation of the space-radiation environment--the radiation environment includes geomagnetically trapped radiation (Van Allen belts), solar particle event radiation, and galactic cosmic radiation;
- 3) Determination of the radiation flux and energy spectra encountered in a given space mission;
- 4) Calculation of the primary and secondary absorbed dose per incident particle (total radiation optional) for a given spacecraft;
- 5) Determination of the total radiation dose, radiation dose rate, and LET spectrum for a given space mission and a given spacecraft by forming the product of the particle flux and the unit flux dose.

Each section in this volume is self-contained in order to develop the topic and show its relationship to the over-all computer program for calculating the radiation dose, dose rate, and LET spectrum incurred in space missions.

2.0 SPACECRAFT TRAJECTORIES

The space-radiation flux is a sensitive function of position and time; hence the radiation flux encountered during a mission depends critically on the accuracy with which the spacecraft trajectory is specified. A number of methods may be employed to calculate the spacecraft trajectory for a given mission, depending on the accuracy and detail of the information required. Experience indicates that the required order of accuracy, compatible with the variability of the radiation environment, is generally \pm tens of kilometers in altitude, \pm one degree in latitude and longitude, and \pm one minute in time; these values are also compatible with present uncertainties of flux values in the radiation belts.

An exact method, accurate to within 1 part in 10^8 but requiring much computer time, can be generated by numerically integrating the equations of motion (Reference 1), considering the accelerations caused by the moon, the sun, and major planets, the atmosphere, and the higher harmonics of the earth's gravitational field to an equal accuracy. To reduce computing time, an approximate method for trajectory determination has been adopted for radiation-flux calculations.

A second method, which accepts trajectories given point by point, has been included to treat certain missions, such as powered flight, which cannot be determined by the approximate method. In these cases, the input trajectories are usually those that have been computed for other mission-planning purposes.

2.1 APPROXIMATE TRAJECTORIES

An earth satellite follows an orbit that can be approximated by a perturbed Keplerian orbit. The magnitude of these perturbations depends on the initial conditions of the orbit and the time. The main perturbing influences for near-earth orbits are the earth's oblateness, the earth's atmosphere, and the moon. These influences cause periodic as well as secular changes in the Keplerian elements of the orbit. The periodic changes can be neglected because their amplitudes are small; the secular change increases linearly with time and cannot be neglected for missions in excess of a few hours.

The effect of the atmosphere is to reduce the semimajor axis of the orbit (Reference 2). In general this effect is bypassed because the radiation environment is sharply attenuated in the atmosphere.

The moon exerts an average torque on the orbit causing it to precess about, approximately, the pole of the ecliptic. The resulting precession increases with the cube of the semimajor axis until it is the dominant, although small, perturbation outside the 24-hour orbit. Since the radiation environment is slowly varying with position at these high altitudes, the effects caused by the moon will be neglected.

Highly eccentric orbits, which penetrate close to the earth, do experience a perigee variation of the order of a kilometer per day (Reference 3). Even this variation is not considered to lead to sufficient change in the encountered flux to warrant its inclusion.

The secular changes due to the earth's oblateness are dominant for all orbits that encounter a significant position-dependent environment. The effect of the higher harmonics falls off more rapidly with altitude. Also the coefficients J_i of the harmonic terms with $i > 2$ are of the order of the square of J_2 (Reference 4). Since the oblateness term yields a latitude-longitude correction which is less than 1 degree per orbit, the higher order terms yield corrections of the order of 1 degree per 300 orbits. Accordingly, all corrections except the earth's oblateness correction will be neglected and this correction will be treated only to the first order in J_2 .

The secular changes in the elements due to the earth's oblateness are well known (Reference 4). They are:

- 1) The reduction in the period of the orbit;
- 2) The regression of the line of nodes;
- 3) The precession of the line of apsides in the orbital plane.

To this order, the geographic position and time after initial perigee of an earth satellite are given by:

$$r = \frac{\ell}{1 + \epsilon \cos \phi}$$

$$\theta = \cos^{-1} [\sin i \sin (\phi + \beta)]$$

$$\phi = \begin{cases} \Omega + \tan^{-1} [\cos i \tan (\psi + \beta)], & \cos (\psi + \beta) > 0 \\ \Omega + \pi + \tan^{-1} [\cos i \tan (\psi + \beta)], & \cos (\psi + \beta) < 0 \end{cases}$$

$$t = \frac{P}{2\pi} M = \frac{P}{2\pi} (E - \epsilon \sin E)$$

where r , θ and ϕ are the geocentric radius, colatitude, and longitude of the satellite; ℓ , i , ϵ , and P are the semilatus rectum, the inclination, the eccentricity and the anomalous period of the orbit; ψ , M , and E are the true, the mean, and the eccentric anomaly; Ω is the longitude of the ascending node; and β is the argument

of perigee. The relationships of these quantities (Figure 1) to the input quantities (apogee altitude h_a , perigee altitude h_p , initial latitude Λ_o , initial longitude ϕ_o) are given by (Reference 4):

$$E = 2 \tan^{-1} \sqrt{\frac{1-\epsilon}{1+\epsilon}} \tan \frac{\phi}{2}$$

$$\epsilon = \frac{h_a - h_p}{2R_e + h_a + h_p} = \frac{h_a - h_p}{2a}$$

$$\ell = a(1 - \epsilon^2)$$

$$P = \frac{2\pi a^{3/2}}{k_e} \frac{1}{1 + (R_e/\ell)^2 J' \sqrt{1 - \epsilon^2} (1 - \frac{3}{2} \sin^2 i)}$$

$$k_e = 1.9965 \times 10^{-2} (Mm)^{3/2}/\text{sec}$$

$$\beta = \beta_o + J' k_e t (R_e/\ell)^2 (2 - \frac{5}{2} \sin^2 i) / a^{3/2}$$

$$J' = (3/2) (R_{eq}/R_e)^2 J_2 = 1.63197 \times 10^{-3}$$

$$\Omega = \Omega_o - \omega_e t - J' k_e t (R_e/\ell)^2 \cos i / a^{3/2}$$

$$\Omega_o = \phi_o - \tan^{-1} (\cos i \tan \beta_o)$$

$$\beta_o = \sin^{-1} (\cos \theta_o / \sin i)$$

where the initial heading determines the quadrant of the inclination angle i . For example, a southeasterly initial heading places the inclination angle in the fourth quadrant. The quantities R_e and R_{eq} are respectively the mean and equatorial radii of the earth.

These expressions give the approximate position for bound orbits. The circular orbit case follows from these by setting $\epsilon = 0$. Since the form is quite simple for this case, extraneous computations of ℓ , ϵ , a , and E are avoided by programming the circular case separately.

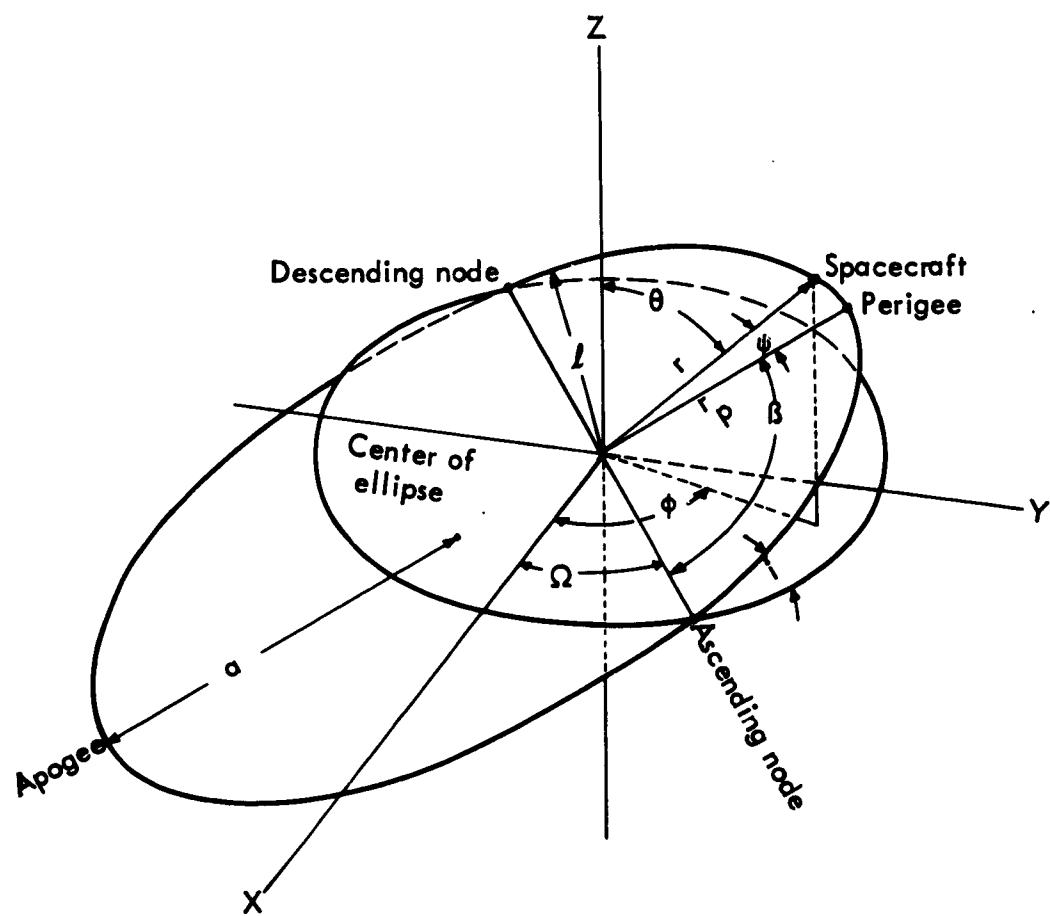


FIGURE 1. Orbit geometry

2.2 POINT-BY-POINT TRAJECTORIES

Trajectories that cannot be approximated by perturbed Keplerian orbits include powered-flight trajectories, highly eccentric orbits, and trajectories for missions that have unique requirements of position and time. Such trajectories are computed for other mission requirements, such as power optimization and rendezvous position, and can be used as input for the radiation-hazard trajectory code. Thus, the trajectory code provides for the acceptance or generation of all conceived mission trajectories. To determine dose and dose rates, these trajectories are converted to magnetic coordinates.

2.3 CONVERSION TO MAGNETIC COORDINATES

The magnetic coordinates that regularize the flux data best are the magnetic flux density B and the shell parameter L developed by McIlwain (Reference 5). Alternatively, the invariant radius R and the invariant latitude λ may be useful for simple geometric visualization. For trapped radiation the validity of the B - L system is directly related to the first and second adiabatic invariants of motion of the trapped particles. Therefore, it is assumed that the environment is given in terms of B and L . In addition, it is assumed that the magnetic field can be represented by a combination of n -tuples of the order 6 or less; in particular the 48 gaussian coefficients of Jensen and Cain (Reference 6). McIlwain's program, adapted and supplied by Hess with the Goddard Space Flight Center's code designation C-3, is used to calculate L . The method is to calculate the integral invariant of Northrup and Teller (Reference 7) and convert this to the shell parameter L , with a control error ERR . ERR is the average fractional error in L (Reference 8). The typical error is 0.1 ERR , while about 1 in 100 cases will have fractional errors of 10 ERR . The first-generation code used $ERR = 0.03$. Since this error can be expected to be too large for some missions with unique requirements, the present code has been set to $ERR = 0.01$. The change added about 1 minute of computer time per trajectory day to the existing code. Test runs indicated that roughly 60 percent of the run time was used in calculating B and L . Therefore, an efficient program avoids extraneous calculations of B and L . A systematic study of the B - L program is outside the scope of this work. However, as more geomagnetic data become available, such a study should be undertaken. For our purposes we assume that the B and L values can be calculated to any degree of accuracy by adjusting ERR so that it is consistent with the most stringent mission requirements. During the present investigation, where the environment does not warrant such accuracy, methods were sought to reduce the computing time by avoiding the calculation of B and L with the C-3 code.

2.4 TIME-SAVING TECHNIQUES

The most obvious method to decrease computer time is to bypass McIlwain's program where the flux is known to be negligible. For low-altitude orbits the flux of trapped radiation is zero for more than half the geocentric spherical surface. With a

limited survey of the low-altitude flux data (References 9 and 10) one deduces that the flux of trapped particles for altitudes under 800 km is confined to the Atlantic between 110 degrees West to 80 degrees East. For altitudes under 400 km the region shrinks somewhat so that it is contained between 75 degrees West and 60 degrees East. Therefore, if one bypasses the calculation outside this region, a 50-percent reduction in run time will be realized. Since the shape and location of this region are only approximately known, we make it generously large and set the flux of trapped particles equal to zero for longitudes west of 120 degrees and east of 90 degrees East for altitudes below 800 km. An option to bypass this geographic test is provided because, if one is interested in the untrapped radiation, magnetic coordinates must be calculated at all longitudes. In regions suspected of having significant radiation, whether trapped or untrapped, other means of saving computer time must be employed.

A very promising method of computing B and L efficiently is based upon using the C-3 code only at controlled points along the trajectory. Let $B_i = B(t_i)$ and $L_i = L(t_i)$ be the values of the smooth functions $B(t)$ and $L(t)$ at n selected points t_i ; $i = 1, 2, \dots, n$; in an interval $t_1 \leq t \leq t_n$. Through the n computed values of L_i , for example, there is a unique polynomial of order $n-1$. This polynomial approximates the shell parameter $L(t)$ in the interval $t_1 \leq t \leq t_n$ and has been used to calculate what may be called interpolated values within each interval $\Delta t = t_{i+1} - t_i$ at a minor cost in computing time compared with the time-consuming integrals of the C-3 code. The magnetic induction $B(t)$ may be similarly treated. For a sample trajectory, Table 1 shows the average percentage differences between the interpolated values at seven points within each interval Δt and calculated values at the same points according to the C-3 code with $ERR = 0.01$ for several interval sizes. The column headed No. of Cases denotes the number of intervals of size Δt considered. The averages are then taken over points which are, in number, seven times the number of cases. The quantities called

$$\left(\left\langle \frac{|\Delta L|}{L} \right\rangle \right)_{\max}$$

are the maximum over the number of cases of averages taken in each case.

Table 1

AVERAGE AND MAXIMUM AVERAGE PERCENTAGE DIFFERENCES OF
COMPUTED AND INTERPOLATED MAGNETIC COORDINATES

Δt (sec)	No. of Cases	$\left\langle \frac{ \Delta B }{B} \right\rangle$ (percent)	$\left\langle \frac{ \Delta L }{L} \right\rangle$ (percent)	$\left(\left\langle \frac{ \Delta B }{B} \right\rangle \right)_7$ _{max} (percent)	$\left(\left\langle \frac{ \Delta L }{L} \right\rangle \right)_7$ _{max} (percent)
60	7	.0001	.0061	.0006	.0147
80	5	.0002	.0036	.0006	.0110
120	7	.0017	.0056	.0063	.0203
160	10	.0084	.0127	.0236	.0262
320	4	.0460	.2050	.076	.380
960	3	6.3	8.6	12.6	15.1

That is:

$$\left\langle \frac{|\Delta B|}{B} \right\rangle = 100 \frac{1}{7N} \sum_{i=1}^N \sum_{k=1}^7 \frac{|\Delta B|}{B_i^k}$$

$$\text{and} \quad \left(\left\langle \frac{|\Delta B|}{B} \right\rangle \right)_7 \text{max} = 100 \max \left\{ \frac{1}{7} \sum_{k=1}^7 \frac{|\Delta B|}{B_i^k} \mid i=1, \dots, N \right\}$$

where N denotes the number of cases and B_i^k denotes the computed B values at the k^{th} point in the i^{th} case.

These results indicate that the interpolation routine maintains the accuracy of the C-3 code for small time intervals. This test run is too limited to justify a blanket recommendation to use this interpolation method for time intervals less than a specified single value. However, for any region of space, some range of time intervals exists where the interpolation method will suffice and the C-3 code may be passed. Hence, there is promise of securing any required density of trajectory points in magnetic coordinates with little more machine time than that required by the former program (Reference 11). The requirements on the density of points is imposed by the flux and dose integration, which will be treated in Section 8.0. A discussion of various aspects of the radiation environment relating to the dose rate will be useful in understanding these requirements.

3.0 RADIATION ENVIRONMENT

The ionizing radiation environment in cis-lunar space may be categorized as geomagnetically trapped or untrapped radiation. In principle, the trapped radiation consists of charged particles that remain in periodic orbits in the magnetosphere for several drift periods. In practice, however, this categorization is subjective; most radiation detectors do not distinguish between particles in trapped orbits and those that are momentarily trapped. The raw data obtained in the Van Allen belts is processed to obtain a flux which must be considered trapped radiation; that is, the galactic background is subtracted, the transient behavior is separated, and the data are smoothed in B-L coordinates. Thus the resulting flux is the best present estimate of the trapped component. All other radiation, such as galactic-cosmic and solar-particle radiation will be treated as untrapped radiation. The level of the ionizing neutral components, chiefly photons and neutrons, is so low that they are neglected in this radiation hazard study.

3.1 TRAPPED RADIATION

The trapped-particle flux is given experimentally in B and L, the magnetic coordinates of McIlwain (Reference 5). B is the magnetic induction at the point in space. L is the magnetic shell parameter that labels the shell upon which the guiding center of the trapped particles is adiabatically confined as it drifts around the earth. McIlwain has shown that L is approximately constant along the real magnetic field line. In a dipole field, L is rigorously constant along the field line and has the geometric property of being the equatorial distance from the dipole center to the field line. The B surfaces and L surfaces for a dipole field are shown in Figure 2. For the real field these smooth, symmetrical surfaces become warped and asymmetrical, particularly at low altitudes. Because of the connection to the adiabatic invariants of the trapped-particle motion, the trapped particle flux is a function of B and L.

For analysis, all reported fluxes are considered to arise from particles adiabatically trapped for several drift periods. The characteristics of this flux that are important for dose calculations are the omnidirectional flux, the spectral distribution, and the angular distribution at any point.

The most common presentation of the omnidirectional fluxes, the isoflux contours in B-L space, is called an omnidirectional flux map. This map is converted to tabular form for the computer. The simplest tabulation to use is that of the fluxes at B-L grid points. Whether the conversion is accomplished automatically or by hand, the most efficient grid must be determined from the flux map. In general, this grid is not uniform. A particularly successful method of conversion proceeds as follows: on each of a large number of L shells the logarithm of the flux is plotted versus B. The density of B grid lines is then chosen high enough to enable linear interpolation to reasonably approximate the logarithm of the flux at intermediate B values for all chosen L shells.

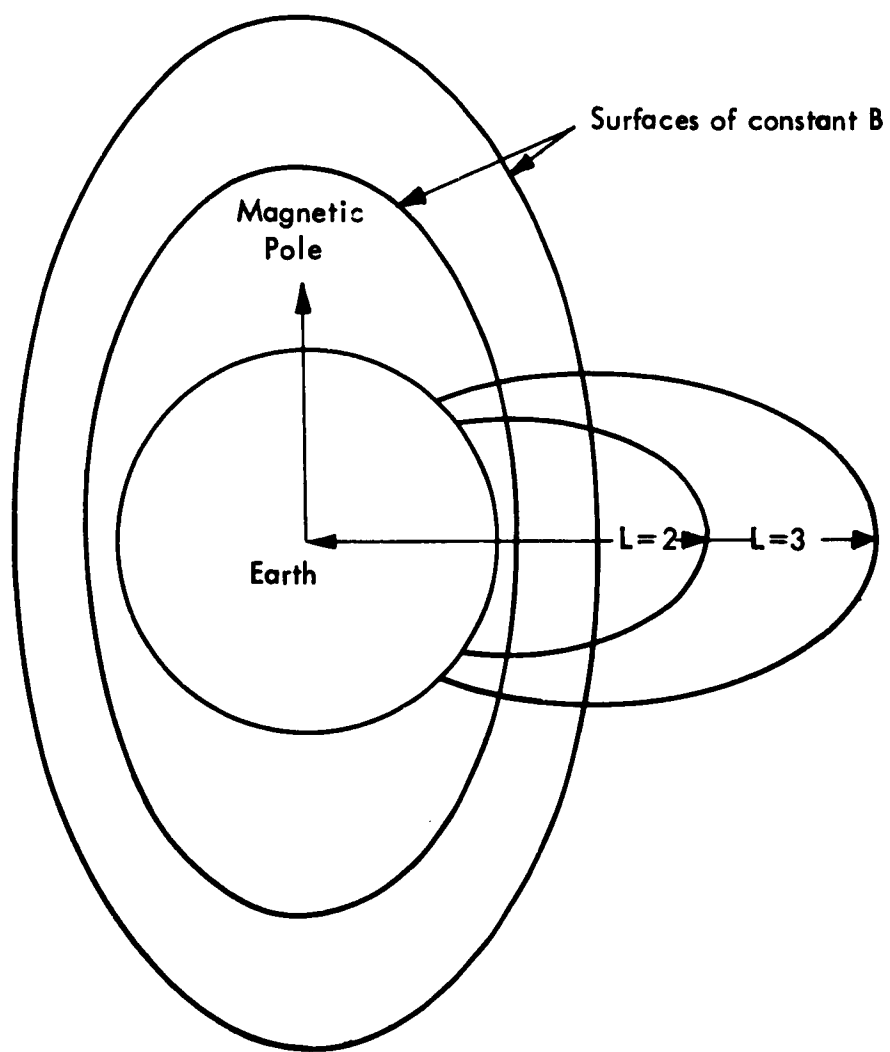


FIGURE 2. The geometry of the B-L coordinate system

Then the logarithm of the flux at each B grid line is plotted as a function of L and the density of L grid lines is chosen to validate linear interpolation. These plots are then used to extrapolate in B and L beyond the magnetic equator so as to completely surround the magnetic equator by grid points with non-zero fluxes. This ensures that the linear interpolation of the logarithm of the flux will give a reasonably accurate value of the flux throughout the map. The flux maps are reported to be accurate within a factor of two. Since the above conversion to tabular form can easily be accomplished while maintaining a 10 to 20 percent accuracy, higher-order interpolation schemes are not necessary. The proton map constructed by W. Hess from the 1958 measurements, and the Aerospace proton and electron maps compiled by J. Vette (Reference 12) from the 1962 measurements are used in the program. Other tabulations can be substituted if desired. Since the grid and extent of a new flux table may be different, such information must be provided as flux table input data.

The angular distributions presented in this section are based on the maps of Hess and Vette; furthermore, the energy spectra were synthesized to be appropriate for these maps.

3.1.1 Omnidirectional Flux Maps

The omnidirectional flux is the count rate of a spherical counter of unit cross sectional area and of unit efficiency. The omnidirectional flux of each particle type measured in the magnetosphere is reported in B and L, as determined by McIlwain's code. The low altitude is averaged in longitude; additionally the data on high L-shells are averaged in time.

The low-altitude smoothing affects the fluxes that are at least 3 orders of magnitude down from the maximum values. The longitudinal variations occur in regions of B and L that map into the earth and dense atmosphere in the Atlantic. The minimum altitude of a B-L trace is called h_{min} . The B-L plots for a family of h_{min} are shown in Figure 3. The particles at B values lying above the $h_{min} = 100$ curve will be severely scattered over the anomaly. Hence, they do not remain trapped for a drift period. The errors introduced by treating low-altitude fluxes as trapped particles will be insignificant for the normal trajectory which also passes through the South Atlantic region where the fluxes are much higher.

The high L shell smoothing affects large-magnitude fluxes. The diurnal variations, which can amount to an order of magnitude, have been averaged out. In most instances, the periodic variations that can be correlated to the sun's rotation period have also been averaged out. These also are an order of magnitude at $L = 4$ (Reference 13). Although such data give only the average flux and dose rate, these averages are useful estimates in any case and become correct for long-term orbital missions. A discussion of the time variations in flux and dose rate which chiefly affect short missions is given in Section 3.1.3.

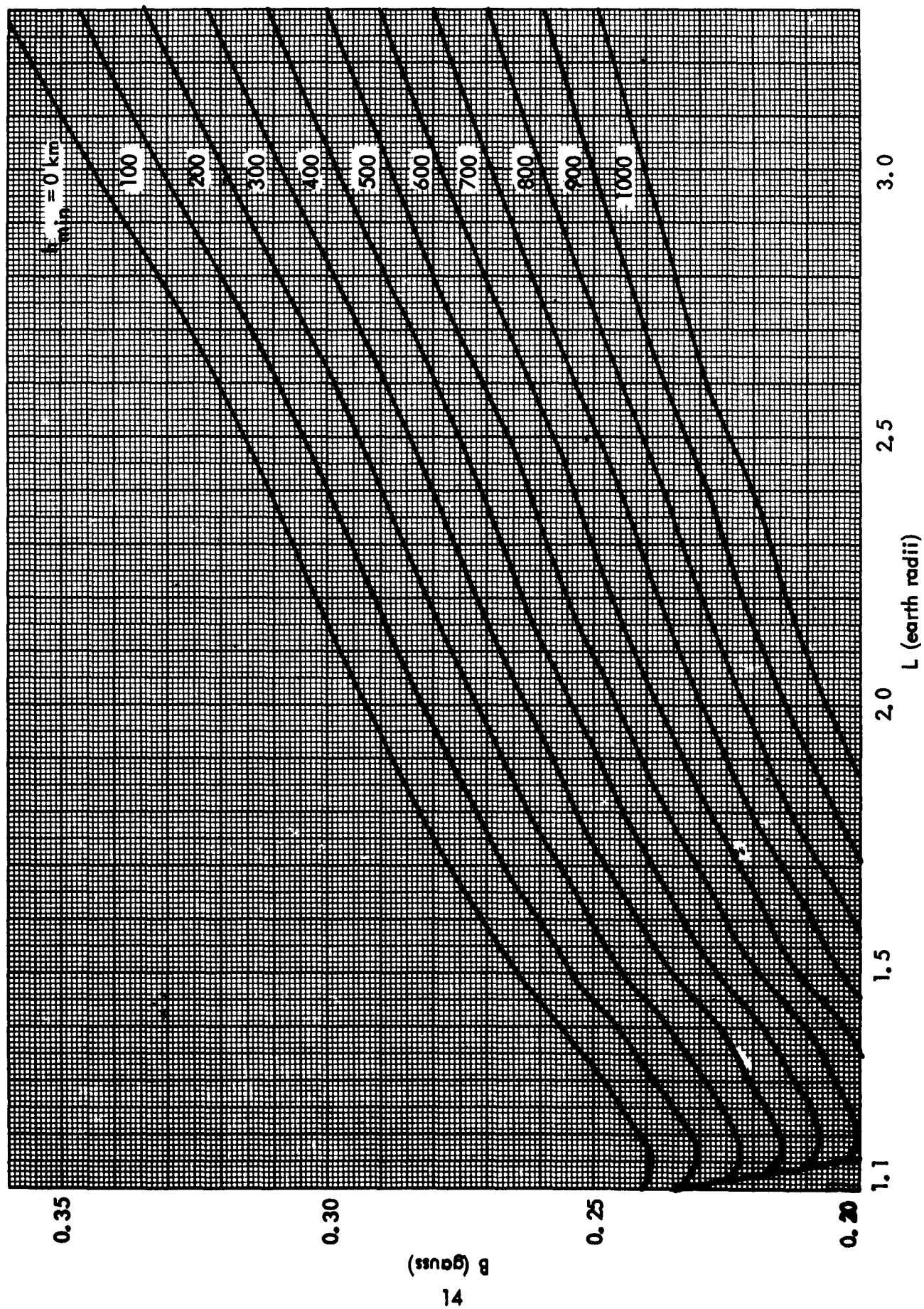


FIGURE 3 A B-L plot of the minimum altitude h_{\min}

The flux map compiled by Hess from data obtained by Explorer IV (Reference 5) and Pioneer III and IV is shown in Figure 4. The contours are labeled by the integral omnidirectional flux of protons of energies greater than 30 Mev. The composite spectrum normalized to 1 above 30 Mev which was proposed by Hess is given by:

$$\begin{aligned} j(E) &= 0.009019 & 20 \leq E \leq 40 \text{ Mev} \\ &= 0.014431 \exp(-E/85) & 40 \leq E \leq 200 \text{ Mev} \\ &= 0.0044095 \exp(-E/172) & 200 \leq E \leq 400 \text{ Mev} \\ &= 0.0022047 \exp(-E/245) & 400 \leq E \leq 1000 \text{ Mev} \end{aligned}$$

This spectrum is portrayed graphically in Figure 5. The high-energy proton map compiled by Vette (Reference 12) from data obtained by McIlwain on Explorer XV augmented by data of Freden (Reference 10) is shown in Figure 6. The contours are labeled by the integral flux from 40 to 80 Mev. The spectrum proposed by Vette normalized to one between 40-80 Mev is given as:

$$\begin{aligned} j(E) &= 0.0314 & 20 \leq E \leq 40 \text{ Mev} \\ &= 0.0505 \exp(-E/84) & 40 \leq E \leq 150 \text{ Mev} \\ &= 0.0276 \exp(-E/125) & 150 \leq E \end{aligned}$$

This spectrum is compared with Hess' in Figure 5. The electron flux map representing the environment on about 1 November 1962 was compiled by Vette and is portrayed in Figure 7. The contours are labeled by the integral flux of electrons of energies greater than 0.5 Mev. The spectrum, also proposed by Vette, normalized to one above 0.5 Mev is given as:

$$\begin{aligned} j(E) &= 1.024 \exp(-0.575E - 0.055E^2) & L \leq 1.5 \\ &= 4.082 \exp(-E/0.58) & L > 1.5 \end{aligned}$$

This spectrum is portrayed in Figure 8. The low-energy-proton map compiled by Vette, based on Freden's data in 1962, is shown in Figure 9. The contours are labeled by the integral flux of protons of energies between 5 and 20 Mev. The spectrum that is suggested by Vette, normalized to one between 5 and 20 Mev is given by:

$$\begin{aligned} j(E) &= 974.79 E^{-4.5} & 4 \leq E \leq 15 \text{ Mev} \\ &= 974.79 (15)^{-4.5} = 4.972 \times 10^{-3} & 15 \leq E \leq 20 \text{ Mev} \end{aligned}$$

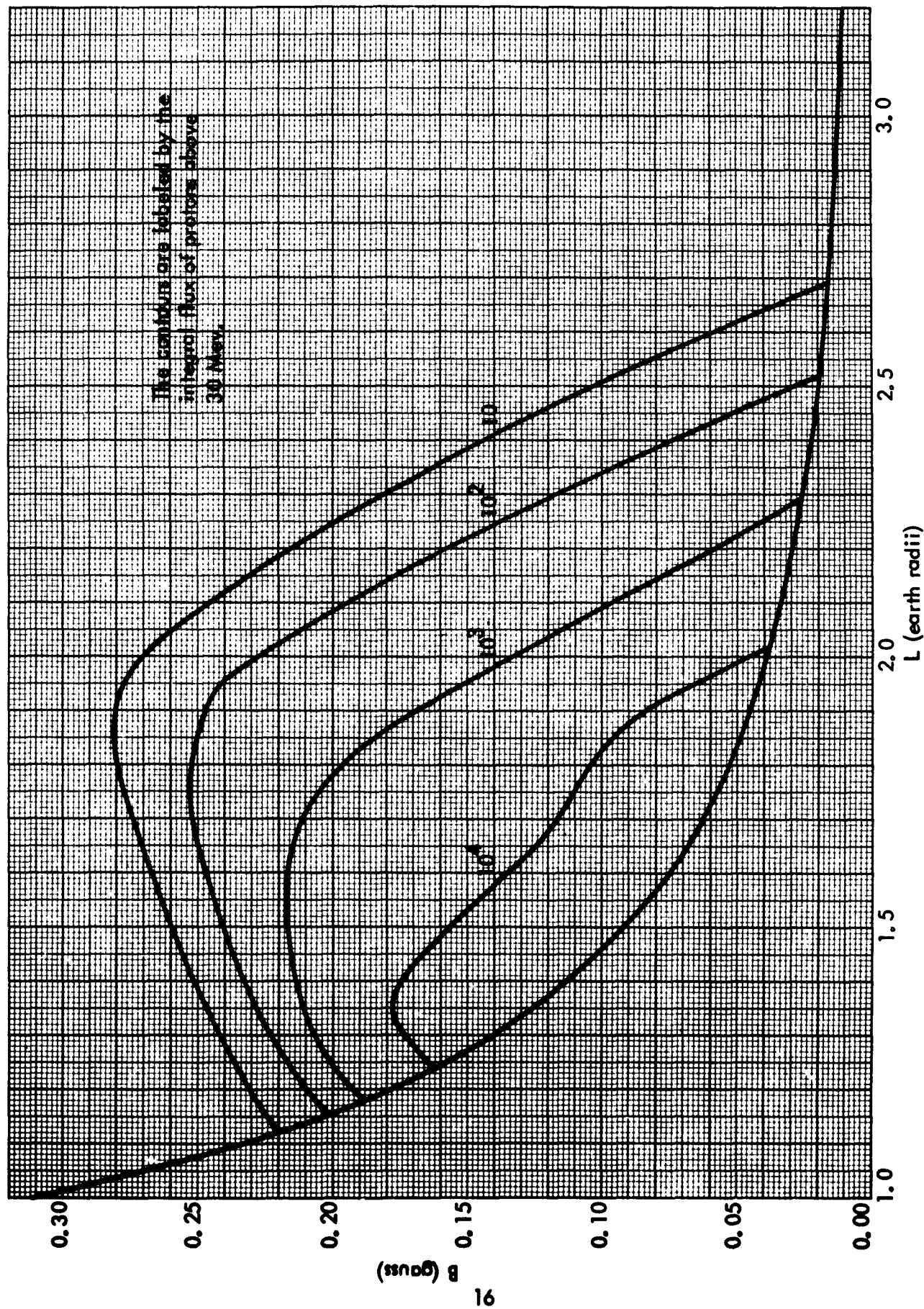


FIGURE 4. The Hess P-1 proton flux map

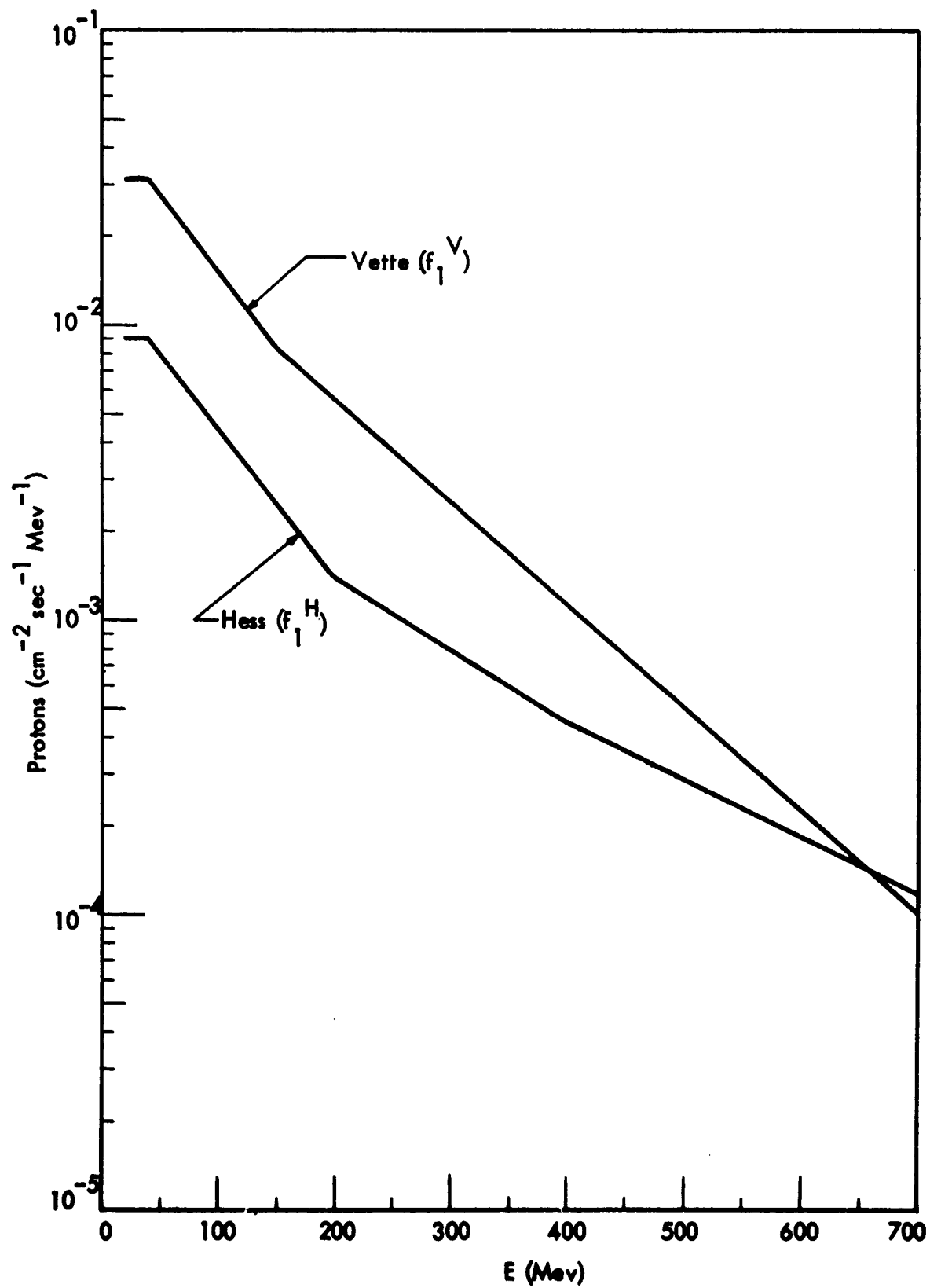


FIGURE 5. The composite spectra of Hess and Vette

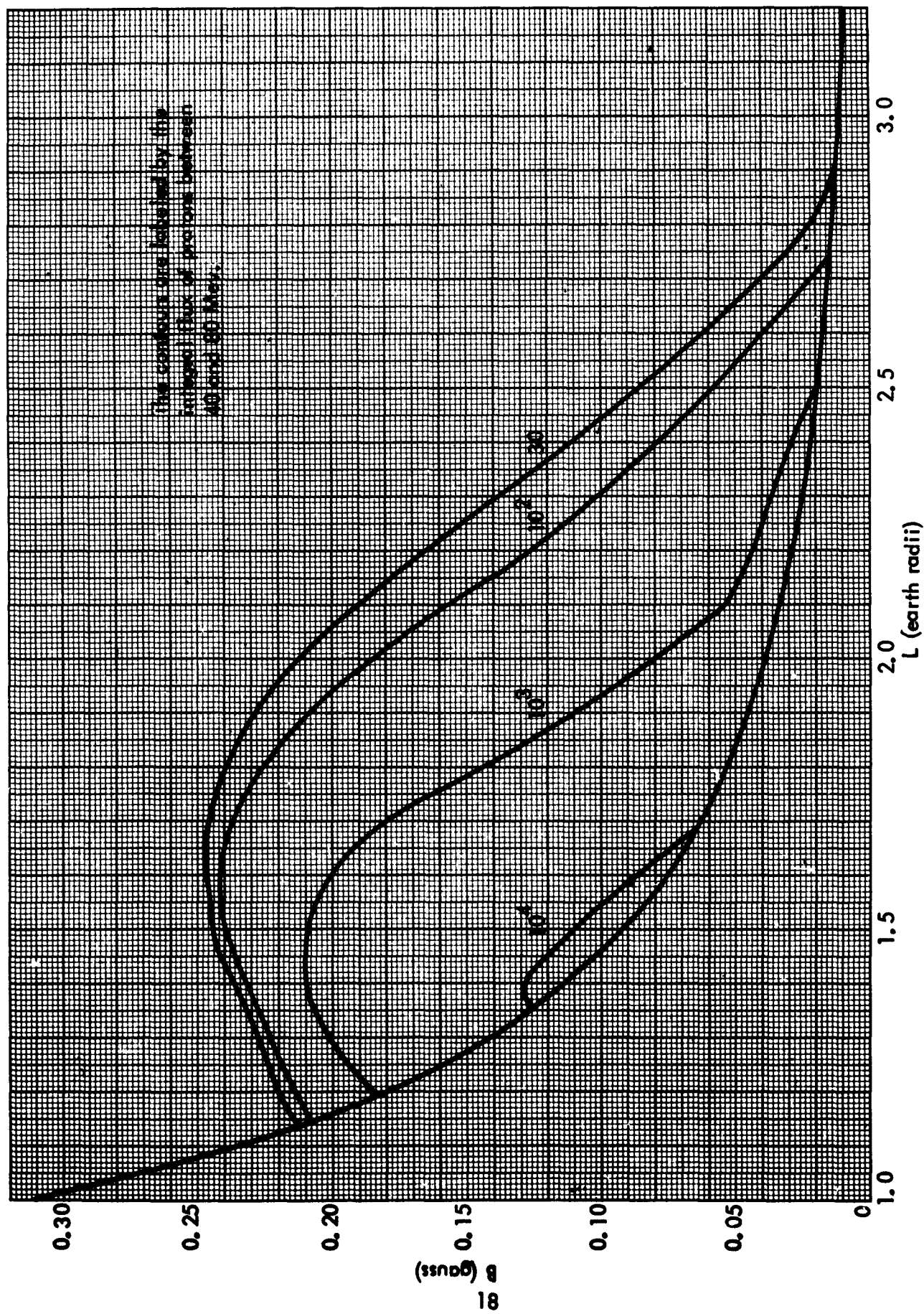


FIGURE 6. The Vette high-energy proton map

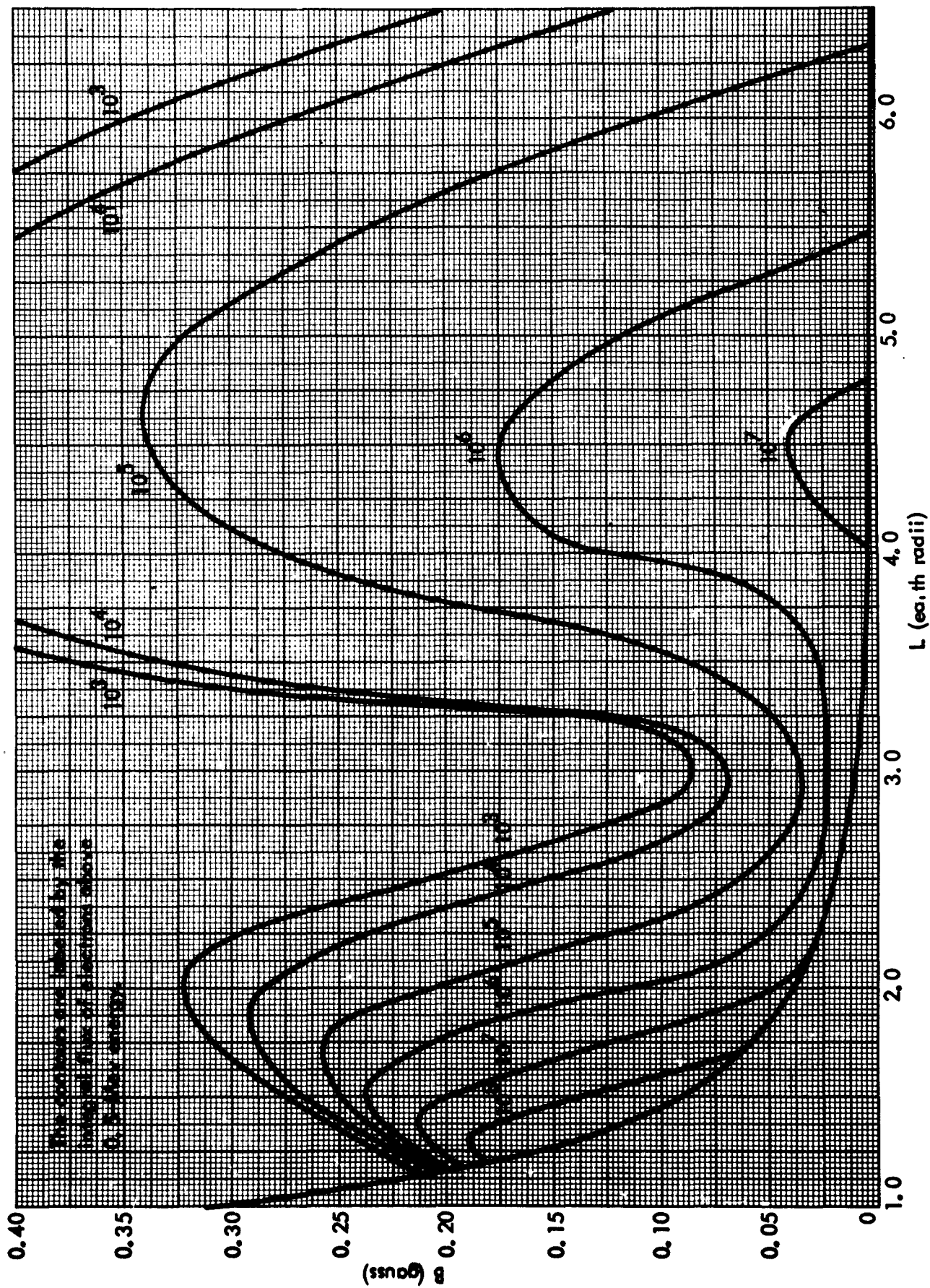


FIGURE 7. The electron flux map (November 1962)

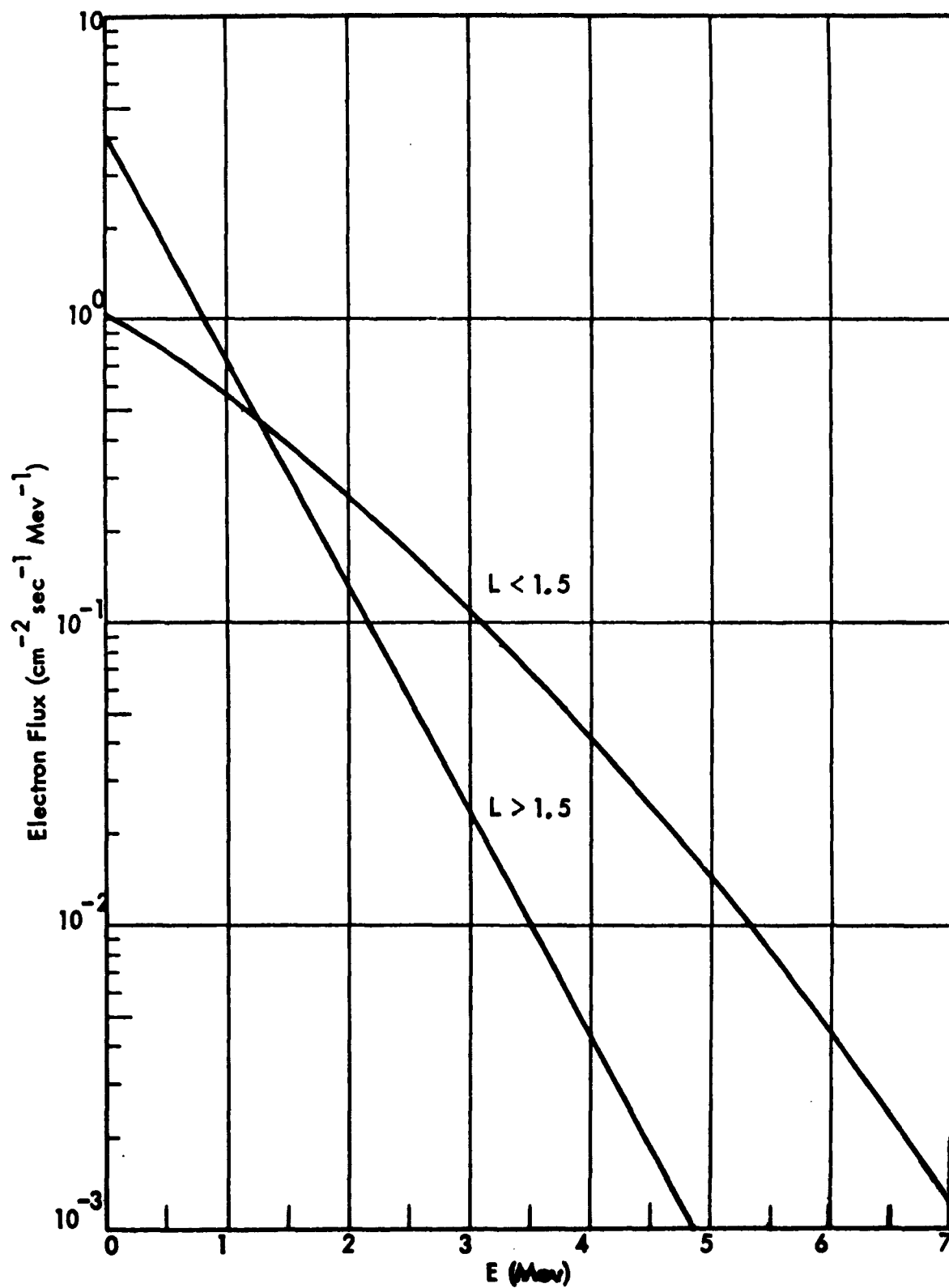


FIGURE 8. The electron spectrum proposed by Vette

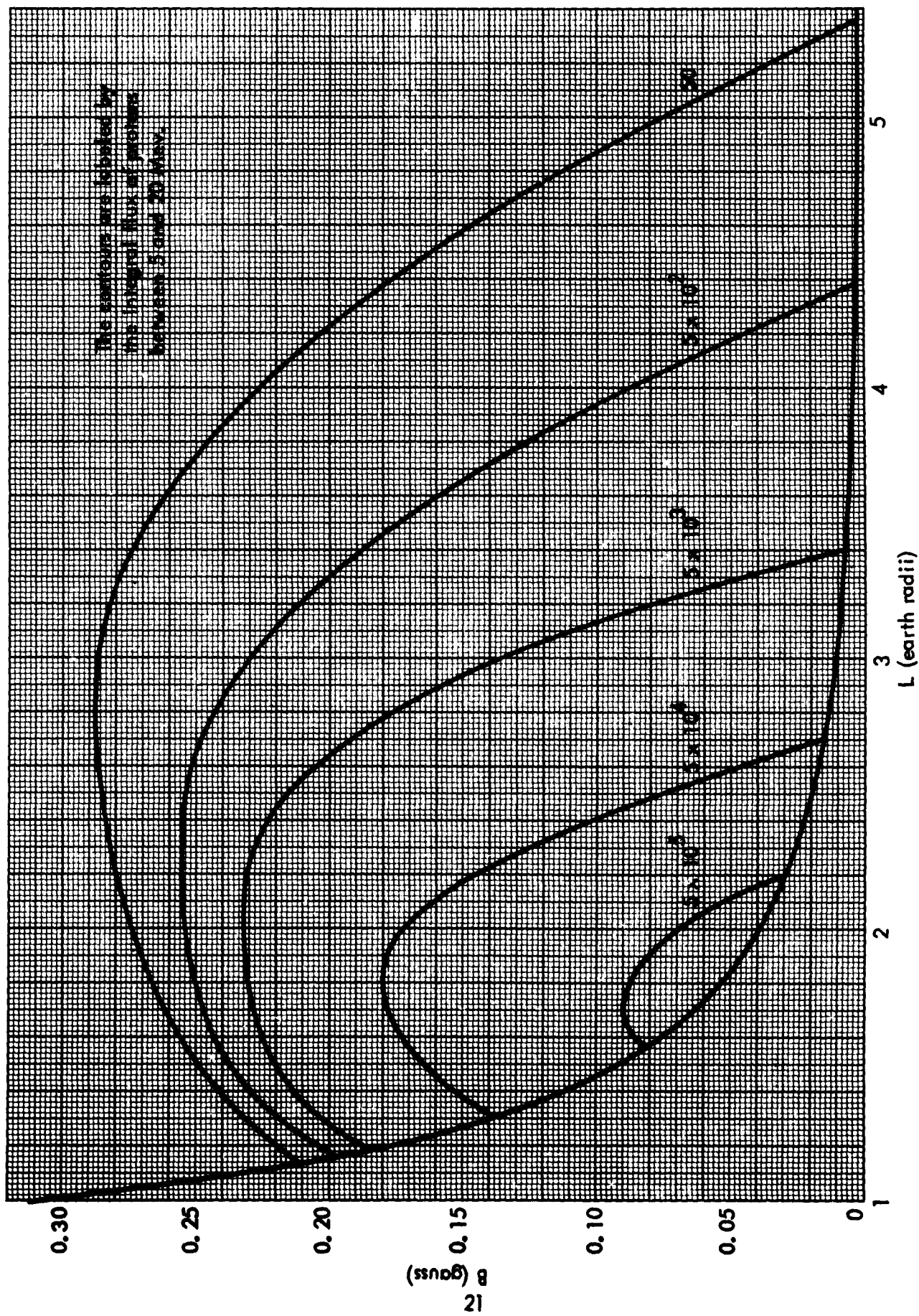


FIGURE 9. The Vette low-energy proton map

Use of these spectra would yield a one-to-one correspondence between the omnidirectional flux and the dose rate inside a uniformly shielded chamber. Dosimetry measurements (Reference 14) show that there is no one-to-one correspondence and that spectral and angular variations must be considered.

3.1.2 Spectral Dependence

Direct spectral measurements of the protons (Reference 15) and of the electrons (Reference 16) have established that the spectrum is strongly L-dependent and at least slightly B-dependent. Additional analysis of Explorer IV data (Reference 17) and of Midas data (Reference 18) supports this conclusion. To determine the dose rates at any point it is necessary to know the appropriate energy spectrum for each particle type as well as its respective flux. Hence, a radiation environment program must specify the spectra as well as the fluxes of all particles at a particular B-L point. In addition, this specification must be in a form in which the flux can be integrated from point to point, retaining the spectral dependence so that the total differential energy flux for any mission can be determined.

It is possible, of course, to specify the differential energy flux at any point on an energy grid and then simply integrate, in mission time, these energy-grid fluxes. To calculate the dose rate and mission dose from these data would require that the many spectra generated be processed by the shielding code. This extremely costly process requires, at the very minimum, 20 separate runs, one for each grid point. It appears more efficient to fit the measured spectrum at each point to a linear combination of a finite number (≤ 10) of basic spectra and determine the flux and total mission flux of each spectral type. Then the dose rate and mission dose are easily obtained through multiplication by the respective dose conversion numbers obtained with a finite number (≤ 10) of runs of the shielding code and through summing these contributions. In addition, if the basic spectra are chosen to be characteristic of the sources and of the predominant modulations by the loss mechanisms, this decomposition of the spectral dependence might aid attempts at understanding these mechanisms. Unfortunately, the source and loss mechanisms have not been well enough determined to realize this additional value.

The electron spectra, as measured by H. West (Reference 16) in the late fall of 1962, provide a fair coverage of the electron belt. The measurements were performed with a five-channel, permanent-magnet, 180-degree-focusing beta-ray spectrometer. The five energy channels were 0.325, 0.955, 1.63, 2.40 and 3.25 Mev. Sixty representative spectra, measured in the range $B \leq 0.24$ gauss for $L < 1.7$ and $B \approx 0.010$ gauss for $L > 1.7$, were kindly supplied by H. West. These measurements indicated that the electron spectrum softens from a fission-like spectrum as L increases out to about 1.6. Here an inflection in the spectrum between 1 and 2 Mev is apparent and is portrayed as a depletion in the flux near 1 Mev as L increases to 2.7. As L increases from 2.7, the flux at 1 Mev builds back up while the spectrum above 2.4 Mev becomes steeper until at $L = 4$ the spectrum resembles that at $L = 1.5$. Then

as L increases above 4, the spectrum continually softens. At low L values and large B values the differential flux was depleted at low energies in a manner consistent with the calculations of Walt (Reference 19) on the atmospheric scattering loss mechanism.

On the basis of this qualitative behavior, the spectra measured at $L \geq 1.7$ on October 27, 1962, were processed utilizing five basic spectra. These measured spectra contain an undetermined contribution from a Russian high-altitude test conducted earlier in October. These five spectra included as source-characterizing spectra the Carter (Reference 20) fission spectrum, a steep low-energy spectrum expected from a neutron albedo source, and an exponential spectrum with a mean energy of 0.5 Mev for the outer belt. The loss-modulated spectra were represented by a Gaussian idealization of the spectrum measured by West at $L = 1.15$, $B = 0.258$, and a spectrum resembling the one measured at $L = 2.7$, $B = 0.08$. Linear combinations of these five were least-squares fitted to the smoothed spectra of West at every 0.5 Mev from 0.5 to 4.0 Mev. Although the fit in this range was promising (relative standard deviations σ on the eight points from 0.01 to 0.2), the spectrum was unrealistic outside this range, in a number of cases. This can be expected; even a negative differential flux can occur. For example, suppose the best fit in the 1- to 3-Mev range requires a negative coefficient for the fission spectrum; then, since the fission spectrum is the hardest spectrum of the set, the resultant fitted spectrum must become negative at some higher energy.

Another disturbing aspect of the use of this set occurred when a fit to the spectra measured at L values less than 1.7 was attempted. Although the fit was reasonable ($\sigma \leq 0.25$), none of the spectra were as well fit as in the slot region, $2.0 < L < 3$, where $\sigma \approx 0.01$. Evidently, this basic set was securing the best fit where the flux and the expected dose rate were relatively small.

The complexity of the spectral variations at low L values, which are evident in the 60 representative experimental spectra plus the promise of better definition at low altitudes as more of West's data are reduced, called for a more flexible basic set. The following set of eight spectra, normalized to unity above 0.5 Mev, were chosen:

$$f_1(E) = 39.745 \begin{cases} \exp(-7.35E) & E \leq 0.8 \text{ Mev} \\ 6.093 \times 10^{-5} \exp(-24E) & E \geq 0.8 \text{ Mev} \end{cases}$$

$$f_2(E) = 5.2603 \exp[-5.555(E - 0.3)^2]$$

$$f_3(E) = 1.4633 \exp[-5.555(E - 0.9)^2]$$

$$f_4(E) = 1.3303 \exp[-5.555(E - 1.5)^2]$$

$$f_5(E) = 1.3298 \exp [-5.555(E - 2.1)^2]$$

$$f_6(E) = 1.3298 \exp [-5.555(E - 2.7)^2]$$

$$f_7(E) = 1.28866 \begin{cases} \exp[-5.555(E-3.3)^2] & E \leq 3.3 \text{ Mev} \\ 3,827.5 \exp(-2.5E) & E \geq 3.3 \text{ Mev} \end{cases}$$

$$f_8(E) = 0.77189 \begin{cases} \exp[-5.555(E-3.3)^2] & E \leq 3.3 \text{ Mev} \\ 12.139 \exp(60.575E - 0.0055E^2) & E \geq 3.3 \text{ Mev} \end{cases}$$

These eight spectra are displayed in Figure 10.

To reduce the probability of obtaining unrealistic differential flux at high and low energies, West's spectra were extrapolated down to zero energy and out to 7 Mev. A 15-point least-squares fit (at each 0.5 Mev) was then obtained for the amplitudes of these eight basic spectra. Thus each of the 60 spectra $G_i(E)$ is fitted to an analytic function of the form

$$G_i(E) \approx \sum_{j=1}^8 C_i(j) f_j(E) = F_i(E)$$

such that

$$\sigma_i^2 = \frac{1}{14} \sum_{k=1}^{15} \left(1 - \frac{F_i(E_k)}{G_i(E_k)} \right)^2$$

is minimized. Nearly all values of σ_i were in the range $0.01 \leq \sigma_i \leq 0.04$.

Each spectrum $G_i(E)$ was based on the measured spectrum at a point (B_i, L_i) . The resulting coefficients $C_i(j)$ were normalized to a unit sum. That is, coefficients $C_i(B_i, L_i)$ were defined such that:

$$C_i(B_i, L_i) = \frac{C_i(j)}{\sum_{j=1}^8 C_i(j)}$$

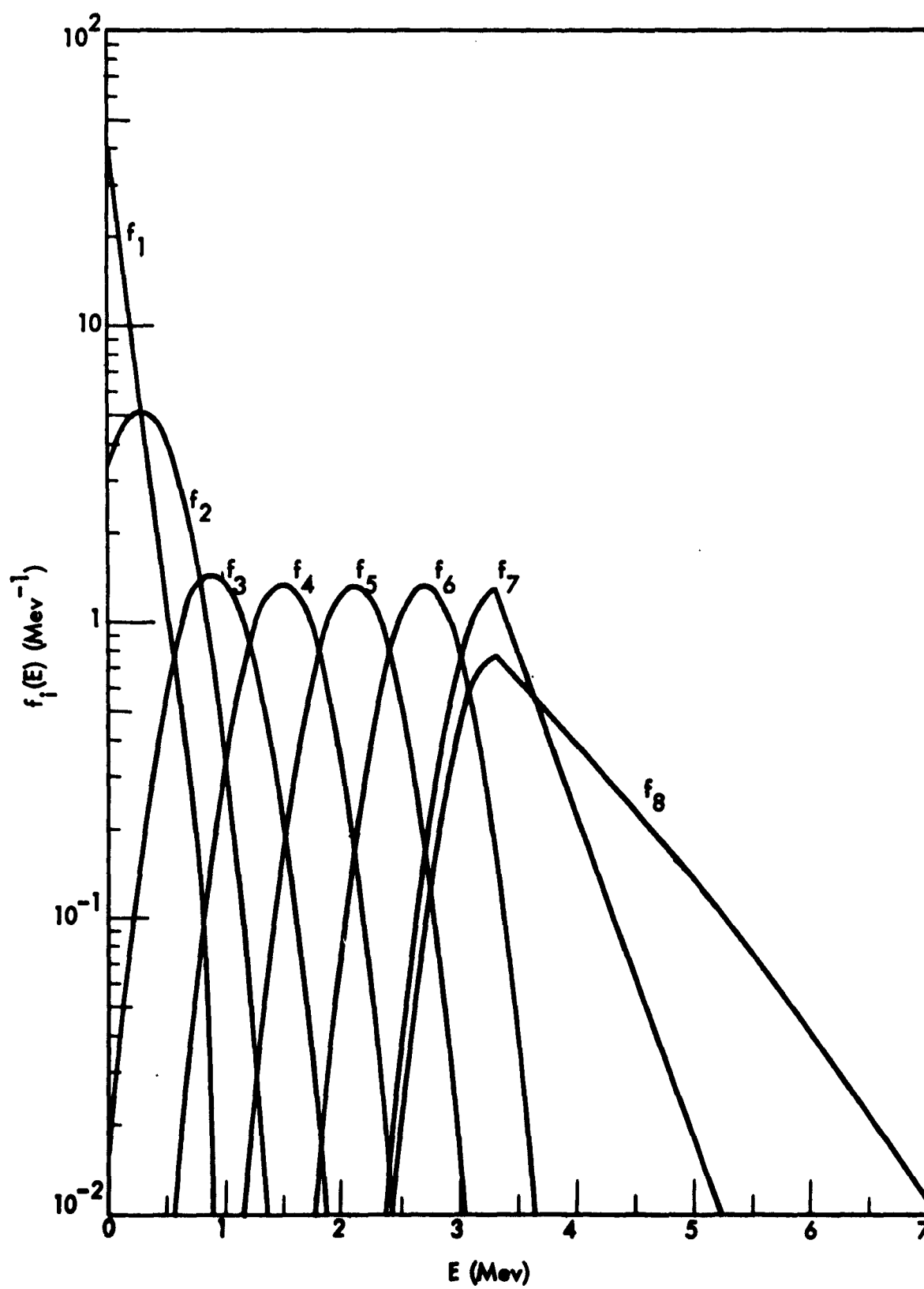


FIGURE 10. The basic electron spectra used in the program

Hence:

$$\sum_{i=1}^8 C_i(B_i, L_i) = 1$$

These coefficients, grouped into the B ranges 0 to 0.10, 0.125 to 0.17, 0.17 to 0.20, were plotted against L. Smooth curves through the data were then interpreted as the L dependence of the coefficients on the B grid lines $B_i = 0.08, 0.14,$ and 0.18 gauss. The density of L-grid lines was chosen so as to validate linear interpolation. The L dependence at the equator is shown graphically in Figures 11 and 12. The B dependence is less pronounced as seen from the example in Figure 13. The resultant C tables of the coefficients $C_i(B, L)$ were then checked for unit normalization and submitted as data to the trajectory and environment code.

This detailed approach employed for electrons is not feasible for protons because the spectral data are so limited. Where available, measured spectra were chosen as basic spectral forms. On the higher L shells, the direct spectral measurements were supplemented with some geiger counter data. In general, the spectrum of the trapped protons softens with increasing L. McIlwain (Reference 17) deduces that the data above $L = 1.4$ are consistent with a spectrum for protons above 30 Mev of the form:

$$j(E) = \frac{1}{E_0} \exp[-(E - 30)/E_0(L)]$$

with $E_0 = a L^{-b}$.

A least squares analysis of Explorer IV data from 31 to 43 Mev gave

$$a = 306 \pm 28$$

$$b = 5.2 \pm 0.2$$

Imhof and Smith (Reference 18) find that their data are consistent with the same form if

$$a = 460 \pm 110$$

$$b = 4.8 \pm 0.4$$

These are Geiger counter and scintillation counter measurements and as such are not comprehensive measurements of the energy spectrum. The only comprehensive measurements of the positional dependence of the proton energy spectrum are reported by Naugle and Kniffen (Reference 15).

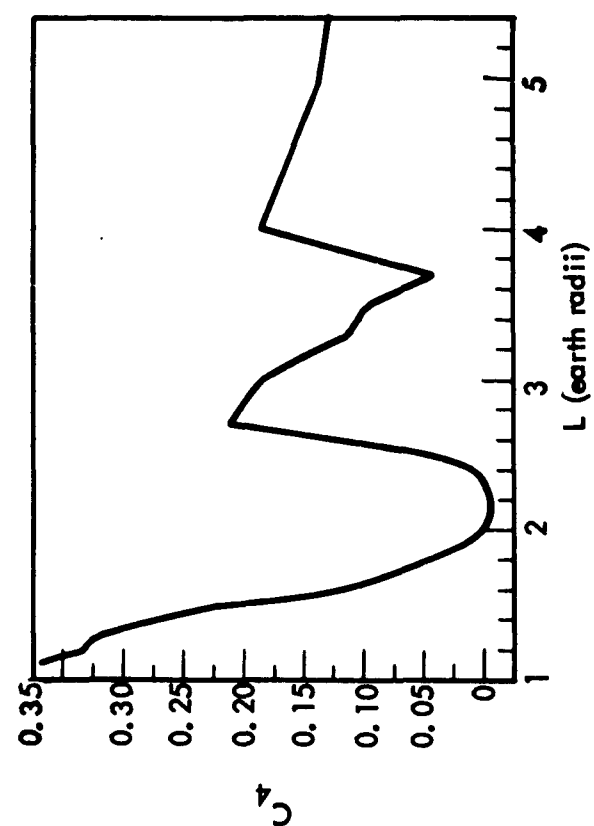
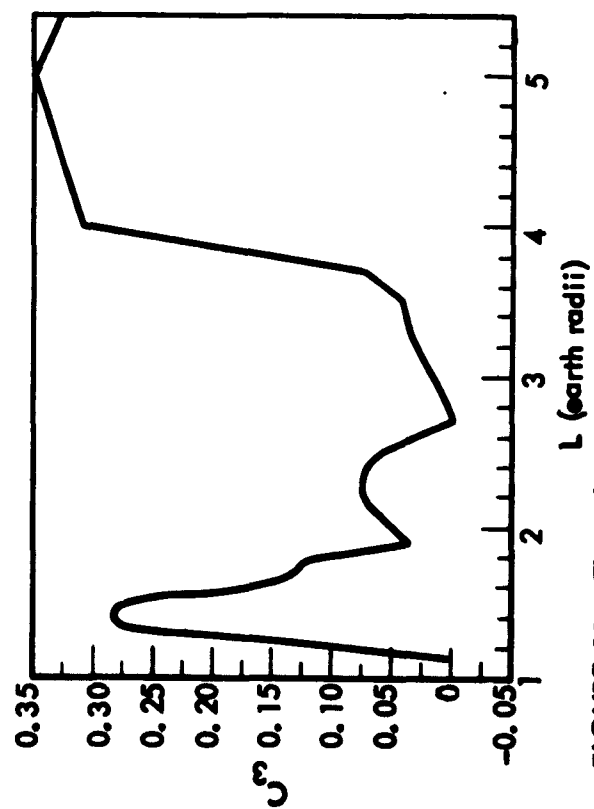
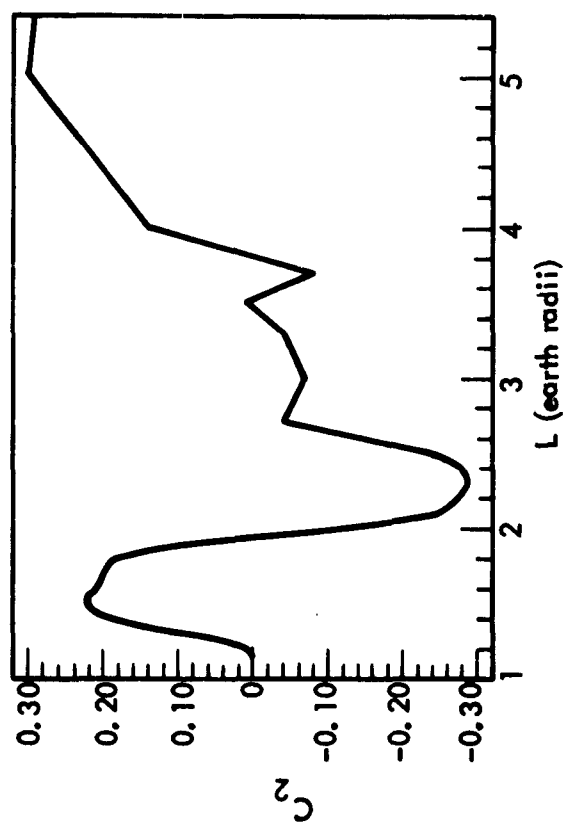
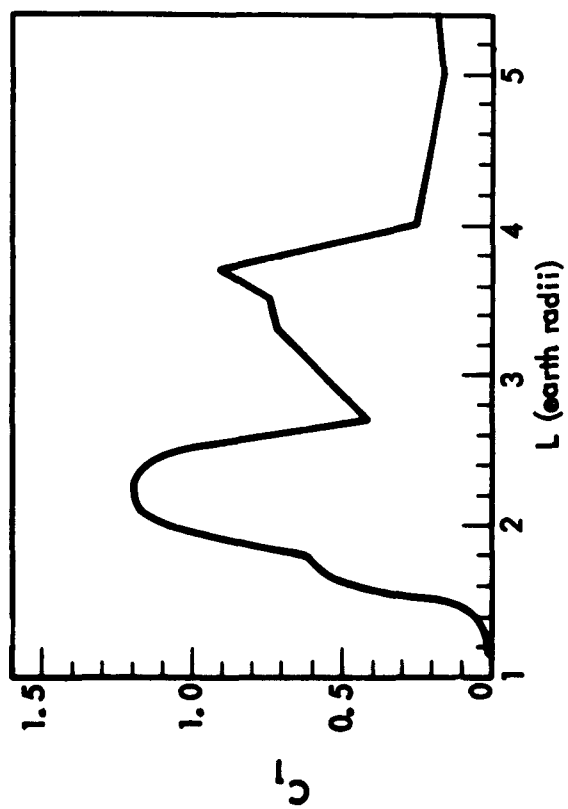


FIGURE 11. The relative amplitudes of the first four basic electron spectra as determined from West's measured spectra

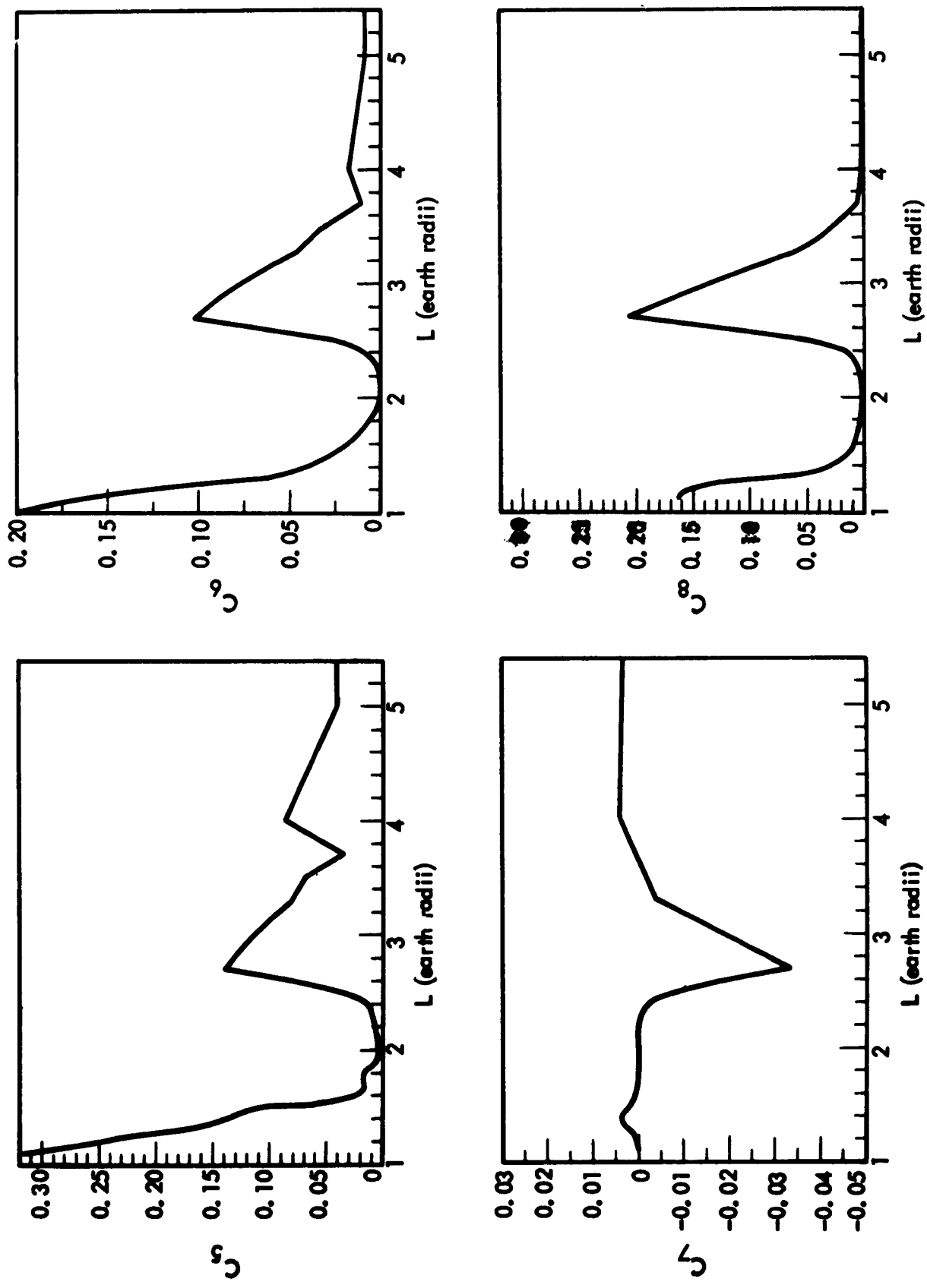


FIGURE 12. The relative amplitudes of the last four basic electron spectra as determined from West's measured spectra

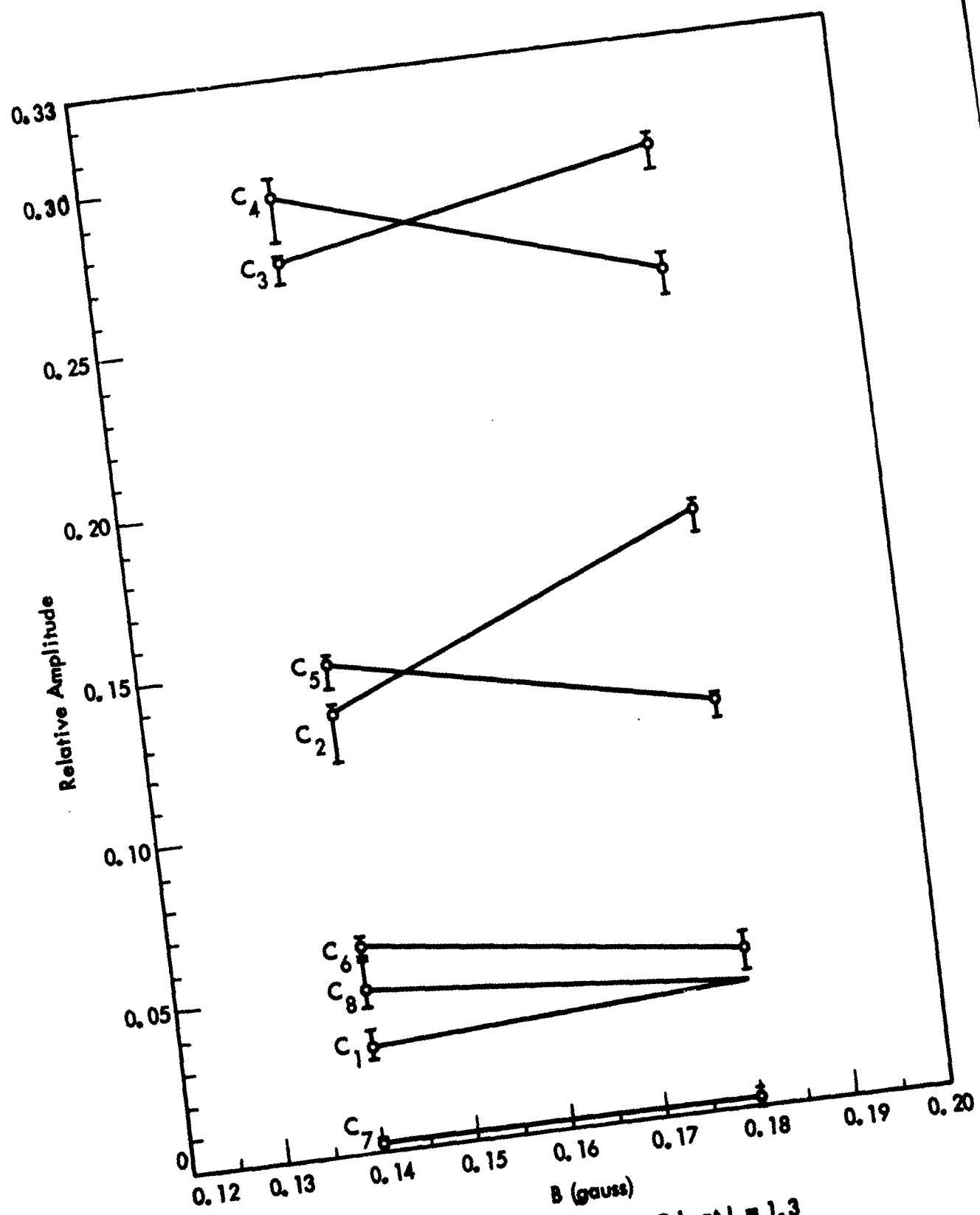


FIGURE 13. The B dependence of the C_i 's at $L = 1.3$

As a reasonable description of the spectral dependence of protons greater than 30 Mev, the following spectra are proposed.

1) For the Hess P-1 Map (see Figure 4) the following spectra on an L grid are to be normalized to one above 30 Mev.

- a) For $L \leq 1.2$ the composite spectrum of Hess (see Figure 5).
- b) At $L = 1.3$ the measured spectrum of Freden and White (Reference 21) labeled f_2 .
- c) At $L = 1.47, 1.54, 1.64$, and 1.72 the measured spectra of Nangle and Kniffen (Reference 15) labeled f_3, f_4, f_5 and f_6 , respectively.
- d) And

$$f_7^H = 0.22408 \exp(-E/20) \quad \text{at } L = 1.9$$

$$f_8^H = 80.645 \exp(-E/5) \quad \text{for } L \geq 2.5$$

The measured spectra, f_2 through f_6 , are given in Tabel 2 along with the factors f_i^H/f_i which normalize each to one above 30 Mev. These spectra are also displayed in Figure 14. At L values between two grid values a linear combination of the grid spectra is used. For example, at $L = 1.6$ the spectrum would be given by:

$$f^H(E) = 0.4 f_4^H + 0.6 f_5^H$$

2) For the high-energy proton map (see Figure 6) the following spectra on an L grid are to be normalized to one between 40 and 80 Mev.

- a) For $L \leq 1.2$ the composite spectrum of Vette (see Figure 5)
- b) At $L = 1.3, 1.47, 1.54, 1.64$, and 1.72 the measured spectra f_2, f_3, f_4, f_5 , and f_6 , respectively.
- c) And

$$f_7^V = 0.42727 \exp(-E/20) \quad \text{at } L = 2.0$$

$$f_8^V = 597.8 \exp(-E/5) \quad \text{for } L \geq 2.5$$

The factors f_i^V/f_i which normalize the measured spectra to one between 40 and 80 Mev are included in Table 2. The coefficients C_i are linearly interpolated as before. Thus at $L = 1.6$, $C_4 = 0.4$, $C_5 = 0.6$ and the remaining $C_i = 0$.

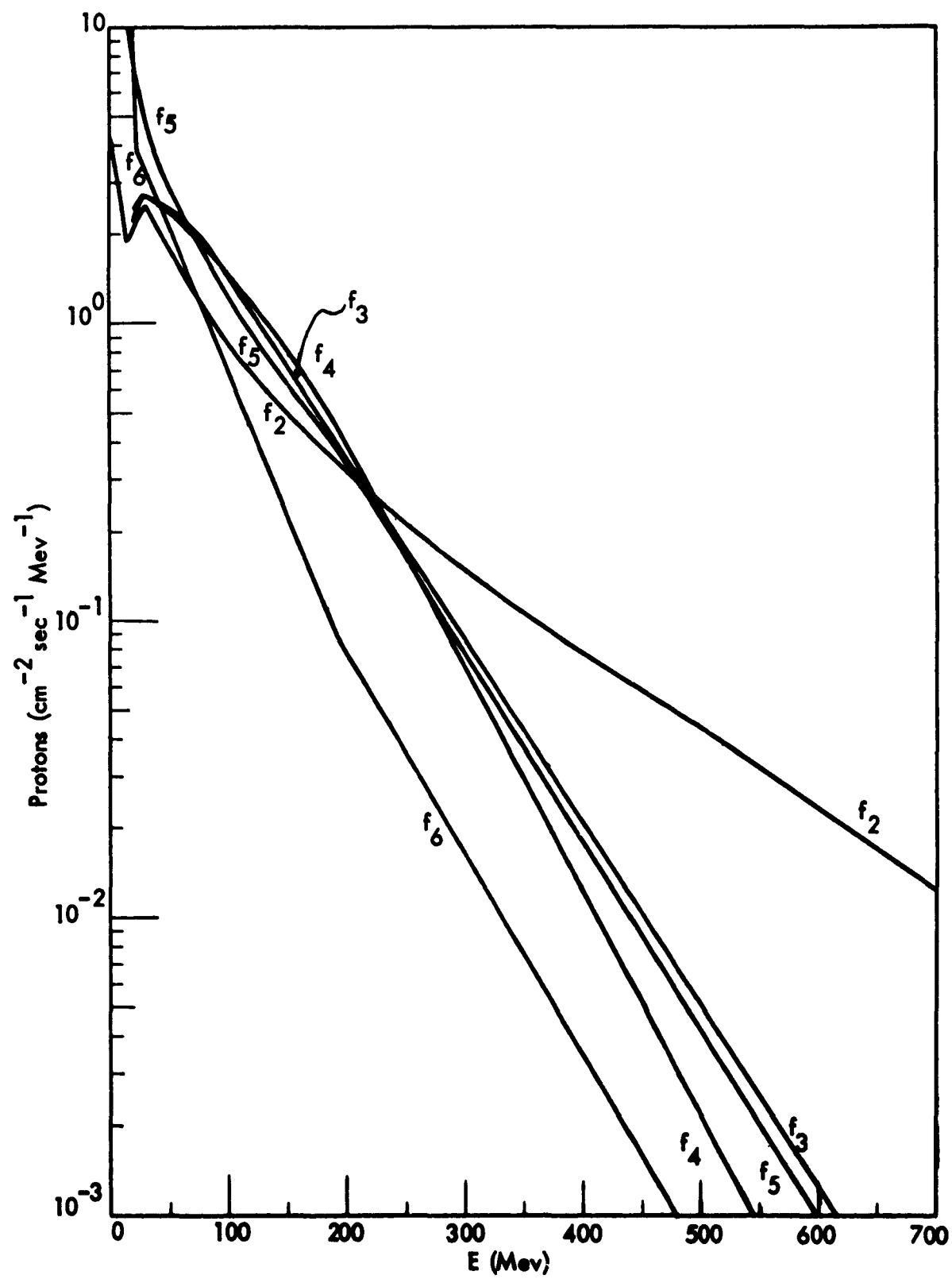


FIGURE 14. The basic proton spectra used in the program

Table 2
BASIC PROTON SPECTRA ADAPTED FOR HESS AND VETTE FLUX MAPS

E(Mev)	f_2 B = 0.20 L = 1.3 (arbitrary units)*	f_3 B = 0.223 L = 1.47 (arbitrary units)	f_4 B = 0.209 L = 1.54 (arbitrary units)	f_5 B = 0.196 L = 1.64 (arbitrary units)	f_6 B = 0.196 L = 1.72 (arbitrary units)
20	2.06	2.2	2.4	10.0	14.0
30	2.5	2.5	2.7	4.6	3.4
40	2.08	2.7	2.6	3.6	2.7
50	1.76	2.5	2.4	2.95	2.2
75	1.2	2.0	1.9	1.9	1.3
100	0.88	1.4	1.5	1.26	0.71
150	0.51	0.72	0.8	0.61	0.22
200	0.32	0.35	0.4	0.335	0.076
250	0.21	0.17	0.17	0.17	0.035
300	0.146	0.085	0.071	0.088	0.016
Extrapolation formula E \geq 300	$10^3 \exp(-3 \times 10^6 E^2/E^{1.5})$	$5.668 \exp(-E/72)$	$12.57 \exp(-E/58)$	$7.957 \exp(-E/65)$	$1.91 \exp(-E/63)$
f_i^H/f_i	.00525	.00399	.00394	.00382	.00653
f_i^V/f_i	.0163	.0109	.0114	.0099	.0137

* In Columns f_2 through f_6 the units are in particles per Mev.

For the low-energy-proton map (Figure 9) no spectral variation with position is given. Hence the recommended spectrum for this map is that one given in Section 3.1.1. Therefore the C tables for the proton maps will consist of ones and zeros.

As more spectral data is reduced and obtained, the C tables for the electron and proton maps can be improved. It is believed, however, that the predominant spatial variations of the spectra have already been incorporated.

3.1.3 Time Dependence

The time dependence of the trapped-radiation flux is not well determined. Hence it is difficult and perhaps misleading to develop a specific subroutine to treat this dependence. Another barrier to such a program involves a lack of agreement as to what types of time dependence are most important to a radiation-hazard study. A brief discussion is given of the features of the time variation of the belts and a model is proposed which treats the predominant features.

Theoretically, the temporal variations of the trapped-particle flux can be qualitatively decomposed into transient behavior and non-transient behavior. The transient behavior is expected following impulsive injection such as that experienced during a high-altitude nuclear detonation or following an eruption on the sun. The nontransient behavior is expected from the quasi-periodic variations of the sources or loss mechanisms for the belts. In addition, an apparent nontransient phenomena is expected from the slowly varying B-L coordinates at a particular geographic point. No quantitative theory of these variations has been developed.

Experimentally, a separation of these variations is hampered by the lack of a quantitative theory. However, for $L < 2.5$ it appears that the protons above 30 Mev energy do not experience any transient behavior. These protons, in comparison with less energetic protons, exhibit only a relatively slight solar-cycle variation. The electron belts do experience a complex time history. Van Allen (Reference 22), Brown (Reference 13), and Pizzella (Reference 24) have observed the transient behavior of the electron flux following July 9, 1962—the date of the high-altitude test in the Pacific—as well as during geomagnetic storm activity in the outer belt. It was formerly supposed that the predominant variation would be in the integral flux. West's spectral data indicate that for L values above 1.7 the spectral variations with time are quite severe at about 1 Mev. Also the low-altitude data is consistent with the theory of Walt (Reference 19) which predicts time-dependent spectra. These considerations invalidate the use of a spectrum that is constant. Pizzella (Reference 24) observed diurnal variations in the outer belt. Brown (Reference 23) has noted quasi-periodic variations at $L = 4$ which have roughly a 27-day period. Considerable work remains to determine the specific causes, although they are evidently associated with the sun's influence.

The importance of temporal variations in the environment to a space-radiation-hazard study is intimately dependent on the duration of the mission and specific requirements of the mission upon the time-dependent dose. Thus, orbital missions longer than a day without specific requirements on the maximum dose rate do not require a detailed treatment of the diurnal variation. To evaluate the hazard for short-term missions and those with specific requirements a program to systematically evaluate the data on time dependence is required. For example, the diurnal variation should be decomposed into variations that are actually associated with source-and-loss variations and those that are associated with local-time variations in B and L. At this point a code to calculate B and L as a function of local time would be useful.

At present, the only reasonable requirement on the electron code is compatibility with a time-dependent subroutine. Construction of the explicit form of the subroutine will have to wait for better understanding of the time dependence.

Data on the protons has been gathered for a longer period of time. A reasonable method of evaluating the solar-cycle variation of the hazard from these protons is as follows. The flux map of Hess is interpreted as the environment at solar maximum while that of Vette is interpreted as the environment at solar minimum. The dose derived for any mission from Hess' map can be labeled D_{\max} and that derived from Vette's map can be labeled D_{\min} . These will represent the range of the proton dose for the given mission. Hopefully, the dose during the cycle can be approximated by

$$D(t) = \frac{D_{\max} + D_{\min}}{2} + \frac{D_{\max} - D_{\min}}{2} \cos \left(2\pi \frac{t - t_{\max}}{11 \text{ years}} \right)$$

For the transient belt of artificially produced electrons the environment code is compatible with a subroutine which would modulate in time the flux map or the C tables. That is, the subroutine would calculate a time dependence of the form:

$$F(B, L, t) = G_{B, L}(t) F(B, L)$$

and/or

$$C_i(B, L, t) = H_{i, B, L}(t) C_i(B, L)$$

The time modulating operators $G(t)$ and $H_i(t)$ are still to be determined from the data. Their determination should be one of the objectives of future work planning.

3.1.4 Angular Distributions

The angular distribution of geomagnetically trapped particles is generally not isotropic, although in some cases isotropy is a reasonable approximation as the following discussion will show. The following derivation of the relationships for determining

the angular dependence of trapped radiation was undertaken to determine the effect of angular dependence on the radiation dose within a spacecraft. The effect for a particular case is given in Section 7.0. Another purpose in developing this code is to facilitate the interpretation of experimental data and the design of space-borne radiation detection systems.

In the steady state the angular distribution at any point has the general property, which greatly simplifies the description, that it may be specified by the distribution in the pitch angle α , the angle between the velocity vector and the local magnetic-induction field B . If the direction of the B field is considered as a polar axis, then the distribution in the azimuthal angle is uniform (two-dimensionally isotropic in the plane perpendicular to the field line). At low altitudes for particles of large radius of gyration, the variation in the atmospheric density is appreciable over one radius of gyration and thus produces the "East-West asymmetry" (Reference 25). In this treatment of angular dependence these atmospheric effects will not be considered nor will a description of the "edges" of the trapped belts be obtained. Rather, effort will be concentrated on the regions where the adiabatic invariants provide a working description of the particle motion. Most of the flux lies in such regions. There the flux is uniformly distributed in azimuthal angle because the particles spiral about the field lines and the phase or azimuthal angle along this trajectory is random.

The first part of the discussion will show that the pitch-angle distribution at any point along a given field line, labeled by L , can be determined from knowledge of the flux as a function of position (References 26, 27, and 28). The flux maps are designed to provide the latter quantity. Thus the problems involved in determining the pitch-angle distributions were chiefly numerical. They have been solved successfully. Figure 15 illustrates the geometry and the parameters.

However, to evaluate the relative merits of various shielding configurations with accurate account of the angular distributions, the distributions must be transformed at each point into coordinates fixed in the space vehicle. The additional variables required to keep track of the orientation of the vehicle at all times and to transform the angular distribution to this coordinate system as a function of time demands, in general, an impractically large amount of time and storage space in the computer.

Hence, the approach has been that the routine will generate the pitch-angle distributions at any or all points. The comparison of shielding configurations will then be made point by point, by hand. Two somewhat realistic mission plans can be treated exactly by just summing such data; one where the vehicle has a fixed orientation with respect to the B field, and the other where the vehicle spins rapidly about an axis that maintains a constant angle with the B field. Such missions will usually include the "best" and "worst" cases for a given shield because the angular distributions quite consistently are largest perpendicular to the field line and decrease monotonically towards the field line. For example, some typical distributions at the equator are shown in Figures 16 through 20. The equatorial distributions are the

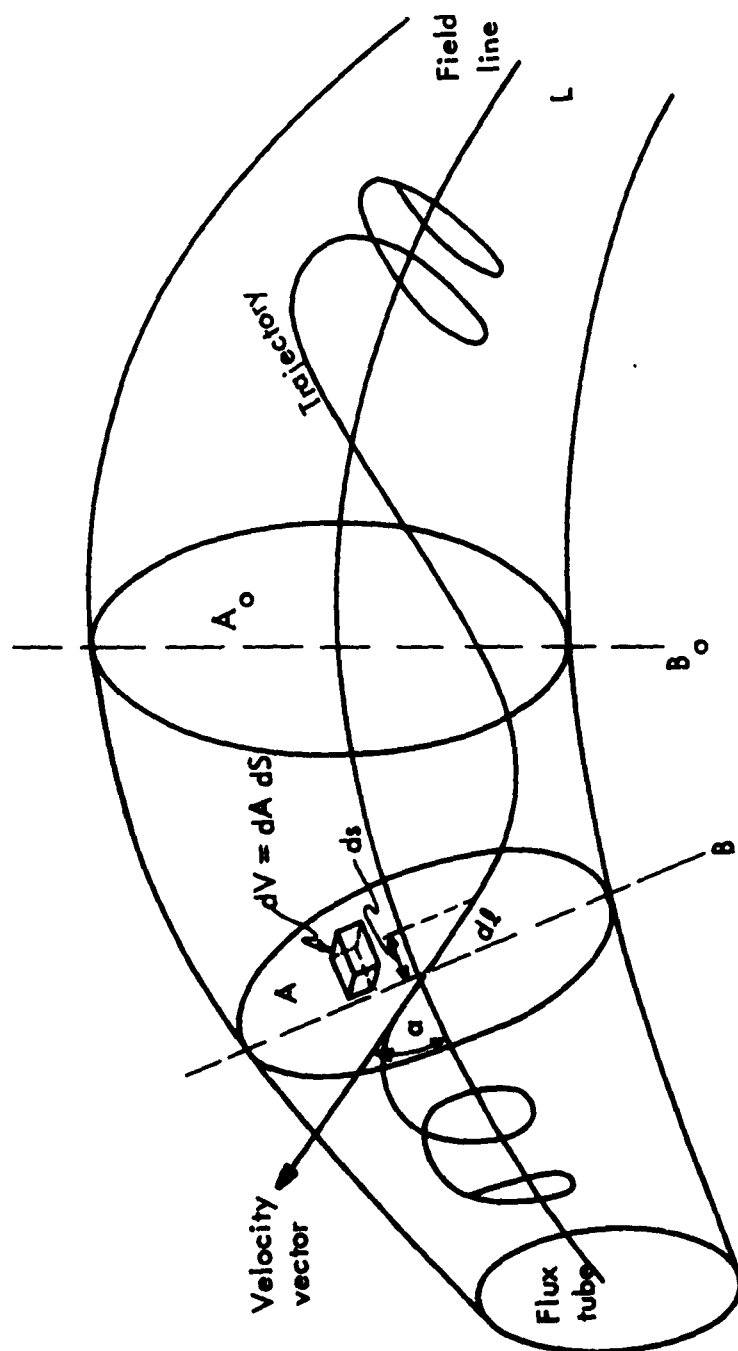


FIGURE 15. Parameters of the pitch angle distribution

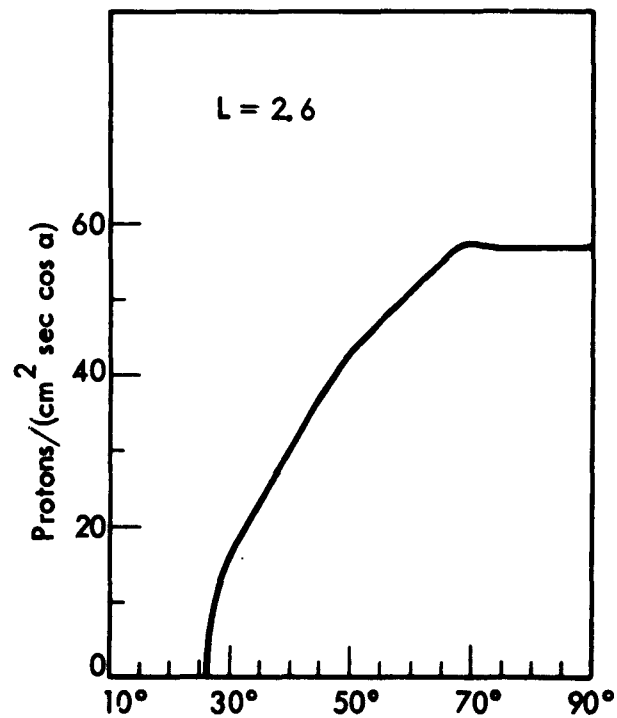
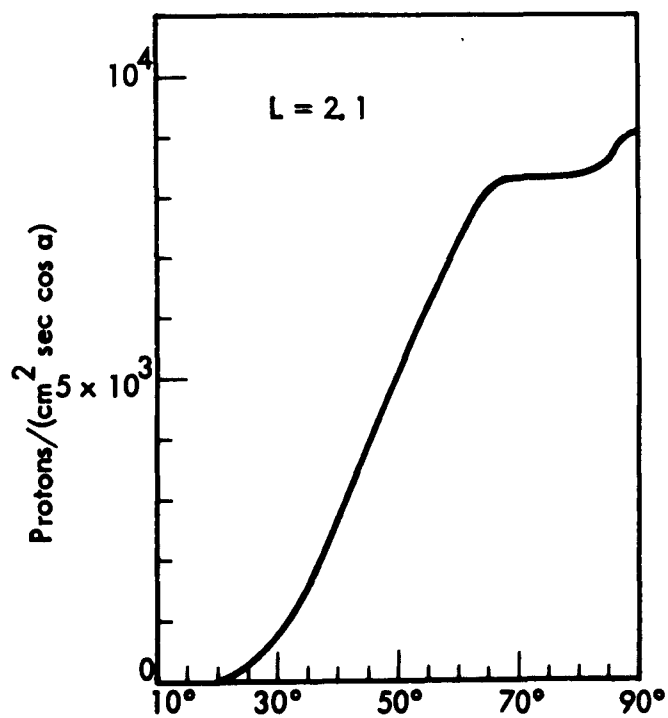
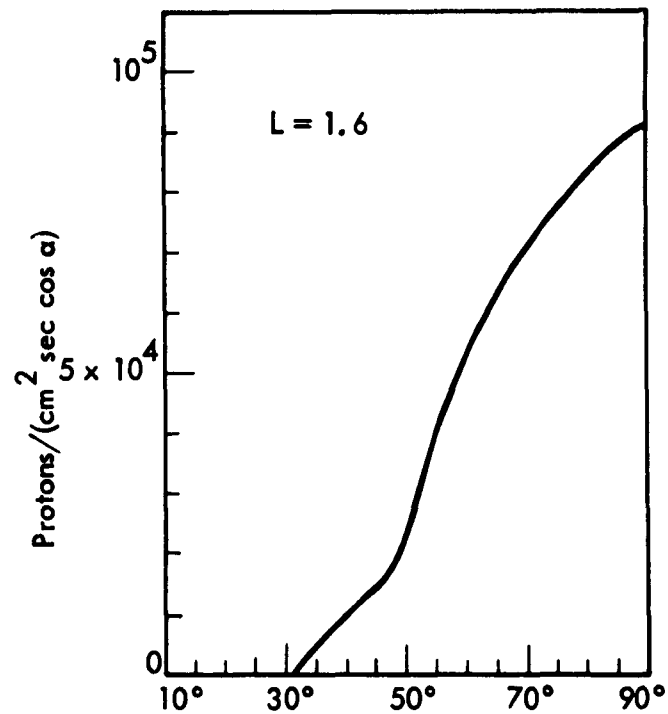
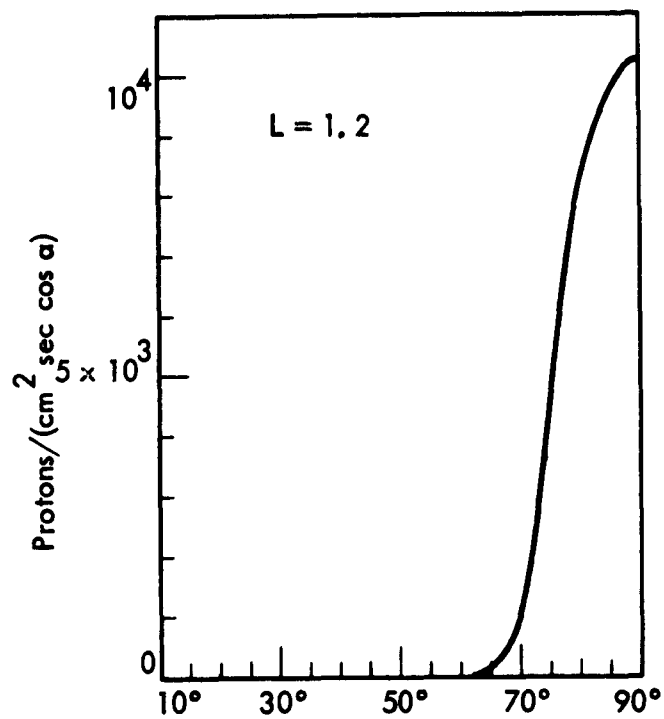


FIGURE 16. Equatorial pitch angle distributions for the Hess P-1 proton map

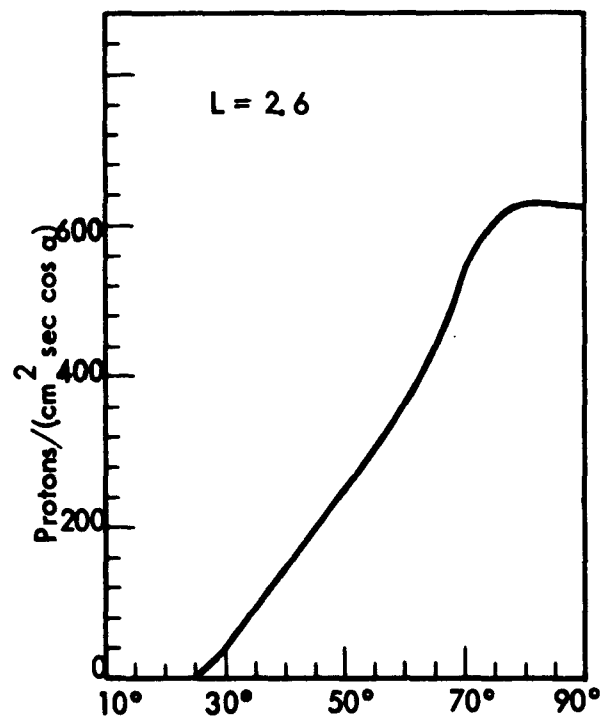
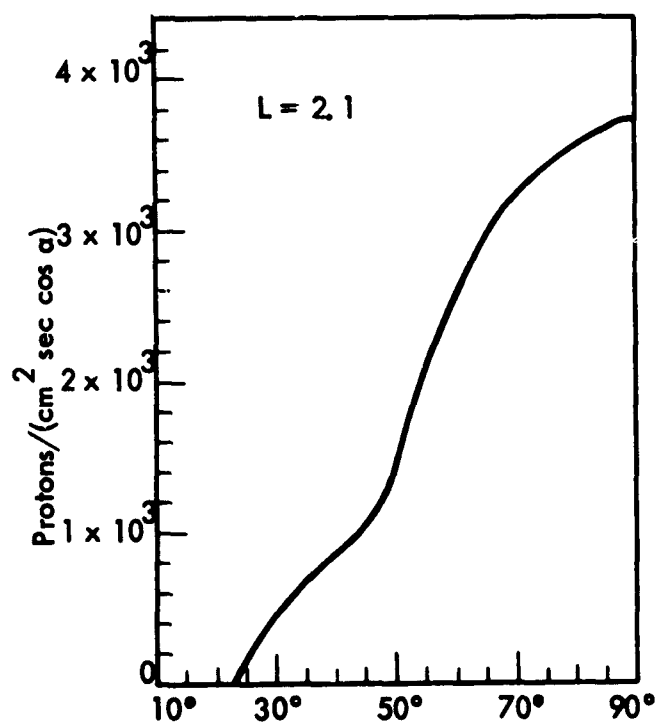
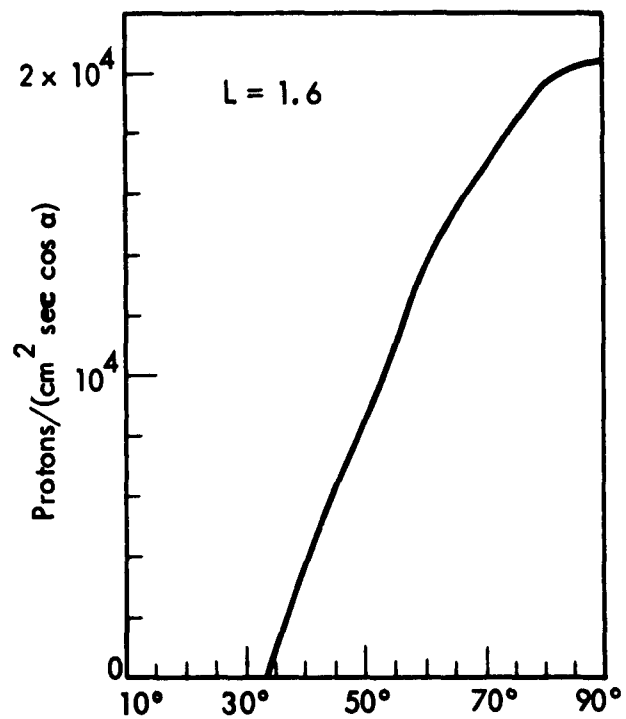
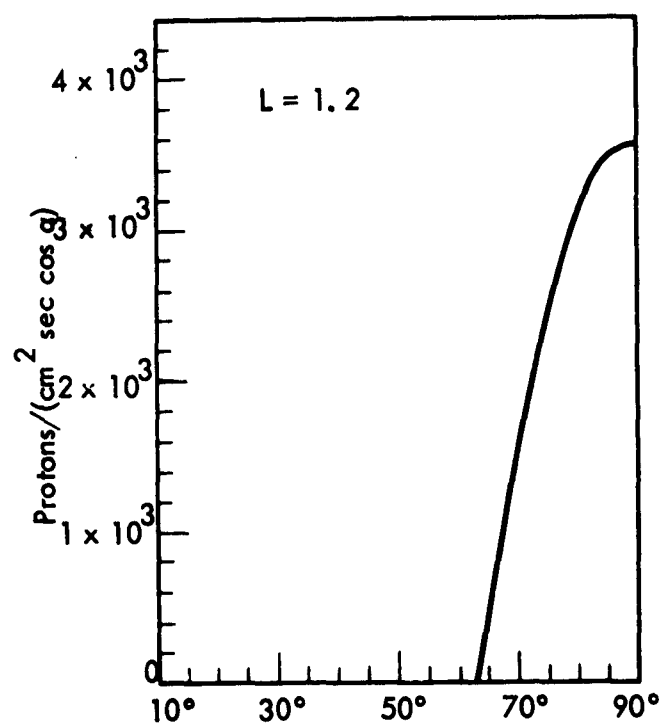


FIGURE 17. Equatorial pitch angle distributions for the high-energy proton map

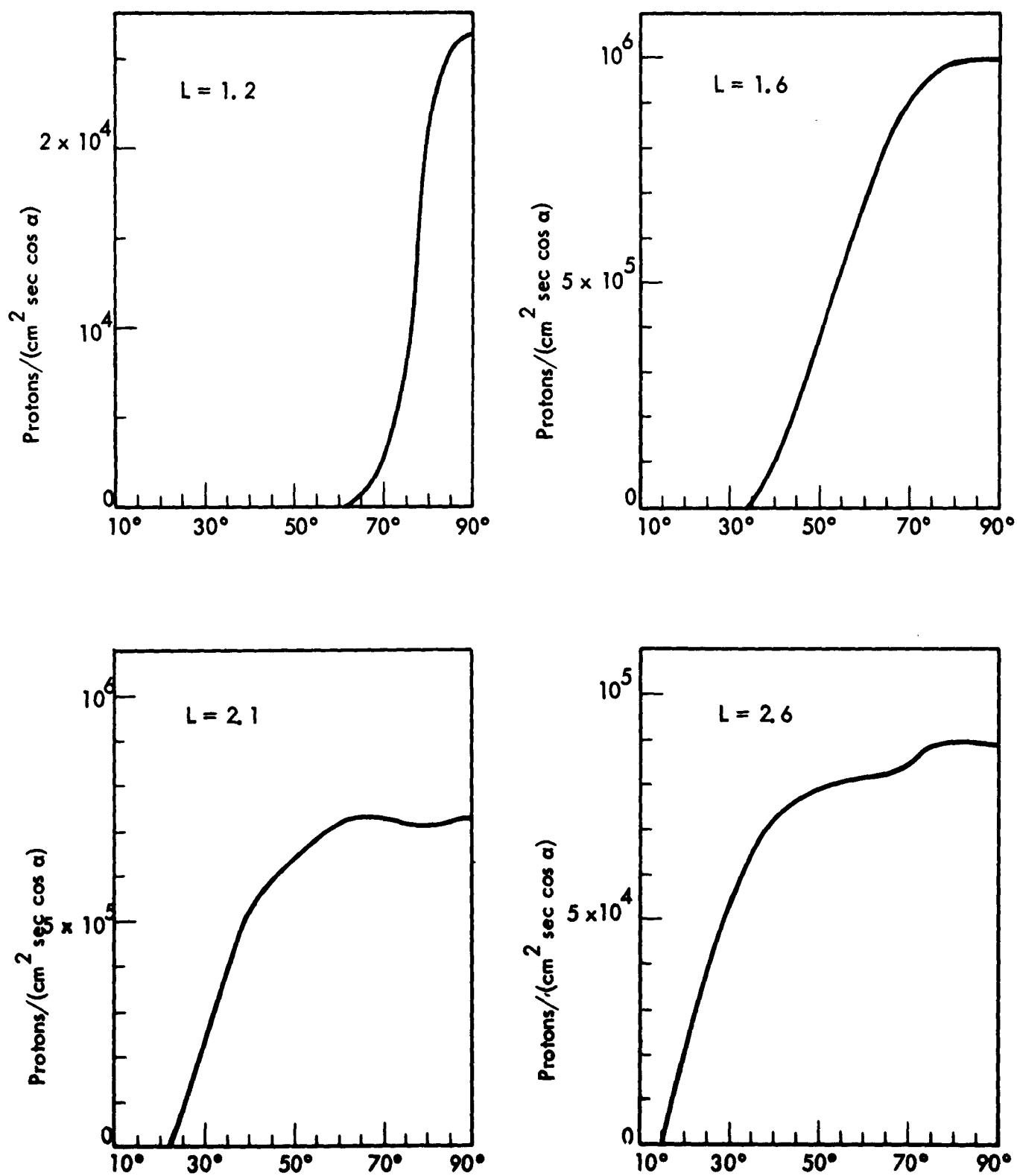


FIGURE 18. Equatorial pitch angle distributions for the low-energy proton map

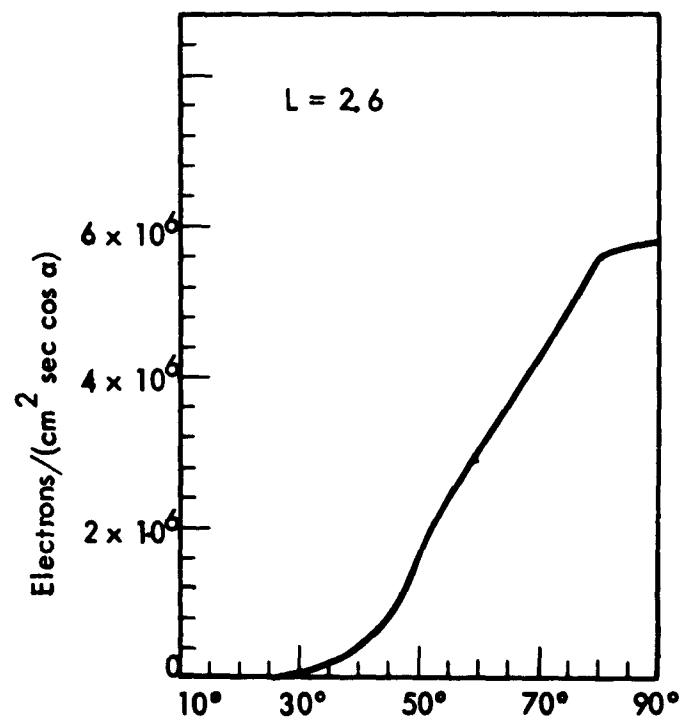
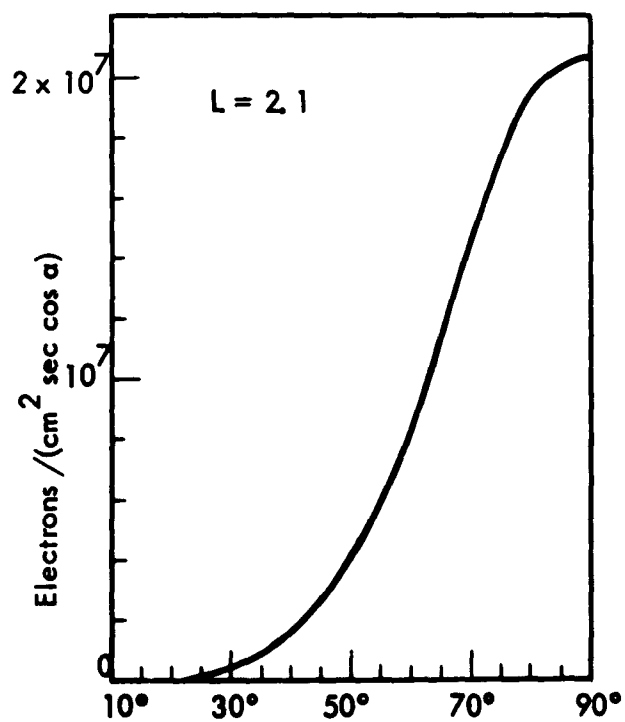
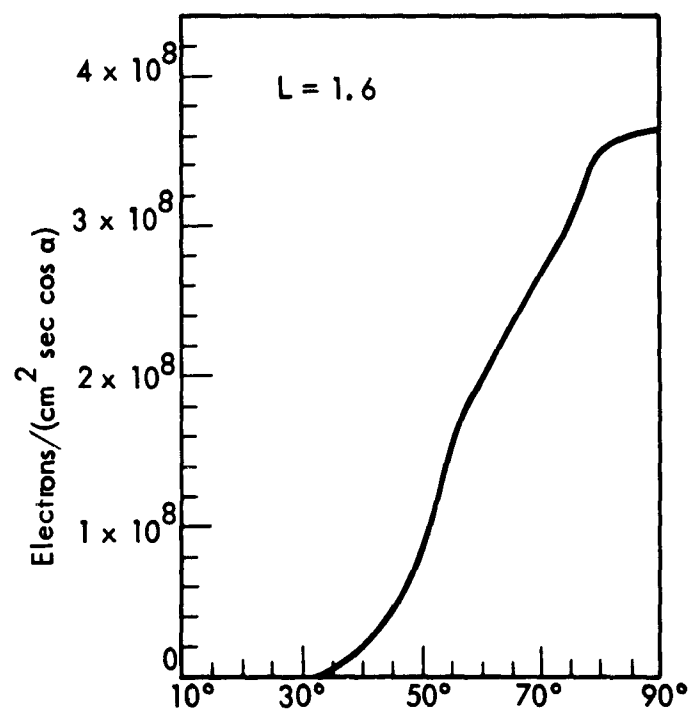
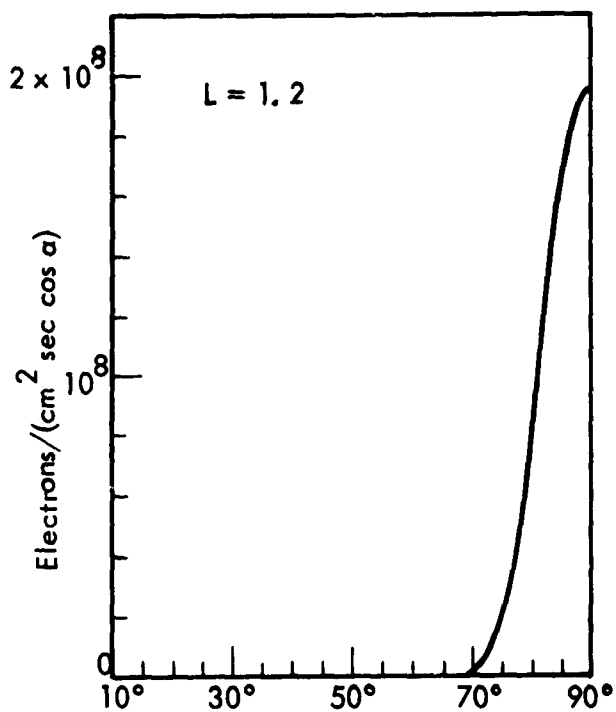


FIGURE 19. Equatorial electron pitch angle distributions

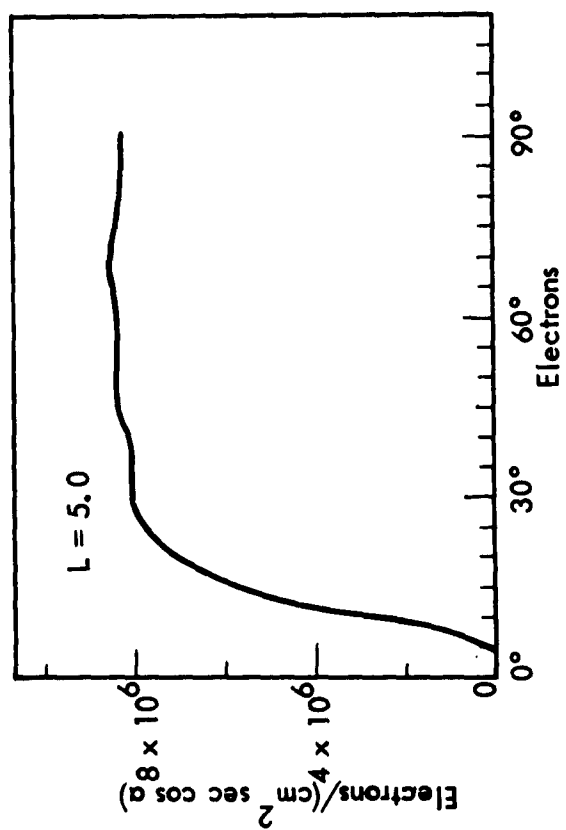
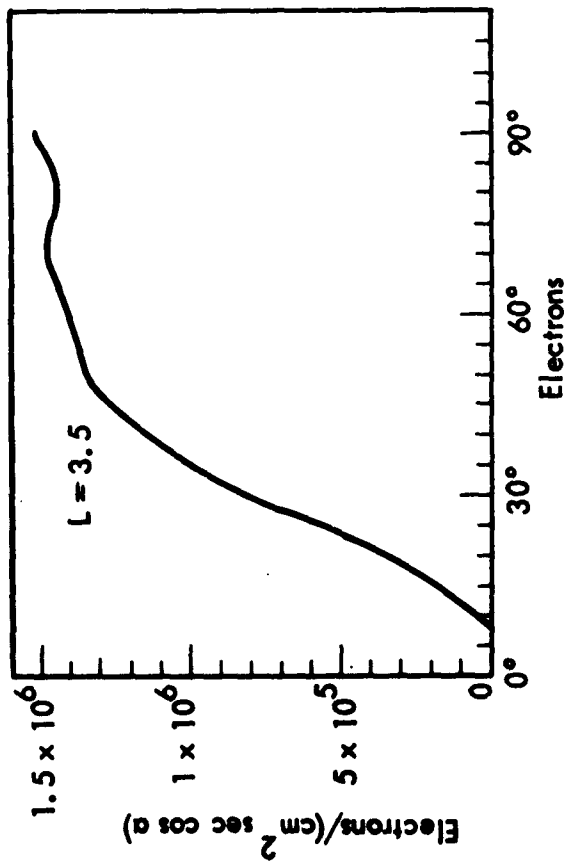
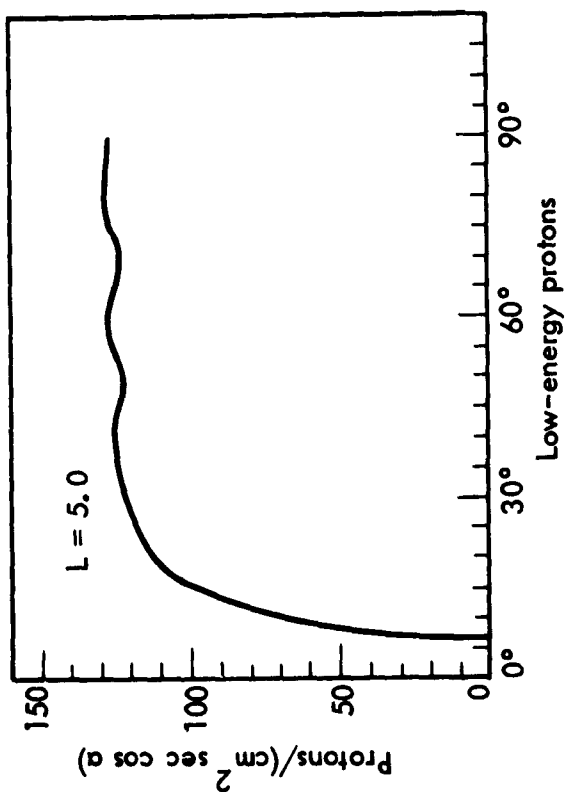
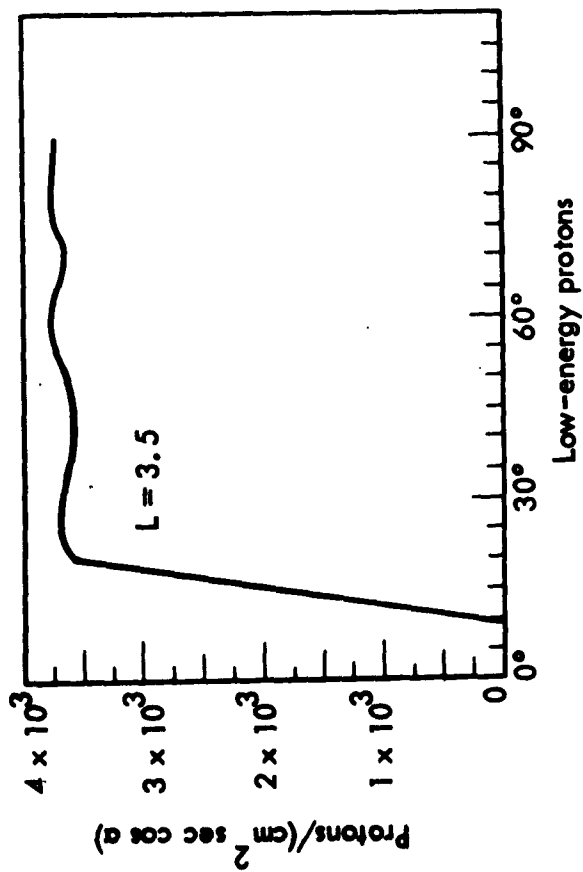


FIGURE 20. Equatorial pitch angle distributions at L = 3.5 and L = 5.0 for the electron and low-energy proton maps

broadest and have the greatest chance to peak away from perpendicular. But none of the natural ones appear to have statistically significant peaks at angles other than 90 degrees with the field line.

The equations to be derived here relate an experimentally measured quantity, the omnidirectional flux $F(B, L)$ as a function of the B-L coordinates to an experimentally measurable directional flux $F_\alpha(B, L)$. The fluxes are equal to the products of the density and the average speed (magnitude of velocity) of the particles accepted by each flux measurement, respectively. If the energy spectrum is constant along a field line, then the average speed is the same for the directional fluxes and the omnidirectional flux. This is approximately true in the belts described by the flux maps. Thus there is just a constant factor between density and flux so that in the following deviations, density may be replaced everywhere by flux.

Under steady-state conditions, let N be the total number of particles contained in a small flux tube labeled by L . Since $\nabla \cdot \vec{B} = 0$, the cross-sectional area A of this tube will vary with magnetic induction as

$$BA = B_0 A_0 \quad (1)$$

where the subscript zero refers to quantities evaluated at the equator or mid-plane. A is chosen small enough that the particle density is uniform over A .

Let α_0 denote the pitch angle at the equator and α the pitch angle at some other point which is located by its magnetic induction. See Figure 15 for a geometrical interpretation of these quantities. Then conservation of magnetic moment, an adiabatic approximation, implies that a particle follows a trajectory such that

$$\mu = \sin^2 \alpha_0 = \frac{B_0}{B} \sin^2 \alpha = \text{constant} \quad (2)$$

Let $f(\mu)d\mu$ = the fraction of the N particles which have their "magnetic moment" between μ and $\mu + d\mu$. The quantity μ , called here the magnetic moment, is really a dimensionless quantity proportional to the conventional magnetic moment. The latter is given by $\mu pv/(2 B_0)$, or nonrelativistically by $\mu m v^2/(2 B_0)$ (p = momentum, m = mass, v = velocity). The dimensional factors are constants.

If α is related to μ by Equation 2, and if $|\sin \alpha| \leq 1$ so that particles of "magnetic moment" μ penetrate at least as far as B before mirroring, then this fraction $f(\mu)d\mu$ is equal to the fraction of the N particles which have the cosine of their pitch angles between $\cos \alpha$ and $\cos \alpha + d(\cos \alpha)$ when they cross a section normal to the tube at B . Denote this latter fraction by $f_B(\cos \alpha) d(\cos \alpha)$. The previous statement corresponds to the equation

$$f_B(\cos \alpha) |d(\cos \alpha)| = f(\mu) |d\mu| \quad (3)$$

Equation 3 really serves to define $f_B(\cos \alpha)$.

The function of primary interest, however, is a density denoted by $n_B(\cos \alpha)$ such that

$n_B(\cos \alpha) d(\cos \alpha) dV$ = the number of particles with the cosine of their pitch angle between $\cos \alpha$ and $\cos \alpha + d(\cos \alpha)$ and in the small volume dV about a point B at any instant of time.

Let

$$dV = dA ds$$

where

dA = small element of A

ds = small element of length along the field line at B

Then

$\frac{1}{N} n_B(\cos \alpha) d(\cos \alpha) dV$ = fraction of all particles in this flux tube with cosine of pitch angle between $\cos \alpha$ and $\cos \alpha + d(\cos \alpha)$ and which also lie in the volume $dA ds$ at any one time.

The fraction of the particles with pitch angle α which actually is in the length ds of the flux tube at any one time is just the fraction of their trajectory which is in ds ; namely,

$$\frac{d\ell}{\ell(\alpha, B)} = \frac{1}{\ell(\alpha, B)} \frac{ds}{\cos \alpha} \quad (4)$$

where

$\ell(\alpha, B)$ = length of the trajectory of particle at B with pitch angle α

$d\ell$ = length of the part of the trajectory in ds

since the angle between the trajectory and the field line is simply α .

The trajectory length is given by

$$\ell(\alpha, B) = \int \frac{ds}{\cos \alpha}$$

but this quantity will disappear in the final result. Actually, ℓ only depends on one parameter, which can be taken to be μ , which is in turn a function of α and B by Equation 2. Therefore

$$\ell(\alpha, B) = \ell(\mu(\alpha, B))$$

Finally, since the density is uniform across the area A , the fraction of particles in the volume Ads of the tube and also in $dV = dAds$ is just dA/A . Thus,

$$\begin{aligned} n_B(\cos \alpha) d(\cos \alpha) dV &= (\text{total number of particles}) \times \\ &\quad (\text{fraction of all particles with cosine of pitch angle} \\ &\quad \text{between } \cos \alpha \text{ and } \cos \alpha + d(\cos \alpha)) \times \\ &\quad (\text{fraction of these in } ds \text{ at any one time}) \times \\ &\quad (\text{fraction of preceding fraction in } dA) \\ &= N f_B(\cos \alpha) d(\cos \alpha) \frac{ds}{\ell(\mu(\alpha, B)) \cos \alpha} \frac{dA}{A} \end{aligned}$$

Or

$$n_B(\cos \alpha) = \frac{N f_B(\cos \alpha)}{A \ell(\mu(\alpha, B)) \cos \alpha} \quad (5)$$

The total number density at B (an experimentally measurable quantity — number per unit volume) is then

$$n(B) = \int_0^{\cos \alpha_L} n_B(\cos \alpha) d(\cos \alpha) = \frac{N}{A} \int_0^{\cos \alpha_L} \frac{f_B(\cos \alpha) d(\cos \alpha)}{\ell(\mu(\alpha, B)) \cos \alpha} \quad (6)$$

where α_L is the minimum pitch angle for trapped particles at a given B and L . The integrand can be related to the function $f(\mu)$ by changing the variable of integration to μ where α and μ are again related by Equation 2. Thus

$$\cos \alpha = \sqrt{1 - \frac{B}{B_0} \mu} \quad (7)$$

Equation 3 may be used to eliminate the necessity for computing $\frac{d(\cos \alpha)}{d\mu}$.
That is,

$$\begin{aligned} f_B(\cos \alpha) \cdot |d(\cos \alpha)| &= f_B(\cos \alpha(\mu)) \left| \frac{d(\cos \alpha(\mu))}{d\mu} d\mu \right| \\ &= f(\mu) |d\mu| \end{aligned}$$

Since the limits of the integral Equation 6 are

$$0 \leq \cos \alpha \leq \cos \alpha_L$$

and

$$\mu = \frac{B_0}{B} \sin^2 \alpha = \frac{B_0}{B} (1 - \cos^2 \alpha)$$

the limits on μ are

$$\frac{B_0}{B} \geq \mu \geq \frac{B_0}{B} \sin^2 \alpha_L = \mu_L \quad (8)$$

The minimum magnetic moment for trapping is independent of position and hence μ_L does not depend on B . Thus, substitution of Equations 1, 3, 7, and 8 into Equation 6 gives

$$n(B) = \frac{N}{A_0} \sqrt{\frac{B}{B_0}} \int_{\mu_L}^{B_0/B} \frac{\chi(\mu) d\mu}{\sqrt{B_0/B - \mu}} \quad (9)$$

where $\chi(\mu) = f(\mu)/\ell(\mu)$ is the unknown function we wish to determine, because the flux per steradian at B with pitch angle α is

$$\begin{aligned} F_\alpha(B, L) &= \frac{\bar{v}}{2\pi} n_B(\cos \alpha) \\ &= \frac{\bar{v}}{2\pi} \frac{NB}{A_0 B_0} \frac{\chi(\mu)}{\sqrt{1 - \frac{B}{B_0} \mu}} \left| \frac{d\mu}{d(\cos \alpha)} \right| \bigg|_{\mu = \mu(\alpha, B)} \\ &= \frac{\bar{v}}{2\pi} \frac{2N}{A_0} \chi(\mu(\alpha, B)). \end{aligned} \quad (10)$$

Equation 9 is an integral equation for $\chi(\mu)$ in terms of the measured density $n(B)$. The equation is of a type called Abel's equation (Reference 29). To reduce (9) to standard form let $B_0/B = x$ and $\sqrt{x} n(B_0/x) = v(x)$. Thus

$$v(x) = \frac{N}{A_0} \int_{\mu_L}^x \frac{\chi(\mu') d\mu'}{\sqrt{x-\mu'}}$$

To solve for χ multiply both sides of the equation by $(\mu-x)^{-1/2}$ and integrate over x from μ_L to μ . Thus

$$\begin{aligned} \int_{\mu_L}^{\mu} \frac{v(x)}{\sqrt{\mu-x}} dx &= \frac{A_0}{N} \int_{\mu_L}^{\mu} \int_{\mu_L}^x \frac{\chi(\mu')}{\sqrt{x-\mu'} \sqrt{\mu-x}} d\mu' dx \\ &= \frac{A_0}{N} \int_{\mu_L}^{\mu} \int_{\mu'}^{\mu} \frac{\chi(\mu')}{\sqrt{x-\mu'} \sqrt{\mu-x}} dx d\mu' \\ &= \frac{A_0}{N} \int_{\mu_L}^{\mu} \chi(\mu') \left(\int_{\mu'}^{\mu} \frac{dx}{\sqrt{x-\mu'} \sqrt{\mu-x}} \right) d\mu' \\ &= \frac{A_0}{N} \frac{[\Gamma(1/2)]^2}{\Gamma(1)} \int_{\mu_L}^{\mu} \chi(\mu') d\mu' = \frac{A_0 \pi}{N} \int_{\mu_L}^{\mu} \chi(\mu') d\mu' \end{aligned}$$

Now differentiate both sides with respect to μ . Let $dv(x)/dx = v'(x)$.

$$\begin{aligned} \text{Then} \quad \chi(\mu) &= \frac{N}{\pi A_0} \frac{\partial}{\partial \mu} \int_0^{\mu} \frac{v(x) dx}{\sqrt{\mu-x}} \\ &= \frac{N}{\pi A_0} \frac{\partial}{\partial \mu} \left[-2\sqrt{\mu-x} n(B_0/x) \Big|_{\mu_L}^{\mu} + 2 \int_{\mu_L}^{\mu} \sqrt{\mu-x} v'(x) dx \right] \end{aligned}$$

Since $n(B_0/\mu_L) = 0$

$$\begin{aligned}\chi(\mu) &= \frac{2A_0}{\pi N} \frac{\partial}{\partial \mu} \int_{\mu_L}^{\mu} \sqrt{\mu-x} \, v'(x) \, dx \\ &= \frac{A_0}{\pi N} \int_{\mu_L}^{\mu} \frac{v'(x) \, dx}{\sqrt{\mu-x}}\end{aligned}\quad (11)$$

Equation 11 is the form actually used to determine the function $\chi(\mu)$ in the machine calculations. This relationship may alternatively be expressed in terms of fluxes

$$F_{\alpha}(B, L) = \frac{\bar{v}}{\pi^2} \int_{\mu_L}^{B_0/B(1-\cos^2 \alpha)} \frac{v'(x) \, dx}{\sqrt{B_0/B(1-\cos^2 \alpha) - x}} \quad (12)$$

where

$$\bar{v} \, v(x) = \sqrt{x} \, F(B_0/x, L)$$

L is held a constant during the integration.

Equation 12 multiplied by 2π has been machine-programmed to calculate the distribution of flux $\Phi_{BL}(\alpha)$ per unit cosine of the pitch angle. Thus the machine evaluates

$$\Phi_{BL}(\alpha) = \frac{2}{\pi} \int_{\mu_L}^{B_0/B \sin^2 \alpha} \frac{\bar{v} \, v'(x)}{\sqrt{B_0/B \sin^2 \alpha - x}} \, dx \quad (13)$$

Equation 13 has one interesting immediate application. If L is held constant, the numerical value of the flux per steradian about some pitch angle α_1 at a location B_1 is the same as the flux per steradian measured about some other angle α at another location B , if α and B are related to α_1 and B_1 by

$$\frac{\sin^2 \alpha}{B} = \frac{\sin^2 \alpha_1}{B_1}$$

In other words, $\phi_{BL}(\alpha)$ is determined completely by knowledge of either $\phi_{BL}(\pi/2)$ for all B and L , or by $\phi_{B_0L}(\alpha)$ for all L and α . Again $B_0 = B_0(L)$ is the equatorial magnetic induction.

Some plots of $\phi_{B_0L}(\alpha)$ for selected L values are shown here (Figures 16 through 20). The graphs were constructed by drawing a smooth curve through points calculated at intervals of 10 degrees in α . From these graphs the pitch-angle distribution anywhere on the selected L values may be determined.

The graphs are shown for the four maps: electrons, the Hess P-1 protons, high-energy protons, and low-energy protons. For each map the graphs are arranged in order of increasing L . A few interesting properties of these curves may be noted. Many of them, as shown, have a nearly linear rise in the plot as a function of α . At the larger L values, the curves seem to have a flat top or plateau with some "wiggles." Thus the curves shown for $L = 5$ are nearly isotropic except for a cone of about 10 degrees half-angle about the B line. The behavior of the curves near the loss cone angle is the most uncertain feature, but this depends on the "edges" of the belt. Work should be done on a description of the edges of the belts, but that problem is altogether different from the descriptive type of problems treated here. Presumably, a better understanding of the loss mechanism is required. In these edge regions, the pitch-angle distribution is not so simply related to the density because scattering affects the orbits of a significant fraction of the particles passing through the edges.

These curves could probably be improved by some smoothing. Many of them have wiggles, possibly caused by inaccuracies of the maps. Already, however, some smoothing has occurred in their construction. New flux maps, perhaps more accurate than the original, could then be calculated with Equation 9. This integral is the inverse of that used to determine the pitch-angle distribution from the flux map. Since the integral (Equation 9) and its inverse are similar in form, with some small modifications the angular distribution routine could also be used to calculate its own inverse. There is still some controversy (Reference 30) over the accuracy of the numerical methods used to evaluate the integral (11). That is, the flux maps have been smoothed before applying the transformation. However, one may apply a matrix transformation (Reference 31) to approximate the integral. The matrix may be defined so as to operate only on measured flux points. This can lead to strange "bumps" in the angular distribution, and apparently some significant deviations from the distribution shown here. Further investigation of the validity of several numerical procedures would be worthwhile for application as better flux maps become available, but the approach presented here seems best for now.

Furthermore, from the calculated pitch-angle distributions, better geometrical factors and efficiencies could be computed for counters. In this light, data already gathered could be reinterpreted and future experiments could be designed for better accuracy.

3.2 UNTRAPPED RADIATION

Galactic cosmic rays and high-energy particles ejected from the sun during large solar flares comprise the untrapped radiation environment in the vicinity of the earth. Experimental results indicate that both types of radiation are approximately isotropic outside the magnetosphere. That is, the maximum amplitude of the average galactic cosmic ray anisotropy is 4×10^{-3} times the average cosmic ray flux (Reference 32). Solar flare particles usually reach the earth nearly isotropically, within 5 to 10 percent (References 33 and 34). However, during a short time at the beginning of some events high energy particles of intensities 10 to 100 times the maximum isotropic radiation intensity do arrive with significant anisotropies (Reference 35). At the present stage of development, the insensitivity of total mission dose to such anisotropy does not warrant the extensive computer analysis required to determine the effects of the anisotropy on the flux.

The method adopted for computing doses from untrapped radiation is to specify effective spectra, discussed below, for a set of L shells and to determine the total flux that reaches the vehicle in each L shell. The dose is then computed from a set of dose conversion numbers calculated by the shielding codes, using as input the spectra for the different L shells. The input spectra can include both sources together if desired. However, since the galactic cosmic radiation constitutes a small contribution to the dose for orbiting vehicles, and since it changes very slowly in time, its effect is easier to compute separately, as is discussed in Section 3.2.2.

3.2.1 Solar Particle Events

In constructing the solar-flare proton subroutine several simplifying assumptions have been made about the time development of the energy spectrum of the protons outside the magnetosphere. The available experimental data indicate that solar particle events have the following general features. A few minutes after the optical maximum of the solar flare, the first high-energy particles reach the earth. The particle intensity increases as the lower-energy particles arrive until a maximum is reached. The time of the maximum intensity is from 8 to 30 hours after the beginning of the event. After the maximum, the intensity decreases slowly to zero. The total duration of the event ranges from 2 to 5 days. Except for the first few minutes of the event, the velocity distribution outside the magnetosphere is roughly isotropic. In most events the particles reaching the earth are predominantly protons, although, in a few events, appreciable numbers of alpha particles have been observed. For this subroutine, it will be assumed that all the particles are protons. At any time during the event, the particle spectrum can be adequately described by an expression of the form

$$J(>P) = J_0(t) \exp[-P/P_0(t)]$$

where P is the particle rigidity (momentum/change), $j_0(t)$, and $P_0(t)$ are functions of the time only, and $j(>P)$ is the flux of particles with rigidity $>P$. The rigidity is related to the kinetic energy E of the particle as follows:

$$P(E) = \frac{1}{Z} \sqrt{E^2 + 2 mc^2 E}$$

A convenient set of units gives P in Mv , if Z is the number of electronic charges, mc^2 is the particle rest mass in energy units (Mev), and E is expressed in Mev.

The functions $j_0(t)$ and $P_0(t)$ are, in general, quite complicated. However, it has been observed that the integral spectrum for the whole event can usually be expressed in the same general form. Thus

$$J(>P) = J_0 \exp(-P/P_0) = \int_{t_0}^{\infty} j_0(t) \exp[-P/P_0(t)] dt$$

where P_0 is roughly equal to the value $P_0(t)$ at the time of maximum flux. To simplify the input data requirements, the following assumptions are made concerning the time behavior of $j_0(t)$ and $P_0(t)$.

$$j_0(t) \exp[-P/P_0(t)] = J_0 \exp(-P/P_0) F(t)$$

where

$$F(t) = \begin{cases} 0, & t < t_{\max} - 7\tau_R \\ \frac{1.001}{\tau_R + \tau_D} \exp[(t - t_{\max})/\tau_R], & t_{\max} - 7\tau_R \leq t \leq t_{\max} \\ \frac{1.001}{\tau_R + \tau_D} \exp[(t_{\max} - t)/\tau_D], & t_{\max} \leq t \leq t_{\max} + 7\tau_D \\ 0, & t_{\max} + 7\tau_D < t \end{cases}$$

and τ_R , τ_D and t_{\max} are the rise time, decay time and time of maximum intensity

for the event. For the purpose of this subroutine, the exponential rise and decay in intensity will adequately predict the total dose and dose rate.

The effect of the earth's magnetic field on the incident radiation must be included. The theory of the allowed cone, as developed by Störmer (Reference 36), will be used as the basis for calculating the modification of the energy spectrum. This theory is based on a dipole approximation to the geomagnetic field. The constants of the motion of a charged particle in a dipole field are the energy and the canonical momentum about the dipole axis. With these constants, the differential equations governing the trajectory can be reduced to one equation of motion in the meridian plane (References 37 and 38). Störmer obtains an expression for the angle that the trajectory makes with the meridian plane and deduces that the trajectory must lie within a cone of allowed directions around the normal to the meridian plane. The angle of the cone varies with the energy of the particle and with the position of the observation point. Lemaitre used Liouville's theorem to prove that if the flux of particles is isotropic outside the magnetosphere, then the intensity in a given direction within the allowed cone is the same as the intensity outside the magnetosphere. Hence, the energy spectrum inside the magnetosphere is given by that outside times the ratio as a function of energy of the solid angle of the allowed cone to 4π . Störmer finds that the allowed cone is defined by the equation

$$P = \frac{M}{R^2} \frac{\cos^4 \lambda}{(1 + \sqrt{1 - \cos \gamma \cos^3 \lambda})^2}$$

where M is the dipole moment of the earth (0.311653 gauss earth radii³) λ is the geomagnetic latitude, R is the invariant radius in earth radii, P is the particle rigidity defined above, and γ is the half angle of the allowed cone about the normal to the meridian plane. Thus, we see that the cone is completely closed for particles of rigidity less than

$$P = \frac{1.497 \times 10^4}{L^2} \left(\frac{2}{1 + \sqrt{1 + (R/L)^{3/2}}} \right)^2$$

These particles cannot reach the point (R, L) from outside the magnetosphere. The cone is completely open for particles of rigidity greater than

$$P = \frac{1.497 \times 10^4}{L^2} \left(\frac{2}{1 + \sqrt{1 - (R/L)^{3/2}}} \right)^2$$

Figure 21 is a plot of these two expressions at an altitude of 300 nautical miles as a function of L . From the expressions above, it is easy to see that the spectral

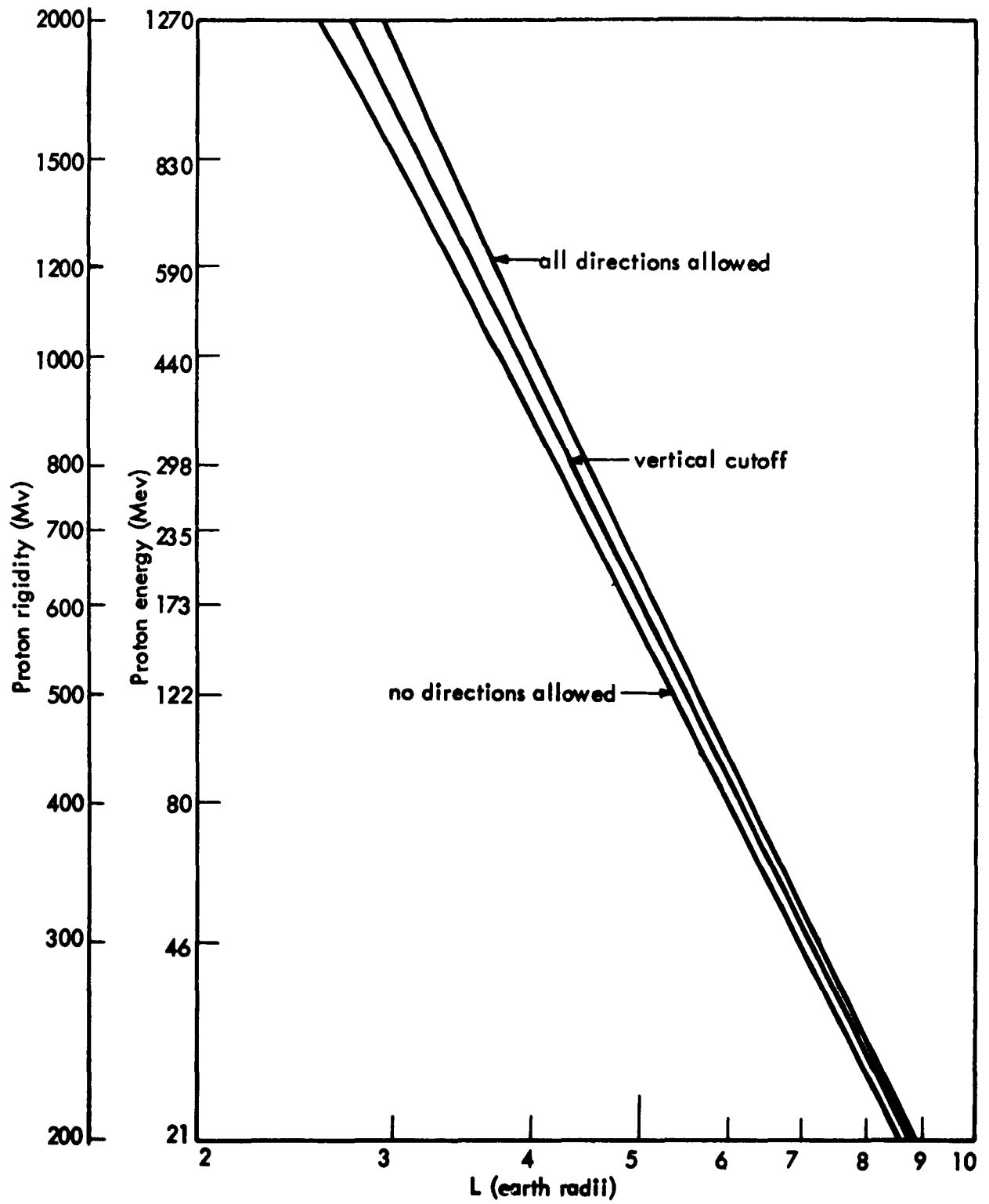


FIGURE 21. Proton cutoff energies versus L

modification is most strongly dependent upon L . Thus, we assume that a resultant spectrum can be defined for any L shell such that at any point on the shell, the instantaneous spectrum is approximated by

$$J(>P) = J_0 G_i(P, P_0) F(t)$$

where the G_i are the modified spectra on the i^{th} L -shell and $F(t)$ describes the flux-time dependence. The flux for a specific mission is calculated as follows. The L range is divided into 7 macro-shells such that the spectral modification is relatively slight within each macro-shell. The values L_i will be used to designate the interval $L_{i-1} < L \leq L_i$. The seven L_i 's are given as input data. Since the trajectory code calculates L as a function of time, it is possible to obtain a time integration of the function $F(t)$ for that portion of the mission spent in each of the L intervals. The total flux reaching the vehicle is then

$$J(>P) = \sum_{i=1}^7 J_0 G_i(P, P_0) F_i$$

where F_i is the time integral of $F(t)$ over the time spent in the corresponding L interval.

In addition to calculating the time integral of $F(t)$ the subroutine also keeps a running total of the dose received in the i^{th} L interval by using a set of dose conversion numbers k_i provided by the shielding code.

The subroutine has been designed for modified exponential rigidity spectra. Since the functions G_i must be specified as input data, other functional forms may be used such as power laws in energy. The suggested modification of the exponential rigidity spectrum is an abrupt cutoff below the vertical cutoff rigidity. Thus,

$$G_i(P, P_0) = \begin{cases} 0 & , P < P_c(L_i) \\ \exp(-P/P_0) & , P \geq P_c(L_i) \end{cases}$$

where

$$P_c(L_i) = 1.497(10^4)/L_i^2$$

The geomagnetic storm that accompanies the larger events produces a reduction in the strength of the magnetic field so that the effective L value at a given point is larger than the normal L value (see Figure 22). This modification of the geomagnetic field can be included in the spectra G_i by using the effective L rather than the normal

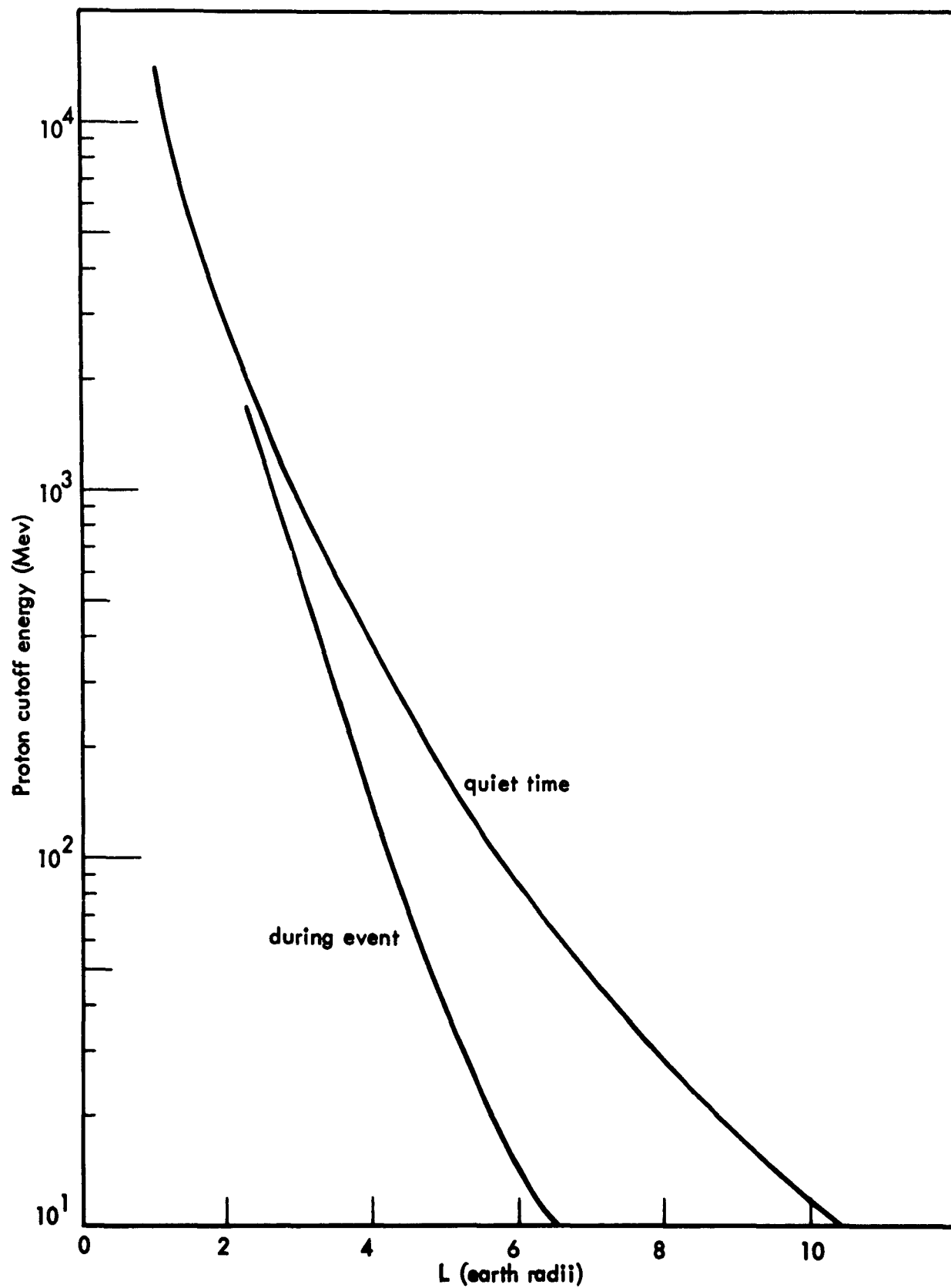


FIGURE 22. Variation of vertical cutoff

L in the definition of P_c . For example, the set of L_i given by $L_1 = 3.0$, $L_2 = 3.6$, $L_3 = 4.2$, $L_4 = 4.7$, $L_5 = 5.2$, $L_6 = 5.6$, and $L_7 = \infty$ would correspond to proton vertical-cutoff energies in Mev, of $E_1 = 610$, $E_2 = 241$, $E_3 = 106$, $E_4 = 58.3$, $E_5 = 32.5$, $E_6 = 20.5$, and $E_7 = 0$ during the event. During quiet times the corresponding vertical-cutoff energies would be $E_1 = 980$, $E_2 = 560$, $E_3 = 325$, $E_4 = 217$, $E_5 = 150$, $E_6 = 114$, $E_7 = 0$.

The accuracy of the experimental data on fluxes and energy spectra does not justify a completely rigorous treatment of the problem. The L-shell approximation could be improved upon by a method that computes the modified spectrum at each point on the trajectory. It is recognized that the L-shell approximation is a first attempt to compute the effect of the geomagnetic field on untrapped radiation and does have the advantage of fitting easily into the calculational procedures established for the trapped radiation.

3.2.2 Galactic Cosmic Rays

The radiation dose to space vehicles from the galactic cosmic radiation can be calculated from the measurements of Neher and Anderson (References 39 and 40) and Lin, et al. (Reference 41). Neher and Anderson have flown ion chambers in balloons at polar latitudes for a number of years. They flew a similar ion chamber aboard the Mariner 2 space probe, and a comparison of the Mariner 2 and the balloon measurements (Reference 40) indicated that 21 percent of the dose to the balloon-borne instruments was due to albedo arising from the interaction of the primary radiation with the earth's atmosphere and magnetic field. These measurements can be expressed as dose in rad hr^{-1} (instead of the $\text{ions cm}^{-3} \text{ sec}^{-1} \text{ Atm}^{-1}$ of air as reported by the authors). The values used in the present treatment include the albedo contribution, and are for particles incident from the upper hemisphere; this treatment is appropriate for vehicles in near-earth orbits, but for vehicles a large distance from the earth these values should be reduced by 20 percent, and then corrected for spherical geometry. Figure 23 shows the variation of ion chamber response with atmospheric depth near the magnetic pole for several times during the solar cycle, with a scale added to indicate the dose rate in mrad/hr . It can be noted that the dose changes very little with atmospheric depth near the top of the atmosphere; thus the maximum dose values can be used to evaluate the dose inside space vehicles for shielding thicknesses currently under consideration. It can also be seen that the dose rate changes by a factor of two during the sunspot cycle, the maximum dose rate from galactic cosmic radiation coming at the same time as the minimum in solar activity.

These measurements of the dose rate can be related to the measurements of Lin, et al. (Figure 24). These results indicate that the counting rate from galactic cosmic rays, as measured by the Explorer VII satellite, is constant above $L = 2.5$ and is approximately a linear function of L between L values of 1.1 and 2.5. Hence, the dose rate will also depend linearly on L , provided that the dose per particle is

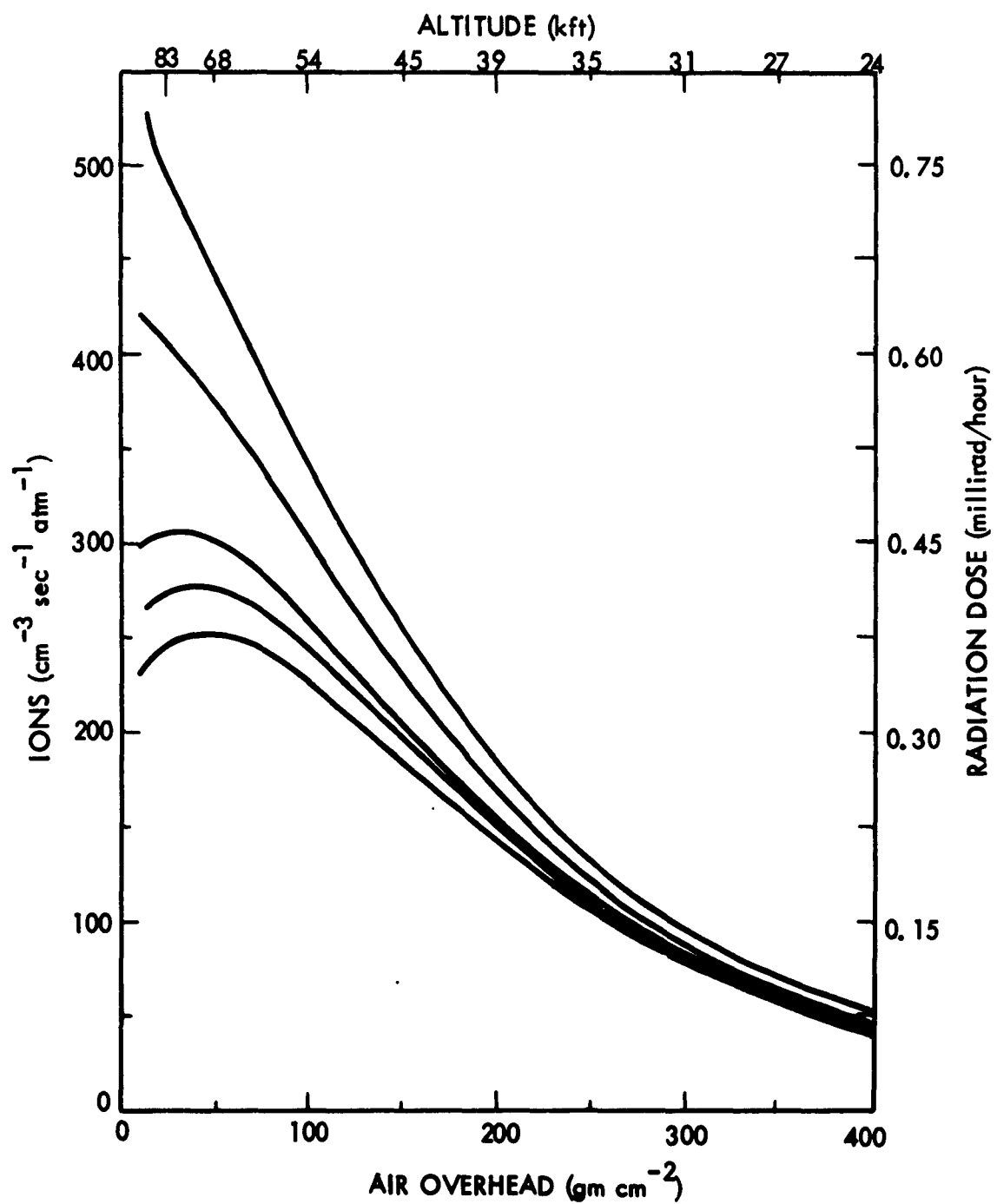


FIGURE 23. The time variation of cosmic radiation at Thule Greenland
 $\lambda_m = 88^\circ\text{N}$

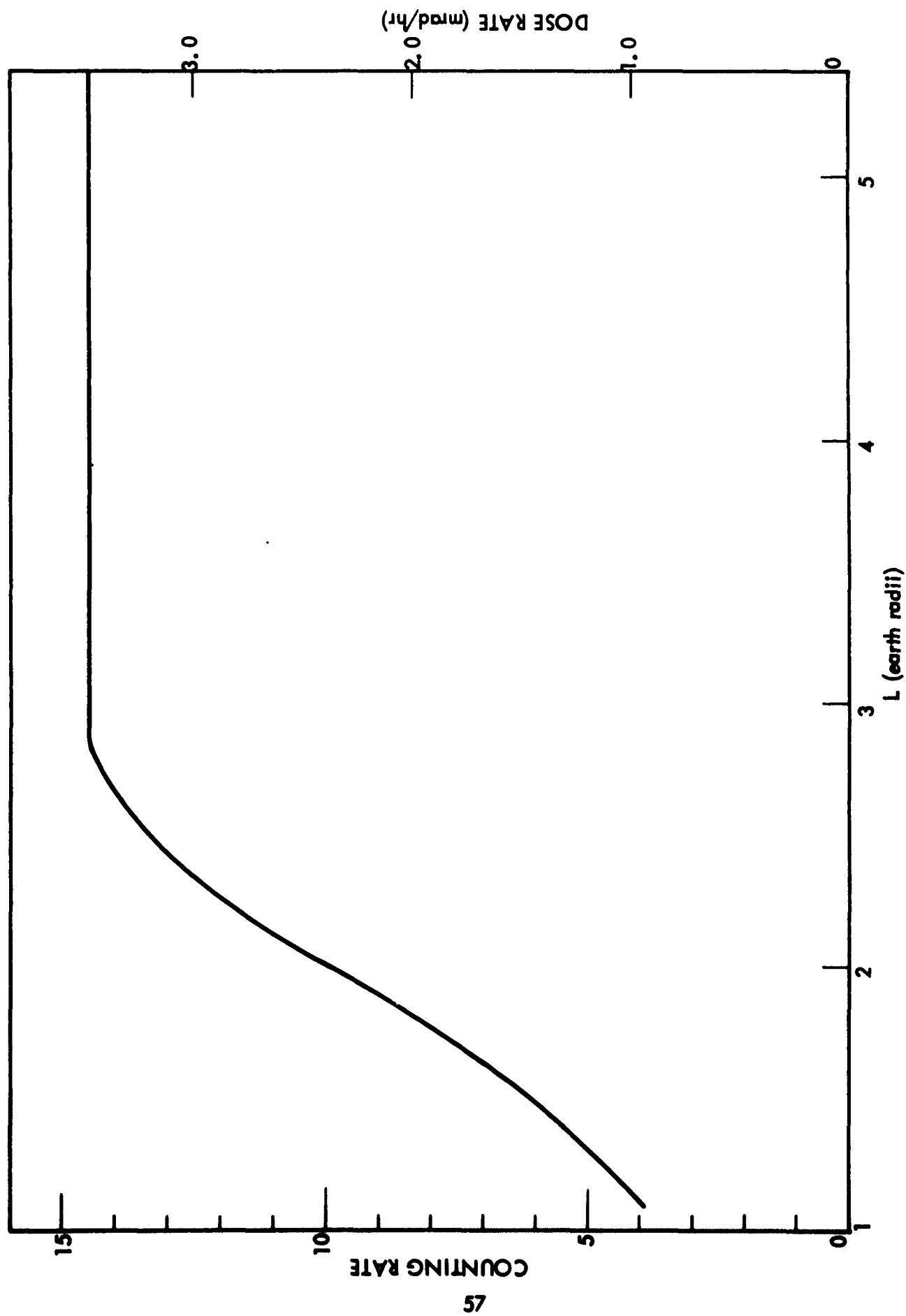


FIGURE 24. Cosmic ray counting rate as measured by Explorer VII satellite (November 1959 to December 1960)

constant. However, the variation in dose per particle is such that estimates based on this approximation are conservative: the dose is slightly overestimated in equatorial regions, where the dose is small anyway due to a smaller particle flux.

Normalizing the dose rate measurements of Neher and Anderson to the L variation, we have the dose rate D as a function of L

$$D = \begin{cases} [1.92(L-1) + 0.72] (10^{-7}) \text{ mrad/hr,} & \text{for } 1 < L < 2.5 \\ 3.6(10^{-7}) \text{ mrad/hr,} & \text{for } L > 2.5 \end{cases}$$

at the time of maximum in the solar cycle. For the time of solar minimum

$$D = \begin{cases} [4.32(L-1) + 0.72] (10^{-7}) \text{ mrad/hr,} & \text{for } 1 < L < 2.5 \\ 7.2(10^{-7}) \text{ mrad/hr,} & \text{for } L > 2.5 \end{cases}$$

The resulting dose rates will be much smaller than those arising from the trapped particles for most cases of interest. The maximum galactic dose rate is 17 millirad/day during solar minimum and 9 millirad/day at the time of solar maximum. For cases where the dose from trapped particles exceeds these values significantly, it is recommended that the values for $L > 2.5$ be used to estimate the galactic radiation dose.

4.0 VEHICLE ANALYSIS

An evaluation of the shielding of a space vehicle for any incident radiation flux is dependent on an analysis of the geometry and material composition of the vehicle. This analysis is designated as a "sector analysis" of the vehicle, and is accomplished by placing the origin of a spherical coordinate system at the dose point and determining the shield thickness of the vehicle as a function of solid angle. The vehicle is divided into N sectors, each subtending a solid angle Ω_n where

$$\sum_{n=1}^N \Omega_n = 4\pi$$

The slant thickness of the materials providing shielding in a sector can be determined as Figure 25 will show. Mathematical refinements can be made to improve the accuracy of the analysis by analyzing many vectors per sector and determining some effective average thickness. Boeing and other organizations (References 42 and 43) have been developing computer programs to perform such a geometric analysis automatically. The self-shielding of the human body can also be included in the analysis when the dose point is in an astronaut.

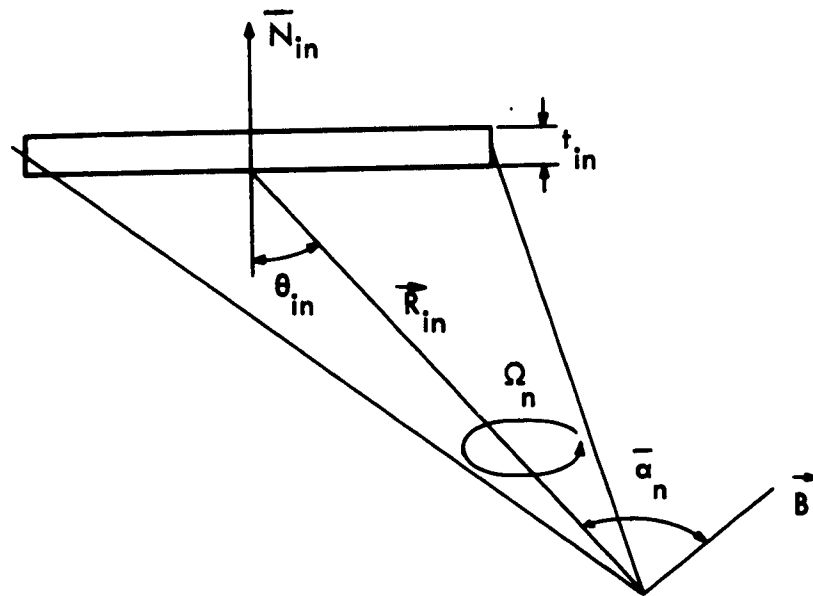
In the original Boeing space-radiation programs the dose penetrating the vehicle was computed by the expression

$$D_i(p) = S_i \sum_{n=1}^N T_{in}(p) \omega_n$$

where $D_i(p)$ is the dose at a point p from radiation of type i ; S_i is the flux of radiation of type i ; $T_{in}(p)$ is the dose transmission factor for radiation type i penetrating section n , and ω_n is a weighting factor defined as $\Omega_n/4\pi$, where Ω_n is the solid angle subtended by section n .

The data necessary to compute $T_{in}(p)$ is the energy spectrum of the incident radiation and the atomic number and thickness of each material in a given sector (ordered from incident face to exit face).

To improve the mathematical model to include the effects of the angular distribution of the penetrating radiation and the scattering within a vehicle, more input data would be required. A simplified sector of a vehicle and the variables that are required for an improved radiation analysis are shown in Figure 25. To achieve an



Required data for each layer, i , in sector n

Z_{in} = atomic number of layer (i, n)

R_{in} = scalar distance between dose point and near surface of layer (i, n)

\vec{N}_{in} = normal to layer (i, n)

t_{in} = thickness of layer (i, n)

ρ_{in} = density of layer (i, n)

θ_{in} = angle between \vec{N}_{in} and \vec{R}_{in}

Ω_n = solid angle subtended by sector n

\vec{B} = vector of axis of azimuthal symmetry for incident flux

α_n = angle between \vec{R}_{in} and \vec{B}

FIGURE 25. Input data for improved vehicle analysis

improved analysis, eight variables for each layer in each sector must be specified compared to the three variables required for the original analysis. The following sections of this report describe the improved computations of the dose transmission factor using either 3 or 8 input variables for various types of incident radiation and their secondaries. It will be established that the use of an improved analysis employing the eight variables is not justified at this time because the small increase in accuracy does not warrant the extra effort required to obtain the input data and perform the additional analyses.

5.0 ELECTRON SHIELDING

The prediction of dosage within a space vehicle exposed to electron radiation is a complex problem influenced by many variables. The purpose of this study was to examine variables such as:

- 1) The incident angular and energy distributions;
- 2) The LET and energy spectra;
- 3) The angular distribution of the penetrating radiation;
- 4) The use of multislabs of various materials; and
- 5) The details of input geometric sectoring for the vehicle and crew.

The prior Boeing electron shielding codes (References 44, 45, and 46) were used in some of the analyses and formed the basis for the codes developed in this study. In many situations, these codes are satisfactory for space shielding calculations.

5.1 MONTE CARLO STUDIES

5.1.1 Interactions

The object of this study was to develop a mathematical model to compute the transmitted number, energy spectrum, and angular distribution of electrons penetrating a shield. An electron penetrating a shield will follow a tortuous path as it interacts with atomic electrons and nuclei of the shield. Even though the total path length of monoenergetic electrons is relatively constant, the distance between the face of the shield and the end of an electron path will vary greatly due to scattering. This fact makes the electron range a poor parameter in electron shielding calculations.

Electrons in a shield can be scattered by four principal interactions:

- 1) An inelastic collision with atomic electrons, where one or more atomic electrons are raised to an excited state or unbound state. This is the predominant scattering mechanism for electrons with a few hundred kev kinetic energy;
- 2) An inelastic collision with a nucleus, where the electron is deflected and a quantum of radiation is emitted (bremsstrahlung);
- 3) An elastic collision with a nucleus, where the electron loses only the kinetic energy necessary to conserve momentum between the two particles; and

4) An elastic collision with the atom, only of importance for electrons with energies less than 100 ev.

Detailed descriptions of these electron interactions are presented by Evans (Reference 47) and Birkoff (Reference 48).

The Boeing electron Monte Carlo code (BEMC) (Reference 45) was developed using the computational models of Perkins (Reference 49) and Leiss, Penner, and Robinson (Reference 50). The complicated process of electron interaction in a shield is simplified into two mechanisms: radiation loss and ionization loss. An electron is followed through a series of thin slabs where it is assumed to have suffered discrete energy losses and angular deflection. In each increment the energy loss due to ionization was obtained from the average ionization loss tables of Nelms (Reference 51). As shown in Figure 26, the ionization energy loss in aluminum changes rapidly with energy below 1 Mev. Therefore, the slab increments should decrease with decreasing electron energy below 1 Mev so that the loss can be described by

$$E_{\text{ion loss}} = \Delta x \frac{dE}{dx}(E)$$

where Δx is the increment thickness and $\frac{dE}{dx}(E)$ is the energy loss for an electron of energy E . The machine program permits the use of three forms of Δx : a constant value, a constant multiplied by the electron energy, and a constant divided by the electron energy. Values of Δx from 0.025 to 0.1 of the electron range were tested and found to provide answers within the statistical error associated with the number of histories processed. Minimum deviations were observed using $\Delta x/E$, where $\Delta x = 0.05 R$ (R is the range in gm/cm^2 and E is in Mev).

The second criterion for the increment thickness was that a small net angular deflection of the electron be obtained in the increment. For the BEMC, the scattering angle is determined by the Bethe modifications to the Moliere relationships (Reference 52) which are only valid for small scattering angles (less than 20 degrees). A thickness of 1/20 of the electron range is normally used for Δx . (See Reference 44 for full details). A study of the current multiple-scattering theories for electron penetration was conducted and the analysis is presented in the Appendix. The Goudschmidt-Saunderson (Reference 53) multiscattering theory was found to be superior at large angles; however, the computation time required on a computer is excessive. This method has been employed by Berger (Reference 54) in an electron Monte Carlo study and reasonable agreement is obtained between his data and the BEMC data using thin slabs.

The probability of radiation loss $P(E_0 - E)$ is obtained from the relationships derived by Bethe and Heitler (Reference 55) expressed as

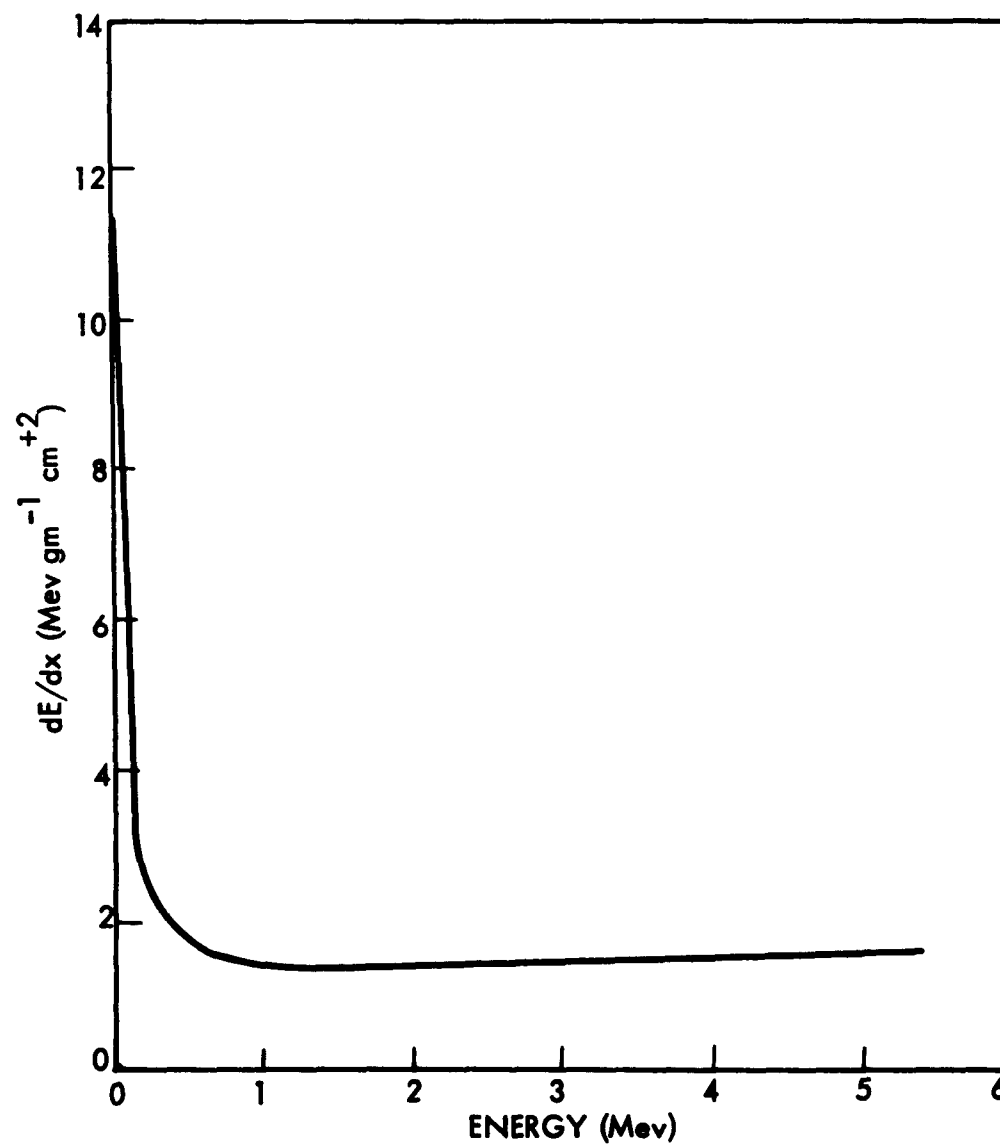


FIGURE 26. Electron energy loss in aluminum (Reference 51)

$$P(E_0 - E) = \frac{\ln(E_0/E) [(t/\ln 2) - 1]}{E_0 \ln(t/\ln 2)}$$

In this equation E_0 is the initial electron energy, E is the final energy after radiation loss, and t is the ratio of the slab thickness to the radiation length X_0 where

$$\frac{1}{X_0} = \frac{4\alpha N_0}{A} Z^2 r_0^2 \ln(183Z^{-1/3})$$

where $\alpha = 1/137$, N_0 is Avogadro's number, and $r_0 = 2.28 \times 10^{-13}$ cm

The Monte Carlo method neglects straggling and does not follow delta or knock-on electrons. Comparison of BEMC data with existing information shows that these phenomena are not important to the primary electron number density or angular distribution. These corrections were made by Perkins (Reference 49) in his Monte Carlo study and were found to be negligible.

5.1.2 Modifications

The original BEMC was written in machine language and was converted to Fortran for compatibility with the AFWL computers. Modifications were made to provide the computation of:

- 1) The cosine of the exit angle of the electron;
- 2) The summation of number spectra over angle;
- 3) The summation of number spectra over energy;
- 4) The energy spectrum of the bremsstrahlung; and
- 5) The LET number spectrum.

The modified code will accept (1) any spectrum of electron energies including a monoenergetic spectrum treated as a special case, (2) a monodirectional or isotropic distribution in incident angle, and (3) a combination of twelve shielding materials. The code will compute either number and energy spectra for various exit angles or LET spectrum for various exit angles, and/or bremsstrahlung production. The changes are described in the operator's manual, Volume II of this report.

5.1.3 Angular Distribution of Penetrating Electrons

Modifications were made in the treatment of the angular distribution to examine the scattering of electrons penetrating a shield, to obtain a model for scattering inside

of a vehicle, and to establish the angular distribution of the penetrating electrons. The average cosines were calculated for each increment of a target slab according to the formula

$$\langle \cos \theta \rangle = \frac{\sum_i n_i \cos \theta_i}{\sum_i n_i}$$

where n_i is the number of electrons scattered out of the increment at the angle θ_i .

The angular distributions in the forward direction were computed in increments 15 degrees wide for an initial flux of 10^3 electrons incident at 0, 30, and 60 degrees with energies of 1, 3, and 6 Mev. In order to cover a wide range of Z uniformly, aluminum, iron, silver, and lead were used as target materials.

A general analysis of the Monte Carlo electron angular distributions is not attempted here, since no completely rigorous multiple-scattering theory exists which takes into account all the effects of energy loss, straggling, and various boundary conditions. The Monte Carlo method itself is the only technique available at present for treating a general class of problems.

The following analysis is based on a consideration of the angular distribution for target thicknesses comparable to the range of the incident electrons. It has been previously hypothesized that the electron angular distribution becomes essentially isotropic after passage through sufficiently thick targets. This assertion has been verified theoretically by Rohlich and Carlson (Reference 56) for the simplest case of an infinite medium. Obviously, if this also held true for bounded media, the problem of angular distributions could be effectively eliminated by taking sufficiently thick targets. However, for plane parallel targets of thickness comparable to the total range, the experimental results obtained by Frank (Reference 57) indicate that the angular distribution is not isotropic, but remains sharply peaked in the forward (and backward) direction. In addition, Frank states that after the electrons have reached a certain "diffusion" depth σ_0 , the half-width of the angular distribution remains constant so that further penetration by the electrons may be dependent only on the transmission factor. In accordance with these results, the Monte Carlo data was first analyzed to determine the diffusion lengths and then the actual angular distributions were compared at σ_0 .

The diffusion depth σ_0 for each energy and target material was determined from the Monte Carlo data by estimating the point at which the average cosine of the scattering angles for normal incidence appeared to reach its asymptotic value. The "asymptotic" point was assumed to be equal to σ_0 . This assumption was justified by the agreement in the asymptotic $\langle \cos \theta \rangle$ values for Frank's results and the Monte Carlo data. The average cosine is defined by

$$\langle \cos \theta \rangle = \int \cos \theta f(\theta, \phi) d\Omega / \int f(\theta, \phi) d\Omega$$

Frank's experimental angular distributions are accurately described at σ_0 by the distribution function $f(\theta) = f(0) \cos^2 \theta$, regardless of the target material. This gives an average cosine of 0.75. The Monte Carlo results for all materials and energies investigated indicated a value of $\langle \cos \theta \rangle = 0.74 \pm 0.03$ which agrees within statistical error with Frank's data — if the "asymptotic" point is identified with the diffusion length σ_0 . It should be noted here that the assumption of an isotropic distribution gives $\langle \cos \theta \rangle = 2/3$.

The average cosines for aluminum at 1 Mev for incident angles of 0, 30, and 60 degrees are shown in Figure 27. The error brackets on the curve for normal incidence were determined by the statistical error in the number of electrons transmitted through each increment. The diffusion lengths for aluminum, iron, silver, and lead at 1, 3, and 6 Mev are shown, with estimated errors in Table 3.

Table 3
MONTE CARLO DIFFUSION LENGTHS
(σ_0 in g/cm²)

Element (Z)	Initial Energy		
	1 Mev	3 Mev	6 Mev
Al (13)	0.17 ± 0.02	0.85 ± 0.10	1.90 ± 0.10
Fe (26)	0.11 ± 0.01	0.55 ± 0.08	1.65 ± 0.10
Ag (47)	0.08 ± 0.02	0.48 ± 0.05	1.35 ± 0.10
Pb (82)	0.075 ± 0.01	0.40 ± 0.05	0.95 ± 0.10

Since Frank's data were taken only at 1.75 Mev, the diffusion lengths can be approximately compared through the modified Mollere theory which Frank used to obtain σ_0 . Frank defined the condition of "total diffusion" to occur at the point where the angular half-width θ_H was equal to 45 degrees. A good approximation for θ_H , according to Hanson, Lanzl, Lyman and Scott (Reference 58), is

$$\theta_H = 0.833 \times_c \sqrt{B - 1.2} \quad (14)$$

which is obtained by considering only the dominant Gaussian term of the angular distribution. According to Frank, this formula holds for half-widths in excess of 20 degrees.

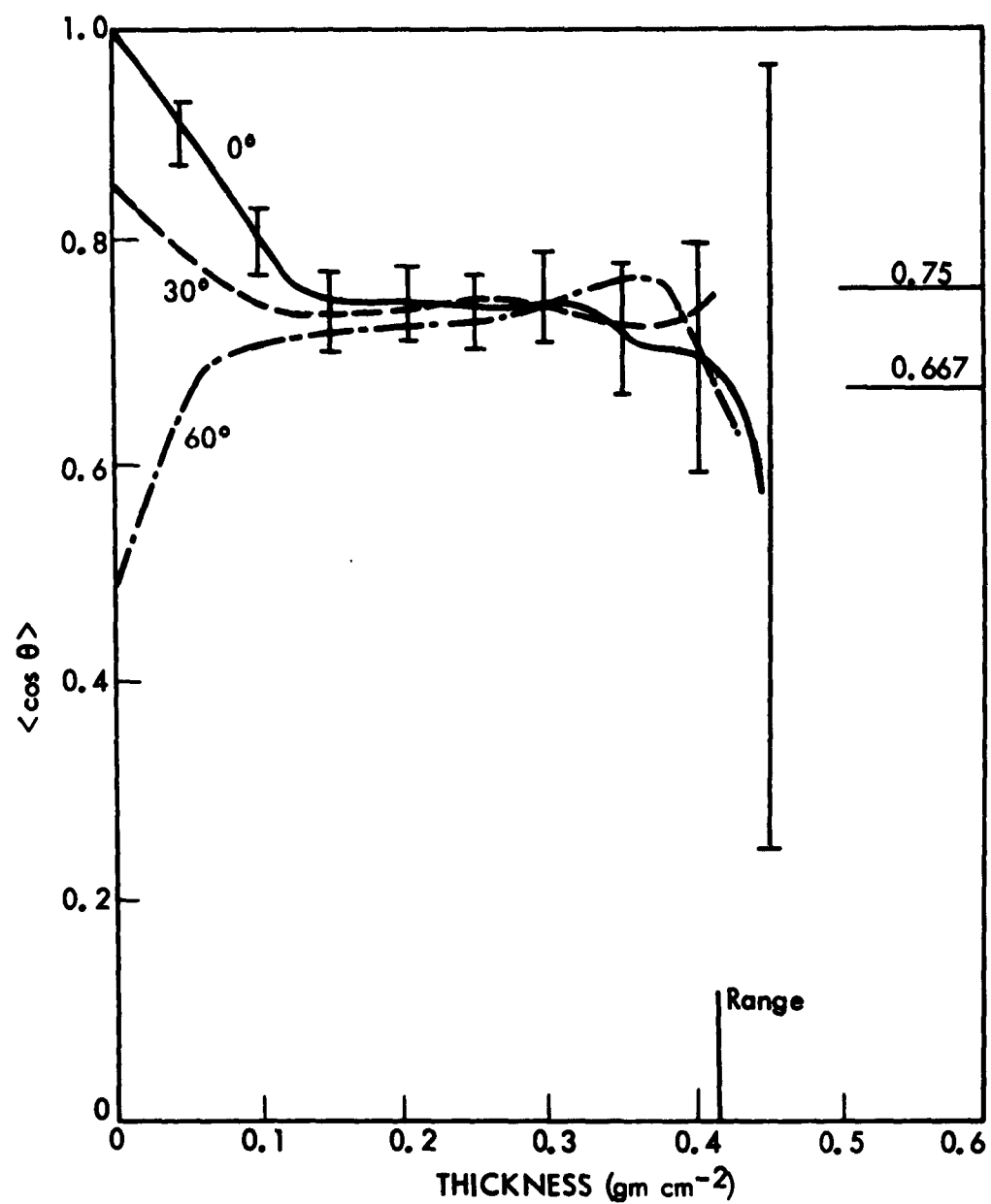


FIGURE 27. Average cosines for 1-Mev electrons incident at 0, 30, and 60 degrees on aluminum

The quantities X_c and B are given in the Molière-Bethe theory (Reference 52) by

$$X_c^2 = 4\pi N d e^4 Z(Z+1)/(pv)^2 \quad (15)$$

$$B - \ln B = b$$

where

$$b = \ln \left[\frac{6680 \rho d}{\beta^2} \frac{(Z+1) Z^{1/3}}{A(1 + 3.34 \alpha_1^2)} \right]$$

$$\alpha_1 = Z_e^2 / \hbar v$$

N = atom number density

A = atomic weight

v = electron velocity

β = v/c

P = momentum

ρ = target density

These equations are coupled in the thickness d . To find the diffusion length $\sigma_o \equiv \rho d$ for $\theta_H = 45$ degrees, we combine Equations 14 and 15.

Then

$$\begin{aligned} \sigma_o &= \frac{9.58 \theta_H^2 A (pv)^2}{Z(Z+1) (B - 1.2)} \\ &= 5.90 \left[\frac{A}{Z(Z+1) (B - 1.2)} \frac{4T^2 (T+1)}{1 + 4T (T+1)} \right] \end{aligned}$$

where T is the kinetic energy in Mev of the incident electrons and $m_o c^2$ is set equal to 0.5. Designating

$$f = 5.90 \left[\frac{A}{Z(Z+1)} - \frac{4T^2(T+1)}{1+4T(T+1)} \right]$$

$$g = \frac{(Z+1) Z^{1/3}}{A(1+3.34 \alpha_1^2)}$$

the resulting expressions for σ_0 become

$$\sigma_0 = f/(B - 1.2) \quad (16)$$

$$B - \ln B = \ln \left[\frac{6680 fg}{B^2 (B - 1.2)} \right] \quad (17)$$

For specified values of Z and T , Equation 17 is solved for B by iteration and σ_0 is then obtained from Equation 16. The calculated values of σ_0 can be expected to agree only qualitatively with the Monte Carlo values since the effects of energy loss have been neglected. The results are shown in Figures 28, 29, and 30 for the energies 1, 3, and 6 Mev, respectively. The values given by Frank at 1.75 Mev are also shown in Figure 28. The qualitative agreement is good, although large deviations occur for high and low Z values.

The diffusion length is measured along the incident electron direction and is observed to increase slightly with angle measured from the normal. The diffusion lengths for the 30° and 60° curves shown in Figure 27 are obtained by dividing the normal areal density by the cosine of the angle.

The angular distributions of transmitted electrons were tabulated as histograms with 15-degree increments. Figure 31 shows an example for 1-Mev electrons incident on aluminum of thickness 0.175 gm/cm². The distribution appears to be best described by Frank's empirical cosine-squared law. The function $(0.717 \cos\theta + \cos^2\theta) \sin\theta$ obtained by Bethe, Rose, and Smith (Reference 59) neglecting energy loss effects. In a previous Monte Carlo calculation, Berger (Reference 54) obtained a better fit to his data with this function than with the cosine-squared law. However, Berger's distribution was calculated for a lower energy of 0.5 Mev which apparently resulted in an increase of large-angle scatterings.

The value of the average cosine at σ_0 also indicates that the cosine-squared law provides a better description of the angular distribution. The function $(0.717 \cos\theta + \cos^2\theta) \sin\theta$ gives $\langle \cos\theta \rangle = 0.706$ compared with 0.750 for Frank's cosine-squared law and 0.74 ± 0.03 for the Monte Carlo calculation. For target thicknesses greater than σ_0 , the cosine-squared law also provides a reasonable fit as shown in Figure 32. For $pd > 2\sigma_0$, the results are uncertain due to the large statistical errors which occurred in the Monte Carlo data. For the case shown in Figure 30, the angular

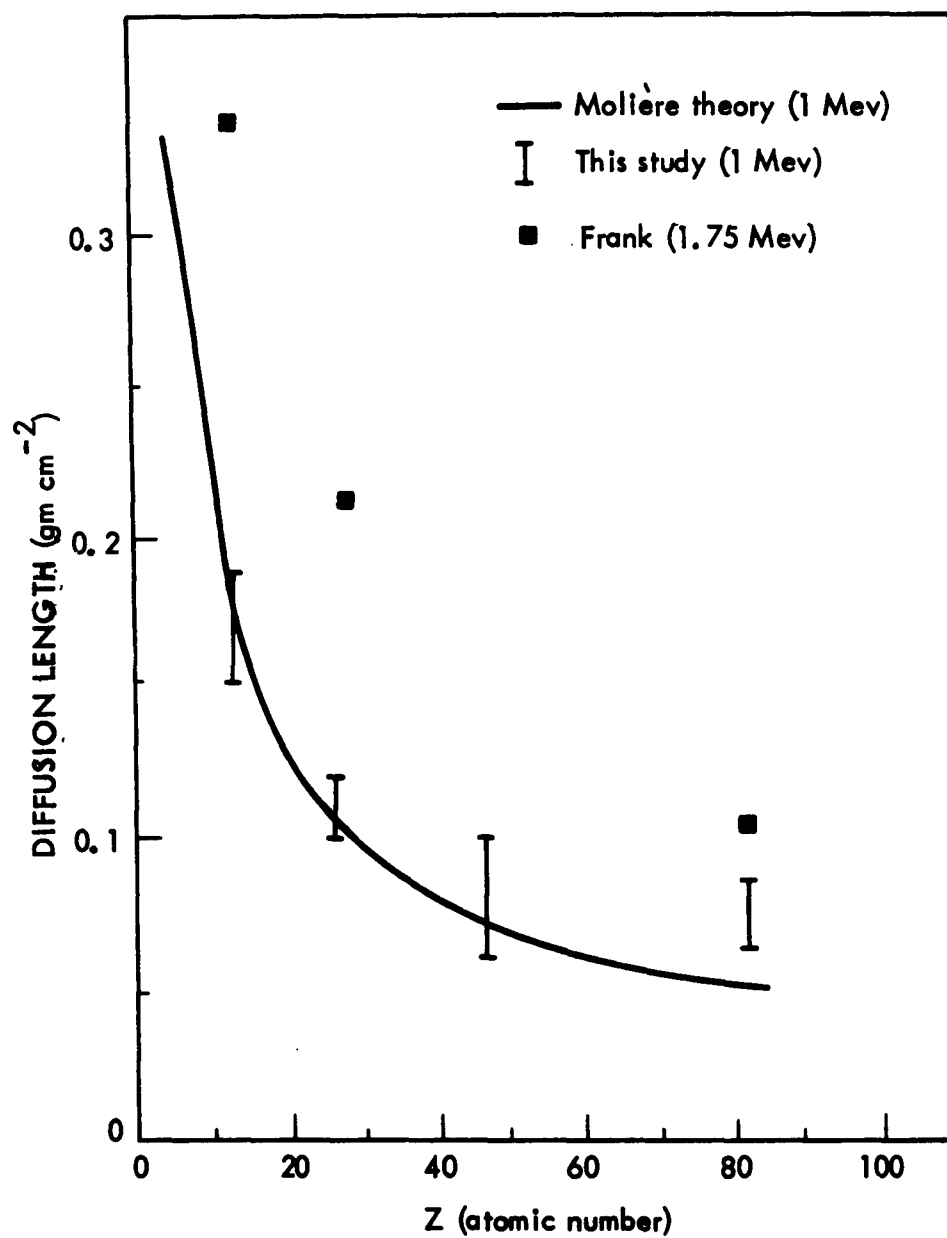


FIGURE 28. Diffusion lengths for 1-Mev electrons, normal incidence

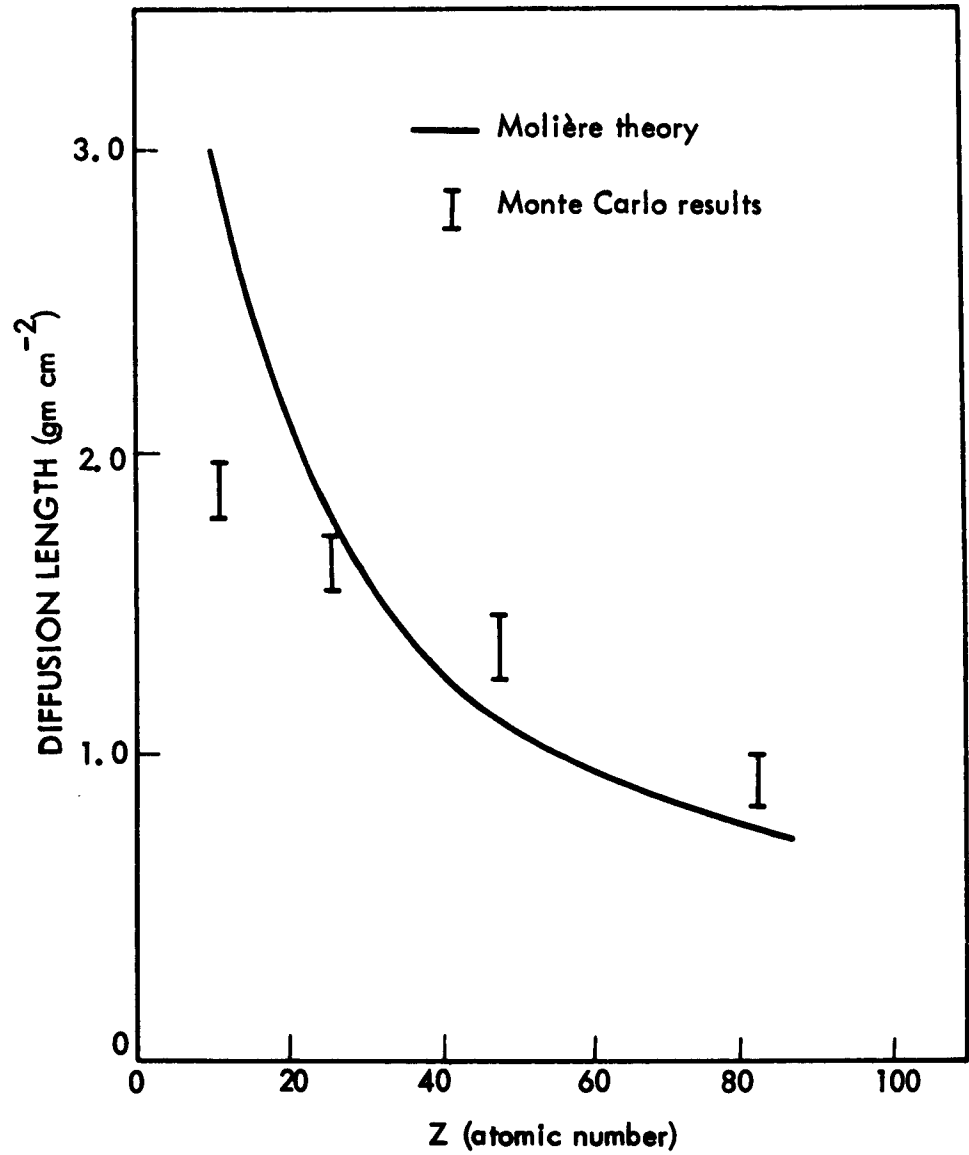


FIGURE 29. Diffusion lengths for 3-Mev electrons, normal incidence

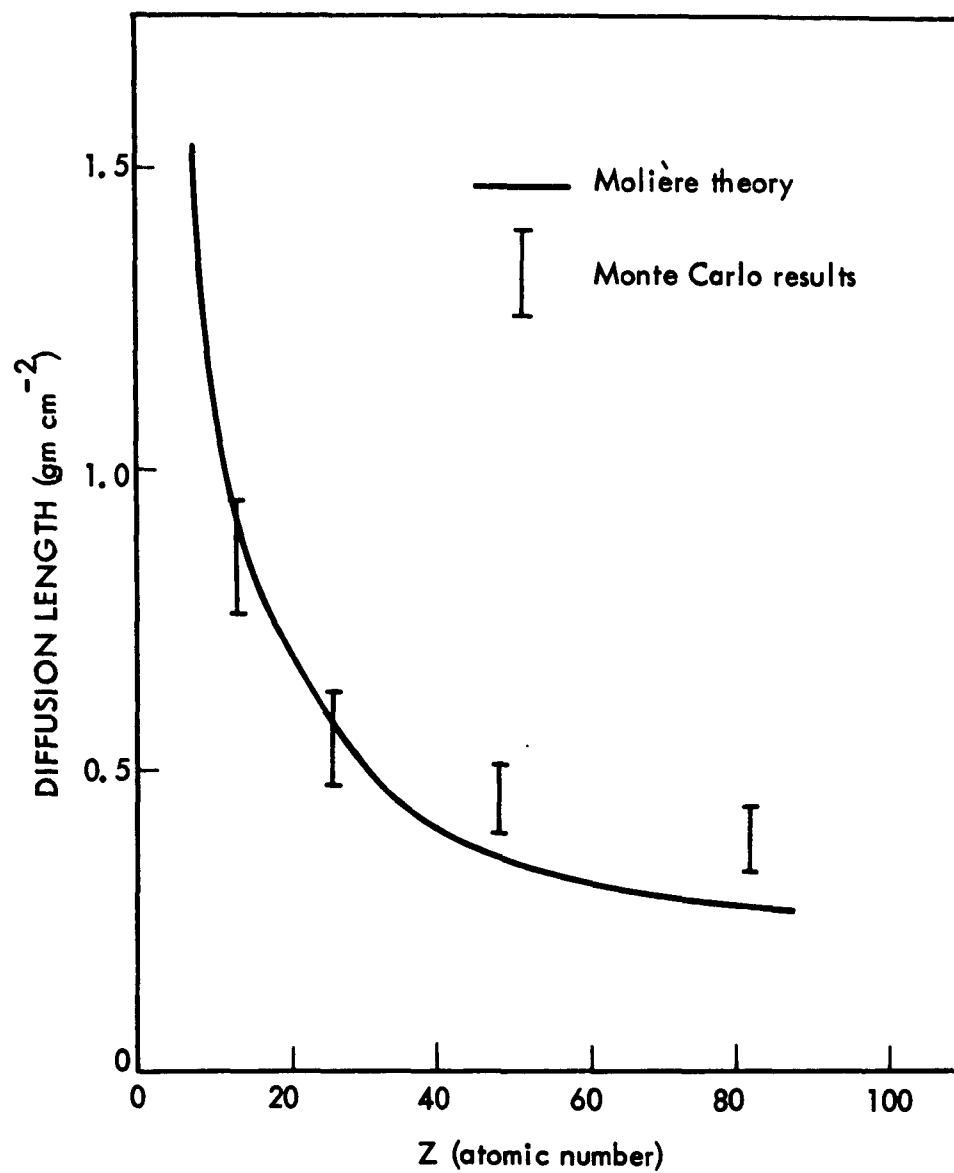


FIGURE 30. Diffusion lengths for 6-Mev electrons, normal incidence

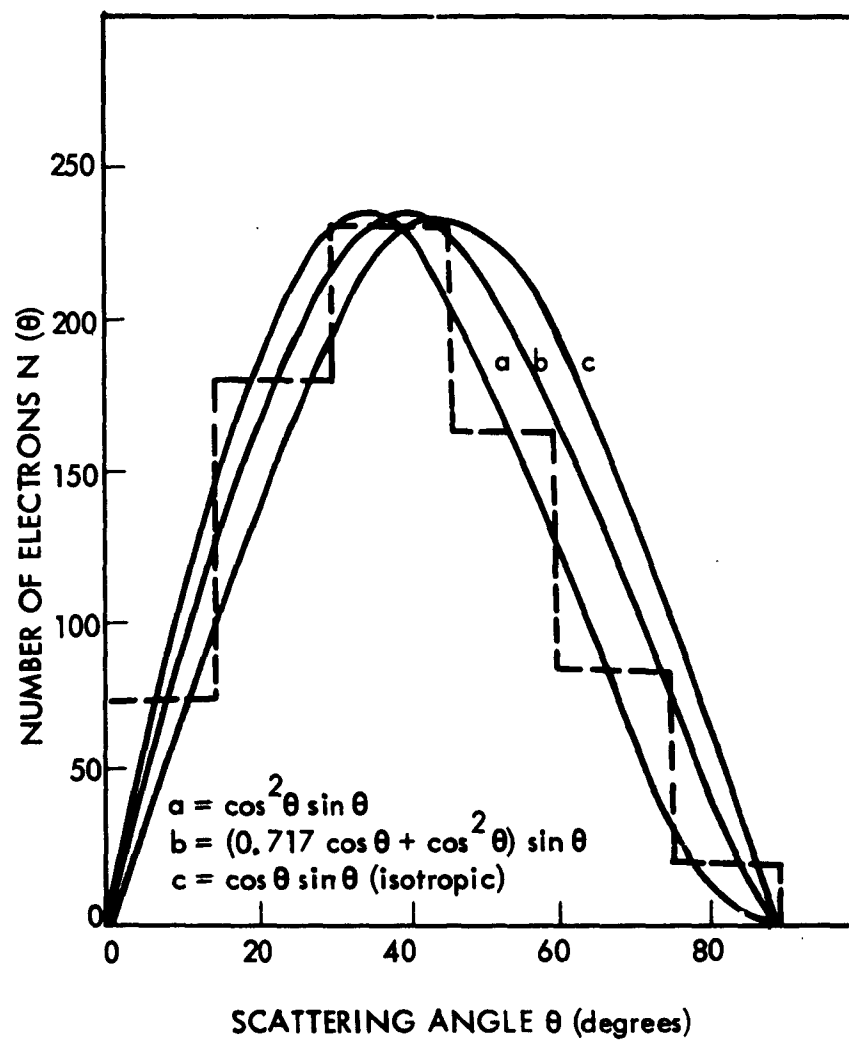


FIGURE 31. Angular distribution of 1-Mev electrons transmitted through 0.175 gm/cm² of aluminum, normal incidence

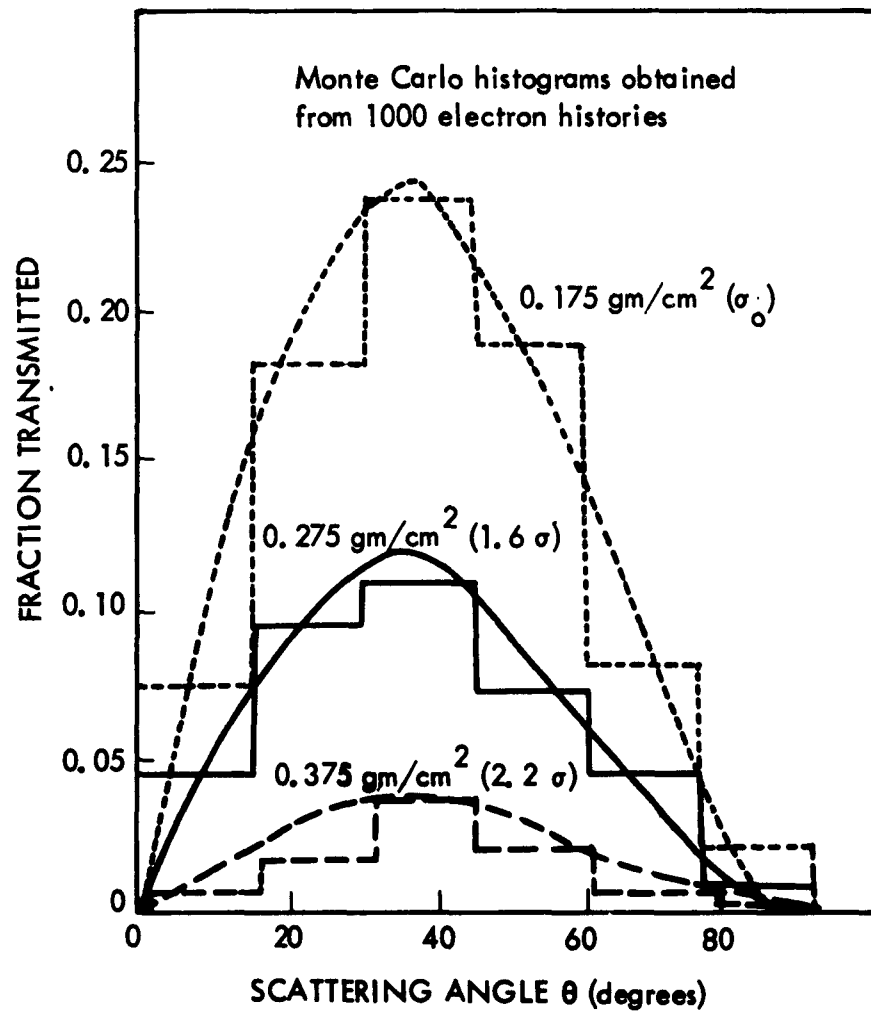


FIGURE 32. Angular distribution of 1-Mev electrons transmitted through aluminum, normal incidence

increments at $2.2 \sigma_0$ each contained less than 40 electron histories, resulting in a statistical error greater than 15 percent.

From the preceding considerations, the Monte Carlo results indicate that the electron angular distributions can be approximately described by

$$f(\theta) d\Omega = f_0 \cos^2\theta \sin\theta d\theta d\phi \quad (18)$$

in the range $\sigma_0 \leq d\theta \leq 2\sigma_0$. The normalizing factor f_0 is a function of the thickness, the incident energy and flux, and the target material. It can be determined from the Monte Carlo data by fitting Equation 18 at the peak angle. The results for 1-Mev normal incidence with an initial flux of 10^3 electrons are shown in Figure 33. For all materials investigated, f_0 varies linearly with thickness. The two deviating points of the iron Monte Carlo calculations are considered uncertain due to the relatively poor curve fit obtained. However, they could easily have been made colinear with the other points if the distributions within the angular increments used were appropriately skewed. The linear behavior of f_0 is associated with the approximately linear behavior of the transmission factor in the range of thicknesses considered. The relation between f_0 and the transmission factor can be used to obtain values of f_0 for different energies, incident fluxes, and target materials. Since f_0 is independent of the scattering angle, it is proportional to the transmitted flux and thus to the transmission factor. Consequently, the ratio of different values of f_0 is equal to the ratio of the appropriate transmission factors. This proportionality may also justify extending Equation 18 as far as the extrapolated range of the electrons.

Analysis of the Monte Carlo electron angular distributions has indicated that the Monte Carlo method is essentially in agreement with experimental results. The hypothesis of isotropy has been shown to be invalid for thick, bounded media.

The behavior of the angular distribution for thicknesses greater than σ_0 can be described by Equation 18. The general transmission factor can then be written as the product of the distribution function $f(\theta)$ and the usual angle-independent factor f_0 . Utilization of this distribution will be discussed in Section 7.0, the analysis of the importance of angular distribution of incident and penetrating electrons.

5.1.4 Accuracy of Monte Carlo Calculation

The two principal sources of error in the Monte Carlo treatment of electron multiple scattering are the statistical fluctuations and the basic assumptions of the underlying theory. The statistical error can be made arbitrarily small by increasing the sample size; however, the errors caused by assumptions and approximations in the theory are often neglected and may lead to difficulty if the theory is used beyond its range of validity. This is particularly true in multiple scattering where the requirement of small scattering angles is usually imposed. To estimate the magnitude of such

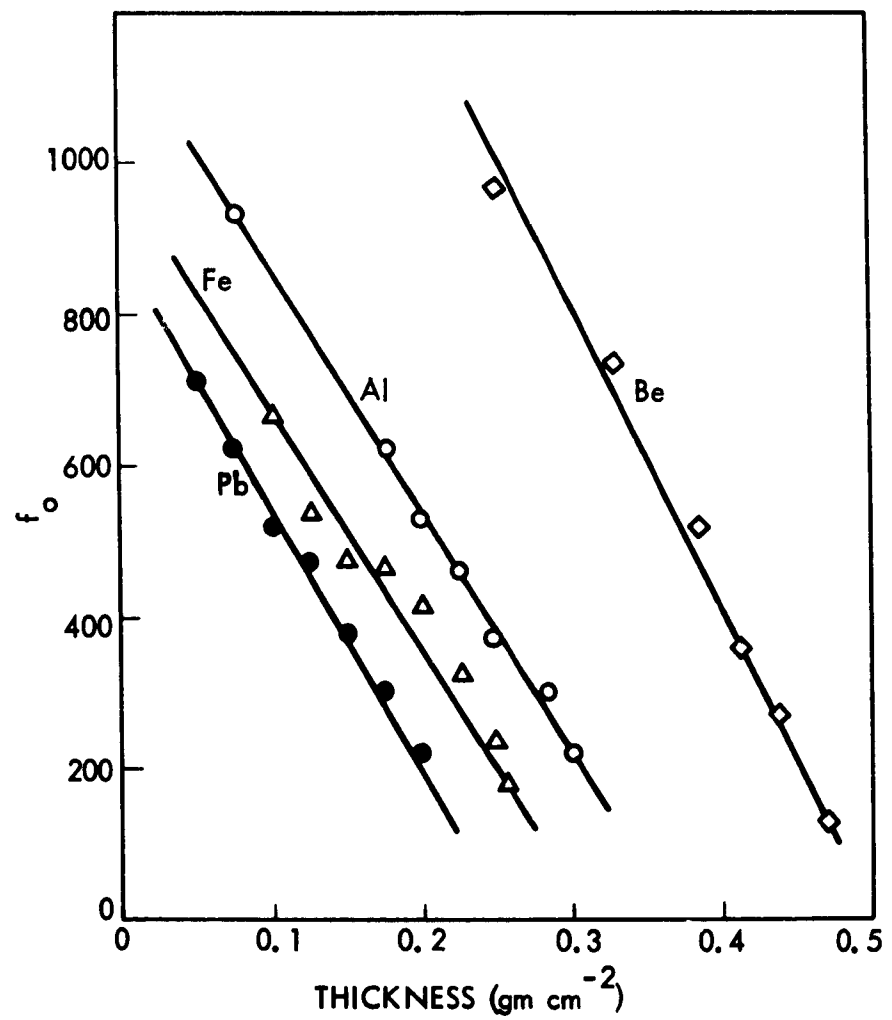


FIGURE 33. Normalizing factor, f_o , for 1000 electron histories (normal incidence at 1 Mev)

"theoretical" errors, an approximate analysis is undertaken here of the consequences involved in applying small-angle theories in the Monte Carlo method.

The Monte Carlo treatment of multiple scattering is considered valid for all scattering angles because of the assumption that all large-angle scatterings are the result of many successive small-angle scatterings. Since the target is usually divided into small increment slabs in the Monte Carlo method, this assumption requires that the angle of scattering from each slab be equal to or less than, the theoretical limit. The "theoretical" error can thus be obtained by considering each slab individually.

For increments much smaller than the electron range, the energy loss may be neglected. For this to be valid for all target increments, the increments may have to be taken successively thinner for very thick targets.

In a beam of electrons passing through a single increment, n_0 electrons will make collisions for which the scattering angle θ exceeds some specified maximum scattering angle θ_{\max} . If it is assumed that any single collision is independent of the others, then

$$n_0 = 2\pi N \phi d \int_{\theta_{\max}}^{\pi} \sigma(\theta) \sin\theta d\theta \quad (19)$$

where N is the number of target atoms per cm^3 , d is the increment thickness and ϕ is the incident flux. For the screened Coulomb potential $V = (Ze/r) \exp(-r/a)$, the scattering cross section in the first Born approximation is given by

$$\sigma(\theta) = \frac{Z^2 e^4}{p^2 v^2 (1 - \cos\theta + 2\delta)^2}$$

where $\delta = \hbar^2/4a^2 p^2$, and p and v are the momentum and velocity, respectively, of the scattered electron. Performing the integration in Equation 19, n_0 is given by

$$n_0 = 2\pi N \phi d \frac{Z^2 e^4}{p^2 v^2} \left\{ (1 + 2\delta - \cos\theta_{\max})^{-1} - [2(1 + \delta)]^{-1} \right\}$$

Using the relation

$$p^2 v^2 = \frac{4T^2(T+1)^2}{1+4T(T+1)}$$

where $m_0 c^2 \approx 1/2$ and T is the kinetic energy in Mev,

$$n_o = (\pi/8) N \phi d Z^2 r_o^2 \left[\frac{1 + 4T(T+1)}{T^2(T+1)^2} \right] \\ \times \left\{ (1 + 2\delta - \cos\theta_{\max})^{-1} - [2(1+\delta)]^{-1} \right\}$$

where $r_o = e^2/m_0 c^2$ is the classical electron radius. The quantity δ is determined from the screening length

$$a = 0.885 a_o Z^{-1/3}$$

where $a_o = 0.5292 \times 10^{-8}$ cm is the Bohr radius. Thus

$$\delta = \frac{\hbar^2}{4a^2 p^2} = 4.44 \times 10^{-6} \frac{Z^{2/3}}{T(T+1)}$$

and

$$n_o = (\pi/8) N \phi d Z^2 r_o^2 \left[\frac{1 + 4T(T+1)}{T^2(T+1)^2} \right] \quad (20)$$

$$\times \left\{ \left[1 + \frac{8.88 \times 10^{-6} Z^{2/3}}{T(T+1)} - \cos\theta_{\max} \right]^{-1} - \left[2 + \frac{8.88 \times 10^{-6} Z^{2/3}}{T(T+1)} \right]^{-1} \right\}$$

Since the use of small-angle scattering theories requires the assumption that no electrons are scattered at angles greater than θ_{\max} , the "theoretical" error can be estimated by the ratio n_o/ϕ .

As an example, Equation 20 is used to determine the errors for a Monte Carlo calculation of 1000 electron histories at 1-Mev energy with an aluminum target. The factor $8.88 \times 10^{-6} Z^{2/3}/T(T+1)$ can be neglected in Equation 20 so that

$$n_o/\phi \approx (\pi/8) r_o^2 N d Z^2 \left[\frac{1 + 4T(T+1)}{T^2(T+1)^2} \right]$$

$$\times [(1 - \cos\theta_{\max})^{-1} - 1/2]$$

For $Z = 13$, the screening length is 1.99×10^{-9} cm and $N = 6.03 \times 10^{22}$ atoms/cm³. The value of θ_{\max} is taken as 30 degrees, for which the Moliere theory is still approximately valid. The average electron energy is used for each increment. The results with the accompanying statistical errors are shown in Table 4.

Although the example shown in the table has been carried out to extremely large error values, the results that are appreciably larger than 10 percent cannot be considered as anything more than a rough indication of the dependence of the error on the electron energy because the assumption that no energy loss occurred within an increment was made in writing Equation 19. However, in the example, the increment thickness is already one-tenth of the electron range after the tenth slab so that the effects of energy loss are no longer negligible. Also, the average energy used in computing the theoretical error contains an uncertainty due to the statistical error in the number of transmitted electrons.

Nevertheless, the monotonic increase of the theoretical error indicates that it may be necessary to take successively thinner increments as the electron energy decreases. A Monte Carlo calculation can decrease the increment by taking the thickness in proportion to the energy, or by specifying that each increment correspond to a certain fractional loss in the electron energy. Either procedure will, of course, require considerably more computation than the use of a constant thickness. For example, Berger (Reference 54), who used a logarithmic energy-dependent spacing, took nearly 50 steps to reach the energy value corresponding to the seventeenth slab of the table. The corresponding theoretical error, however, would have been only five percent.

5.2 RADIATION TRANSPORT

The data generated from the Monte Carlo program and existing theory were used to formulate mathematical models for the transport of electrons and bremsstrahlung through multilayered shields. A series of three electron models are presented: (1) the Monte Carlo program, (2) a dose calculation, and (3) an energy, LET spectra, and dose calculation. There is significant difference in computing time so that each model offers certain advantages in accuracy and detail as a function of computing time. The bremsstrahlung model includes a volume distributed source and the analysis of multilayered shields.

5.2.1 Primary Electrons

5.2.1.1 Transmission

The dimensionless length and energy parameters of Seliger (Reference 60), and Makhov (Reference 61) were used to obtain a mathematical model for the number of electrons of a given energy that penetrate a given shield thickness. In the initial

Table 4
THEORETICAL AND STATISTICAL ERRORS FOR TARGET INCREMENTS
1-Mev Electrons Normally Incident on Aluminum.
Increment Thickness 2.5×10^{-2} g/cm² (9.25×10^{-3} cm).

Slab	Theoretical Error - %	Statistical Error - %
1	4.60	3.16
2	4.65	3.17
3	5.43	3.20
4	5.73	3.25
5	6.31	3.34
6	7.52	3.45
7	8.35	3.63
8	10.15	3.83
9	11.05	4.12
10	13.90	4.50
11	15.35	5.13
12	18.05	5.75
13	22.70	6.65
14	25.95	7.90
15	36.30	10.18
16	42.40	15.10
17	73.50	25.80

electron-transmission code study (Reference 62) the expression

$$T(x, E, Z) = \exp \left\{ - \left[E(0.585 Z^{-0.271}/x)^{0.848} \right] - 7(Z - 3.25)^{-0.24} \right\}$$

was derived based on the dimensionless model for the fraction of electrons of initial energy E which penetrated a shield of material Z and thickness x . This expression was derived from Monte Carlo data for beryllium, aluminum, iron, and silver using 1-, 3-, 4-, 6-, and 8-Mev normally incident electrons. The dose from a spectrum of incident electron energies $\phi_e(E)$ is expressed as

$$D_e = F \int K \phi_e(E) T(E) \frac{dE}{dx}(E) dE$$

where K converts Mev/gm to rad and $dE/dX(E)$ is the energy loss in the target for an electron of energy E . The limitations of this expression are:

- 1) The shield is restricted to one material;
- 2) The electrons are assumed to penetrate the shield and retain their initial energy for dose deposition; and
- 3) The electrons are assumed to be incident normally, but are corrected for number crossing the vehicle surface (F factor).

The first phase of the electron penetration section of this study was to develop a method to estimate the number transmission (ratio of penetrating electrons to incident electrons) through multilayered shields. Approximately 2 hours of computer time was used to obtain Monte Carlo penetration data for monoenergetic and fission-spectrum electrons having normal incidence on various combinations of shield materials. Analysis of these data indicated that the number transmission for the total shield can be obtained by the following scheme:

- 1) The number penetrating the first slab is computed with the "single slab" method;
- 2) The penetration through the material of the second slab is also computed by the single slab method using an "effective thickness,"
- 3) The penetration through any slab i of material j is computed using an effective thickness equal to the thickness of slab i plus an equivalent thickness for slab j , which gives an attenuation equal to that of slabs 1 through $i-1$.
- 4) The number transmission of electrons penetrating a multislabs shield composed of n layers of materials of total thickness

$$X_n = \sum_{i=1}^n x_i$$

is given by

$$T(x_i, Z_i \mid i=1, 2, \dots, n; E_0) = T(\bar{X}_n, E_0, Z_n)$$

where by definition $\bar{X}_n = x_n + \bar{X}_{n-1}$. The individual thickness of the n^{th} slab is x_n and \bar{X}_{n-1} is an equivalent thickness for material n which will yield a transmission equal to that penetrating the first $n-1$ slabs of the multi-layered shield. The quantity \bar{X}_{n-1} is determined from the implicit equation

$$T(\bar{X}_{n-1}, E_0, Z_n) = T(x_i \mid i=1, 2, \dots, n-1; Z_{n-1}, E_0)$$

where the right-hand side of the equation is determined from the previous iteration. Equation 21 is used to evaluate the left-hand side iteratively until a value of \bar{X}_{n-1} is found which satisfies the equation.

In each case the thickness is in terms of an areal density in units of gm/cm^2 . This method assumes that an equivalent thickness of any material that produces an equal attenuation of electrons will also produce an identical energy and angle distribution of electrons at that point. Obviously this is not exact since the ratio of radiation to ionization loss is dependent upon atomic number. However, for an estimate of the number transmission, no better approximation could be developed. Results of the second phase of the study revealed an alternate method of comparable accuracy. A detailed discussion of that method will be presented in the next section.

The accuracy of the single-slab expression was found to be within 10 percent in the range of Z_i from $i = 10$ to 50. Table 5 compares the results of the multislabs analysis using the empirical method with Monte Carlo results. There are no experimental data available for comparison with these data. Figure 34 illustrates the improvement obtained using the multislabs method compared to the single-slab method. The transmission for a multislabs shield will be bracketed by the single-slab transmission curves. For this reason, there is no advantage to using a multislabs approximation when the atomic numbers of the shields are similar since both single transmission curves are close to the multislabs case. A shield of beryllium and lead would be maximum tests of cases where the single slab is not representative of the multislabs transmission. Using the lighter atomic weight material, the maximum error in the single-slab method is a factor of two, while use of the heavier atomic weight material produces factors of 12. The multislabs approximation is in error by less than a factor of two, but at large fractions of the total range the errors again become large.

It is concluded that for shield thicknesses less than one-half the electron range, the multislabs approximation provides 15 percent accuracy in the calculated number

Table 5
MULTISLAB ELECTRON NUMBER TRANSMISSION

E	Slab No.	Material	Thickness	Total Thickness	Trans (Calc.) *	Transmission (Monte Carlo)
f i s s i o n	1	Be	.51 gm/cm ²	.51 gm/cm ²	.358	.378
	2	Pb	.51	1.02	.092	.052
	3	Be	.51	1.53	.020	.026
	4	Pb	.51	2.04	.003	.003
	5	Be	.51	2.55	.0002	.001
f i s s i o n	1	Pb	.51	.51	.107	.134
	2	Be	.51	1.02	.03	.065
	3	Pb	.51	1.53	.01	.019
	4	Be	.51	2.04	.002	.008
	5	Pb	.51	2.55	----	----
f i s s i o n	1	Al	.17	.17	.517	.531
	2	Al	.17	.34	.363	.326
	3	Al	.17	.51	.236	.221
	4	Al	.17	.68	.156	.153
	5	Al	.17	.85	.103	.099
* Using multislabs method.						

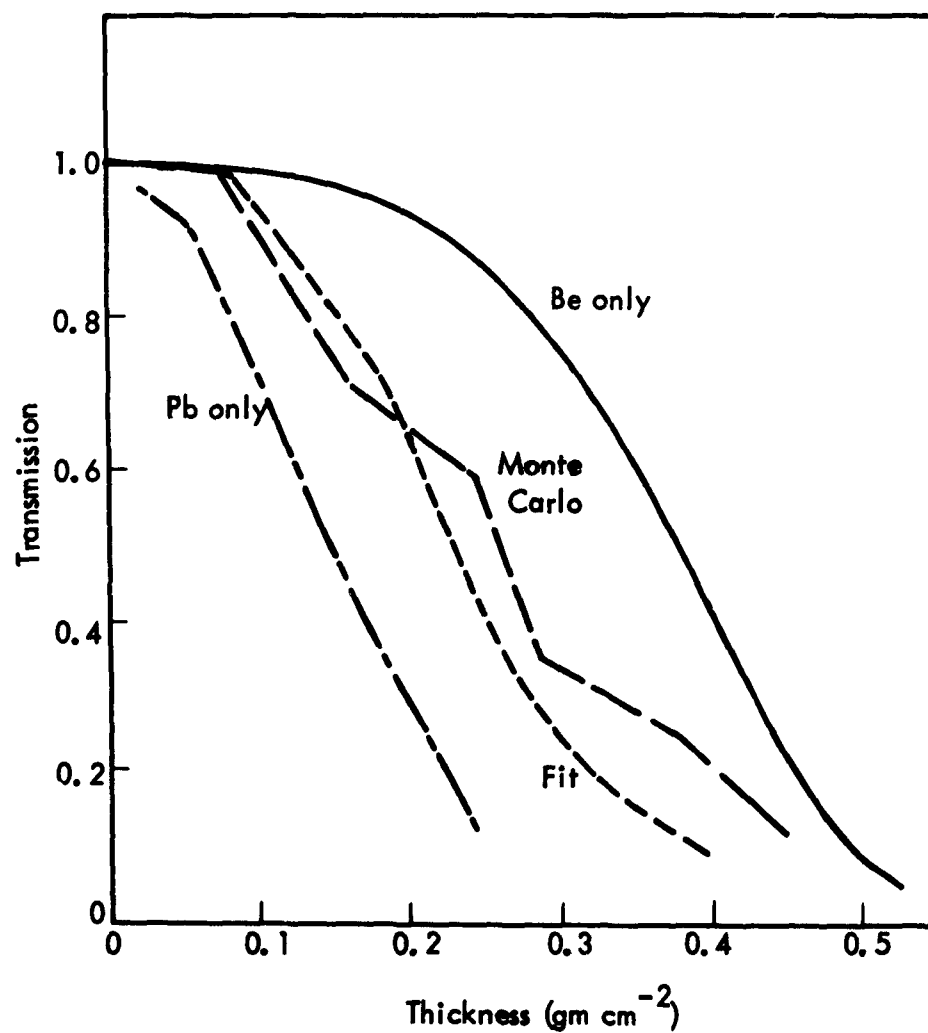


FIGURE 34. Comparison of single and multislabs results for Be-Pb-Be-Pb-Be

transmission. The maximum errors occur at large percentages of the electron range when there are large differences in the atomic numbers of the shield materials. There is no simple modification that can be made to improve this method. However, an alternative method is discussed later.

The second phase of this study was the development of a mathematical expression for the energy spectrum of the penetrating electrons. Monte Carlo electron-penetration runs were made for beryllium, aluminum, iron, silver, and lead for electron energies from 0.4 to 6 Mev. Both normal incidence and isotropic distributions were studied.

The derivation of an empirical expression to describe the differential number spectrum of electrons penetrating a shield required a large effort. A chronological summary of the various methods will be presented to demonstrate the possible mathematical models and their restrictions.

The first method was based on the observation that the differential number spectra for a given energy group appeared to be a family of Gaussian curves. As the final energy decreased, the maximum of the Gaussian decreased. Its center shifted to a larger thickness, and its half-width at half-maximum increased. A typical family of curves for a 1-Mev electron normally incident on aluminum is shown in Figure 35. For aluminum shields this family of curves was represented by the expression

$$\phi_e(E, \chi) = \frac{1.7\epsilon^3}{0.01E} \exp[-2.2 \times 10^3 \epsilon^{2.35} (\chi - 4.5 + 0.41\epsilon)^2]$$

where ϵ is dimensionless energy, the ratio of the final to initial energy, and χ is dimensionless length, the ratio of the thickness x to the range of the initial-energy electron. As this analysis was extended to other materials, the Gaussian curves began to skew. Attempts to correlate data using a translation plus a rotation of the skewed Gaussian yielded an expression too complicated for practical application. This approach was subsequently abandoned, even though a good representation was achieved for aluminum shields.

The second method was based on the shape of the differential number spectrum plotted for various aluminum shield thicknesses. The Monte Carlo data provided a histogram such as shown in Figure 36. Experimental data of White and Millington (Reference 63) were similar to these data and are shown in Figure 37.

Since the quantities of interest to be computed are dose and LET, several assumptions were made in obtaining a mathematical model for the differential number and LET spectra. The first assumption was that a curve of the form shown in the previous two Figures (36 and 37) can be represented by an exponential as shown in Figure 38. The approximation is defined as zero in the region E_{\max} to E_0 , where E_{\max} is defined as

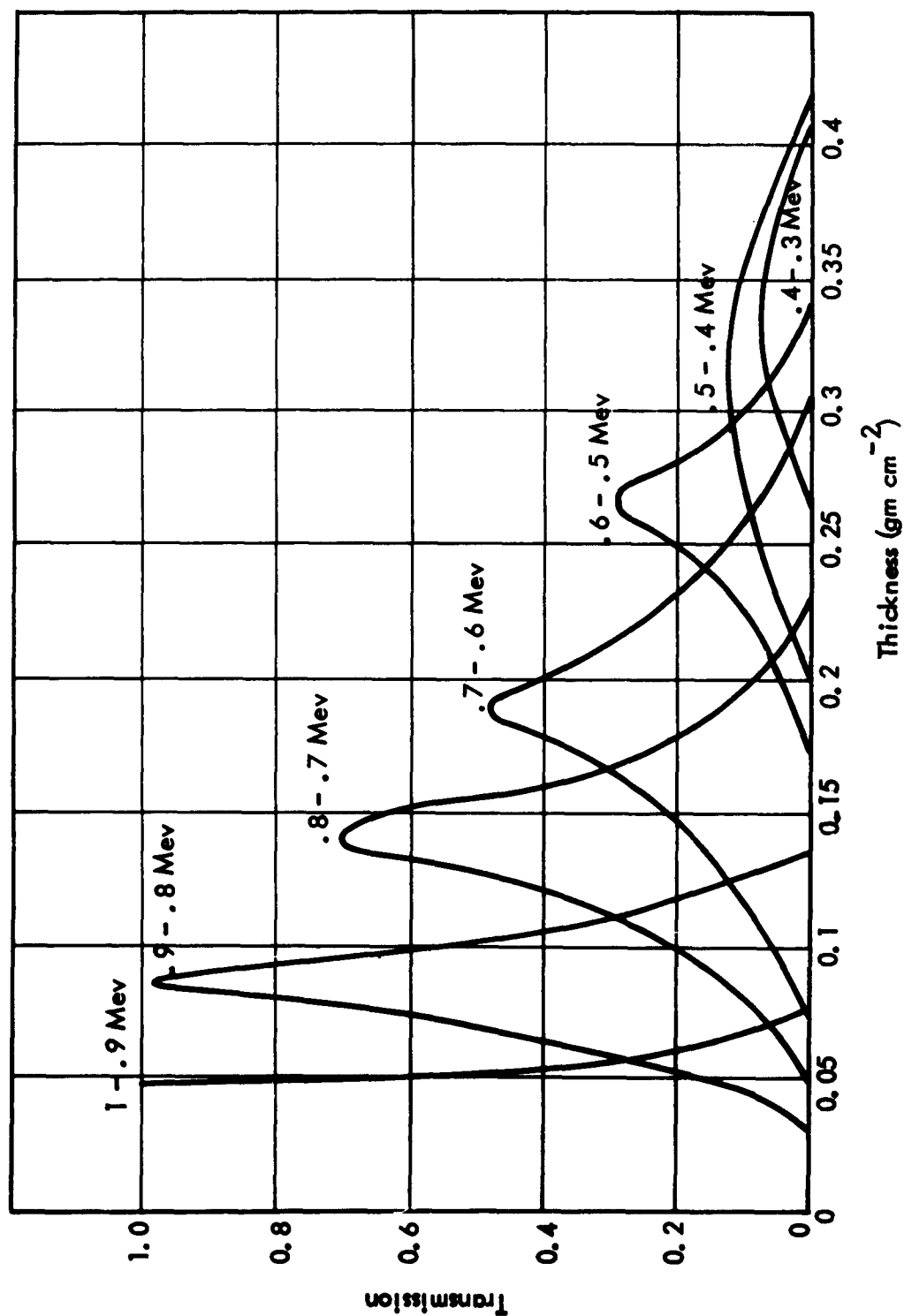


FIGURE 35. Transmission factor of electrons of an energy interval as a function of thickness of aluminum for 1-Mev incident electrons

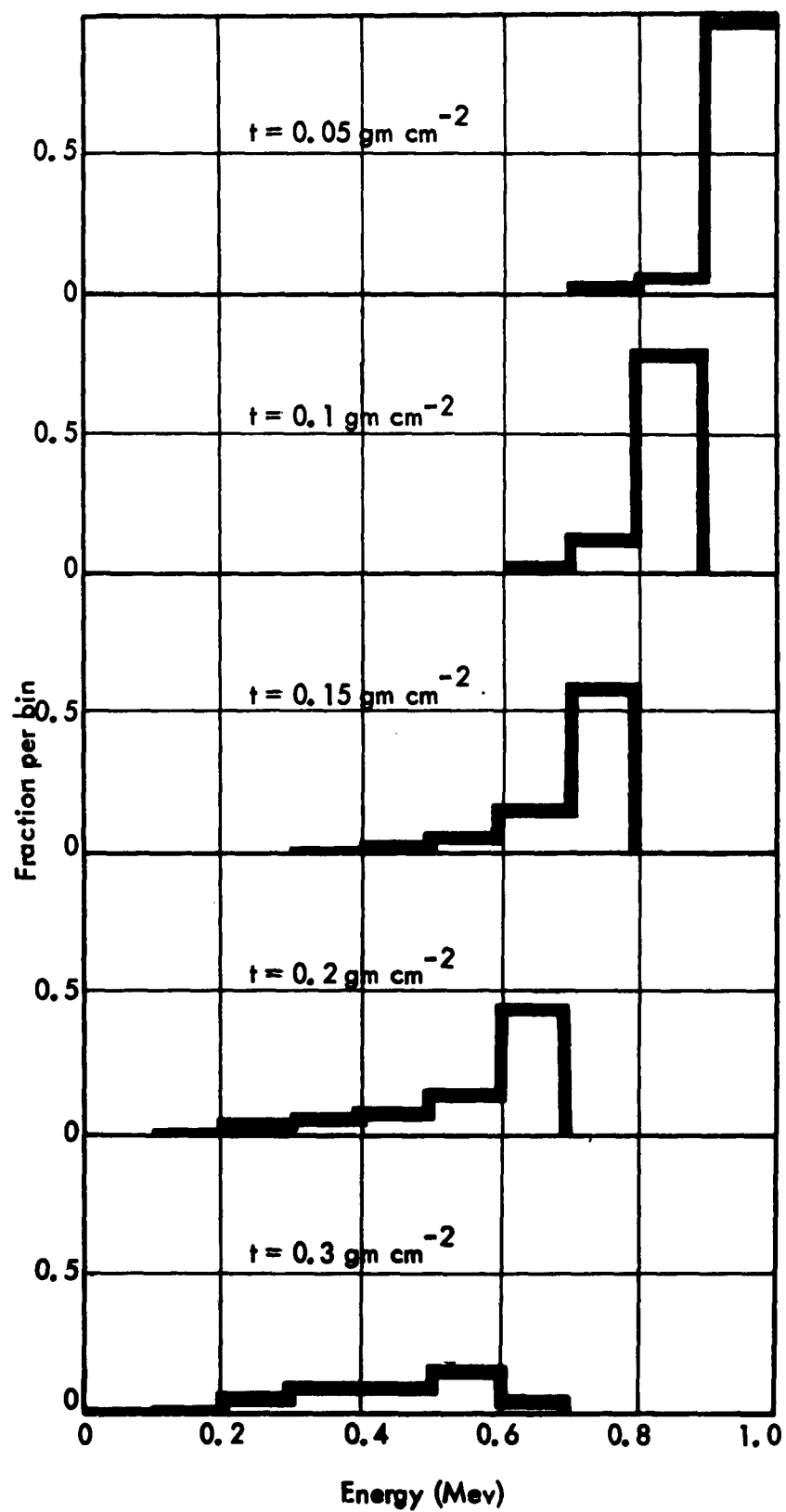


FIGURE 36. Monte Carlo histogram for 1-Mev electrons incident on aluminum

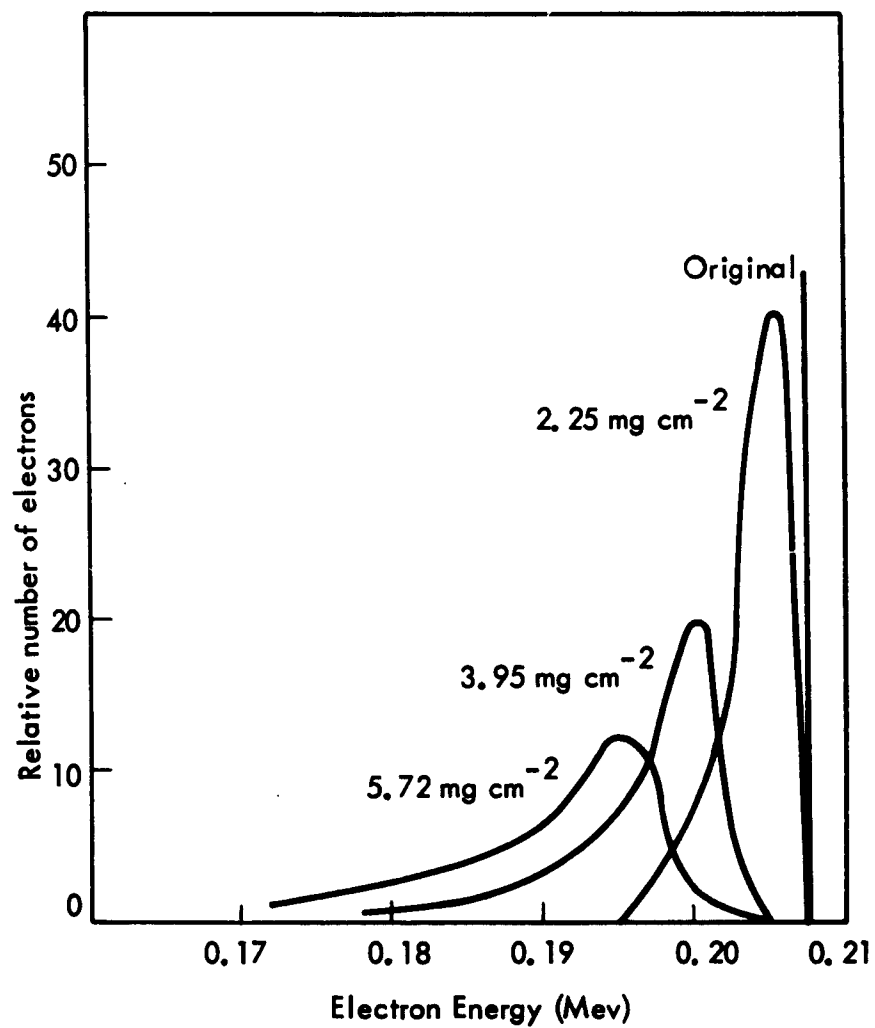


FIGURE 37. Transmission through mica of the monoenergetic electrons of 0.2065 Mev (Reference 63)

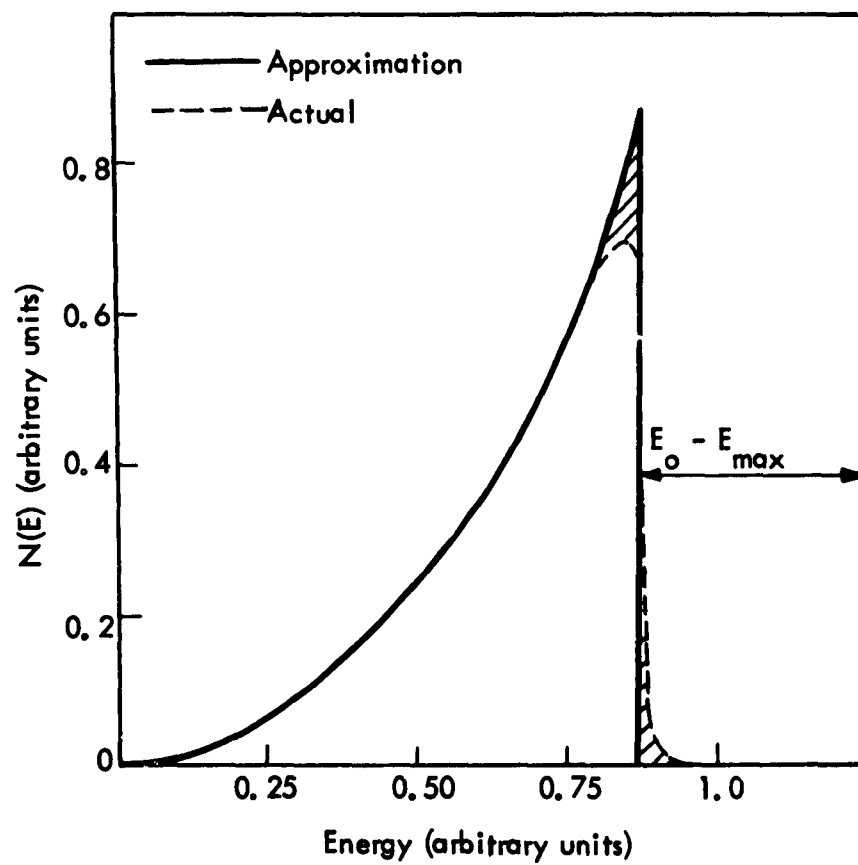


FIGURE 38. Mathematical model for differential number spectrum

the maximum energy an electron of initial energy E_0 can retain when penetrating straight forward through the shield thickness. By adjusting the integral under this curve so that the integral of the fit is equal to the integral of the Monte Carlo data, the proper number LET is retained. It can be observed from Figure 39 that the LET of the higher-energy electrons is a constant, and the assignment of an electron to a slightly lower-energy bin does not effect its LET. The other constraint is that the integral of the total energy in both curves should be equal to retain the same energy or dose. Both restrictions cannot be satisfied simultaneously; however, a compromise that created less than 5 percent error was obtained for aluminum shields.

The procedure for this analysis was to analyze the histogram for the number of electrons in each energy bin penetrating a shield as a function of initial energy, shield material, and thickness. A value for the differential number spectra at the mid point of each bin was obtained by dividing the number of electrons in a bin by the bin width. The differential number spectra was assumed to be represented by the relation

$$\phi_e(E) = A \exp[-b(E_0 - E)] \quad E < E_{\max}$$

$$\phi_e(E) = 0 \quad E \geq E_{\max}$$

where the constants A and b are dependent on the atomic number of the shield, the initial electron energy, and the thickness of the shield. Values for b were obtained from the shape of $\phi_e(E)$ plotted versus $E_0 - E$. The constants A were obtained by averaging the integral of the expression over the limits of each bin to yield the number and energy in each bin. The initial analysis provided the following relations for A and b :

$$A = 1.6(1 - 0.108 E_0) (x/E_0)^{2.5} \exp(-0.0435 Z)$$

$$b = \begin{cases} (x/E_0)^{-1.25} (1.25 - 8.5 \times 10^{-3} Z)/E_0 & x > 0.325 E_0 \\ 4.1(1.25 - 8.5 \times 10^{-3} Z)/E_0 & x \leq 0.325 E_0 \end{cases}$$

This set of constants was satisfactory for small x/E_0 but yielded large values at higher x/E_0 . Also the values were too small at high Z 's.

Re-evaluating the data, the large values at high x/E_0 were corrected by employing a double exponential fit for A which corrected the error at large x/E_0 . The revised constants were

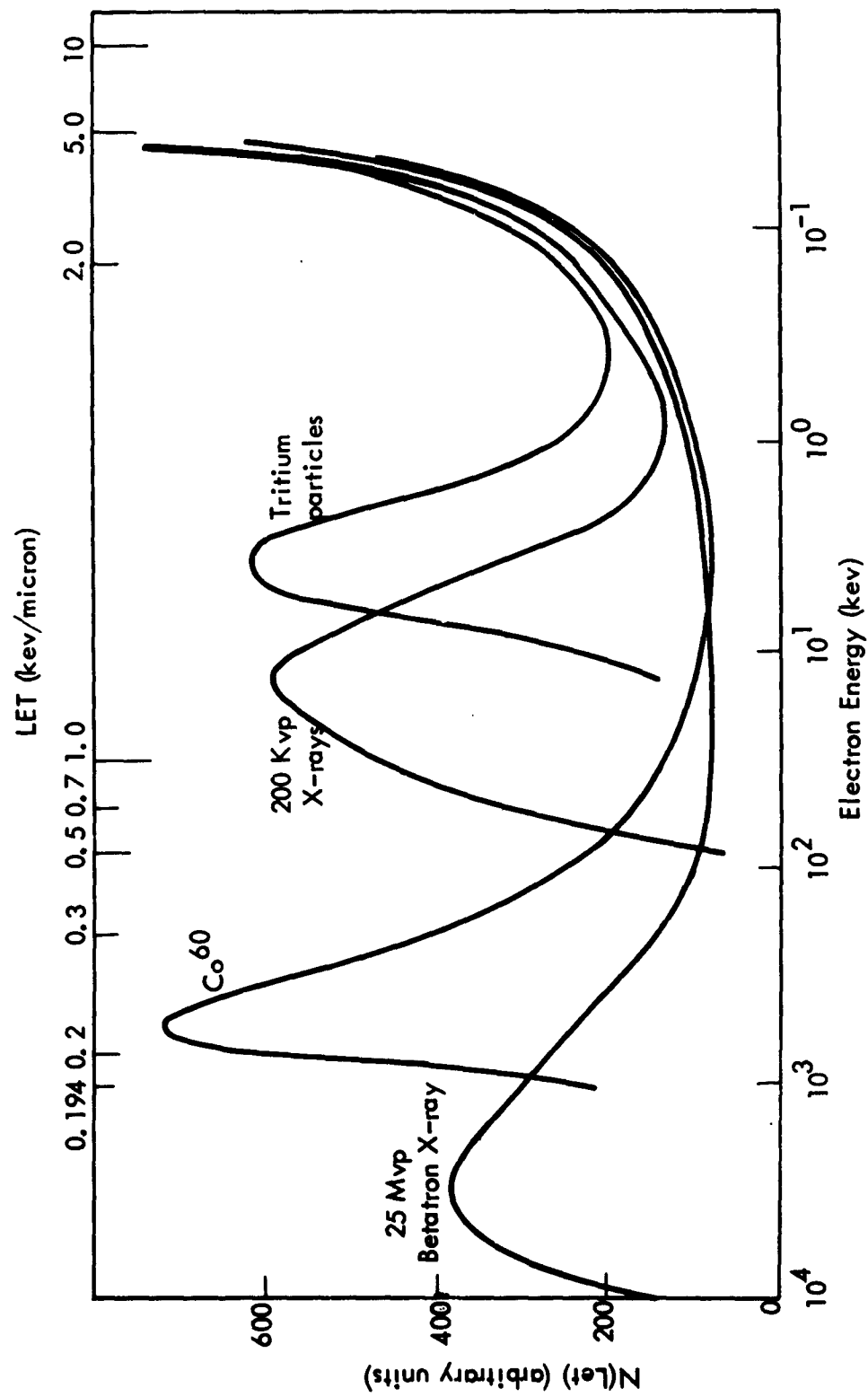


FIGURE 39. LET spectrum of various radiation types (Reference 67)

$$A = 4.4 \times 10^3 Z^{-4.26} E_0^{-1.23} \exp(-141 x/E_0) + 1.35 \times 10^5 \exp(-0.06 Z) \\ \times E_0^{-0.74} \exp(-21 x/E_0) \\ b = (x/E_0)^{-1.46} (1.53 - 0.0104 Z)/E_0 \quad (22)$$

This set of constants was cumbersome and the expression for differential spectra was too sensitive to changes in E_{\max} . The b values for small x/E_0 were large numbers, and a small error in E_{\max} could affect the exponent markedly. The final expressions employed subroutines to compute A where the total number penetrating the shield was determined by the original number transmission relation Equation 21 and then A computed from the relation

$$A = \frac{N_{\text{trans}} b}{\exp(-bE_0) [\exp(bE_{\max}) - 1]}$$

In each case b was found to be represented by Equation 22.

The results were found to be in agreement with the Monte Carlo calculations.

5.2.1.2 Results

Calculations using fission spectrum electrons and aluminum shields produced results within 15 percent agreement of the Monte Carlo calculations. This method was extended to multislabs shields with better agreement than the previous methods. There remains one assumption in the mathematical model which tends to overestimate the final dose. All electron transmission data were fitted to normal-incidence penetration data. Figure 40 shows the number transmission of 1-Mev electrons through aluminum for 0, 30, and 60 degrees and isotropic incidence. (0 degree is normal incidence.)

The isotropic number transmission was found to be about 50 percent of the normal transmission, but the equilibrium spectrum was achieved with a smaller thickness. This softer spectrum caused the dose per transmitted electron to be greater for isotropic distribution than for normal incidence. Comparing the dose transmission from normal and isotropic incident fluxes the values were similar and the larger normal transmission factors were used to retain a safety factor. The integration of the normal-transmission factors over the slant paths encountered by an isotropic distribution was processed for 1-Mev electrons on aluminum. This method produced the same transmission for isotropic flux as the Monte Carlo; however, the multiple-scattering theory is so uncertain and the calculations are so lengthy that this method was not programmed.

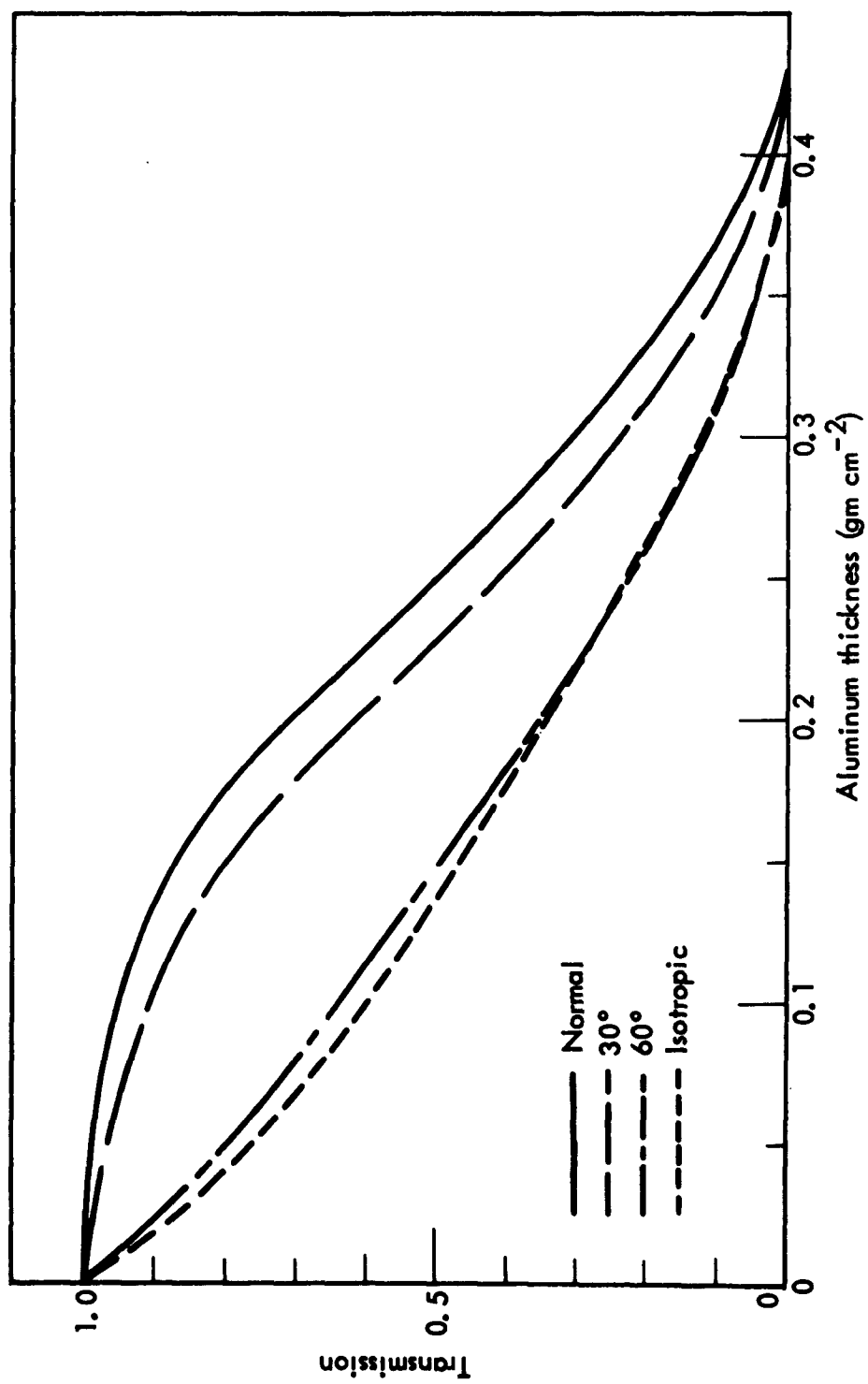


FIGURE 40. The effect of incident angle on electron transmission

5.2.1.3 Dose Calculation

The electron dose transmission factor $D_e(n)$ for a given sector composed of n layers is expressed as

$$D_e(n) = K \int \frac{dE}{dx}(E) \int \phi_e(E_o) T_n(E_o \rightarrow E) dE_o dE$$

where K = conversion factor Mev/gm to rad

$\frac{dE}{dx}(E)$ = rate of energy deposition for electron of energy E , Mev gm⁻¹ cm²

$\phi_e(E_o)$ = spectrum of incident electrons normalized to one

$T_n(E_o \rightarrow E)$ = transmission of electrons with energy E through shield (obtained by use of Equation 21, Section 5.2.1.1)

This operation (1) computes the number of electrons of energy E penetrating the shield from incident electrons of energy E_o , (2) integrates over all incident energies to obtain the total number of electrons of energy E penetrating the sector, (3) computes the energy deposited by these electrons, and (4) integrates over all final electron energies to compute the total dose.

The total dose transmission through all sectors is expressed as

$$D_e = \sum_n D_e(n) S_e F_e(n) \Lambda(n) \omega_n$$

where $D_e(n)$ is defined above, S_e is the free-space flux, $F_e(n)$ is the fraction of the free-space flux incident on sector n , $\Lambda(n)$ is the fraction of electrons penetrating sector n which are incident on the dose point, and ω_n is the fractional solid angle.

The function $F_e(n)$ has been shown by Evans (Reference 64) to be one-fourth for an isotropic distribution. An analysis of the value of $F_e(n)$ for other distributions will be presented in the section 7.0 discussing the effects of the incident angular distribution. It has previously been shown that for electrons a diffusion equilibrium is obtained where the angular distribution can be described by $\cos^2\theta$ (θ is the scattering angle from the normal to the shield). The function $\Lambda(n)$ was previously discussed as a function of $\cos^2\theta$ in Section 5.1.3 as

$$\Lambda(n) = f_o \cos^2\theta$$

where f_o is a normalizing factor.

The Monte Carlo program for electron penetration has been modified for use in computing a detailed analysis of electron penetration in a vehicle. All the output such as number spectrum, LET spectrum, energy loss per unit path length, and dose can be computed with the Monte Carlo electron code as well as the simpler code using the empirical fit. For single material or shields where there is only one sector, the Monte Carlo will provide a much more accurate answer in the same computing time.

5.2.1.4 LET Calculation

The calculation of the energy imparted by each primary electron per unit path length in a given medium to obtain the Linear Energy Transfer (LET), was based on the mean energy loss values of Nelms (Reference 51). An estimate of the secondary, tertiary, and higher-order products was made, but there are insufficient data to justify accurate calculations. It is believed that the small correction which might be obtained would not justify the time required for the calculation. In calculations of permissible exposure levels the 1963 report of the Relative Biological Effect Committee (Reference 65) recommends the use of the concept of the Quality Factor QF in terms of a LET₀ defined for primary particles. It indicates that for X, γ , and β rays, the QF is close to unity and the LET is always low except for very low electron energies. The concept that X, γ , and β radiation has a low QF or RBE has been recognized. Cormack and Johns (Reference 66) and Burch (Reference 67) have made detailed calculations of LET spectra to verify this point. It was noted by Schaeffer (Reference 68), who compared the proton LET spectrum with the X-ray LET spectrum, that the spectrum for LET greater than 10 keV/micron is an artifact for X-rays since the mechanism for energy dissipation below 1 keV is incompletely understood. The maximum LET for electrons has been estimated to be 38 keV/micron, and a limiting value of 30 keV/micron has been recommended by Schaeffer as the dividing line between high and low LET.

Figure 39 is a representation of the data of Burch (Reference 67) smoothed over energy. Since electrons deposit their energy in much the same manner as X-rays (i.e., by production of low-energy electrons) the QF of electrons (Reference 68) should be that of X-rays, namely unity. Figure 41 shows a comparison of the LET spectra of X-rays, solar protons, and recoil protons.

5.2.2 Bremsstrahlung Shielding

5.2.2.1 Transmission

The original computer program developed at Boeing to compute the bremsstrahlung dose in a space vehicle (Reference 62) had two assumptions which limited the accuracy of the calculation to an order of magnitude in some situations. These assumptions were (1) the photons were all produced on the incident surface of the shield, and (2) an infinite slab thickness was used to predict the photon yield. The first assumption is in error when a shield is composed of a thin low-atomic-number shield followed by a high-atomic-number shield. Since the bremsstrahlung production is proportional to atomic number, a low production is predicted even though electrons can penetrate the

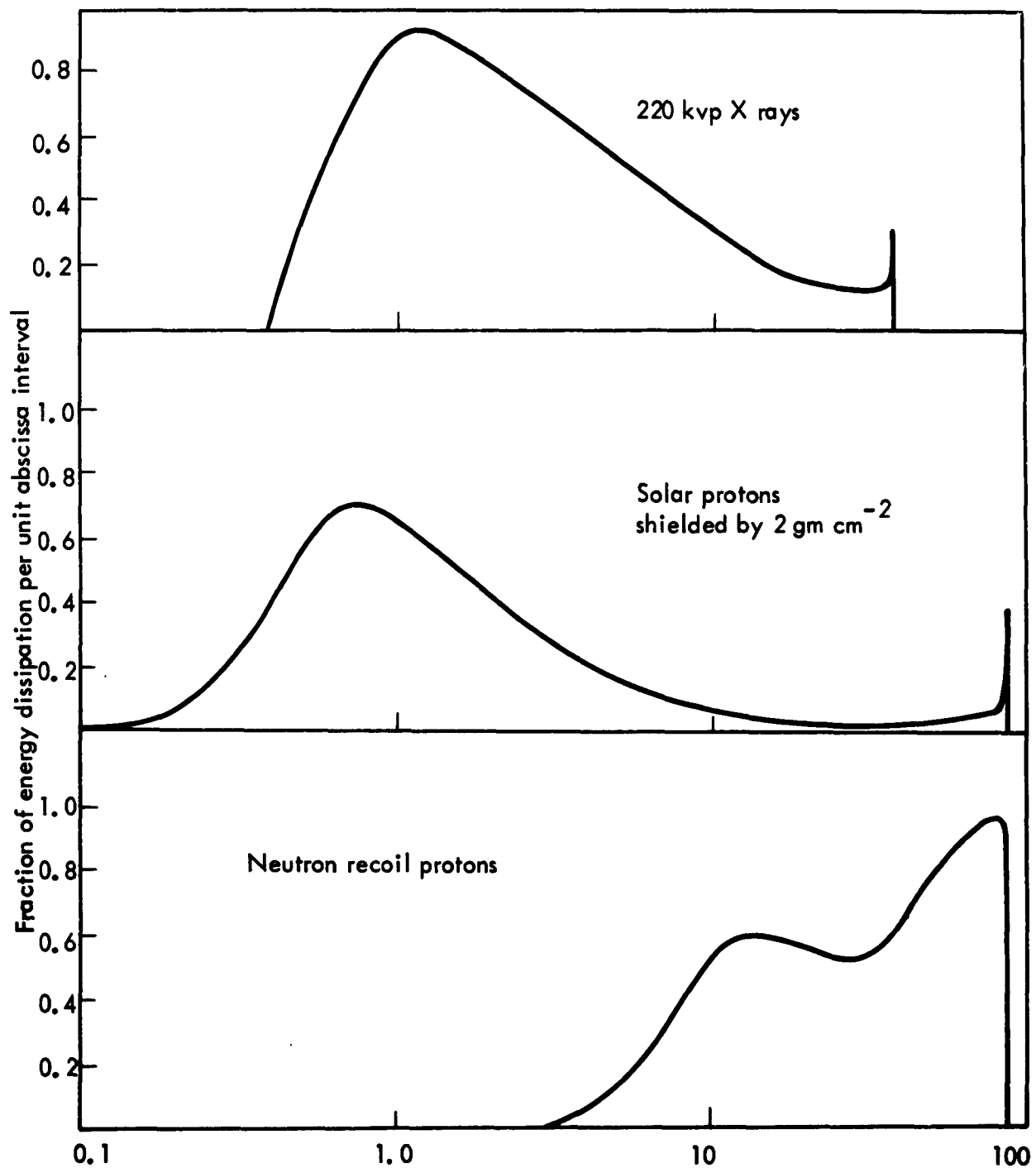


FIGURE 41. LET spectrum of X rays, solar protons, and recoil protons from neutrons (Reference 68)

first layer and produce more photons in the second layer. The second assumption produces errors in thin shields since only part of the electron energy is deposited in the shield. Both these assumptions were eliminated by the modifications made during this study.

The original codes employed the following relation for bremsstrahlung dose

$$D_B = \int_{0.1}^{10} K(h\nu) \prod_{i=1}^N \frac{B_i[\mu_i(h\nu) x_i] \exp[-\mu_i(h\nu) x_i]}{1.25} \times \int_{h\nu}^{10} \frac{1.98 \times 10^{-4} (1.96 E + 2) Z}{[1 + 0.35 \log_{10}(82/Z)]} \phi_e(E) \times \quad (23)$$

$$\left[4 \left(1 - \frac{h\nu}{E} \right) - \frac{3 h\nu}{E} \ln \left(\frac{E}{h\nu} \right) \right] dE d(h\nu)$$

where D_B is the bremsstrahlung dose created in an N -layered shield by an incident spectrum of electrons $\phi_e(E)$. $K(h\nu)$ is the flux-to-dose conversion factor for photons of energy $h\nu$, $B_i(\mu_i(h\nu) x_i)$ is the buildup factor for photons of energy $h\nu$ for $\mu_i x_i$ mean free paths in shield i , μ_i is the mass attenuation coefficient, and x_i is the slab thickness. The expression

$$W(E) = \frac{1.98 \times 10^{-4} (1.96 E + 2)}{1 + 0.35 \log_{10}(82/Z)} ZE \quad (24)$$

is the average amount of energy radiated by bremsstrahlung in a thick target as shown by C. S. Wu (Reference 69). The term in the brackets is the energy radiated per unit energy interval derived by Wyard (Reference 70).

$$l(h\nu, E) = \left[4 \left(1 - \frac{h\nu}{E} \right) - \frac{3 h\nu}{E} \right] \ln(E/h\nu) \quad (25)$$

The electron Monte Carlo code was used to obtain data for bremsstrahlung source distribution. Data for aluminum, iron, silver, and lead for 1-, 3-, and 6-Mev electrons were obtained. It was generally observed that the rate of bremsstrahlung production was approximately constant over the region where the bremsstrahlung of a particular energy group could be produced.

The volume-distributed bremsstrahlung was computed by modifying the original expression (Equation 23). Consider a spectrum of incident electrons and select the number of electrons of energy E per unit energy interval, $\phi_e(E)$. From Equation 24 for the energy radiation per electron $W(E, Z)$ in a thick target, the photon energy release is

$$\begin{array}{l} \text{photon energy release} \\ \text{from} \\ \text{electrons of energy } E \end{array} = \phi_e(E) W(E, Z)$$

The fraction of these releases as photons of energy $h\nu$ is given by Equation 25 defined as $I(h\nu, E)$. Thus, the photon energy of $h\nu$ released by electrons of energy E is

$$\begin{array}{l} \text{photon energy release} \\ \text{of energy } h\nu \text{ from} \\ \text{electrons of energy } E \end{array} = I(h\nu, E) \phi_e(E) W(E, Z)$$

Since only electrons with energy greater than $h\nu$ can create photons of energy $h\nu$, the thickness $X_0(E, h\nu)$ where photons can be created can be defined by

$$h\nu = E_0 - \int_0^{X_0} \frac{dE}{dx}(E_0, x) dx$$

where $dE/dx(E_0, x)$ is the rate of energy loss of an electron of incident energy E_0 at a thickness x in the shield. For this calculation, the electron path is normal to the shield to obtain maximum penetration.

The source strength per unit volume of photons of energy $h\nu$ produced by electrons of energy E is then

$$\frac{I(h\nu, E) \phi_e(E, x) W(E, Z)}{X_0(E, h\nu)} F(x/X_0)$$

where $F(x/X_0)$ can be a distribution of the source along x .

The transmission of the radiation through the source slab n and through the remaining slabs is defined as

$$T(h\nu, x_n, \sum_{i=n+1}^N x_i)$$

where $h\nu$ is the energy of the penetrating photon, x_n is the thickness of the radiating slab and

$$\sum_{i=n+1}^N x_i$$

is the thickness of the remaining slabs. Thus, the photon energy reaching the receiver from photons of energy $h\nu$ created by electrons of energy E in slab n is:

$$\phi(E, h\nu) = \frac{I(h\nu, E) \phi_e(E) W(E, Z_n) T(h\nu, x_n) \sum_{i=n+1}^N x_i}{X_{on}(E, h\nu)}$$

Integrating over all incident electron energies will yield the total photon energy reaching the receiver.

$$\phi(h\nu) = \int \phi(E, h\nu) dE$$

Multiplying this integral by the dose conversion factor for energy $h\nu$, $K(h\nu)$ and then integrating over all photon energies gives the total dose from all photon energies created by $\phi_e(E)$ as

$$D_B = \int K(h\nu) A(h\nu) \phi(h\nu) d(h\nu)$$

where $A(h\nu)$ is a distribution function for angle as a function of photon energy.

The $\phi_e(E)$ penetrating slab n and incident on slab $n+1$ is computed using the electron code (Equation 21). This $\phi_{e, n+1}(E)$ is used to compute the dose D_{n+1} and the computation continued until the dose from photons created in each slab is computed.

Each sector is assumed to be composed of increments of solid angle 0.05 steradians. The dose from a truncated-cone volume source composed of N layers has been derived by Foderaro and Obenshain (Reference 71). For a volume-distributed source where the source strength is constant, the function

$$T(h\nu, X_n, \sum_{j=n+1}^N x_j) \text{ is given by}$$

$$T(h\nu, X_n) = \sum_{i=n+1}^N \frac{S V_n B(b_3)}{Z \mu_n(h\nu)} [E_2(b_1) - E_2(b_3) + \frac{E_2(b_3 \sec \theta)}{\sec \theta} - \frac{E_2(b_1 \sec \theta)}{\sec \theta}]$$

where $\mu_n(h\nu)$ = attenuation coefficient for photon of energy $h\nu$ in slab n

X_n = thickness of slab n containing the source

θ = subtended angle (see Figure 42)

$$b_1 = \sum_{i=n+1}^N \mu_i(h\nu) X_i$$

$$b_3 = \sum_{i=n}^N \mu_i(h\nu) X_i$$

$$E_2(b) = b \int_b^{\infty} \exp(-t)/t^2 dt$$

$$B(b_3) = \text{buildup factor} = A_1 \exp - A_1 b_3 + A_2 \exp - a_2 b_3$$

$$a_2 = 1 - a_1$$

a_1, a_2 as defined in Reference 62.

If the volume source is a linear sum of exponentials, such as $S_V(x) = \sum_i S_i \exp(k_i x)$ the transmission is defined as

$$T(h\nu) = \sum_i \frac{S_i \beta(b_3)}{2k_i} \beta_i$$

where

$$\beta_i = \exp(k_i x_n) [E_1(b_1) - E_1(b_1 \sec \theta)]$$

$$- \exp(k_i b_3 / \mu_n) [E_1(b_1 \frac{\mu_n + k_i}{\mu_n}) - E_1(b_3 \frac{\mu_n + k_i}{\mu_n})]$$

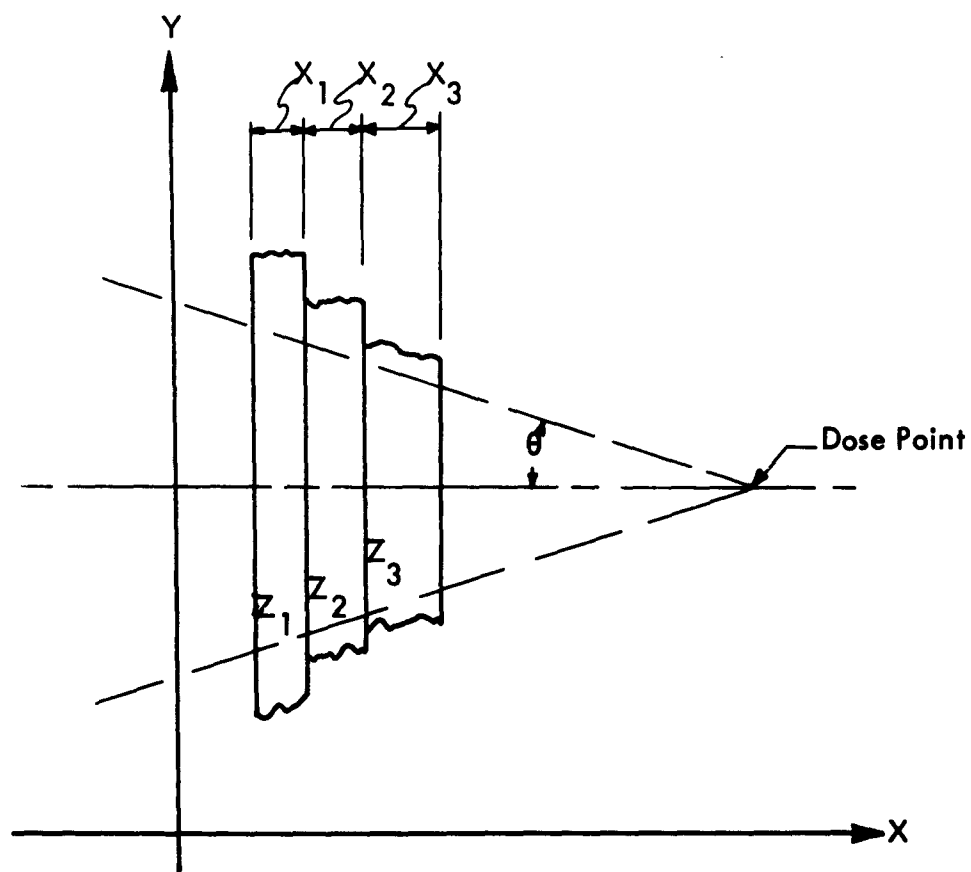


FIGURE 42. Geometry for bremsstrahlung calculations

$$- E_1(b_3) - E_1(b_3 \sec \theta)$$

$$+ \exp(k_i b_3 / \mu_n) [E_1(b_1 \frac{\mu_n \sec \theta + k_i}{\mu_n}) - E_1(b_3 \frac{\mu_n \sec \theta + k_i}{\mu_n})]$$

$$E_1(b) = \frac{\exp(-t)}{b}$$

Special cases when (1) $b_1 \neq 0$, $k_i = 0$; (2) $b_1 = 0$, $k_i \neq 0$; (3) $b_1 \neq 0$, $k_i = 0$; (4) $b_1 \neq 0$, $k_i \neq -\mu_s$; (5) $b_1 \neq 0$, $k_i = -\mu_s \sec \theta$; and (6) $b_1 \neq 0$, $k_i \neq 0$, $k_i \neq -\mu_s$, $k_i \neq -\mu_s \sec \theta$ were evaluated and are summarized in Table 6. These special cases require additional analysis of the general expression since otherwise division by zero would occur. The quantity b_1 is the number of mean free paths of shielding following the source layer and k_i is the coefficient of the equipment of the i^{th} term in the series. $S_V(\chi) = \sum S_i \exp(k_i \chi)$. The quantity β is the argument for the i^{th} term in the series. In Case 1 ($b_1 \neq 0$, $k_i = 0$) there is shielding beyond the source layer but the i^{th} source term is unity. Case 2 ($b_1 = 0$, $k_i \neq 0$) has no shielding after the source layer but the i^{th} source term has a finite value. Case 3 ($b_1 = 0$, $k_i = 0$) has no shielding and the i^{th} source term is unity. Case 4 ($b_1 \neq 0$, $k_i = -\mu_s$) has a shield but the coefficient of the i^{th} source term is equal to the photon attenuation coefficient μ_s . Case 5 ($b_1 = 0$, $k_i = -\mu_s \sec \theta$) has a shield but the coefficient of the i^{th} source term is equal to the photon attenuation coefficient times the secant of the subtended angle. Case 6 ($b_1 = 0$, $k_i \neq 0$, $k_i \neq -\mu_s$, $k_i \neq -\mu_s \sec \theta$) has a shield and the coefficient of the i^{th} source term does not have the values 0, $-\mu_s$, or $-\mu_s \sec \theta$.

The angular distribution of bremsstrahlung has been described in the mathematical model by the function $F(h\nu, E, \theta = 0, \theta_0)$ which represents the fraction of the total bremsstrahlung created by an electron of energy E incident at an angle θ_0 which will have an energy $h\nu$ and be directed in the direction of $\theta = 0$. This function is required for a thick target, since the differential cross sections are only useful in a Monte Carlo or transport-type analysis. The existing data are integrated over the final energy and data are reported as energy per square centimeter (References 72, 73, and 74). Typical data are shown in Figure 43. Analysis of these data indicates that a sum of exponentials may be an approximation to the distribution function. There were insufficient data to develop a successful expression; however, the machine program has the flexibility to accept any analytical expression developed. Until more information is available, a $\cos^2 \theta$ distribution appears to be a reasonable approximation to the bremsstrahlung distribution. If the angular distribution of the incident radiation is assumed to be isotropic, the radiation produced will also be isotropic over 2π and independent of the scattering distribution. This situation is usual, but an analysis of a nonisotropic incident distribution will be presented in a separate discussion.

Table 6
SUMMARY OF SPECIAL CASES

Case 1 $b_1 \neq 0, k_i = 0$

$$\beta_i = \frac{A_i}{2\mu_s} [E_2(b_1) - E_2(b_3) + \frac{E_2(b_3 \sec \theta)}{\sec \theta} - \frac{E_2(b_1 \sec \theta)}{\sec \theta}]$$

Case 2 $b_1 = 0, k_i \neq 0$

$$\beta_i = \frac{A_i}{2k_i} \left\{ \exp(k_i h) \ln(\sec \theta) - [E_1(b_3) - E_1(b_3 \sec \theta)] \right\}$$

Case 3 $b_1 = 0, k_i = 0$

$$\beta_i = \frac{A_i}{2\mu_s} [1 - E_2(b_3) - \frac{E_2(b_3 \sec \theta)}{\sec \theta} - \frac{1}{\sec \theta}]$$

Case 4 $b_1 \neq 0, k_i = -\mu_s$

$$\begin{aligned} \beta_i = \frac{A_i}{2k_i} \exp k_i h [E_1(b_1) - E_1(b_1 \sec \theta)] - [E_1(b_3) - E_1(b_3 \sec \theta)] \\ + \exp(k_i b_3 / \mu_s) \left\{ - E_1 [b_3 (\sec \theta - 1)] + E_1 [b_1 (\sec \theta - 1)] - \ln \left(\frac{b_1}{b_3} \right) \right\} \end{aligned}$$

Case 5 $b_1 \neq 0, k_i = -\mu_s \sec \theta$

$$\begin{aligned} \beta_i = \frac{A_i}{2k_i} \left\{ \exp k_i h [E_1(b_1) - E_1(b_1 \sec \theta)] - [E_1(b_2) - E_1(b_3 \sec \theta)] \right. \\ \left. - \exp \left(\frac{k_i b_3}{\mu_s} \right) \left\{ - E_1 [b_3 (1 - \sec \theta)] + E_1 [b_1 (1 - \sec \theta)] - \ln (b_1 / b_3) \right\} \right\} \end{aligned}$$

Table 6
(Continued)

Case 6 $b_1 \neq 0, k_i \neq 0, \neq -\mu_s \sec\theta$

$$\beta_i = \frac{A_i}{2k_i} \left\{ \exp(k_i h) [E_1(b_1) - E_1(b_1 \sec\theta)] - \exp(k_i h) [E_1(b_2) - E_1(b_3 \sec\theta)] \right. \\ \left. + \exp\left(\frac{k_i b_3}{\mu_s}\right) \left\{ E_1 \left[b_1 \left(\frac{\mu_s \sec\theta + k_i}{\mu_s} \right) \right] - E_1 \left[b_3 \left(\frac{\mu_s \sec\theta + k_i}{\mu_s} \right) \right] \right. \right. \\ \left. \left. - E_1 \left[b_1 \left(\frac{\mu_s + k_i}{\mu_s} \right) \right] + E_1 \left[b_3 \left(\frac{\mu_s + k_i}{\mu_s} \right) \right] \right\} \right\}$$

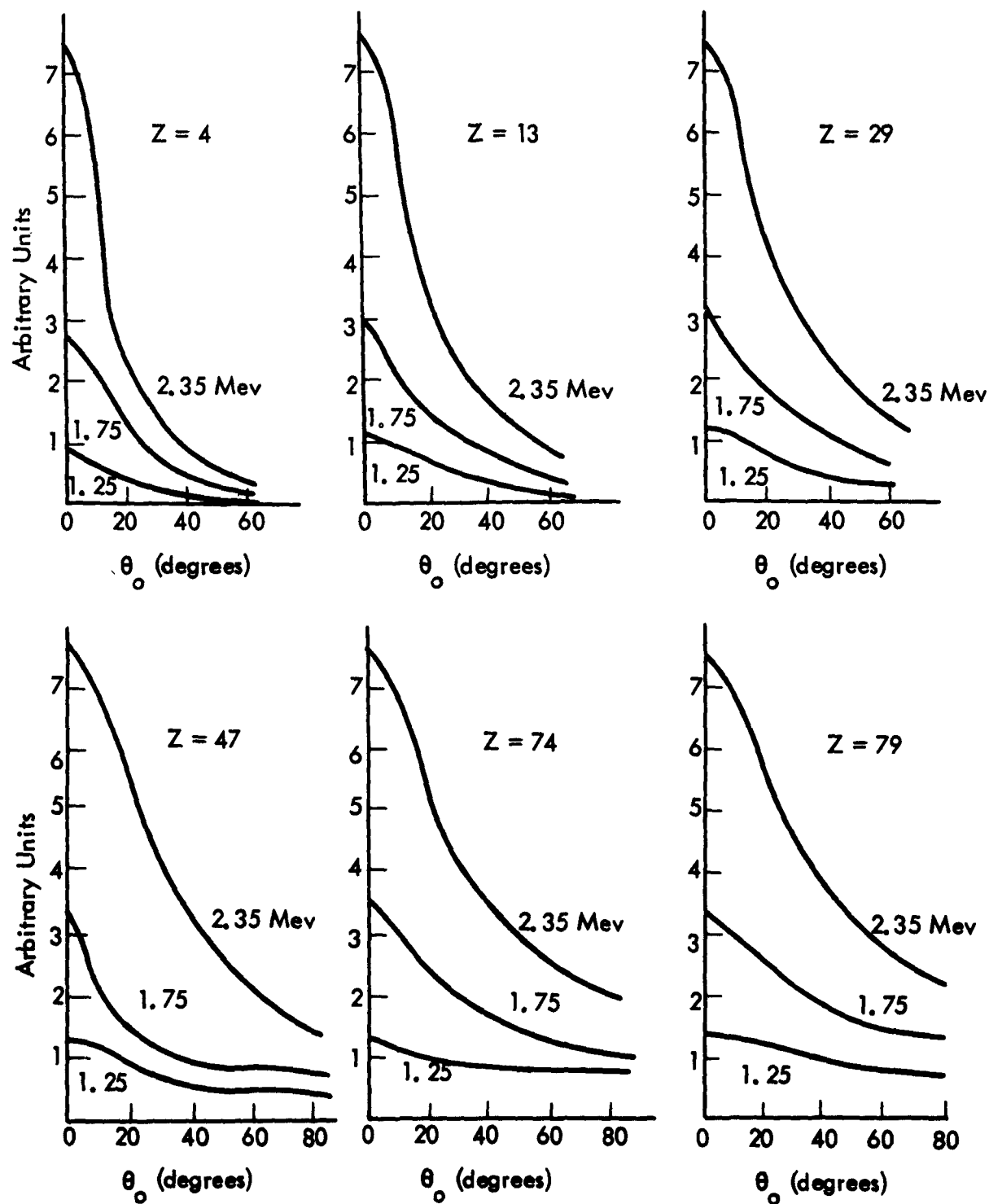


FIGURE 43. Thick target bremsstrahlung angular distribution

5.2.2.2 Dose Calculations

The mathematical model for bremsstrahlung shield was incorporated in the original vehicle shielding code for bremsstrahlung. The bremsstrahlung dose, D_B , inside a vehicle is computed from the expression

$$D_B = \sum_i \phi_{ei}(E) T_{Bi} A_i \omega_i$$

where $\phi_{ei}(E)$ is the flux of electrons incident on sector i of the vehicle. T_{Bi} is the bremsstrahlung penetrating sector i resulting from an incident flux of $\phi_{ei}(E)$ electrons of a specific spectrum and is the transmission factor discussed previously. A_i is the angular weight factor which is the ratio: dose scattered to the receiver/isotropic dose to the receiver, and ω_i is the fractional solid angle subtended by the receiver. A discussion of the computation of A_i is presented in Section 7, which describes the general effects of angular distribution.

5.2.2.3 Results

The results of the modified bremsstrahlung model were compared with the data from the original model. These data are shown in Table 7. The agreement is within five percent. Since the source has been distributed uniformly for each energy group of photons, the amount of bremsstrahlung penetrating a shield should be slightly greater than the surface source. The difference is the decrease in absorption of the photons. For an aluminum shield, the source volume is approximately 3 gm/cm² thick. This would reduce the 1-Mev photons by 15 percent, the 3-Mev photons by 10 percent, and the 6-Mev photons by 8 percent. For shields less than the source volume, only a fraction of the total bremsstrahlung is produced, so the volume source results should be lower than the surface source. The exponential series distribution has been validated with hypothetical constants; however no meaningful data were generated. Tables 8 to 11 show results obtained from this code for lead, iron, aluminum, and beryllium shields and a 75-percentile man as a function of shell thickness and location of dose point in the man.

Table 7
COMPARISON OF BREMSSTRAHLUNG RESULTS

Target	Fission Spectrum All Incident Electrons Stopped on Surface	Fission Spectrum Uniform Distribution *
1 gm/cm ² Be	3.44×10^{-9} rads/e/cm ²	2.3×10^{-9} rads/e/cm ²
1 gm/cm ² Al	1.15×10^{-8}	9.4×10^{-9}
5 gm/cm ² Pb	4.75×10^{-8}	4.9×10^{-8}
* Photons of energy E produced over a depth-equivalent electron energy loss of $E_0 - E$ where E_0 is initial electron energy.		

Table 8
BREMSSTRAHLUNG TRANSMISSION VERSUS LEAD SHELL
THICKNESS FOR THREE SPECIFIC BODY POINTS

Shell Thickness (g/cm ²)	Fission Spectrum (Values in Rad/electron/cm ²)			Van Allen Belt Spectrum (Values in Rad/electron/cm ²)		
	EYE	CHEST	WAIST	EYE	CHEST	WAIST
1	2.08×10^{-11}	1.78×10^{-11}	1.96×10^{-11}	1.22×10^{-11}	1.02×10^{-11}	1.18×10^{-11}
4	1.47×10^{-11}	1.29×10^{-11}	1.37×10^{-11}	7.52×10^{-12}	6.44×10^{-12}	7.24×10^{-12}
10	9.15×10^{-12}	8.14×10^{-12}	8.34×10^{-12}	4.08×10^{-12}	3.56×10^{-12}	3.83×10^{-12}
25	3.71×10^{-12}	3.36×10^{-12}	3.28×10^{-12}	1.33×10^{-12}	1.19×10^{-12}	1.20×10^{-12}
50	1.05×10^{-12}	9.63×10^{-13}	9.11×10^{-13}	3.05×10^{-13}	2.77×10^{-13}	2.67×10^{-13}
100	1.10×10^{-13}	1.02×10^{-13}	9.44×10^{-14}	2.47×10^{-14}	2.27×10^{-14}	2.13×10^{-14}
200	1.66×10^{-15}	1.55×10^{-15}	1.42×10^{-15}	2.79×10^{-16}	2.59×10^{-16}	2.39×10^{-16}

Table 9
BREMSTRAHLUNG TRANSMISSION VERSUS IRON SHELL
THICKNESS FOR THREE SPECIFIC BODY POINTS

Shell Thickness (g/cm ²)	Fission Spectrum (Values in Rad/electron/cm ²)			Van Allen Belt Spectrum (Values in Rad/electron/cm ²)		
	EYE	CHEST	WAIST	EYE	CHEST	WAIST
1	7.38×10^{-12}	6.18×10^{-12}	6.98×10^{-12}	5.09×10^{-12}	4.12×10^{-12}	4.88×10^{-12}
4	6.98×10^{-12}	5.86×10^{-12}	6.60×10^{-12}	4.74×10^{-12}	3.85×10^{-12}	4.56×10^{-12}
10	5.65×10^{-12}	4.79×10^{-12}	5.34×10^{-12}	3.62×10^{-12}	2.97×10^{-12}	3.50×10^{-12}
25	2.95×10^{-12}	2.56×10^{-12}	2.76×10^{-12}	1.61×10^{-12}	1.36×10^{-12}	1.55×10^{-12}
50	9.55×10^{-13}	8.49×10^{-13}	8.69×10^{-13}	4.19×10^{-13}	3.64×10^{-13}	3.94×10^{-13}
100	1.14×10^{-13}	1.04×10^{-13}	9.95×10^{-14}	3.48×10^{-14}	3.13×10^{-14}	3.11×10^{-14}
200	2.55×10^{-15}	2.37×10^{-15}	2.19×10^{-15}	4.87×10^{-16}	4.48×10^{-16}	4.20×10^{-16}

Table 10
BREMSSTRAHLUNG TRANSMISSION VERSUS ALUMINUM SHELL
THICKNESS FOR THREE SPECIFIC BODY POINTS

Shell Thickness (g/cm ²)	Fission Spectrum (Values in Rad/electron/cm ²)			Van Allen Belt Spectrum (Values in Rad/electron/cm ²)		
	EYE	CHEST	WAIST	EYE	CHEST	WAIST
1	3.42×10^{-12}	2.86×10^{-12}	3.23×10^{-12}	2.36×10^{-12}	1.91×10^{-12}	2.25×10^{-12}
4	3.35×10^{-12}	2.81×10^{-12}	3.17×10^{-12}	2.30×10^{-12}	1.86×10^{-12}	2.20×10^{-12}
10	2.86×10^{-12}	2.41×10^{-12}	2.70×10^{-12}	1.88×10^{-12}	1.53×10^{-12}	1.80×10^{-12}
25	1.51×10^{-12}	1.31×10^{-12}	1.41×10^{-12}	8.70×10^{-13}	7.26×10^{-13}	8.30×10^{-13}
50	4.68×10^{-13}	4.16×10^{-13}	4.26×10^{-13}	2.11×10^{-13}	1.82×10^{-13}	1.97×10^{-13}
100	5.24×10^{-14}	4.79×10^{-14}	4.59×10^{-14}	1.55×10^{-14}	1.39×10^{-14}	1.38×10^{-14}
200	1.19×10^{-15}	1.11×10^{-15}	1.02×10^{-15}	1.94×10^{-16}	1.79×10^{-16}	1.67×10^{-16}

Table 11
BREMSTRAHLUNG TRANSMISSION VERSUS BERYLLIUM SHELL
THICKNESS FOR THREE SPECIFIC BODY POINTS

Shell Thickness (g/cm ²)	Fission Spectrum (Values in Rad/electron/cm ²)			Van Allen Belt Spectrum (Values in Rad/electron/cm ²)		
	EYE	CHEST	WAIST	EYE	CHEST	WAIST
1	1.03×10^{-12}	8.56×10^{-13}	9.75×10^{-13}	7.33×10^{-13}	5.90×10^{-13}	7.01×10^{-13}
4	1.24×10^{-12}	1.02×10^{-12}	1.18×10^{-12}	9.19×10^{-12}	7.35×10^{-13}	8.81×10^{-13}
10	1.29×10^{-12}	1.06×10^{-12}	1.24×10^{-12}	9.59×10^{-13}	7.68×10^{-13}	9.24×10^{-13}
25	8.12×10^{-13}	6.79×10^{-13}	7.78×10^{-13}	5.60×10^{-13}	4.54×10^{-13}	5.42×10^{-13}
50	2.58×10^{-13}	2.22×10^{-13}	2.44×10^{-13}	1.48×10^{-13}	1.24×10^{-13}	1.43×10^{-13}
100	2.70×10^{-14}	2.43×10^{-14}	2.43×10^{-14}	1.01×10^{-14}	8.83×10^{-15}	9.35×10^{-15}
200	7.01×10^{-16}	6.52×10^{-16}	6.03×10^{-16}	1.24×10^{-16}	1.13×10^{-16}	1.07×10^{-16}

6.0 PROTON SHIELDING

Once the proton flux incident on a space vehicle has been selected, the detailed interactions of the incident proton flux with the materials of the space vehicle and the astronaut's body can be considered. The objectives of this phase of the contract were to develop techniques for calculating the absorbed dose, number-LET, and energy-LET spectra at arbitrary points in a space vehicle. A method for calculating semiconductor dislocation densities was also desired. Two computer codes were developed during this study. The first treats those situations in which the incident proton flux is the dominant energy depositor. Basically, the existing Boeing computer code was found to be suitable for this application, and it was revised to generate the required data. A more comprehensive treatment of proton interactions was included in a second computer code, which was developed to verify both the approximations made in the first code and to treat situations in which the secondary radiations induced by the incident proton flux are significant.

6.1 INTERACTIONS OF PROTONS WITH MATTER

As protons pass through an absorber, they lose energy primarily through collisions with the electrons and nuclei of the absorber's atoms. Proton bremsstrahlung is a relatively insignificant energy-loss mechanism in comparison with the collision processes (Reference 75). For protons of low energy, say 10 Mev, collisions with electrons provide the dominant energy-loss mechanism. As protons of increasing energy are considered, collision processes with the nuclei of the absorber assume increasing importance. This includes only the "first order" interactions. Ultimately, the entire kinetic energy of the proton will be dissipated in the ionization and excitation of electrons by charged particles, or carried away from the point of interest by neutral particles. It will be shown that the energy spectrum of solar flare and trapped protons makes collision processes with electrons the primary energy-loss mechanism, although for thicker shields and deep body points, the dose from secondary radiations is not negligible.

6.1.1 Interaction With Electrons

Charged particles in general—and protons in particular—lose energy to atomic electrons in collisions that are conveniently divided into two classes, hard and soft. A quantity H (the amount of energy transferred) defines the division between these two classes. Bethe (Reference 76) has shown that the energy loss per unit path length for "soft" collisions, $Q < H$, is given by

$$\left(-\frac{dE}{ds}\right)_{Q < H} = \frac{2\pi N(Ze^2)^2}{m_o \beta^2 c^2} \left\{ \ln \left[\frac{2m_o \beta^2 c^2 H}{(1-\beta^2)^2} \right] - \beta^2 \right\}$$

where

Q = energy transfer per collision

N = number of electrons per cm^3 of absorber

m_0 = rest mass of the electron

Ze = charge of the penetrating particle

I = the mean excitation potential of the medium

H = the maximum energy transfer in a single soft collision

$\beta = v/c$

v = velocity of the incident particle

c = velocity of light

For H sufficiently large that the binding energy of the electron is small in comparison, the cross section for an energy transfer greater than H is essentially that for a free electron. For incident proton energies less than 93.8 Bev, one may use the cross section for spin zero particles, and, in addition, neglect bremsstrahlung energy losses (Reference 77). This gives an energy loss per unit path length of

$$\left(-\frac{dE}{ds}\right)_{Q>H} = \frac{2\pi N(Ze^2)^2}{m_0 \beta^2 c^2} [\ln(Q_{\max}/H) - \beta^2]$$

where

$$Q_{\max} = \frac{2 m_0 v^2}{(1 - \beta^2)}$$

from relativistic mechanics, and the other symbols are defined as before.

Combining the two expressions gives the well-known relation for the total average energy loss of a heavy particle,

$$\left(-\frac{dE}{ds}\right)_{\text{total}} = \frac{4\pi N(Ze^2)^2}{m_0 \beta^2 c^2} \left\{ \ln \left[\frac{2 m_0 \beta^2 c^2}{(1 - \beta^2) I} \right] - \beta^2 \right\}$$

It is convenient in shielding calculations to use density independent units rather than linear thickness, which gives

$$\left(-\frac{dE}{\rho ds}\right) = \left(-\frac{dE}{dx}\right) = \frac{4\pi N_o Z^2 e^4}{A m_o \beta^2 c^2} \left\{ \ln \left[\frac{2m_o c^2 \beta^2}{(1-\beta^2)} \right] - \beta^2 \right\}$$

where

N_o = Avogadro's number = $6.025 (10^{23})$ atoms/mole

A = atomic weight of the absorber

ρ = density of material

In what follows, thicknesses will be given in the density independent form x .

This expression has been found accurate if the following conditions are fulfilled:

1) The velocity v of the incident particle must be greater than the largest electronic velocity of the absorber, $v = Ze^2/h < v$. For oxygen, this means that the velocity of a proton must be greater than 1 Mev. Fortunately, this otherwise quite serious restriction can be circumvented by the use of a correction factor c_k which takes into account the reduced effectiveness of the more tightly bound electrons (Reference 78). It will also be shown that in space vehicle shielding, the importance of the low-energy protons is small if a few gm/cm² of shielding are present.

2) The velocity of the particle must be great enough that its effective charge is not altered by the capture of atomic electrons. There are no valid theoretical expressions for $(-dE/dx)$ in this region, and experimental results must be used. Fortunately, this energy region is below 1 Mev for protons, although for alpha particles it presents a more serious problem.

Once the average energy loss $(-dE/dx)$ has been acquired, it is possible to derive range-energy tables in the manner of Rich and Madey (Reference 79), or Sternheimer (Reference 80). In addition, further investigation of the relative importance of the hard and soft collisions gives an insight into the exact nature of energy dissipation in tissue. By taking the ratio of the total energy loss to the energy lost in soft collisions, we find

$$\frac{\left(-\frac{dE}{dx}\right)_{Q < H}}{\left(-\frac{dE}{dx}\right)_{\text{total}}} = 0.5 + \frac{\ln(H/I)}{2 \left\{ \ln \left[\frac{2 m_o \beta^2 c^2}{1 (1 - \beta^2)} \right] - \beta^2 \right\}}$$

By examining the amount of energy lost by collisions of greater than say 200 ev, an insight into the relative amount of energy dissipated by local or soft collisions can be gained. The electrons of energy greater than 200 ev have been shown to be less effective in causing biological damage than the soft energy loss component of the protons. Schaffer has examined this subject in detail and concludes that the energy deposited in primary collisions should be divided into these categories for an accurate evaluation of radiation effects on man (Reference 81).

6.1.2 Interactions with the Nucleus

6.1.2.1 Elastic Collisions

Protons also lose energy to an absorber by interactions with the nuclei of the absorber's atoms. These interactions can be divided into elastic and inelastic collisions. An elastic collision is defined as an interaction between two particles in which the kinetic energy of both is conserved in the center-of-mass coordinate system. It can be shown that the energy lost by elastic scattering due to Coulomb or nuclear forces is small in comparison with the electron ionization energy losses (Reference 82). Only in the case of the light nuclei can significant energy be transferred to the nucleus in the event of an elastic collision. (The heavier nuclei are essentially undisturbed by the passage of a proton.)

One basic reason which renders the elastic collision processes ineffectual in transferring energy is the infrequency of large angle scattering events. At high incident-proton energies, inelastic nuclear collisions are dominant because the proton interacts with the individual nucleons. At low energies, where elastic collisions are possible, the total range of the protons is so small that only a small fraction of the protons have elastic collisions. Coulomb scattering, which is possible at all incident-proton energies, has such a small cross section for large angle scatterings that it is also unimportant as an energy dissipation process. Only in the case of hydrogen, where elastic collisions alone are possible up to the pion production threshold near 300 Mev, do elastic collisions deserve attention.

The low probability of large-angle elastic scattering events has another significant result. The incident protons maintain their original direction while traversing the shield to a very close approximation. The atomic electrons, with their low relative mass, do not deflect the incident protons through large angles either in single collisions or by multiple scattering. Multiple scattering resulting from Coulomb forces is also small. For example, the mean square radial spread of a 100-Mev proton

beam passing through 2 gm/cm^2 of aluminum is 0.01 cm (Reference 83). The characteristic of protons can be used to advantage in the analysis of practical shielding problems.

6.1.2.2 Inelastic Collisions

As protons of higher energy are considered, the inelastic collision process represents an increasingly important mechanism for modifying the incident proton flux. This is a result of two factors, the rapid increase of proton range with energy ($R \approx KE^{1.6}$) and the nearly constant value of the inelastic cross section at high energies ($E > 100 \text{ Mev}$). Experimentally, it has been found that an incident proton flux will induce the emission of neutrons, photons, secondary protons and, for energies of greater than 300 Mev , the entire spectrum of other elementary particles. It has been shown (Reference 84) that the emission of particles, other than the first three mentioned, is negligible for the incident spectra of interest (solar particle events and trapped radiation belts); for absorbed dose calculations, they can be neglected. In the special case of a hydrogen absorber, only elastically scattered protons can result from the proton-proton collision for incident proton energies up to the pion production threshold near 300 Mev . The only secondary particles emitted in this case will be protons.

Assume a flux of protons, $\phi_p(E, x)$, at a point x in an absorber. Then the rate at which inelastic collisions are occurring is given by

$$\frac{N_0}{A} \int_{E_{\min}}^{E_{\max}} \phi_p(E, x) \sigma_{\text{in}}(E) dE$$

where

$\phi_p(E, x)$ = incident proton flux at point x

σ_{in} = inelastic collision cross section

E_{\min}, E_{\max} = the energy ranges of the proton flux

The particle emission processes induced by these collisions are energy dependent. The high-energy protons, which are defined as having an energy much larger than the binding energy of the individual nucleons of the struck nucleus, are assumed to interact with individual nucleons by elastic collisions. This intranuclear cascade process has been studied extensively by computer simulation of individual collisions (References 85, 86, and 87), the Monte Carlo technique. When no cascade particle remains with sufficient energy to escape the potential field of the nucleus, the intranuclear cascade process is considered terminated, and the evaporation model is used to further predict

the behavior of the excited nucleus (References 88, 89, and 90). A proton with insufficient energy to initiate a cascade is considered to excite the entire nucleus, and the evaporation theory is used to predict the decay products. These theoretical methods have both strengths and weaknesses, and detailed comparisons with the available experimental data are available in the cited literature. While it would be most desirable to use only experimental results for the analysis of the induced secondary radiations, the sparse data available and the enormous amount of information required make this impossible at present. Theoretical predictions must be utilized to fill the gaps in the present experimental data. This is rather unfortunate, as the present knowledge of the structure of the nucleus and the nature of nuclear reactions is much less precise than our knowledge of the proton-electron collision processes.

The following data must be obtained to quantitatively describe the emission process:

- 1) The inelastic cross section of the absorber. These data are generally available from experiment for most shielding materials of interest. Interpolation on both energy and atomic weight is possible.
- 2) The number of neutrons or protons emitted per inelastic collision of an incident neutron or proton. While experimental values are given in the literature for particular materials and incident particle energies, theoretical calculations provide the bulk of available data.
- 3) The energy distribution of the emitted particles. Theoretical calculations provide a direct prediction of the energy distribution, while the experimental data generally give only an indirect comparison with theory.
- 4) The number and energy distribution of gamma rays emitted by the struck nucleus. Here there is an abundance of experimental data, though little of it is in a form usable for shielding calculations. As the gamma rays are indicative of the energy levels of the nucleus, they have been used for the analysis of nuclear structure. The experimental results of Wakatsuki, et al. (Reference 91) are in a convenient form for this calculation, and his results have been used.

The proton secondary calculations have been formulated in such a way that these basic data, obtained from either theoretical or experimental work, can be used as input information. The results reported here use the data of Wallace and Sondhaus (Reference 92), which are essentially based on the Metropolis calculations (References 85 and 86). The Oak Ridge group has recently published its calculations in a form that is directly compatible with these calculations (Reference 93), and either source may be used.

6.2 RADIATION TRANSPORT

Once the details of the physical interactions between the incident protons and the absorber's atoms are specified, either by theoretical or experimental results, it is then, in principle, possible to determine the radiations emitted by the absorber. While idealized absorber geometries and simplified physical interactions sometime permit exact solutions for the radiation transport, more realistic problems generally force the use of various approximations. It is desirable in shielding calculations to make these approximations in such a way that a conservative estimate of the absorbed dose is made; yet the results must be as accurate as possible or they lose their usefulness. Fortunately for the shielding situations currently of greatest interest, little accuracy need be sacrificed.

The standard transport equations have been used by workers at Oak Ridge (Reference 84), Lockheed (Reference 94), and The Boeing Company (Reference 95) to describe the propagation of an incident proton spectrum, and the resulting cascade and evaporation products through various shield configurations. The approach generally used in the solution of these equations (some form of finite difference approximation) has the disadvantage of requiring considerable computer time to achieve results of reasonable accuracy. By formulating the transport equations as a series of integral equations, it was found possible to achieve a high degree of accuracy with a minimum of computer time.

6.2.1 Protons

6.2.1.1 Incident Protons

Consider a proton spectrum incident normally upon an absorber of finite thickness and infinite extent. Assume the following definitions:

$$\frac{d\phi_p}{dE} = \phi_p(E, x)$$

the proton flux, as a function of energy and position in the absorber in units of protons/cm²-Mev

The total number of protons is then

$$\phi_p(x) = \int_0^{\infty} \phi_p(E, x) dE$$

and definitions of total and average energy of the proton flux follow naturally. The basic problem is to find the proton flux at any point in the absorber

$$\phi_p(E, x)$$

Recall that the incident protons travel in essentially straight lines until they are stopped or make an inelastic collision with a nucleus of an absorber atom. The energy loss per unit path length ($-dE/dx$) can then be used to calculate the total energy loss in passing through the absorber by equating the proton path length and the thickness of the absorber. We then obtain the range-energy relation for protons in terms of the initial and final energy of the proton and the thickness of absorber traversed,

$$R(E_{out}) = R(E_{in}) - x$$

Then

$$\frac{dR(E_{out})}{dE_{out}} dE_{out} = \frac{dR(E_{in})}{dE_{in}} dE_{in}$$

or

$$\frac{dE_{out}}{S(E_{out})} = \frac{dE_{in}}{S(E_{in})} \quad S(E) = -\frac{dE}{dx}$$

If no protons are stopped in the absorber, the number entering must equal the number emerging,

$$d\phi_p = \phi_p(E_{in}, 0) dE_{in} = \phi_p(E_{out}, x) dE_{out}$$

where E_{in} and E_{out} are related by the range-energy relation.

The proton spectrum at point x is then related to the incident spectrum by

$$\phi_p(E_{out}, x) = \phi_p(E_{in}, 0) \frac{S(E_{in})}{S(E_{out})}$$

The proton spectrum at any point in the absorber can be obtained in this manner. For a multilayer absorber of different material types, the procedure is to repeat the calculation as the proton flux passes through each layer.

For thin absorbers, that is, x much less than the mean free path of protons in the absorber between inelastic collisions, this procedure gives proton fluxes of adequate accuracy; as absorbers of increasing thickness are considered, it becomes necessary to attenuate the incident proton flux to account for those protons removed by inelastic collisions. When this is done, we find

$$\phi_p(E_{out}, x) = \phi_p(E_{in}, 0) \frac{S(E_{in})}{S(E_{out})} \exp \left[- \int_{E_{in}}^{E_{out}} \frac{\mu(E)}{S(E)} dE \right]$$

where

$$\mu(E) = \frac{N_o}{A} \sigma_{inelastic}$$

$\sigma_{inelastic}$ = inelastic cross section of material

By using the relation

$$R(E) = R(E_{in}) - x$$

to obtain

$$dE = - S(E) dx$$

the variable of integration is changed from x to E .

6.2.1.2 Secondary Protons

The incident proton flux generates secondary protons in the absorber through inelastic collisions with absorber nuclei. While these secondary protons may be emitted with angular distributions, ranging from isotropic to highly anisotropic, in what follows they will be considered as traveling in the direction of the incident proton. This approximation will be discussed later. For an absorber of thickness X , the generation rate of secondary protons of energy E' at point x in the absorber can be given as follows:

$$d[\phi_{sp}(E', x)] = \frac{N_o}{A} \left[\int_{E'}^{E_{max}} \phi_p(E, x) \sigma_{pp}(E, M) F_p(E, E') dE \right] dx$$

where all terms are defined as follows:

N_o = Avogadro's number = 6.025×10^{23} atoms/mole

A = atomic weight of material M , grams/mole

$\phi_p(E, x)$ = proton flux at energy E and point x in units of proton $\text{cm}^{-2} \text{Mev}^{-1}$

$\sigma_{pp}(E, M)$ = yield cross section for the production of protons by the inelastic collision of protons of energy E with a nucleus of element M

$$\sigma_{pp}(E, M) = N_p(E, M) \sigma_{in}(E, M)$$

$N_p(E, M)$ = number of protons per inelastic collision of protons with energy E on nuclei of material M

$\sigma_{in}(E, M)$ = inelastic collision cross section in units of cm^2/atom

$F_p(E, E')$ = spectral distribution of protons produced by protons of energy E in units of proton/Mev proton

E_{\max} = maximum energy of the incident proton flux

E' = energy of secondary proton

Set

$$P_{pp} = \frac{N}{A} \left[\int_{E'}^{E_{\max}} \phi_p(E, x) \sigma_{pp}(E, M) F_p(E, E') dE \right]$$

Now the flux of secondary protons at energy E_{sp} emerging from the shield of thickness X is

$$\phi_{sp}(E_{sp}) = \int_0^X P_{pp}(E', x) \frac{S(E')}{S(E_{sp})} dx$$

where E_{sp} and E' are related by

$$R(E') = R(E_{sp}) + (X-x)$$

the range-energy relation for the absorber. While this flux of secondary protons in turn is further attenuated by inelastic collisions and produces third-generation particles, the process will be terminated at this point. The results indicate that for the proton spectra and shield materials of interest in space vehicle shielding, no appreciable error is made in terminating the cascade at the second order.

6.2.2 Neutrons

The incident proton flux also generates neutrons in the absorber. These neutrons are moderated in energy by elastic collisions with light nuclei, hydrogen being the most effective. Inelastic collisions, which effectively remove the neutron

from the particle flux, are here considered to be the only attenuation mechanism. In those cases where more precise neutron flux solutions are desired, this calculation can be used to obtain the neutron source terms. The neutron is assumed to travel in the direction of the incident proton.

For a single absorber, the source distribution of neutrons of energy E can be written as follows:

$$d[\phi_n(E', x)] = -\frac{N_o}{A} \left[\int_{E'}^{E_{\max}} \phi_p(E, x) \sigma_{pn}(E, M) F_n(E, E') dE \right] dx$$

Now let

$$P_{pn}(E', x) = \frac{N_o}{A} \int_{E'}^{E_{\max}} \phi_p(E, x) \sigma_{pn}(E, M) F_n(E, E') dE$$

The symbols are defined as follows:

N_o = Avogadro's number = $6.025 (10^{23})$ atoms/mole

A = atomic weight of material M , grams/mole

$\phi_p(E, x)$ = proton flux at energy E and point x in units of protons $\text{cm}^{-2} \text{Mev}^{-1}$

$\sigma_{pn}(E, M)$ = yield cross section for the production of neutrons by the inelastic collision of protons of energy E on a nucleus of element M

$\sigma_{pn}(E, M) = N_n(E, M) \sigma_{in}(E, M)$

N_n = number of neutrons per inelastic collision of protons of energy E with atoms of material M

σ_{in} = inelastic collision cross section in units of cm^2/atom

$F_n(E, E')$ = spectral distribution of neutrons produced by protons of energy E (in units of neutrons/Mev proton)

E_{\max} = maximum energy of incident proton flux (Mev)

Integrating the neutron generation function $P_{pn}(E, x)$ over the shield thickness X gives the total number of neutrons of energy E generated in the absorber.

$$\phi_n(E') = \int_0^X P_{pn}(E', x) dx$$

If it is assumed that all the neutrons generated travel in the direction of the incident protons, and that those neutrons that undergo inelastic collisions are effectively removed from the neutron beam, the number of neutrons both generated and penetrating the absorber is

$$\phi_n(E', x) = \int_0^X P_{pn}(E', x) \exp[-\mu_n(E', M)(X-x)] dx$$

where $\mu_n(E', M)$ is the attenuation coefficient for neutrons of energy E' and material M in cm^2/gm .

6.2.3 Gammas

The inelastic collisions of the incident protons with absorber nuclei lead to gamma emission by the excited nuclei. These gamma rays are quite penetrating, and their contribution to the absorbed dose must be evaluated.

The rate at which the incident protons are suffering inelastic collisions in the absorber may be expressed as follows:

$$\frac{dN_c}{dx} = \frac{N_o}{A} \int_0^{E_{\max}} \phi_p(E, x) \sigma_{in}(E, M) dE$$

where the symbols are as defined previously.

Integrating over the absorber thickness and including a transmission factor for the attenuation of the gammas gives the following expression for the flux of gamma rays at the surface of the absorber, assuming all the gammas are emitted in the direction of the incident proton.

$$\phi_\gamma(E') = F_\gamma(E', M) \int_0^X \left[\frac{N_o}{A} \int_0^{E_{\max}} \phi_p(E, x) \sigma_{in}(E, M) dE \right] \exp[-\mu_\gamma(E', M)(X-x)] dx$$

where

$\phi_{\gamma}(E')$ = photon flux at energy E' in photons/Mev

$F_{\gamma}(E', M)$ = spectral density of photons of energy E' from material M

N_0 = Avogadro's number

A = atomic weight of the material

$\sigma_{in}(E, M)$ = inelastic cross section of nuclei of type M at incident proton energy E

$\mu_{\gamma}(E', M)$ = attenuation coefficient for gammas of energy E' in material M

X = total thickness of the absorber

6.2.4 Geometrical Considerations

By the solution of the radiation transport equations, the radiation flux behind a multilayer slab shield can be found. To relate the one-dimensional shielding problem considered by the transport equations to a realistic three-dimensional space vehicle, the angular distributions of the primary and secondary radiations must be considered. The incident proton flux is defined by an isotropic flux intensity J_0 . This is the number of protons per second that pass through a hypothetical sphere of 1 cm^2 cross-sectional area. The number that enters the sphere from a given solid angle, $\Delta\Omega$, is then

$$\Delta N = \frac{J_0}{4\pi} \Delta\Omega$$

It can be shown that the average path length of a particle striking the hypothetical sphere is such that if a monodirectional flux and an isotropic flux of the same intensity (particles/ cm^2) are incident on an absorber, the resulting doses are equal. If the incident particles travel essentially in straight lines through the absorber, the three-dimensional vehicle analysis can be reduced to a series of one-dimensional slab shielding problems.

When the generation of secondary radiation is considered, their angular distributions pose a complex problem. The basic difficulty is not only, as one might suppose, finding an adequate representation for the respective angular distributions as a function of particle energies, but also finding the angular distribution of the protons generating secondaries in the absorber. To accomplish this would require a three-dimensional treatment of the entire vehicle, a prohibitively lengthy analysis for any realistic space vehicle. To avoid this, the angular distribution of each radiation type will be analyzed and a simplified correction term will be selected.

The angular distribution of the secondary protons depends on the ratio of the emitted secondary to the incident primary proton. Collision kinematics require that secondaries of relatively high energy be emitted with a distribution highly peaked in the direction of the incident particle. As lower-energy particles are considered, the distribution gradually broadens to cover the entire forward hemisphere. Evaporation particles are emitted isotropically.

As only the high-energy particles have appreciable range, and as the low-energy particles deposit all their energy locally, assume that all secondary protons are transmitted in the forward direction — the straight-ahead approximation.

The angular distribution of the emitted neutrons is similar to that of the secondary protons. Because of the greater penetrating power of the neutrons, it would be incorrect to assume local absorption of the low-energy neutrons. A rigorous treatment of neutron transport would involve a complete consideration of the entire space vehicle. As this would involve a very time-consuming analysis, for the purposes of this program it will be assumed that all neutrons are transmitted in the direction of the incident proton. The gamma rays are also treated by the straight-ahead approximation. These approximations insure that the secondary dose calculation will give an upper limit in nearly all situations. For a strongly anisotropic incident flux, special configurations of shielding can invalidate this approximation and these situations should be treated with caution.

6.3 DOSE CALCULATIONS

6.3.1 Energy Deposition

When the spectra of incident protons and their induced radiations have been found at any point in the astronaut's body or equipment, the absorbed dose can be found. The unit of absorbed dose used is the rad, defined as 100 ergs of absorbed energy per gram of material. The crucial element in the definition is that the energy actually be absorbed in the material. To calculate the absorbed dose in an accurate manner, it is necessary to know not only the energy loss to the absorber through primary collisions of the incident radiation, but also the secondary and higher-order radiations created by the primary energy loss must be followed until their energy is low enough to ensure that their remaining energy will be deposited locally, or that they have left the area of interest. The general result of this requirement is that the absorbed dose at a particular point in an absorber depends not only on the primary radiation spectrum at that point, but also on the secondary radiations generated in the entire absorber that penetrate to the point of interest.

The incident proton flux deposits energy in an absorber by ionization of the absorber electrons. The energy lost per gm/cm^2 is given by the Bethe-Bloch equation and can be used to find the energy lost in the following ways

$$D(x) = \int_{E_1}^{E_{\max}} \phi_p(E, x) \frac{dE}{dx}(E) dE$$

Due to the mass difference between the incident proton and the electron, the maximum energy that can be imparted to an electron is only

$$Q_{\max} = \frac{2 m_o \beta^2 c^2}{(1 - \beta^2)}$$

These electrons have then a very limited range for the incident proton energies of interest (≤ 1000 Mev), and their total ionization energy loss is quite localized. The secondary protons may be treated in the same manner.

The neutrons generated by the incident protons present a more complex problem. As the neutron is not a charged particle, it deposits energy only by collisions with the absorber's nuclei. These collisions in turn result in a transfer of energy to the struck nucleus, either by absorption of the incident neutron, or by elastic or inelastic scattering. In any case, the initial energy of the neutron can be dissipated in a variety of ways, ranging from emission of a γ -ray, neutron, proton, or heavier particle by the excited nucleus to the ionization in the absorber resulting from the kinetic energy imparted to the nucleus in the collision. An exact calculation of the absorbed dose would follow these tertiary particles through their respective histories as energy depositors. As this would take a great deal of time, an approximate dose conversion factor developed by W. A. Gibson (Reference 96) is used which gives an upper-limit estimation of the absorbed dose.

For space vehicle shielding analysis, where thin shields and low secondary doses are the rule, this method provides sufficient accuracy. The dose at a point x is then expressed as follows:

$$D(x) = \int_{E_{\min}}^{E_{\max}} \phi_n(E, x) D_n(E) dE$$

where

$\phi_n(E, x)$ = neutron flux at point x in neutron/Mev cm^2

E_{\max} = maximum neutron energy considered

E_{\min} = minimum neutron energy considered

$D_n(E)$ = neutron flux to dose conversion factor in rads/neutron/cm²

$D(x)$ = dose in rads at point x

The gamma rays present a problem similar to, though less complex, than the neutrons. The primary absorption mechanisms of high-energy gammas, Compton scattering and pair production, result in energetic electrons and photons of degraded energies. The range of the electrons is small, and their energy can be considered as deposited locally. The secondary gammas, however, have mean absorption ranges that can be significant in comparison to the human body. Due to their relative lack of importance in comparison to the other radiations, a simple upper-limit dose conversion factor will be used. The expression for the gamma dose then has the same form as the other dose expressions,

$$D_\gamma(x) = \int_{E_{\min}}^{E_{\max}} \phi_\gamma(E, x) D_\gamma(E) dE$$

6.3.2 Linear Energy Transfer (LET) Spectrum

The response of a biological system to radiation has been shown to depend not only on the total energy deposited — the absorbed dose — but also on the rate at which the radiations deposit energy to the tissue they traverse, the LET, or dE/dx . A charged particle has, for any energy, a given dE/dx , available either from the Bethe-Bloch equation, or from experimental results. A monoenergetic beam of protons incident upon a tissue slab would have a particular energy and dE/dx at each point in the tissue, neglecting beam straggling. An incident spectrum of protons would, of course, produce a spectrum of dE/dx values at any point in the absorber.

From the previously discussed proton transport relations, the proton flux at a point x in the absorber can be obtained. From this a transformation of variables is made:

$$d\phi_p = \phi_p(E, x) dE = \bar{\phi}_p(y, x) dy$$

where

$$y = \frac{dE}{dx}$$

$$dy = d \frac{dE}{dx}$$

now

$$\Phi_p\left(\frac{dE}{dx}, x\right) = \phi_p(E, x) \frac{dE}{d\frac{dE}{dx}}$$

The relation between E and dE/dx is given by the Bethe-Bloch equation. An empirical expression can be used to fit the dE/dx versus E plot, thus permitting rapid evaluation of the derivative, and in addition, extending the range of valid LET spectrum determinations below the limits of the Bethe-Bloch equation. The secondary proton spectrum can be evaluated in the same way. One precaution must be observed. For the straightforward transformation from $\phi_p(E, x)$ to $\Phi_p(dE/dx, x)$ to be valid one must operate in a region where E is a single-valued function of dE/dx . For tissue, the region of 0.1 to 1000 Mev satisfies this requirement, and is also the region of primary interest in dose calculations.

Once the number LET expression $\Phi_p(dE/dx, x)$ has been obtained, it can be used to determine some quantities of interest. For example, the number of protons between any two values of dE/dx is given by

$$\Phi_p(x) = \int_{\frac{dE}{dx}_1}^{\frac{dE}{dx}_2} \Phi_p\left(\frac{dE}{dx}, x\right) d\left(\frac{dE}{dx}\right)$$

the energy deposited by protons having dE/dx values in the range from $(dE/dx)_1$ to $(dE/dx)_2$ is then

$$E = \int_{\frac{dE}{dx}_1}^{\frac{dE}{dx}_2} \Phi_p\left(\frac{dE}{dx}, x\right) \frac{dE}{dx} d\left(\frac{dE}{dx}\right)$$

In our calculations the following units are used: dE/dx is in $\text{Mev cm}^2 \text{ gm}^{-1}$, $\Phi_p(dE/dx, x)$ is in $(\text{protons/cm}^2)/(\text{Mev cm}^2 \text{ gm}^{-1})$ and E is in Mev. To convert from the density independent form dE/dx to the common radiobiological units of kev per micron, a density for tissue, or the absorber in question, must be assumed. One finds that the conversion factor K from $\text{Mev cm}^2/\text{gm}$ to kev/micron is

$$K = 0.1 \rho_T \frac{\text{kev/micron}}{\text{Mev cm}^2/\text{gm}}$$

where ρ_T is the density of tissue in gm/cm³, usually taken to be unity.

6.3.3 Semiconductor Damage

In addition to the effect of absorbed energy on the human body, semiconductor devices have also been found sensitive to radiation damage. The defects produced by an incident radiation are related to the operating parameters of various solid-state electronic components (Reference 97). As the defect density, defects per cm², is an energy-dependent function of the incident protons, it can be calculated in a manner similar to the absorbed dose:

$$DD(x) = \int_{E_{\min}}^{E_{\max}} \phi_p(E, x) D(E) dE$$

where

$\phi_p(E, x)$ = proton spectrum at point x in protons/(cm² Mev)

$D(E)$ = (dislocations/cm³) per(proton/cm²)

$DD(x)$ = defect density at x in defects/cm³

The function $D(E)$ has been deduced from a variety of experimental results on silicon, shown in Figure 44. Similar curves for germanium will be available when the experimental data presently available are reduced.

6.4 RESULTS

6.4.1 Program Descriptions

Two computer programs have been developed to evaluate the radiation transport equations and to perform the dose calculations described for incident protons. The computational techniques used to solve these equations and detailed operating instructions are given in Volume II of this report. One program, the proton primary-dose code, was developed for the evaluation of the absorbed dose resulting from the direct ionization energy loss of penetrating protons. The number LET and energy LET spectra, as well as the local dose, are also evaluated. The basic approximation made in this code is the neglect of proton inelastic collisions. It will be shown that this approximation is of adequate accuracy for the thin shields of present space vehicles and most incident proton fluxes. Only for the very soft spectra are the secondary radiations important for thin shields. The proton secondary code evaluates the contribution made by the secondary radiation to the total dose. The number LET spectra of the primary and secondary protons are also calculated. The proton primary code has the advantage

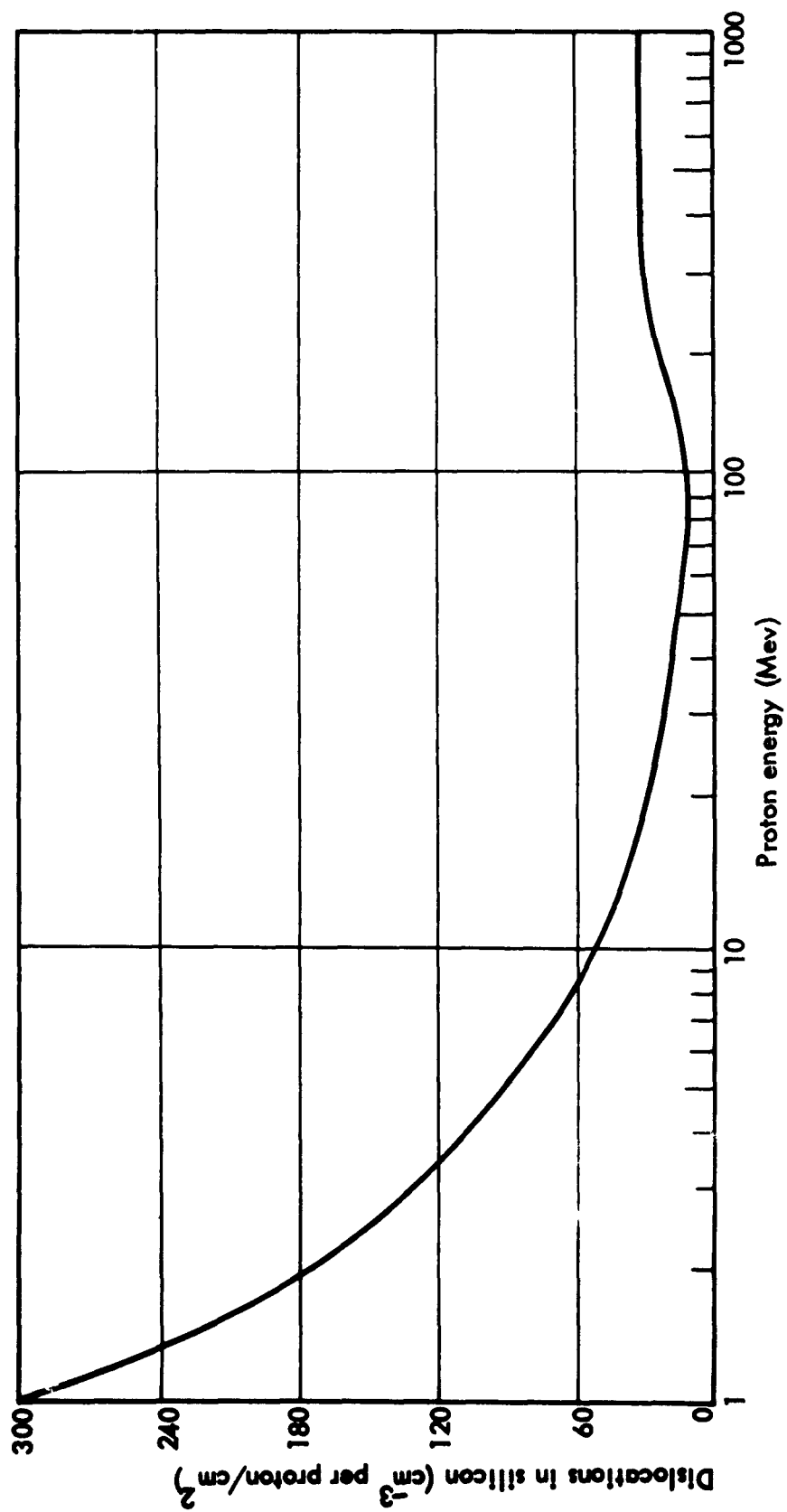


FIGURE 44. Density of dislocation formation in silicon due to monoenergetic protons

of great speed, allowing many combinations of shielding and incident proton spectra to be evaluated in a minimum time. The run time T in minutes per sector for each shielding combination or sector is approximately

$$T = 0.03 N \frac{M}{50}$$

where

N = number of layers of material in the sector

M = number of output energy points, usually 50

The more accurate proton secondary code has a run time of

$$T = 0.4 N \frac{M}{50}$$

6.4.2 Sample Calculations

To demonstrate the general features of the calculations, some representative results are given. First, in Figures 45 through 48 are shown curves of dose versus aluminum thickness for a trapped proton spectrum and three solar particle event spectra. The relative importance of the primary and secondary dose components is heavily dependent on the spectral form of the incident proton flux. The region of validity of the proton primary code is a function of the "hardness" of the incident proton spectrum. It can be seen that with the exception of the 40-Mv solar particle event spectrum, the proton primary code will give reasonable dose estimates for even very thick shields. The two outstanding features of these dose curves are the very rapid decrease in dose in the first few gm/cm^2 of absorber, and the gradual transition to a very slow attenuation with thickness region as the low-energy protons are removed and the more penetrating secondary radiations begin to be felt.

The number-LET spectra plotted in Figures 49 through 51 for representative solar particle events show that a few gm/cm^2 of shielding quickly harden the LET spectra. The energy-LET spectra given in Figure 52 show that even for the softest incident proton spectrum, a few gm/cm^2 of shielding shifts the peak energy deposition region to low LET values.

The differential energy spectrum of protons from a 100-Mv particle event passing through various thicknesses of aluminum are shown in Figure 53. The proton spectrum quickly assumes a constant spectral shape which gradually hardens as increasing thicknesses are reached.

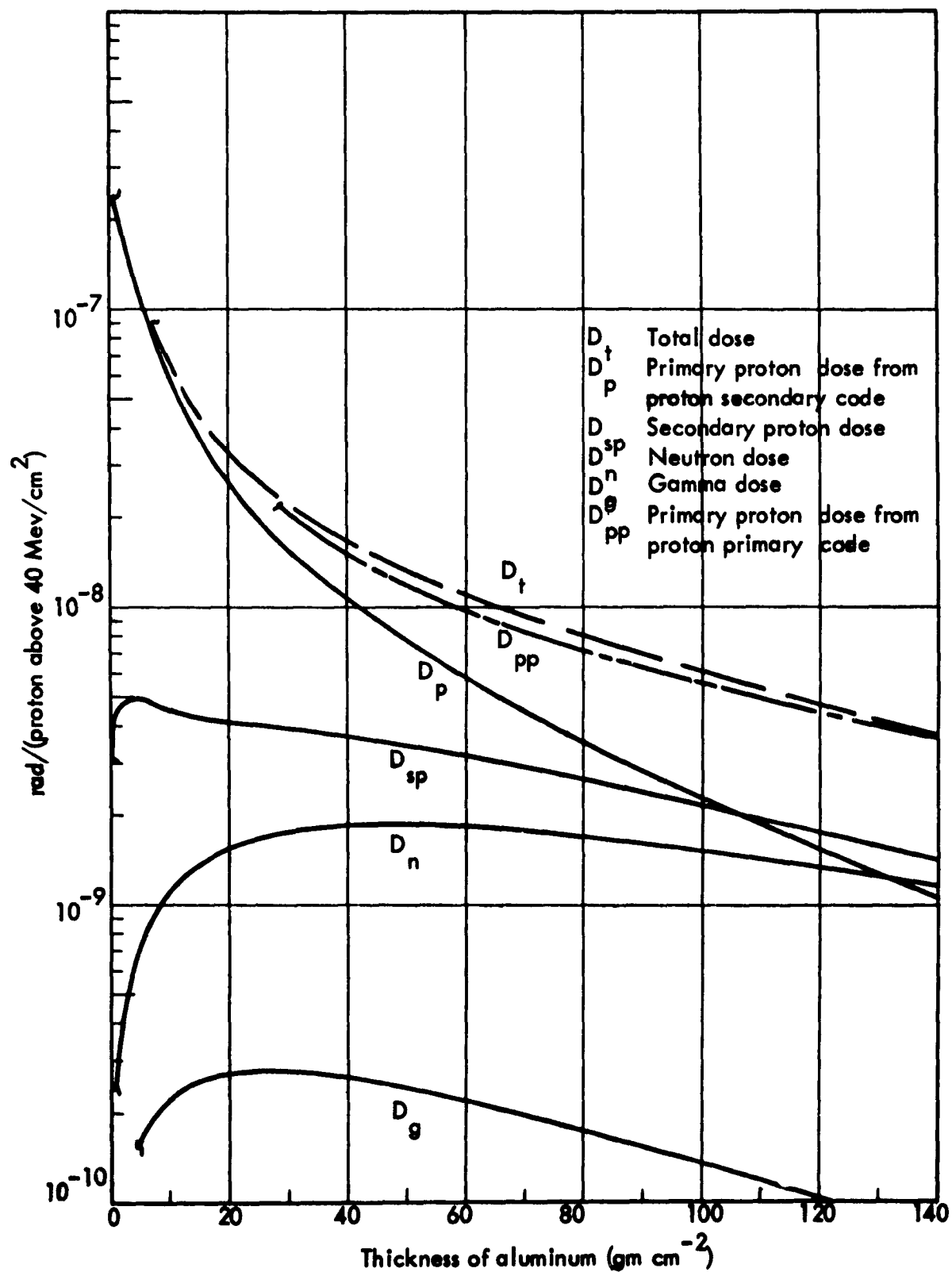


FIGURE 45. Freden-White spectrum — protons incident

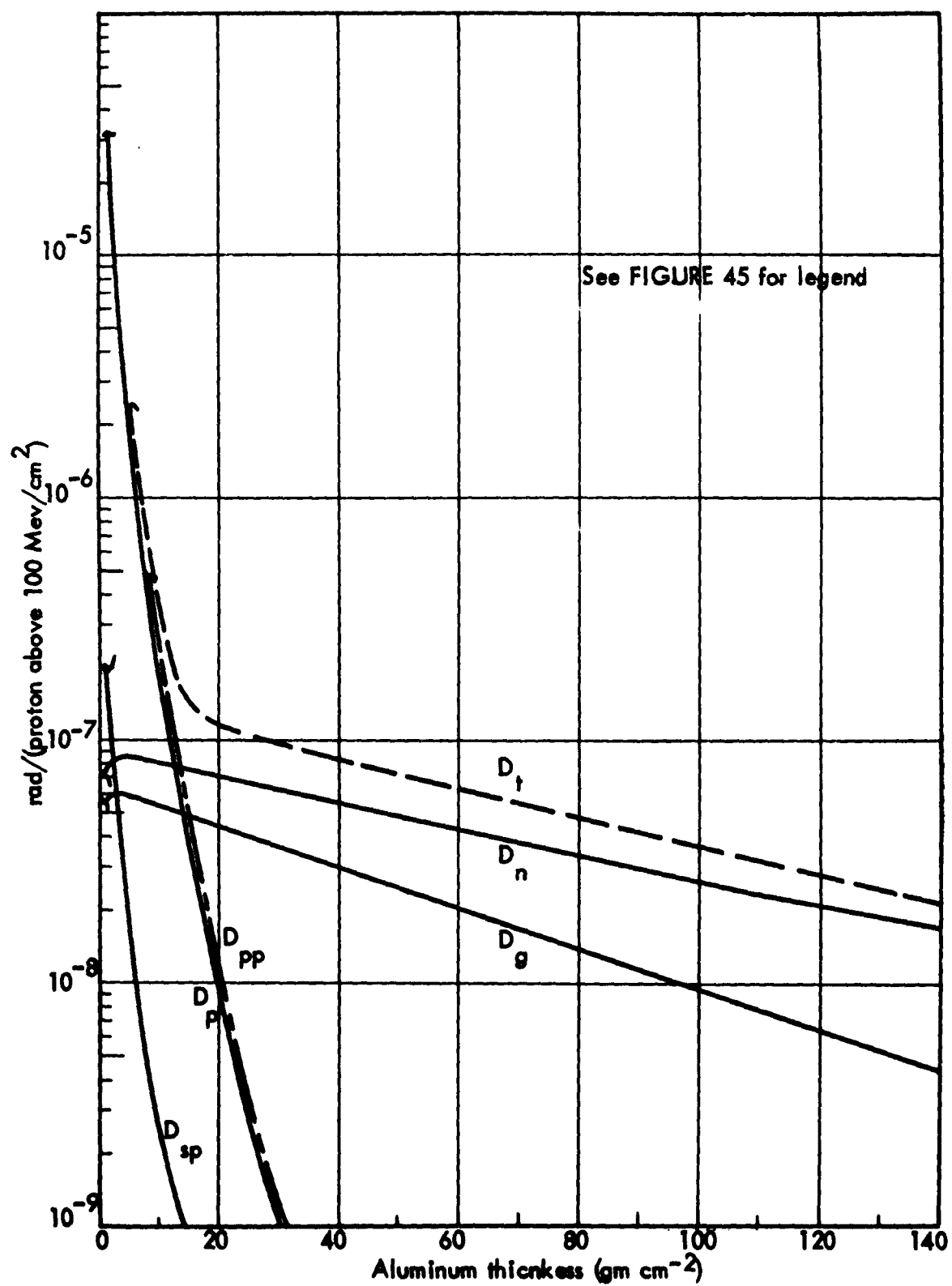


FIGURE 46. 40-Mv solar event spectrum — protons incident

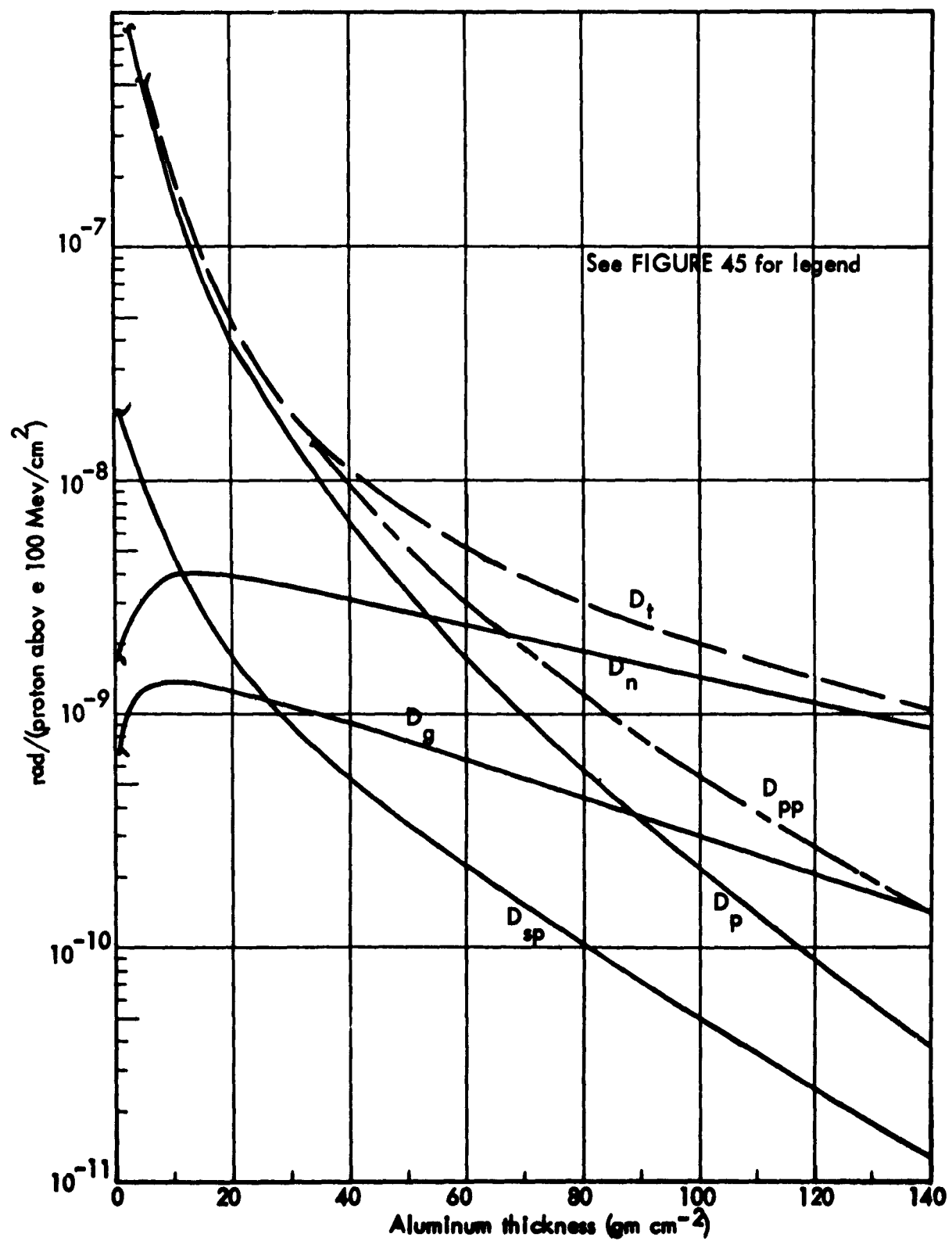


FIGURE 47. 100-Mv solar event spectrum — protons incident

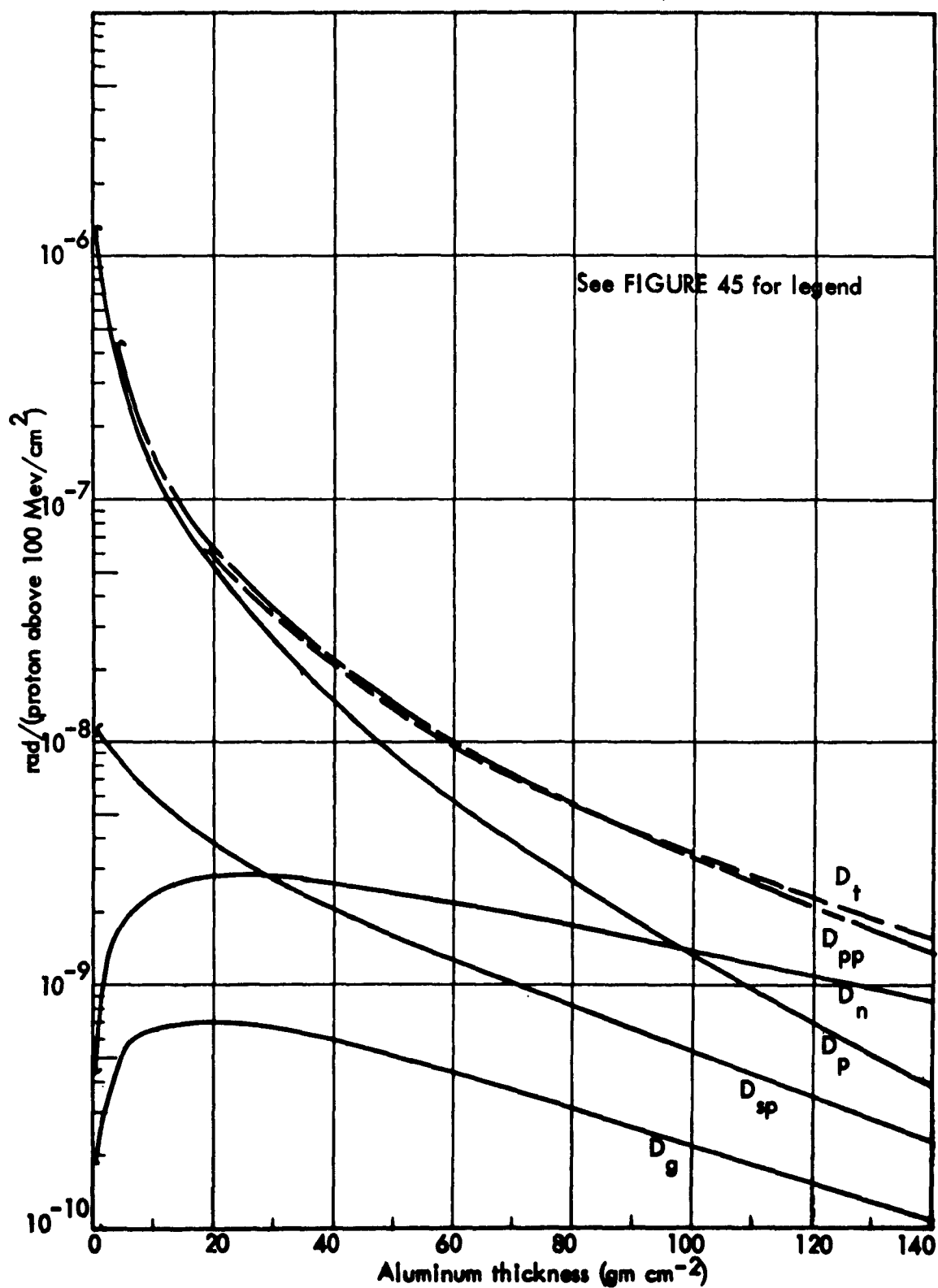


FIGURE 48. 160-Mv solar event spectrum — protons incident

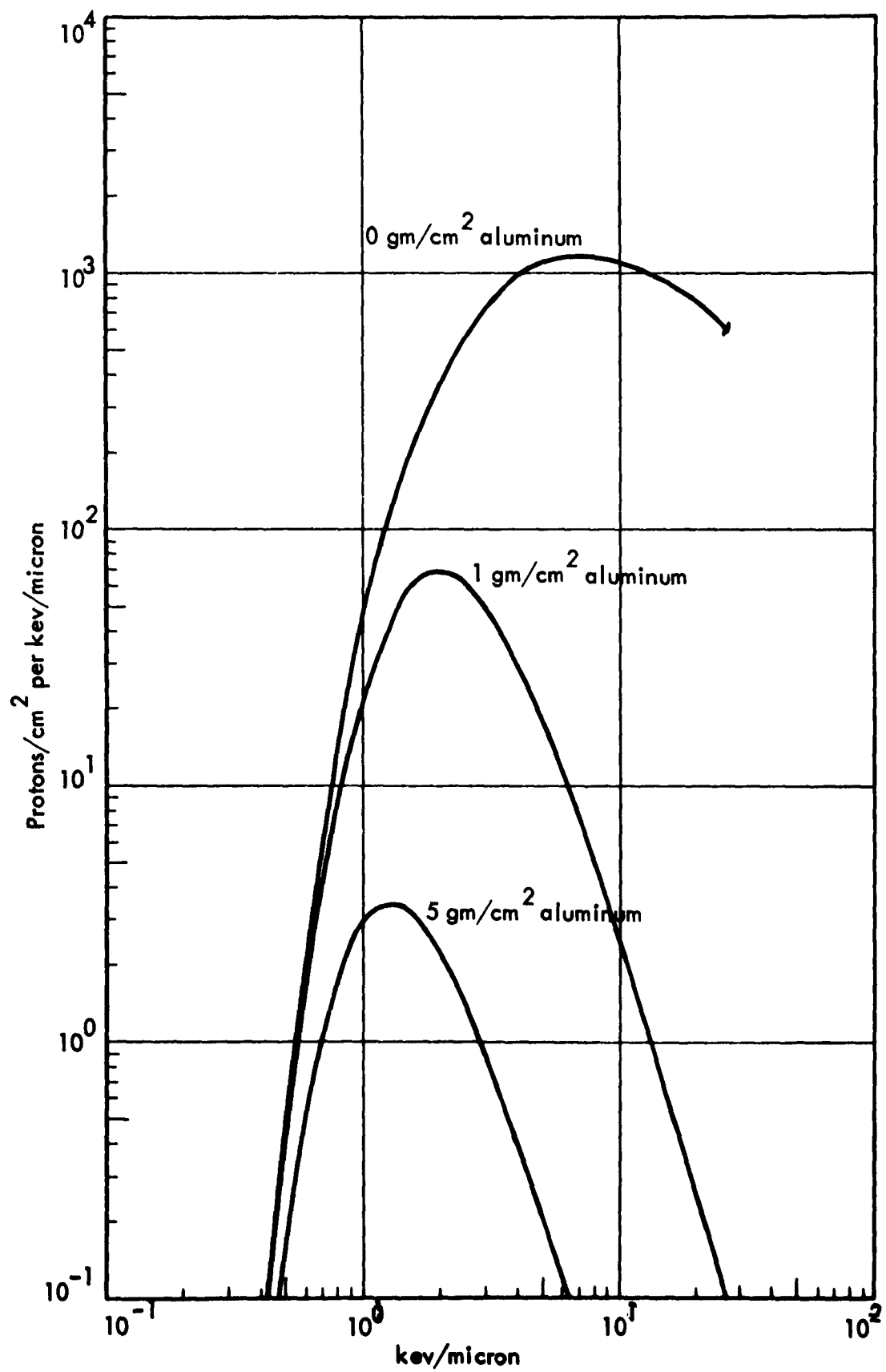


FIGURE 49. Number-LET spectrum for 40-Mv solar event

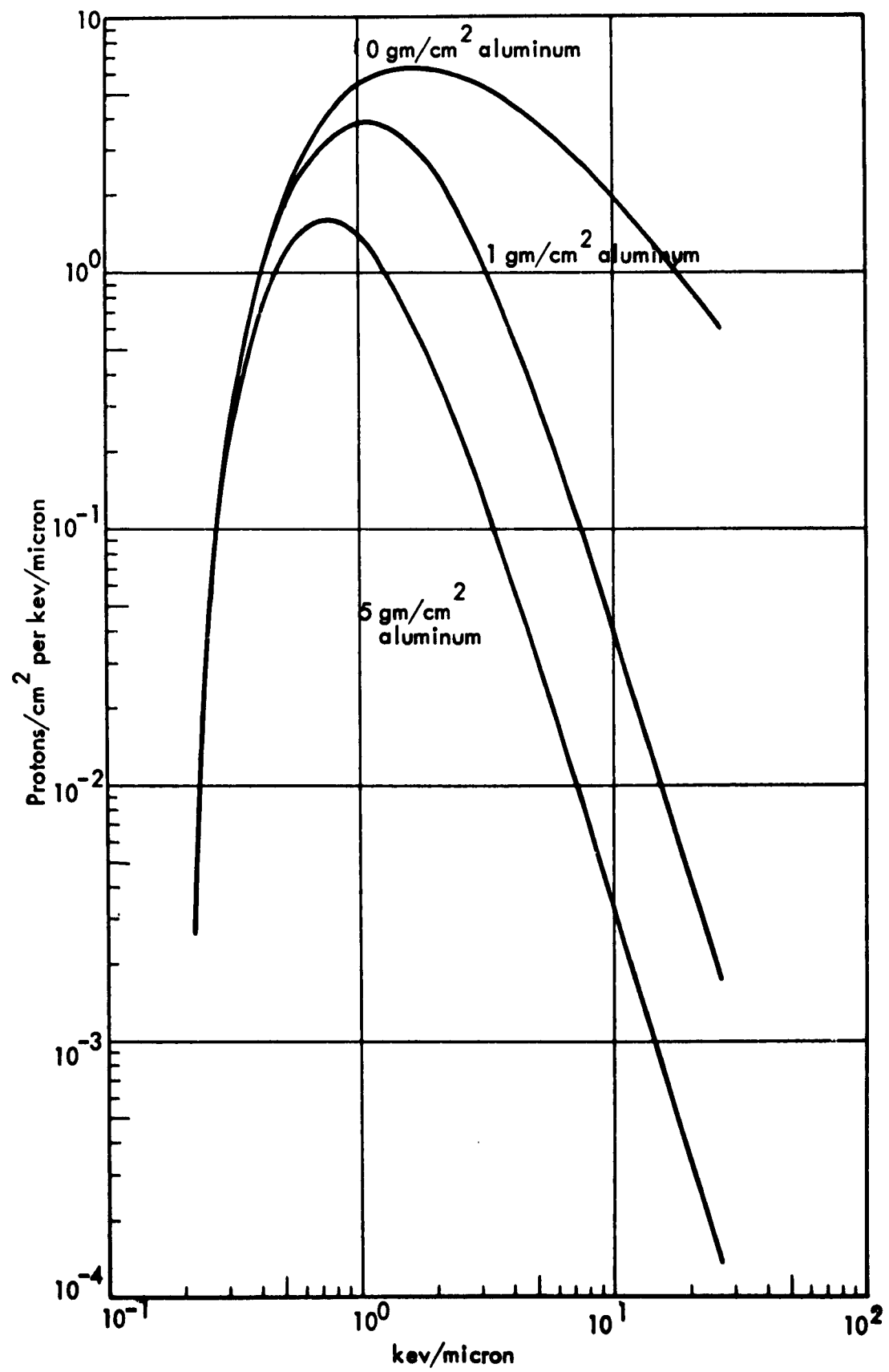


FIGURE 50. Number-LET spectrum for 100-Mv solar event

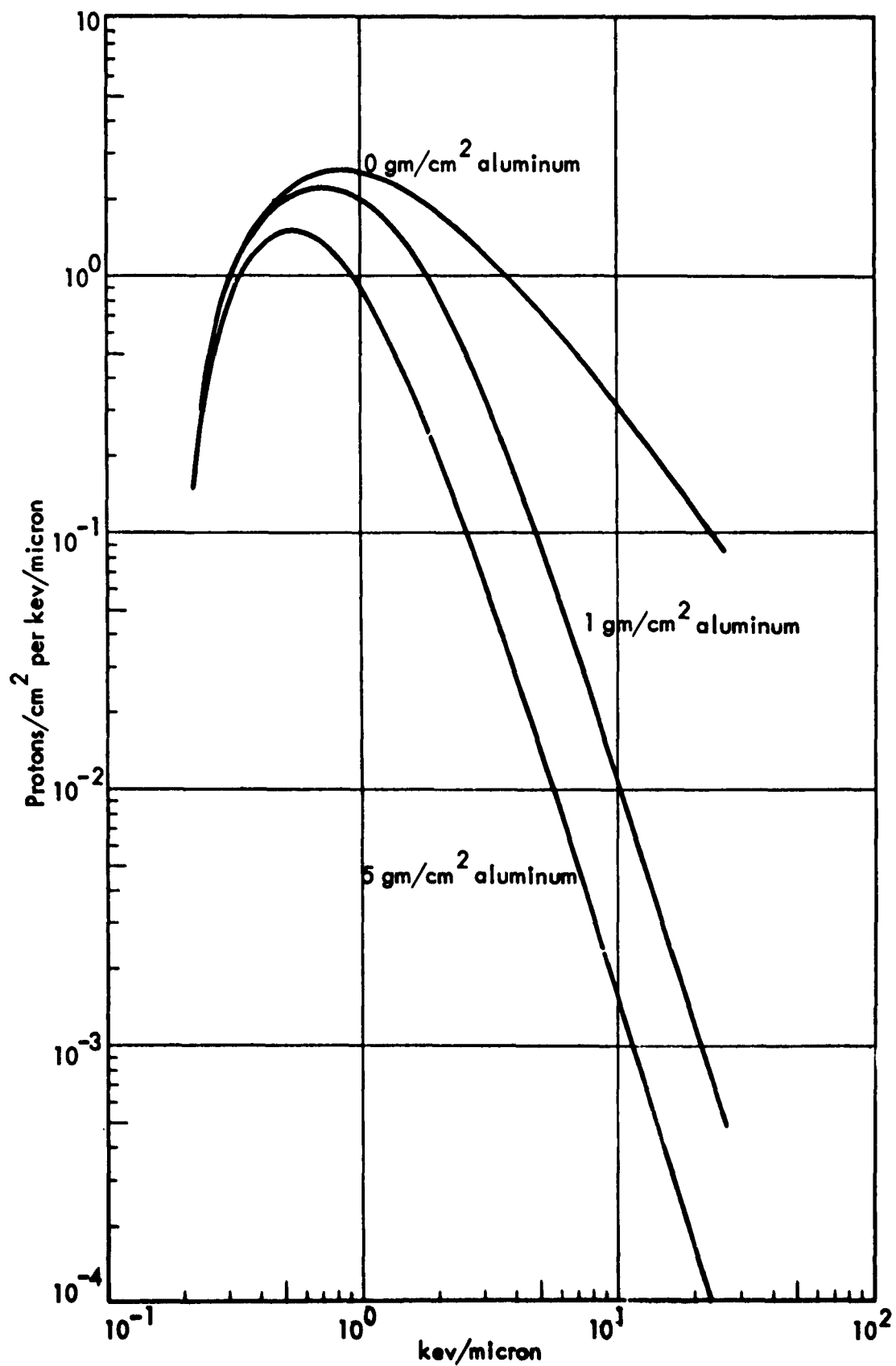


FIGURE 51. Number-LET spectrum for 160-Mv solar event

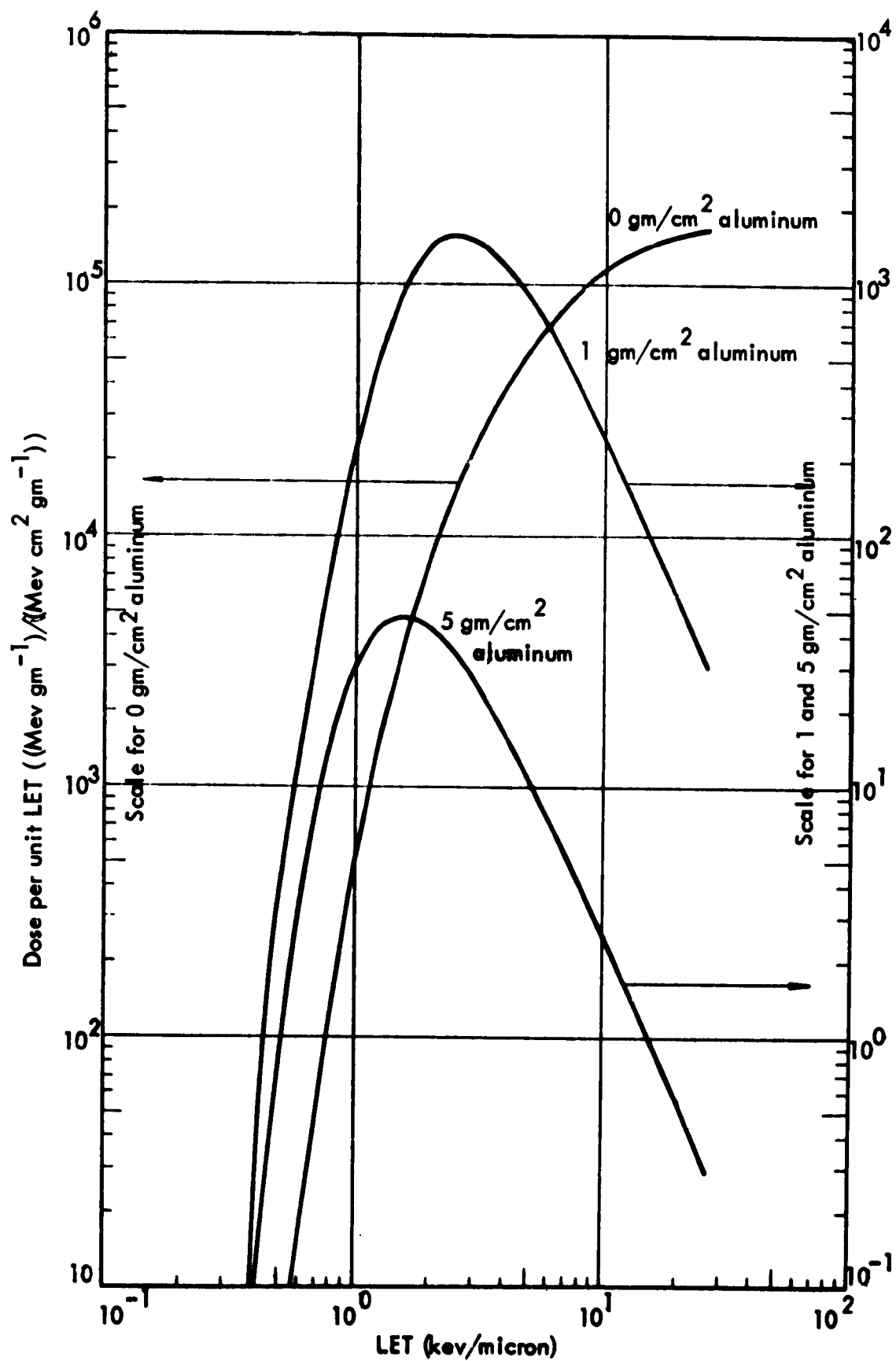


FIGURE 52. Energy-LET spectrum for 40-Mv solar event

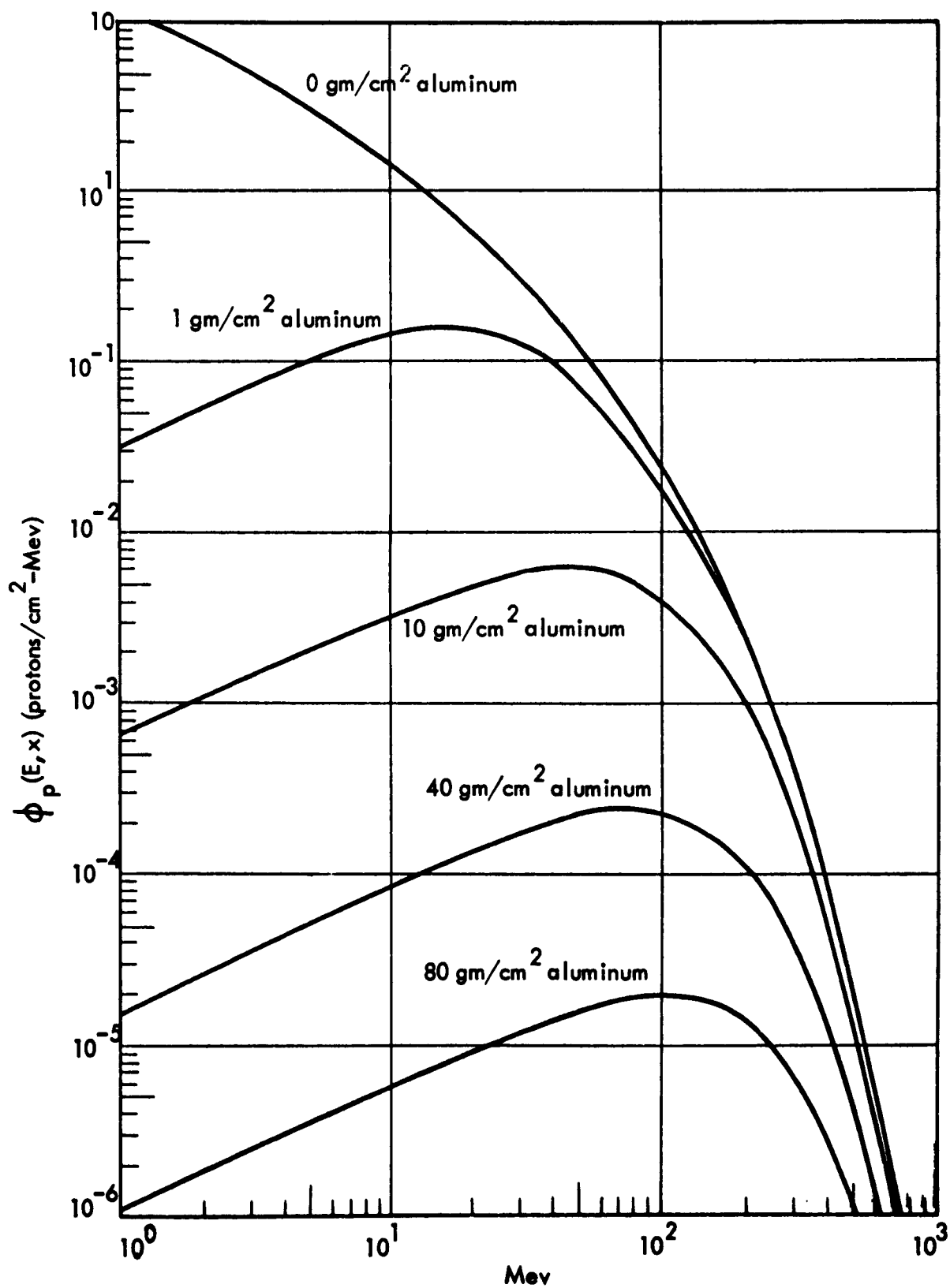


FIGURE 53. Differential energy spectrum for 100-Mv solar event

6.4.3 Comparison with Oak Ridge Calculations

In Figure 54, a comparison between the results of Alsmiller and Murphy (Reference 84) and the present proton secondary calculation is given. Although the calculations were made as comparable as possible, certain differences remain. The results of Alsmiller are given for particles of energy 32 Mev or greater, and the incident proton spectrum has a finite cutoff at 1000 Mev. In the present calculations, the lower energy limit is 30 Mev, and the incident spectrum is extended past 1000 Mev by extrapolation. The nuclear input data of Alsmiller was obtained from cosmic ray measurements, while our results were based on the data of Wallace and Sondhaus. Because of these differences in the calculations, it is felt that the results are in satisfactory agreement.

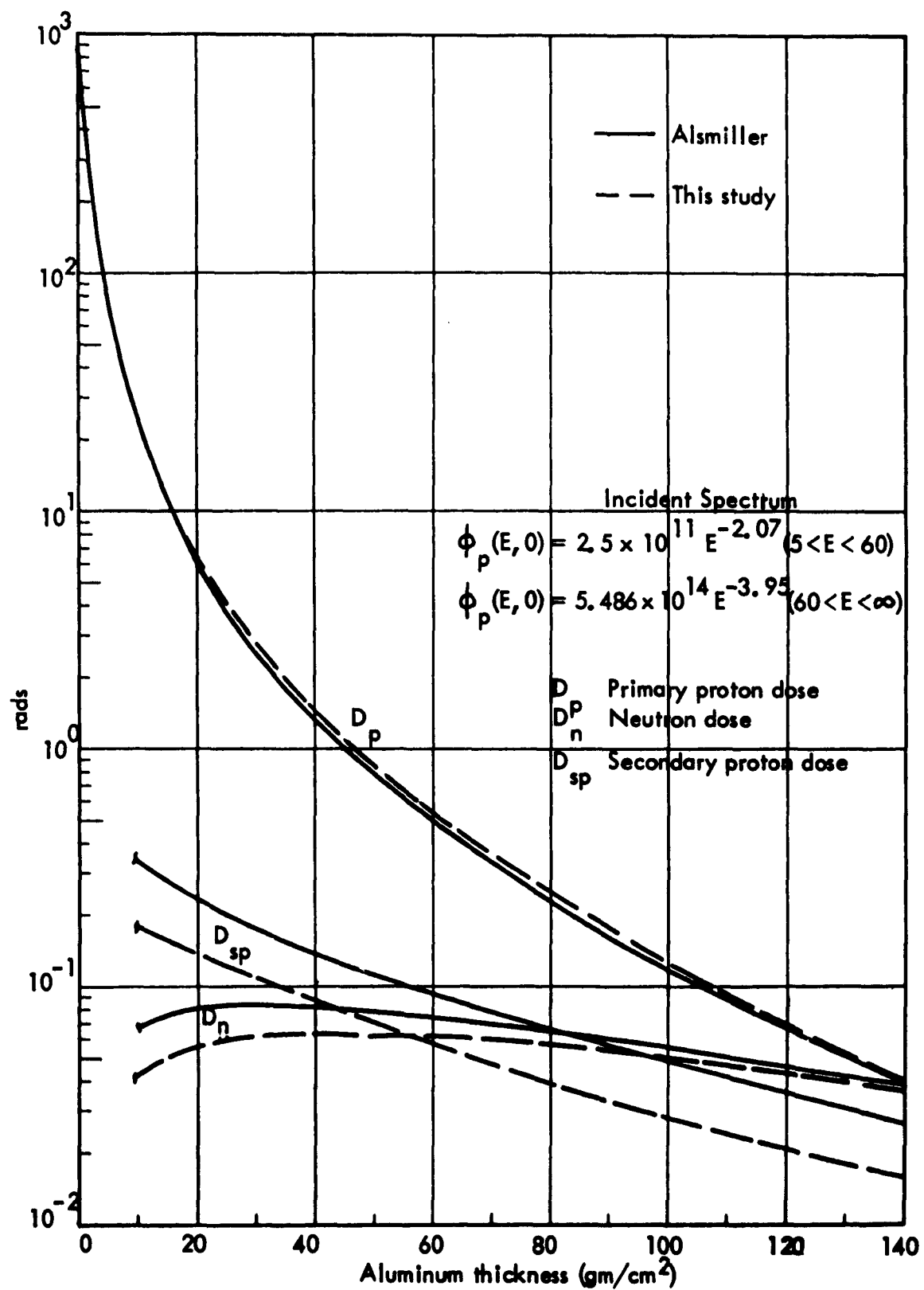


FIGURE 54. Comparison of the results of Alsmiller with this study

7.0 ANGULAR DISTRIBUTION OF INCIDENT RADIATION FLUXES AND THE EFFECT OF VEHICLE ORIENTATION

In previous space-radiation shielding analyses (References 42 and 98), the incident flux was assumed to be isotropic. This study was made to establish the perturbation on the isotropic flux results when the incident flux is nonisotropic. All cases studied assumed that the specified incident flux is symmetric about an axis \vec{B} and is dependent only upon the angle θ , measured about \vec{B} , and not the angle ψ , as shown in Figure 55.

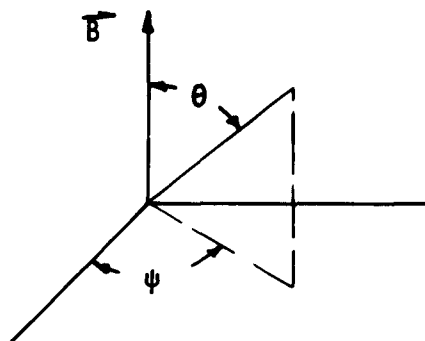


FIGURE 55. Definition of angles

Three types of particle deflections were studied: (1) transmission where an incident particle is degraded in energy but retains its original direction, (2) transmission where the incident particle is degraded and the distribution in final direction is described by $f(\theta)$, and (3) transmission of secondary particles of definite directional distribution.

In the first case, the vehicle was characterized by a fixed coordinate system as shown in Figure 56. The transmission where the initial direction was maintained after a collision was typical of proton penetration.

Three positions of \vec{B} , the axis of symmetry for the incident flux, were studied $(0, 0, 1)$, $(0.707, 0, 0.707)$, and $(1, 0, 0)$ (see Figure 57), and three differential angular distributions of the form

$$\begin{aligned} f(\theta) d\Omega &= A \sin(\theta - \theta_0) d\Omega && \text{for } \theta \geq \theta_0 \\ &= 0 && \text{for } \theta < \theta_0 \end{aligned}$$

where A is a normalization constant which allows the integral of $f(\theta)$ about 4π steradians to be equal to unity. Values of 30, 45, and 60 degrees were used for θ_0 .

The Boeing automatic sector analysis program (Reference 42) was used to generate the sector data for the test cylinder, using 146 sectors. Each sector was analyzed to find the slant thickness in the sector, the angle θ between the incident

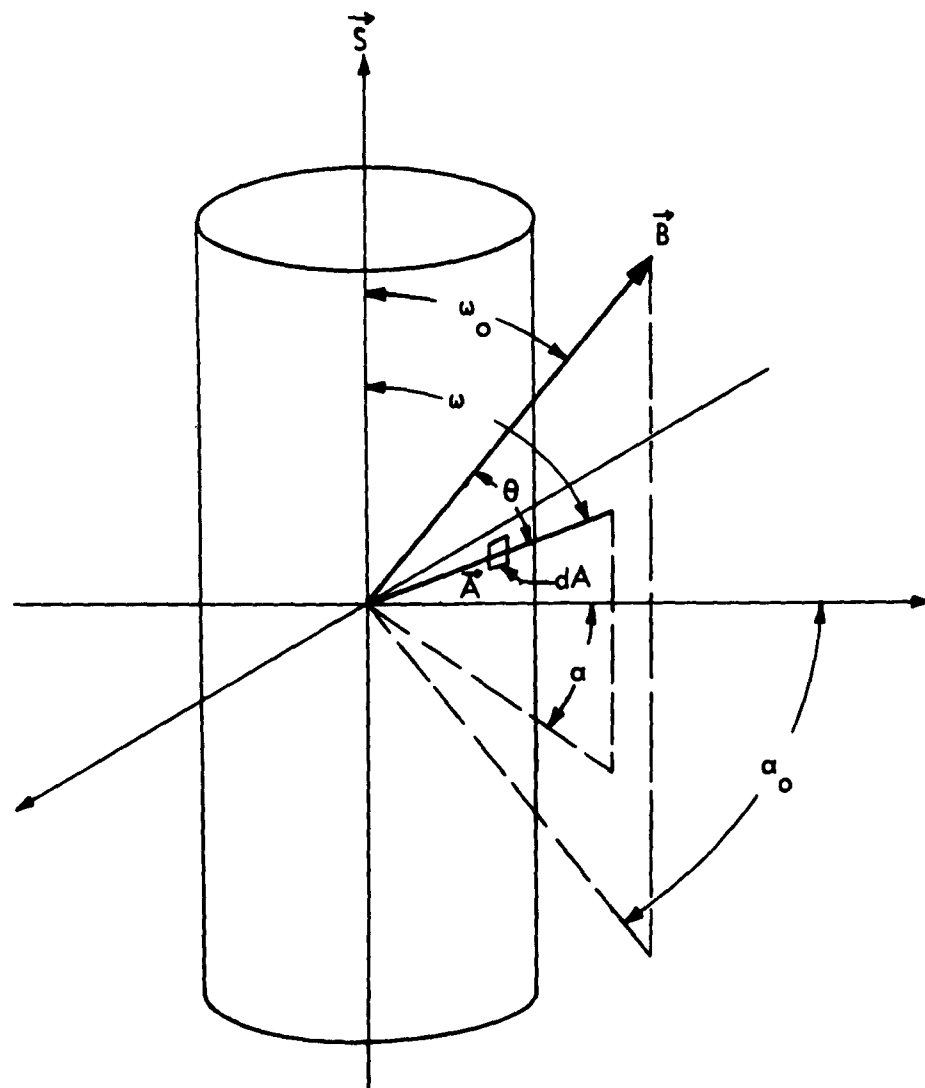


FIGURE 56. Coordinate system for angular distribution calculations

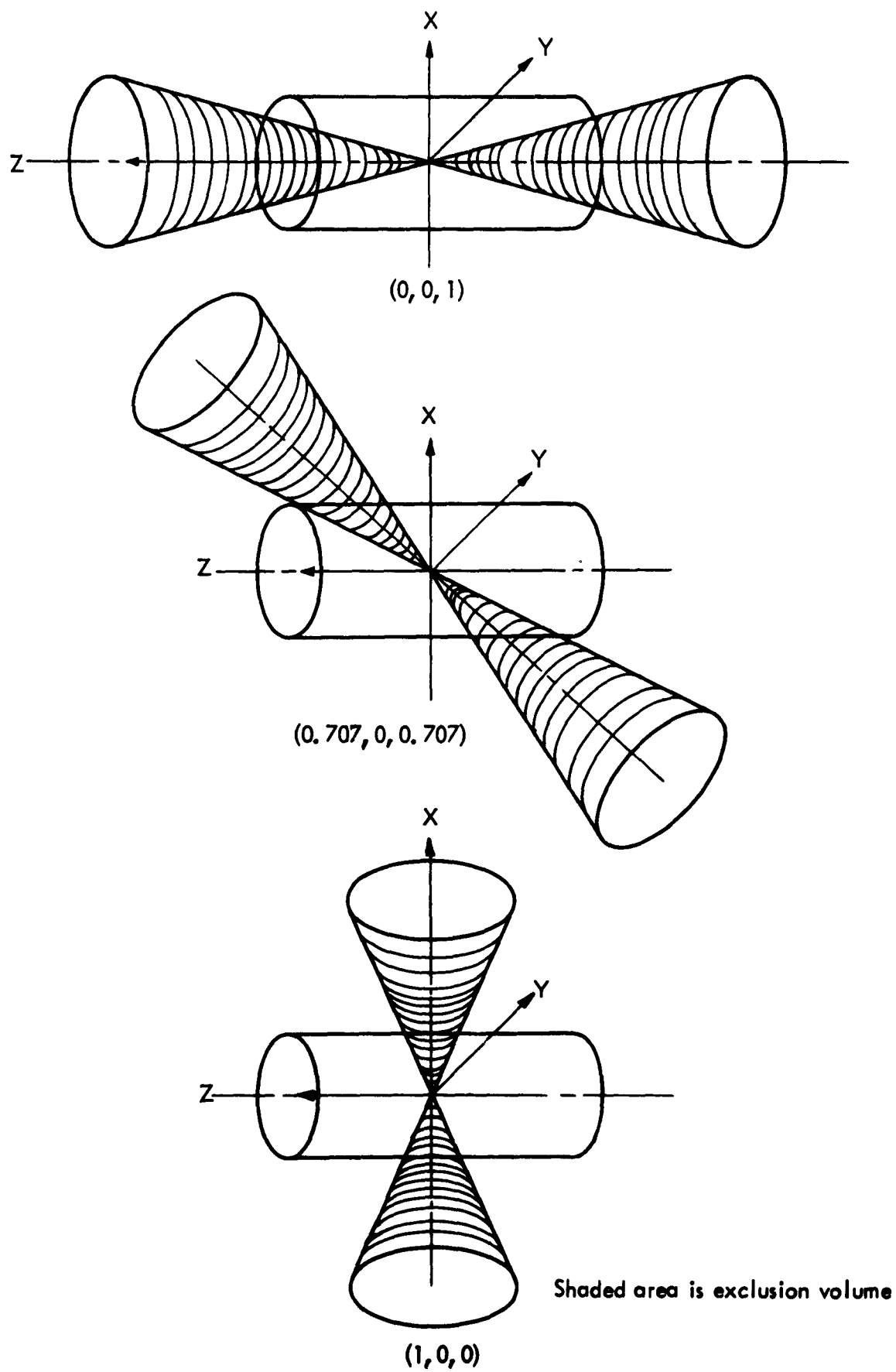


FIGURE 57. Geometry for example studied

particle path and \vec{B} , the angle $\xi_p = (\pi/2) - \omega$ between the normal to the sector \vec{N} and \vec{B} , and the angle γ between the incident particle path and the normal to the sector \vec{N} . The angles ξ_p and γ will be used for the electron and bremsstrahlung analysis and are further described in Figure 58. The receiver point for this study was defined as the center of the cylinder.

The sector data was used as input for the proton code and the total dose transmission factor was computed from the relation

$$D_p = \sum_{i=1}^I \omega_i f_i(\theta) T_i$$

where ω_i is the fractional solid angle subtended by sector i , $f_i(\theta)$ is the fraction of incident radiation entering sector i traveling towards the dose point, and T_i is the transmission of the incident flux through sector i . It is assumed in this analysis that the angular distribution of the incident radiation is independent of the incident energy spectra.

A cylinder is drawn to represent the vehicle, \vec{S} is the reference axis (in this case possibly the spin axis), and a point is located by angles ω measured from the \vec{S} and an azimuthal angle α . If the vehicle is oriented with respect to the axis of symmetry of the radiation flux so that ω and α define \vec{B} relative to \vec{S} , the number of particles $N(\vec{AO})$ incident on a surface element dA and penetrating to the origin of the coordinate system can be expressed as:

$$N(\vec{AO}) = N(\theta) T(A)$$

where

$$\cos \theta = \vec{A} \cdot \vec{B}$$

$N(\theta)$ is the number of particles $|\vec{A}| |\vec{B}|$ incident at angle θ on area dA and $T(A)$ is the transmission of proton through the shield thickness in area A .

The example used in this analysis was a simple orbiting laboratory in the shape of a right circular cylinder, 20 feet long and 130 inches in diameter. Eight wall thicknesses studied are shown in Table 12.

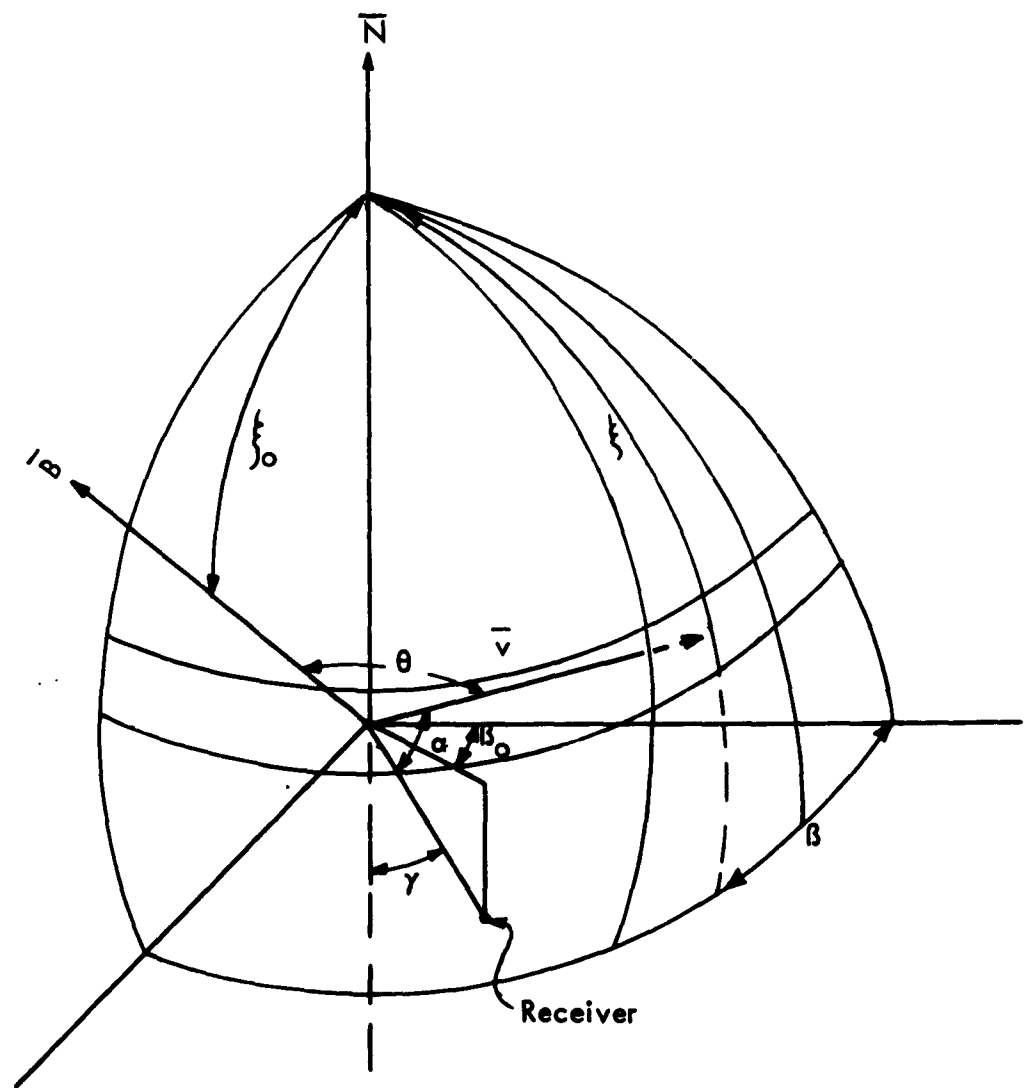


FIGURE 58. Geometry for case 2 and case 3 examples of nonisotropic angular distribution

Table 12
SHIELD CONFIGURATION FOR STUDY OF PROTON
ANGULAR DISTRIBUTION

Case	Side Thickness (gm/cm ²)	End Thickness (gm/cm ²)
1	1	1
2	2	2
3	5	5
4	0	1
5	0	2
6	1	2
7	1	5
8	2	5

The results of this study are shown in Table 13. The major effect of the non-isotropic distribution was the redistribution of the flux through sectors of greatest thickness resulting in a lower dose transmission factor. A sine distribution produces a dose transmission factor 20 percent lower than the isotropic flux, and the change in cutoff angle from 30 to 60 degrees had a very small effect. For the proton transmission, these results indicate that a nonisotropic flux distribution of the sine type will produce lower transmission factors and will provide a safety factor when isotropic flux distributions are used in the design of space radiation shields.

Case 2 considers the electron penetration which is assumed to diffuse through the shield. The number of electrons/cm² $N_i(\xi)$ crossing the surface of a sector is described as

$$N_i(\xi_0) = \phi_0 \int_{\beta=0}^{2\pi} \int_{\xi=0}^{\pi} F(\theta) \cos \xi \sin \xi \, d\xi \, d\beta$$

For an isotropic distribution, $F(\theta)$ becomes unity, and $N_i(\xi)$ becomes $\phi_0/4$ as derived by Evans (Reference 64), where ϕ_0 is the free-space flux.

The fraction of the free-space flux which crosses a surface can be computed by integrating the fraction entering per solid angle over the 2π solid angle above the surface. An analytical solution could not be obtained, so the automatic sector analysis was used to divide the 2π space into 50 sectors of equal solid angle. Using a given angle ξ_0 between the β axis and the normal to the surface, the angle θ between the incident path through a sector and β was computed. The fraction $N_i(\xi_0)$

Table 13

DOSE TRANSMISSION FACTOR FOR HESS PROTONS — RAD/CM²

Case	Side Thickness (gm/cm ²)	End Thickness (gm/cm ²)	\vec{B} Orientation	$\theta = 30^\circ$	$\theta = 45^\circ$	$\theta = 60^\circ$	Isotropic Flux
1	1	1	0, 0, 1	7.9×10^{-9}	7.8×10^{-9}	8.1×10^{-9}	
1	1	1	0.707, 0, 0.707	8.1×10^{-9}	8.1×10^{-9}	8.0×10^{-9}	
1	1	1	1, 0, 0	8.2×10^{-9}	8.1×10^{-9}	7.5×10^{-9}	
2	2	2	0, 0, 1	6.9×10^{-9}	6.8×10^{-9}	7.1×10^{-9}	9.6×10^{-9}
2	2	2	0.707, 0, 0.707	7.2×10^{-9}	7.1×10^{-9}	7.0×10^{-9}	
2	2	2	1, 0, 0	7.1×10^{-9}	7.0×10^{-9}	7.0×10^{-9}	
4	0	1	0, 0, 1	1.3×10^{-8}	1.2×10^{-8}	1.3×10^{-8}	8.3×10^{-9}
4	0	1	0.707, 0, 0.707	1.3×10^{-8}	1.3×10^{-8}	1.3×10^{-8}	
4	0	1	1, 0, 0	1.2×10^{-8}	1.1×10^{-8}	1.0×10^{-8}	
6	1	2	0, 0, 1	7.9×10^{-9}	7.8×10^{-9}	8.1×10^{-9}	1.5×10^{-8}
6	1	2	0.707, 0, 0.707	8.0×10^{-9}	8.0×10^{-9}	8.0×10^{-9}	
6	1	2	1, 0, 0	8.1×10^{-9}	7.8×10^{-9}	7.8×10^{-9}	9.5×10^{-9}

penetrating the surface can be expressed as

$$N_i(\xi_o) = \sum_{i=1}^{I=50} F(\theta_i) \Delta\Omega_i \cos \xi_i$$

where $F(\theta_i)$ is the fraction of the flux entering through solid angles $\Delta\Omega_i$. When the angle ξ_o is zero, the expression could be solved analytically. This case was used as a check on the numerical integration. The accuracy was better than 10 percent. Results of the analysis of $N_i(\xi_o)$ are shown in Table 14. Again the effect of a non-isotropic flux was to reduce the number of particles transmitted, since in the dose expression

$$D_e = \sum_{i=1}^I T_i \phi_i N_i(\xi_o) F_i(\gamma)$$

$N_i(\xi_o)$ will be less than the isotropic case and all other factors are unaffected by the angular distribution. T_i is the transmission through sector i , ϕ_i the incident free-space flux, and $F_i(\gamma)$ the fraction of penetrating particles which will be intercepted by the receiver.

The transmission programs contain at least two dummy variables to describe the angular behavior. In the case of protons, the function $f_i(\theta)$ to describe the fraction of incident flux incident on sector i is present. For bremsstrahlung, in addition to $N_i(\xi_o)$ and $F_i(\gamma)$, expressions describing the thick-slab angular distribution as a function of incident and exit angle can be employed. At the time of this writing, there are insufficient data to employ these improvements; however, these methods can be used to evaluate hypothetical situations.

In Case 3, where the direction of the secondary is related to the direction of the incoming particles, the problem is a combination of Case 1 and Case 2. For bremsstrahlung production, each sector should be analyzed to determine the fraction of bremsstrahlung produced which will be directed towards the receiver. The fraction of photons $FB_i(\gamma)$ is expressed as (see Figure 58)

$$FB_i(\gamma) = \int_A G_1(a) G_2(\theta) \sin \xi \, d\xi \, d\beta$$

where $G_1(a)$ is the probability to scatter toward the receiver, and $G_2(\theta)$ is the probability to be incident at an angle θ with β , the axis of symmetry. The dose D_B

Table 14

FRACTION OF FREE SPACE FLUX CROSSING A UNIT SURFACE

Angle Between Normal and Axis of Symmetry (degrees)	Cutoff Angle for Sine Distribution (degrees)	Fraction of Free Space Flux Crossing Unit Surface
0	0	0.21
0	30	0.13
30	30	0.23
45	30	0.20
60	30	0.17
90	30	0.13
0	45	0.13
30	45	0.27
45	45	0.23
60	45	0.18
90	45	0.13
0	60	0.048
30	60	0.14
60	60	0.08
90	60	0.048
Isotropic Flux		0.25

will be,

$$D_B = \sum_{i=1}^I \phi_{ei} N(\xi_o) T_i FB_i(\gamma)$$

where

ϕ_{ei} = incident electron flux

$N_i(\xi_o)$ = fraction of the flux crossing the surface

T_i = dose transmission factor

$FB_i(\gamma)$ = fraction directed toward the receiver

Provision has been made to incorporate $G_1(\alpha)$ and $FB_i(\gamma)$ in the calculation of T_i (see Volume II). No sample calculations were made in this case since $G_1(\alpha)$ could not be evaluated.

The problem of scatter in a vehicle was briefly examined; however, this problem was not serious enough in conventional spacecraft to warrant additional code development. It is suggested that for protons, no correction be made since all scattering is predominantly forward. For electrons, the backscattering increases with atomic number and with electron energy. Fortunately, the electrons are usually almost totally absorbed in the vehicle structure (i. e., 2 gm/cm²) and the penetrating particles are degraded to an extent where the backscattered fraction is a negligible quantity. If a very thin structure is encountered, it is recommended that the backscatter correction factor be expressed as

$$B = \sum_{i=1}^J Ra^i$$

where B is the enhancement of the penetrating flux by backscattering, R is the backscatter coefficient, and a the average fraction of the interior surface which can be viewed from a point on the interior surface. For a complicated vehicle, the interior may be divided into several areas, such as the crew member, the visible walls, and the subsystems. For low-Z materials, such as man and aluminum structure, the reflection coefficient will be 0.15, and a typical a is about 0.5, which would yield a B of less than 10 percent.

In conclusion, the nonisotropic flux distribution appears to be less penetrating than an isotropic flux for a uniform shield thickness. When only a small area is

thinly shielded, a nonisotropic flux could create a higher penetrating dose than an isotropic distribution. Each shielding code contains parameters to describe the non-isotropic flux, but in some instances experimental data are required to establish the relationship.

8.0 PROGRAM INTEGRATION AND UTILIZATION

The program has been designed so that the various codes can be utilized independently. This has advantages when studying the variations in the environment when no specific vehicle is given, or when studying the effects of varying shielding configurations that are independent of the detailed variations of the environment or of mission trajectories. The use of these codes in this manner naturally requires the analyst to exercise judgment. This is an essential element in increasing the flexibility of the program.

Once a particular vehicle has been chosen, it is useful to automate the whole trajectory dose-rate study. The sectoring code and environmental codes provide the necessary inputs for the shielding code. The shielding code generates the dose delivered to each body point per unit flux of each spectral type and particle. All dose rates are in rads/hr from one particle $\text{cm}^{-2} \text{sec}^{-1}$. This dose conversion factor labeled $k_i(j)$ for the i^{th} spectral type and the j^{th} body point for each particle type are submitted as input to the trajectory code. The trajectory code then automatically calculates the flux of each spectral type, converts to dose rate and integrates the flux and dose rate along each of a family of specified trajectories. A description of how this is accomplished, using a variable step integration routine, follows.

The environment has been placed on B-L grids in such a way that through logarithmic interpolation of the flux, and linear interpolation in the C table, the differential energy flux is obtained in the form:

$$f(B, L, E) = F(B, L) \sum_{i=1}^8 C_i(B, L) f_i(E)$$

The trajectory code gives the trajectory at any required number of points t_n , principally as $B_n(t_n)$, $L_n(t_n)$. The flux at t_n is $F(B_n, L_n)$; the differential flux at t_n is given by:

$$f(B_n, L_n, E) = F(B_n, L_n) \sum_{i=1}^8 C_i(B_n, L_n) f_i(E)$$

The shielding code will predict a per-unit-particle dose conversion, designated by $k_i(j)$, at the j^{th} body point due to the i^{th} basic spectrum. Then the dose rate to the j^{th} point at time t_n is given by

$$d_i(t_n) = F(B_n, L_n) \sum_{i=1}^8 C_i(B_n, L_n) k_i(i)$$

The cumulative flux to t_n encountered in the mission is given by the integral

$$F(t_n) = \int_0^{t_n} F[B(t), L(t)] dt$$

The dose encountered by the i^{th} point up to t_n is given by the integral

$$\begin{aligned} D_i(t_n) &= \int_0^{t_n} d_i(t) \\ &= \int_0^{t_n} F[B(t), L(t)] \sum_i C_i[B(t), L(t)] k_i(i) dt \\ &= \sum_i k_i(i) \int_0^{t_n} F[B(t), L(t)] C_i[B(t), L(t)] dt \end{aligned}$$

The contribution to the dose integral in a small interval of time is given by

$$\Delta D_i(t_n) = \sum_{i=1}^8 k_i(i) \int_{t_{n-1}}^{t_n} F[B(t), L(t)] C_i[B(t), L(t)] dt$$

Since the coefficient C_i is slowly varying in the interval we replace it by its mean value:

$$\bar{C}_i(t_n) = \frac{C_i(B_n, L_n) + C_i(B_{n-1}, L_{n-1})}{2}$$

but normalized to a unit sum;

$$\sum_{i=1}^8 \bar{C}_i(t_n) = 1$$

Then ΔD takes the form:

$$\begin{aligned}\Delta D_i(t_n) &\simeq \sum_{i=1}^8 k_i(i) \bar{C}_i(t_n) \int_{t_{n-1}}^{t_n} F[B(t), L(t)] dt \\ &= \sum_{i=1}^8 k_i(i) \bar{C}_i(t_n) \Delta F(t_n)\end{aligned}$$

which involves the integral $\Delta F(t)$, already evaluated in the cumulative flux integral. Effectively an average differential flux has been defined for the interval as:

$$\bar{f}(t_n, E) = \frac{\Delta F(t_n)}{t_n - t_{n-1}} \sum_i \bar{C}_i(t_n) f_i(E)$$

With this assumption the integrals all reduce to an integral of the flux. Since this flux $F(B, L)$ is a very strong function of B and L in some regions of space and is either zero or a slow function of B and L in the remainder, a uniform time step is not justified. Therefore we adopt a variable step integration routine wherein the step is controlled by the integrand — the flux.

Computation time will generally increase when a variable-step routine is employed. To guard against an unnecessary increase in run time due to poor definition of the flux map at its edges or excessive use of the C-3 Code, the operator must be provided with controls. A minimum time step will eliminate unnecessary interval cut-backs in the edges of the belt where the flux is low but rapidly varying with position. An error criterion for the integral will allow the optimum time step to be chosen by the routine. When the step is such that the error is less than five times the error criterion, an 8-fold interpolation in B and L will generally give an acceptable error. Utilizing the interpolation routine in this manner avoids excessive use of McIlwain's code. If the step increases too much, it is possible to miss a significant flux at low altitudes in the anomaly. Controlling the time step with a maximum allowable time step will guard against this possibility. It is recommended that a maximum time step of 480 sec be employed. Also, the variable-step routine can be eliminated by equating the minimum time interval to the maximum time interval. Such a run could then be employed to study the effectiveness of the variable-step routine.

The following are stored on magnetic tape in a format suitable for automatic plotting:

- 1) trajectory parameters (t, B, L, R, λ)
- 2) flux of each spectral type in particle $\text{cm}^{-2} \text{sec}^{-1}$
- 3) accumulated flux of each spectral type in particle cm^{-2}
- 4) total flux in particle $\text{cm}^{-2} \text{sec}^{-1}$
- 5) accumulated flux in particle cm^{-2}

This tape provides the basic information needed by the environment plotting code which instructs a plotter to automatically display the desired information, such as the time dependence of the dose rate.

9.0 CONCLUSIONS AND RECOMMENDATIONS

9.1 CONCLUSIONS

It is felt that the objectives of this study have been achieved and that a second-generation computer program has been developed commensurate with the experimental data and theory. The program has growth capability in directions presently indicated by experimental and theoretical studies and flexibility in its application to conceptual and detailed design of space systems.

9.1.1 Spacecraft Trajectories

Two methods have been developed to treat the spacecraft trajectories. One method called approximate trajectories computes the parameters r , ϕ , θ , t from the input information: apogee, altitude, geographic location of initial perigee, and the angle of inclination. A second method will accept point-by-point position of the spacecraft from other programs. A code has been incorporated to convert the position in geographic coordinates to magnetic coordinates. Computer machine-time-saving techniques have been included to achieve a compromise between program accuracy, uncertainties in environmental data, and program cost.

9.1.2 Radiation Environment

The radiation environment has been arbitrarily divided into trapped and untrapped radiation and the mathematical representation of these radiation environments has been developed. This treatment includes energy, angular, and time-dependent relationships for each radiation type. It is believed that these mathematical representations will handle any new experimental environmental data.

9.1.3 Vehicle Analysis

The analysis of the effective shielding of the spacecraft is accomplished by the techniques called "sector analysis." In this technique the dose point is the origin of a spherical coordinate system and the slant thicknesses of different materials for each solid angle sector is determined. The self-shielding of the human body is included to determine the dose, dose rate, and LET spectrum of various points in an astronaut.

9.1.4 Electron Shielding

A machine program has been successfully developed to compute the LET and dose from penetrating electrons inside a space vehicle. The program is based on an empirical relationship derived from Monte Carlo data. These results have been compared with experimental and theoretical results of other investigators. The accuracy of the empirical fit is within 15 percent for normal incidence, but errors as great as a factor of two can occur for isotropic incidence when the shield thickness is close to the range.

The bremsstrahlung code has been modified to describe volume-distributed bremsstrahlung and multilayered shields. The significant result is that the attenuation is not changed, but the production in each layer is proportional to the atomic number of the shield.

9.1.5 Proton Shielding

Two computer programs have been developed to give a rapid and accurate evaluation of the absorbed dose resulting from the proton fluxes in space. The primary proton program can be used for evaluating the radiation shielding offered by the majority of present and planned space vehicles. The secondary radiations are of importance only for fluxes of very soft protons or for vehicles with minimum shield thicknesses greater than about 30 gram/cm² of aluminum. As thicknesses greater than 60 gram/cm² are considered, the neutron dose becomes more important than the incident proton dose. The secondary proton code provides an upper limit for the neutron dose contribution. If a more accurate evaluation of the neutron dose becomes necessary, the source terms of the secondary proton code can provide a starting point for a more complete analysis.

9.1.6 Effect of Angular Distribution of Incident Radiation

A study was made to indicate the difference in the internal flux if the incident flux was nonisotropic. All cases studied assumed that the specified incident flux was symmetric about an axis. Three types of particle deflections were studied: (1) transmission where an incident particle is degraded in energy but retains its original direction, (2) transmission where the incident particle is degraded and the distribution in final direction is given by $f(\theta)$, and (3) transmission of secondary particles with a definite directional distribution.

It is concluded that the nonisotropic flux distribution appears to be less penetrating than an isotropic flux for a uniform cylindrical shield. When only a small area of the cylinder is thinly shielded, a nonisotropic flux could create a higher dose than an isotropic distribution. Each shielding code contains parameters to describe the nonisotropic flux, but in some instances experimental data are required to establish the relationship.

9.2 RECOMMENDATIONS

Considerable effort has been made to devise a second-generation computer program with maximum growth capability and with maximum flexibility; nevertheless, there are inevitable shortcomings because of study program limitations, of the rapid pace of space research, and of continued research in particle interactions. The following specific areas of investigation are recommended to keep this computer program current:

- 1) The time dependence of natural and artificially injected geomagnetically trapped radiation;
- 2) The acceptance cone method of determining the magnetic shielding of solar particle radiation;
- 3) Automatic sectoring of vehicle and man;
- 4) Extension of computer programs to include primary, secondary, and LET spectrum for alpha and heavier-Z particles;
- 5) Experimental verification of particle interaction theory, multislabs approximations, and sectoring approximations;
- 6) The updating of flux and spectrum maps as more current information becomes available; and
- 7) Secondary and tertiary components of the LET spectrum.

APPENDIX

SURVEY OF MULTIPLE-SCATTERING THEORIES

I. INTRODUCTION

The difficulties inherent in the problem of multiple scattering of fast charged particles have given rise to a diversity of theories and techniques, both analytical and numerical. Most of these techniques involve some form of approximation and are usually limited in their domain of application. Some of the theories predict only the transmission factor or the angular distribution, while others may include both, but neglect various correction factors. Many "exact" theories often cannot be reduced to a form convenient for numerical evaluation or require so much computation that they are unsuited for practical application. In view of these difficulties, the more useful multiple-scattering theories will be briefly reviewed here in order to present the relative merits of each in terms of correlations with available experimental results and the ease with which computations may be performed.

II. ANALYTICAL METHODS

The various analytic formulations of multiple scattering are based either on the random flight concept or on the process of diffusion. The random-flight treatment is the most rigorous since it exactly duplicates the physical process involved in multiple scattering.

A. Random Flight

Formal solutions of the random flight problem have been obtained by Grosjean (Reference 99), Wigner (Reference 100), Guth and Inonu (Reference 101), Wang and Guth (Reference 102) and Breitenberger (Reference 103). The solutions of Grosjean and Wigner give the exact angular and spatial distributions but apply to an infinite medium and also depend on the actual number of scatterings suffered by the particles involved. Breitenberger has obtained the angular distribution for the case of a beam of particles normally incident on a plane parallel slab of arbitrary thickness, with provisions for including energy loss within the medium. However, his results are in the form of coupled recurrence relations for the scattering function, which are not directly suited for simple computation. Explicit forms for the scattering function are obtained by Breitenberger by successive forward approximations, and the process of extending the results to arbitrarily large angles is outlined. However, the numerical computation involved even at angles as low as 35 degrees is excessive; and, in this range, the results are identical with those obtained through the simpler diffusion process.

Despite the lack of useful solutions, the random flight technique is of interest because it indicates a fallacy, which is usually not mentioned, in the alternative

diffusion process. According to Breitenberger (Reference 103), the diffusion process is based on the assumption that the directional distribution of the particles, after a particular collision, does not depend on the direction in which other particles have already left the target in earlier collisions. But this condition of "stochastic" independence of collisions holds only for small scattering angles.

B. Diffusion Process

The majority of multiple-scattering theories are based on the assumption that the scattering process is adequately described by ordinary diffusion. This involves the solution of the integro-differential transport equation with the desired boundary conditions. Goudschmidt and Saunderson (Reference 53) obtained an expression for the angular distribution by using a Legendre series expansion. Aside from the objection stated by Breitenberger, their result is considered valid for all scattering angles and can be used with any appropriate (convergent) single-scattering cross section. The effects of energy loss are included in the theory, but spatial deflections resulting from multiple scattering are neglected. A difficulty associated with their result is the extensive computation required in evaluating the slowly convergent Legendre series. Spencer (Reference 104) has derived simple recurrence relations for the series coefficients, but a relatively large number of terms must be summed for accurate results. At large angles (150 degrees), Berger (Reference 54) has shown that nearly sixty terms are required to provide convergence to six significant figures. A further problem with the Goudschmidt-Saunderson theory is that it is dependent on the actual path traversed by the particles rather than the thickness of the target.

Lewis (Reference 105) has applied the Goudschmidt-Saunderson theory to the case of an infinite medium, taking the energy loss into account by regarding it only as a function of the residual range of the scattered particles. Some attempts have also been made to adapt the Goudschmidt-Saunderson theory to the case of bounded media. Sidel et al. (Reference 106) investigated the multiple scattering of Compton recoil electrons produced by Co^{60} gamma rays and compared their results with the Goudschmidt-Saunderson theory by assuming the relation $x = t/\cos\theta$ between the path length of the scattered particle and the target thickness. Theoretical values were obtained by summing the first eight terms in the Legendre series expansion of the angular distribution function. Their results indicated reasonably good qualitative agreement for their targets ($\sim 20 \text{ mg/cm}^2$) at most angles out to 140 degrees but much poorer agreement for thick targets ($\sim 200 \text{ mg/cm}^2$).

C. Small-Angle Approximations

Because of the above-mentioned difficulties associated with general solutions of the multiple-scattering problem, various approximate results have been obtained. The approximations usually involve thin targets, small scattering angles, and no energy loss. A complete summary of the many mathematical techniques developed has been compiled by Scott (Reference 107). One of the most useful theories is that of Molière

(References 52 and 108). The Molière theory is basically just the small-angle limit of the Goudschmidt-Saunderson theory, but does not include the effects of energy loss. Hanson et al. (Reference 58) have shown that Molière's theory agrees reasonably well with their results from thin-foil scattering experiments, and the relativistic corrections introduced by Nigam et al. (Reference 109) have improved the agreement. The results indicated that the Molière scattering distribution is valid out to angles as large as 20 to 30 degrees. Bethe (Reference 52) has extended the Molière theory to larger angles by means of a correction factor. Although Breitenberger has stated that small-angle theories cannot be legitimately extended to larger angles due to the nature of the initial small-angle approximation, the recent calculations performed by Berger (Reference 54) with the Goudschmidt-Saunderson theory show excellent agreement with Bethe's large-angle extension.

Other small-angle scattering theories have been developed, notably by Wentzel (Reference 110) and Snyder and Scott (Reference 111). However, most of these are equivalent to the Molière theory or involve slight modifications, usually in the form of various correction factors. Fano (Reference 112), for example, has included inelastic electron scattering by adding a term to the scattering function. At large angles, the correction is equivalent to replacing Z^2 by $Z(Z+1)$. Cooper and Rainwater (Reference 113) and Ter-Mikayelian (Reference 114) have performed extensive calculations of nuclear size effects. They involve corrections to the screening function in terms of a nuclear form factor dependent on the nuclear size. However, according to Scott (Reference 107) the form factor differs appreciably from unity only for angles approximately 10^3 times as large as those for which screening is important. Thus, nuclear size effects are apparently negligible, at least in the small-angle approximation.

III NUMERICAL METHODS

The various numerical techniques which have been developed for multiple scattering are all based on the random flight concept. The basic approach involves grouping of the enormous number of collisions into a sufficiently small number of representative collisions, then sampling the "condensed" random flights by a Monte Carlo process according to an appropriate multiple-scattering theory. The techniques used by Sidel et al. (Reference 115), Leiss et al. (Reference 50), Perkins (Reference 49), Mar (Reference 44), and Berger (References 54 and 116) are all variations of this basic idea.

The primary distinguishing parameters in the various approaches are the path length between each "condensed" collision, the energy loss, angular deflection, and spatial displacement. In terms of these parameters, the most complete Monte Carlo model has been developed by Berger (Reference 54). The models of the other references mentioned above are for the most part restricted to particular choices of the parameters with some variation allowed in a single parameter, usually path length.

Berger used both the Molière and Goudschmidt-Saunderson scattering functions and determined the path length according to the ionization and radiation energy losses by requiring that the particle energy be decreased by a certain fraction after each step. Calculation of the transverse and longitudinal displacements were also included. Mar, Sidei et al., and Perkins all used the small-angle Molière theory but differed in their selections of path length. Perkins determined path length by choosing d/E to be some specified value, usually 0.02. Mar also used this method along with that of constant path lengths. Sidei et al. calculated path lengths from the Molière theory by applying the condition $X\sqrt{B} = 40$ degrees. However, Sidei et al. also imposed several restricting approximations, notably that the final angular distribution is described by $\cos^2\theta$ and that all electrons at a particular depth in the target have the same energy. Leiss et al. used a scattering distribution given by Rossi (Reference 117), equivalent to a first-order Gaussian approximation, and a constant path length of 0.25 cm.

Transmission factors were calculated by most of the above-mentioned authors, but only the Monte Carlo models developed by Mar and Berger were equipped to tabulate angular distributions of transmitted and backscattered electrons. The transmission and backscattering results for different materials and incident angles all agreed within a few percent, with the exception of the results obtained by Sidei et al. at low energies. The deviations, which amounted to as much as 10 to 20 percent, were apparently due to the previously mentioned approximation used by Sidei et al. However, the good qualitative agreement with the more elaborate Monte Carlo models of the other authors indicates the rather wide range of capability of various simplifying approximations. Also, transmission calculations performed by Berger with several different scattering models and cross sections showed agreement to within a few percent.

The angular distributions of transmitted electrons obtained by Mar and Berger agreed reasonably well with each other and with the experimental results of Frank (Reference 57). For penetration depths greater than the "diffusion length," defined by Frank, the results of Mar (see Reference 118) and Frank showed that the angular distribution could be described by a cosine-squared law in agreement with the earlier assumption made by Sidei et al. Berger's results were better fitted by $(0.717 \cos\theta + \cos^2\theta)$ (Reference 59), which indicated a relatively greater number of large angle scatterings.

Mar and Berger have also performed extensive computations in other aspects of multiple scattering. Mar has obtained the energy spectrum for transmitted electrons and has used both isotropic and fission-spectrum sources. Investigations of multiple targets of different materials are also in progress. Berger has calculated both electron and positron transmissions, energy dissipation in bounded and unbounded media, slowing-down spectra and path length straggling, the effects of isotropic and internal sources, and the penetration of protons.

CONCLUSIONS

The brief survey of multiple-scattering theories indicates that the diffusion process using the transport equation is, at present, the only technique that yields practical analytical solutions. The two most useful theories appear to be that of Goudschmidt-Saunderson for thick targets, and the Molière-Bethe approximation for small angles and thin targets. The primary difficulty associated with the Goudschmidt-Saunderson theory is the extensive computation required.

The combination of a diffusion-type multiple-scattering theory with Monte Carlo random-sampling techniques appears to be the most convenient method available for general calculations of problems involving multiple scattering. The Monte Carlo approach effectively simulates the actual physical process and can, therefore, be used to obtain nearly any type of information about the physical problem. The extensive calculations which have already been performed with this method have shown that excellent agreement can be obtained with experimental results. The only limitations appear to be the accuracy of the particular multiple-scattering function used and the large amount of computation involved.

REFERENCES

1. J. A. Ward, Space Trajectories, ed. by Technical Staff Research Division, Radiation Inc., p. 103, 1960.
2. Luigi G. Jacchia, "Variations in the Earth's Upper Atmosphere as Revealed by Satellite Drag, " Rev. Mod. Phys., 35, 973-991, 1963.
3. P. Musen, "Contributions to the Theory of Satellite Orbits, " Space Research, Proceedings of the First International Space Science Symposium, Nice, France Jan. 11-16, 1960. Hilde Kallman Bijl, ed. Interscience Publishers, Inc., New York, 1960 pp. 434-447.
4. Jensen, Townsend, Cork and Kraft, Design Guide to Orbital Flight, McGraw Hill Book Co., New York, 1962.
5. C. E. McIlwain, "Coordinates for Mapping the Distribution of Magnetically Trapped Particles, " J. Geophys. Res., 66, 3681-3692 (1961)
6. D. C. Jensen and J. C. Cain, "An Interim Geomagnetic Field, " in abstracts of the Papers Presented at the Forty-third Annual Meeting, American Geophysical Union, Washington, D. C., April 25-28, 1962. J. Geophys. Res., 67, 3568, 1962.
7. Theodore G. Northrup, "Adiabatic Charged Particle Motion, " Rev. Geophys., 1, 283-304, 1963.
8. E. Stassinopoulos, Goddard Space Flight Center, Private Communication, 1962.
9. W. N. Ness, "The Artificial Radiation Belt Made on July 9, 1962, " J. Geophys. Res., 68, 667-683, 1963.
10. Stanley C. Freden and George A. Paulikas, " Trapped Protons at Low Altitudes in the South Atlantic Magnetic Anomaly, " J. Geophys. Res., 69, 1259-1270, 1964.
11. Wing Y. Wong, Computer Codes for the Evaluation of Space Radiation Hazards, Vol. 2, Van Allen Radiation, Boeing Document D2-90418-2, prepared for NASA Manned Spacecraft Center under Contract NAS 9-1393, 1963.

12. J. Vette, "The Natural Radiation and the Saturated Argus Model Environment, " The Effects of Charged Particle Environment on Military Space Flight, Technical Documentary Report No. SSD-TDR-63-244, Space Systems Division USAF, September 1963, CH. VII (S-RD, title unclassified).
13. W. L. Brown, Bell Telephone Laboratories, Private Communication, 1962.
14. B. Clark and D. Adams, "Experimental Measurements of the Radiation Hazards Associated with Manned Space Flights, " presented at the Fifth International Space Science Symposium, Florence, Italy, May 15, 1964.
15. J. E. Naugle and D. A. Kniffen, "Variations of the Proton Energy Spectrum in the Inner Van Allen Belt, " J. Geophys. Res., 68, 4065-4078, 1963.
16. H. West, "Spectra and Fluxes of Electrons Trapped in the Earth's Magnetic Field Following Recent High Altitude Nuclear Bursts, " UCRL 7309, Rev. 1, 1963.
17. C. E. McIlwain and G. Pizzella, "On the Energy Spectrum of Protons Trapped in the Earth's Inner Van Allen Zone, " J. Geophys. Res., 68, 1811-1824, 1963.
18. W. L. Imhof and R. V. Smith, "Proton Intensities and Energy Spectrums in the Inner Van Allen Belt, " J. Geophys. Res. 69, 91-100, 1964.
19. Martin Walt and William M. MacDonald, "Diffusion of Electrons in the Van Allen Radiation Belt. 1. Treatment of Particles with Mirroring Points at High Altitudes and 2. Particles with Mirroring Points at Low Altitudes, " J. Geophys. Res., 67, 5013-5034, 1962.
20. R. E. Carter, F. Reines, J. J. Wagner, and M. E. Wyman, "Free Anti-neutrino Absorption Cross Section, 2, Expected Cross Sections from Measurements of Fission Fragment Electron Spectrum, " Phys. Rev. 113, 280-286, 1959.
21. S. C. Freden and R. S. White, "Trapped Proton and Cosmic-Ray Albedo Neutron Fluxes, " J. Geophys. Res., 67, 25-30, 1962.
22. J. A. Van Allen, L. A. Frank, and B. J. O'Brien, "Satellite Observations of the Artificial Radiation Belt of July 1962, " J. Geophys. Res., 68, 619-628, 1963.
23. W. L. Brown and J. D. Gabbe, "The Electron Distribution in the Earth's Radiation Belts during July 1962 as Measured by Telstar, " J. Geophys. Res., 68, 607-618, 1963.

24. Guido Pizzella, C. E. McIlwain, and J. A. Van Allen, "Time Variations of Intensity in the Earth's Inner Radiation Zone, October 1959 through December 1960," J. Geophys. Res., 67, 1235-1253, 1962.
25. Harry H. Heckman and George H. Nakano, "East-West Asymmetry in the Flux of Mirroring Geomagnetically Trapped Protons," J. Geophys. Res., 68, 2117-2120, 1963.
26. T. A. Farley and N. L. Sanders, "Pitch Angle Distributions and Mirror Point Densities in the Outer Radiation Zone," J. Geophys. Res., 67, 2159-2168, 1962.
27. Gordon Garmire, "Geomagnetically Trapped Protons with Energies Greater than 350 Mev," J. Geophys. Res., 68, 2627-2638, 1963.
28. Ernest C. Ray, "On the Theory of Protons Trapped in the Earth's Magnetic Field," J. Geophys. Res., 65, 1125-1134, 1960.
29. F. Riesz and B. Sz.-Nagy, Functional Analysis, Frederick Ungar Publishing Co., New York, 1955, p. 143.
30. W. L. Brown, J. D. Gabbe and C. Roberts, Bell Telephone Laboratories, Private Communication, 1964.
31. A. M. Lenchek, S. F. Singer, and R. C. Wentworth, "Geomagnetically Trapped Electrons from Cosmic-Ray Albedo Neutrons," J. Geophys. Res., 66, 4027-4046, 1961.
32. U. R. Rao and K. G. McCracken, "Asymptotic Cones of Acceptance and Their Use in the Study of the Daily Variation of Cosmic Radiation," J. Geophys. Res., 68, 345-369, 1963.
33. W. R. Webber, "Time Variations of Low Rigidity Cosmic Rays during the Recent Sunspot Cycle," Progress in Elementary Particle and Cosmic Ray Physics, VI, 146-154, 1962.
34. W. R. Webber, An Evaluation of the Radiation Hazard due to Solar-Particle Events, Boeing document D2-90469, December 1963, pp. 15-16.
35. K. G. McCracken, "The Cosmic-Ray Flare Effect," J. Geophys. Res., 67, 423-458, 1962.
36. Carl Störmer, Polar Aurora, Oxford University Press, London, 1955.

37. Enrico Fermi, Nuclear Physics, University of Chicago Press, Chicago, 1949, Chapter X.
38. M. S. Vallarta, "Theory of the Geomagnetic Effects of Cosmic Radiation," Handbuch der Physik, Vol. XLVI/1, Cosmic Rays, I. S. Flugge, ed. Springer-Verlag, Berlin, 1961.
39. H. V. Neher and Hugh R. Anderson, "Cosmic Rays at Balloon Altitudes and the Solar Cycle," J. Geophys. Res., 67, 1309-1313, 1962.
40. H. V. Neher and H. R. Anderson, "Cosmic-Ray Intensity at Thule, Greenland, during 1962 and 1963 and a Comparison with Data from Mariner 2," J. Geophys. Res., 69, 807-814, 1964.
41. W. C. Lin, D. Yenkaesaw, and J. A. Van Allen, "Latitude Survey of Cosmic-Ray Intensity by Explorer 7, October 1959 to February 1961," J. Geophys. Res., 68, 4885-4897, 1963.
42. Hawkins, C. T., "MORL Sectoring Program," Boeing Computer Program AS 1822, November 1963.
43. Fortney, R. E., Computer Analysis of Radiation Shielding, Northrop Space Laboratories Report to be published under Contract AF 33(657)-8762
44. B. W. Mar, Electron Shielding Codes for Evaluation of Space Radiation Hazards, Boeing Document D2-90414, June 1963.
45. K. S. McGarrigle and B. W. Mar, Computer Codes for the Evaluation of Space Radiation Hazards, Boeing Document D2-90418, August 1963.
46. C. T. Hawkins, Computer Codes for the Evaluation of Space Radiation Hazards -- Electron Transmission, Boeing Document D2-90418-6, August 1963.
47. R. D. Evans, The Atomic Nucleus, McGraw-Hill Book Company, Inc., New York, 1955.
48. R. D. Birkoff, "The Passage of Fast Electrons Through Matter," Encyclopedia of Physics Vol. 34, Corpuscles and Radiation in Matter II, Springer-Verlag, Berlin, 1958.
49. J. F. Perkins, "Monte Carlo Calculation of Transport of Fast Electrons," Phys. Rev. 126, 1781 1962.

50. J. E. Leiss, S. Penner and L. S. Robinson, "Range-Straggling of High-Energy Electrons in Carbon, " Phys. Rev., 107, 1544, 1957 .
51. A. T. Nelms, "Energy Loss and Range of Electrons and Positrons, " Supplement to National Bureau of Standards Circular 577, July 30, 1958.
52. H. A. Bethe, "Molière's Theory of Multiple Scattering, " Phys. Rev., 89, 1256, 1953 .
53. S. Goudschmidt, and J. L. Saunderson, Phys. Rev. 57, 24, 1940.
54. M. J. Berger, Methods In Computational Physics, Vol. I., Academic Press, Inc., New York, 1963.
55. H. A. Bethe and W. Heitler, "On the Stopping of Fast Particles and on the Creation of Positive Electrons, " Proc. Roy. Soc., A 146, 83, 1934.
56. F. Rohrlich and B. C. Carlson, "Positron-Electron Differences in Energy Loss and Multiple Scattering, " Phys. Rev. 93, 38-44, 1954 .
57. Frank, H., Zur Vielfachstreuung und Rückdiffusion schneller Elektronen nach Durchgang durch dicke Schichten, (On the Multiscattering and Back-Diffusion of Rapid Electrons after Passage through thick layers), Z. Naturforsch., 14a, 247-261 1959 .
58. A. O. Hanson, L. H. Lanzl, E. M. Lyman, and M. B. Scott, "Measurement of Multiple Scattering of 15.7-Mev Electrons, " Phys. Rev. 84, 634-637, 1951.
59. H. A. Bethe, M. E. Rose, and L. P. Smith, Proc. Am. Phil. Soc., 78, 573, 1938 .
60. H. H. Seliger, "Transmission of Positrons and Electrons, " Phys. Rev., 100, 1029-1037, 1955.
61. A. F. Makhov, "Penetration of Electrons Into Solids, " Fizika Tverdogo Tela, 2, 2161, 1960.
62. B. W. Mar, The Calculation of Bremsstrahlung Radiation Penetrating a Space Vehicle, Boeing Document D2-90411, July 1963.
63. P. White and G. Millington, Proc. Roy. Soc. (London), A120, 701, 1928.

64. R. D. Evans, "Principles for the Calculation of Bremsstrahlung Radiation Dose Rates in Space Vehicles, " NASA report 63270-05-01, July 1961.
65. "Report of the RBE Committee to the International Commission on Radiological Protection and on Radiological Units and Measurements, " Health Physics, 2, 357, 1963.
66. D. V. Cormack and H. E. Johns, "Electron Energies and Ion Densities in Water Irradiated with 200-kev, 1-Mev, and 25-Mev Radiation, " Brit. J. Radiol., 25, 369, 1952.
67. P. R. J. Burch, "Calculations of Energy Dissipation Characteristics in Water for Various Radiations, " Rad. Res., 6, 289, 1957.
68. H. J. Schaefer, "The December 1962 Report of the RBE Committee to the ICRP and ICRU in Its Implications for the Assessment of Proton Radiation Exposure in Space, " Research Report, U. S. Naval School of Aviation Medicine Project MR005. 13-1002, Report No. 26, October 1963.
69. C. S. Wu, "The Continuous X-rays Excited by the Beta Particles of p^{32} , " Phys. Rev., 59, 481, 1941.
70. S. J. Wyard, "Intensity Distribution of Bremsstrahlung from Beta Rays, " Proc. Phys. Soc. (London), A65, 377, 1952.
71. A. Foderaro and F. Obenshain, Fluxes from Regular Geometric Sources, Westinghouse Electric Corporation Document WAPD-TN-508, June 1955.
72. C. P. Jupiter, C. R. Hatcher, and N. E. Hansen, "Measurement of the Angular Distribution of Bremsstrahlung Intensity for 10-Mev and 20-Mev Electrons on Thick Targets, " unpublished Lawrence Radiation Laboratory data.
73. W. W. Buechner, R. J. Van de Graaff, E. A. Burrill, and A. Sperduto, "Thick-Target X-ray Production in the Range from 1250 to 2350 Kilovolts, " Phys. Rev., 74, 1348-1352, 1948.
74. Paul Farrell, "The Bremsstrahlung Radiation Field of a Monoenergetic Electron Beam, " Trans. Am. Nucl. Soc., 7, 202, 1964.
75. V. Z. Jankus, "Radiative Correction for the Collision Loss of Heavy Particles, " Phys. Rev., 90, 4-6, 1953.

76. H. A. Bethe and J. Ashkin, in E. Segrè (ed.), "Experimental Nuclear Physics, Vol. I, John Wiley and Sons, Inc., New York, 1953, p. 168.
77. E. A. Uehling, "Penetration of Heavy Charged Particles in Matter, " Annual Review of Nuclear Science, 4, 318, 1954.
78. H. A. Bethe and J. Ashkin in E. Segrè (ed.), Experimental Nuclear Physics, Vol. I, John Wiley and Sons, Inc., New York, 1953, p. 169.
79. M. Rich and R. Madey, "Range Energy Tables, " University of California Radiation Laboratory Report, UCRL 2301, 1954.
80. R. M. Sternheimer, "Range-Energy Relations for Protons in Be, C, Al, Cu, Pb, and Air, " Phys. Rev., 115, 137-142, 1959.
81. H. J. Schaefer, "Energy Dissipation Characteristics in Tissue for Proton Radiation in Space, " Research Report U. S. Naval School of Aviation Medicine Project MR005. 13-1002, Report No. 24, January 1963.
82. H. A. Bethe and J. Ashkin in E. Segrè (ed.), Experimental Nuclear Physics, Vol. I, John Wiley and Sons, Inc., New York, 1953. p. 248.
83. H. A. Bethe and J. Ashkin in E. Segrè (ed.), Experimental Nuclear Physics, Vol. I, John Wiley and Sons, Inc., New York, 1953. p. 251.
84. R. G. Alsmiller Jr. and F. E. Murphy, "Space Vehicle Shielding Studies-- Calculations of the Attenuation of a Model Solar Flare and Monoenergetic Proton Beams by Aluminum Shields, " Oak Ridge National Laboratory Report ORNL-3317, 1963.
85. N. Metropolis, R. Bivins, M. Storm, M. Turkevich, J. M. Miller, and G. Friedlander, "Monte Carlo Calculations on Intranuclear Cascades, Part I Low Energy Studies, " Phys. Rev., 110, 185, 1958.
86. N. Metropolis, R. Bivins, M. Storm, M. Turkevich, J. M. Miller and G. Friedlander, "Monte Carlo Calculations on Intranuclear Cascades, Part II High Energy Studies and Pion Processes, " Phys. Rev., 110, 204, 1958.
87. H. W. Bertini, "Monte Carlo Calculations on Intranuclear Cascades, " Oak Ridge National Laboratory Report ORNL-3383, 1963.
88. I. Dostrovsky, Robinovitz, and Bivens, "Systematics of Nuclear Evaporation, " Phys. Rev., 111, 1659, 1958.

89. I. Dostrovsky, Z. Frankel, and G. Friedlander, "Monte Carlo Calculations of Nuclear Evaporation Processes, III. Applications to Low-Energy Reactions," Phys. Rev., 116, 683, 1959.
90. L. Dresner, "EVAP--a Fortran Program for Calculating the Evaporation of Various Particles from Excited Compound Nuclei," Oak Ridge National Laboratory Report ORNL CF-61-12-30, December 1961.
91. T. Wakatsuki, Y. Hirao, E. Okada, I. Miura, K. Sugimoto and A. Mizobuchi, "Gamma Rays from Several Elements Bombarded by 10- and 14-Mev Protons," Journal of the Physical Society of Japan, 15, 1141, 1960.
92. R. Wallace and C. Sondhaus, "Techniques Used in Shielding Calculations for High-Energy Accelerators: Applications to Space Shielding," University of California Radiation Laboratory Report UCRL 10439, 1962.
93. H. W. Bertini, "Parametric Study of Calculated Cascade and Evaporation Reaction for 25- to 400-Mev Nucleons Incident on Complex Nuclei," Oak Ridge National Laboratory Report ORNL-3499, Vol. II, p. 31, 1963.
94. R. I. Allen, F. Bly, A. Dessler, C. Douglass, J. Perkins, H. Price, E. Smith, and W. Schofield, "Shielding Problems in Manned Space Vehicles," NR-140, 1961.
95. D. L. Dye, "Space Proton Doses at Points Within the Human Body," Proceedings of the Symposium on Protection Against Radiation Hazards in Space, USAEC TID-7652, pp. 633-661, 1962.
96. W. A. Gibson, "Energy Removed from Primary Proton and Neutron Beams by Tissue," Oak Ridge National Laboratory Report ORNL-3260, 1962.
97. R. R. Brown, "Correlation of Nuclear Induced Dislocation Density with Reduced Minority Carrier Lifetime in Silicon and Germanium Devices," Bull. Am. Phys. Soc., Series II, 7, 619, December 1962.
98. D. L. Dye, A Geometric Analysis of the Seated Human Body for Use in Radiation Dosage Calculations, Boeing Document D2-90107, July 1962.
99. C. C. Grosjean, Mededel, Koninkl, Vlaam, Acad. Wetenschap. Belg., 13, No. 36, 1951.
100. E. P. Wigner, "The Problem of Multiple Scattering," Phys. Rev., 94, 17-25, 1954.

101. E. Guth and E. Inonu, J. Math. Phys., 2, 451, 1961.
102. M. C. Wang and E. Guth, "On the Theory of Multiple Scattering, Particularly of Charged Particles," Phys. Rev., 84, 1092-1111, 1951.
103. E. Breitenberger, "Theory of Multiple Scattering," Proc. Roy. Soc. (London), A250, 514-523, 1959.
104. L. V. Spencer, "Theory of Electron Penetration," Phys. Rev. 98, 1597-1615, 1955.
105. H. W. Lewis, "Multiple Scattering in an Infinite Medium," Phys. Rev., 78, 526-529, 1950.
106. T. Sidel, T. Higashimura, and K. Kinoshita, "The Self-Scattering of the Compton Recoil Electrons Produced by Co^{60} Gamma Rays," Mem. Fac. Eng. Kyoto Univ., 19, 367-377, 1957.
107. W. T. Scott, "The Theory of Small-Angle Multiple Scattering of Fast Charged Particles," Rev. Mod. Phys., 35, 231-313, 1963.
108. G. Molière, Z. Naturforsch., 3a, 78, 1948.
109. B. P. Nigam, M. K. Sundareson, and T-Y. Wu, "Theory of Multiple Scattering: Second Born Approximation and Corrections to Molière's Work," Phys. Rev., 115, 491-502, 1959.
110. G. Wentzel, Ann. Physik, 69, 335, 1922.
111. H. S. Snyder and W. T. Scott, "Multiple Scattering of Fast Charged Particles," Phys. Rev., 76, 220-225, 1949.
112. U. Fano, "Inelastic Collisions and the Molière Theory of Multiple Scattering," Phys. Rev., 93, 117-120, 1954.
113. L. N. Cooper and J. Rainwater, "Theory of Multiple Coulomb Scattering from Extended Nuclei," Phys. Rev., 97, 492-504, 1955.
114. M. L. Ter-Mikayelian, "On the Theory of Multiple Scattering," Nucl. Phys., 9, 679-686, 1959.
115. T. Sidel, T. Higashimura, and K. Kinoshita, "Monte Carlo Calculation of the Multiple Scattering of the Electron," Mem. Fac. Eng. Kyoto Univ., 19, 220-228, 1957.

116. M. J. Berger, "Transmission and Reflection of Electrons by Aluminum Foils," Nat. Bur. Stds., Tech. Note 187, U. S. Government Printing Office, Washington, D. C., April 1, 1963.
117. B. Rossi, High-Energy Particles, Prentice-Hall, Inc., New York, 1952.
118. K. Moriyasu, "Analysis of Monte Carlo Electron Angular Distributions," The Boeing Company Technical Note, August 1963. (Unpublished).

DISTRIBUTION

No. cys

HEADQUARTERS USAF

1	Hq USAF (AFCOA), Wash, DC 20330
1	Hq USAF (AFXOP), Wash, DC 20330
1	Hq USAF (AFRDP), Wash, DC 20330
1	Hq USAF (AFORQ), Wash, DC 20330
1	Hq USAF (AFRNE-B, Maj Lowry), Wash, DC 20330
1	Hq USAF (AFNIN), Wash, DC 20330
1	Hq USAF (AFTAC), Wash, DC 20330
2	Hq USAF (AFMSG, Biomedical Science Branch), Wash, DC 20330
1	USAF Dep, The Inspector General (AFIDI), Norton AFB, Calif 92409
1	USAF Directorate of Nuclear Safety (AFINS), Kirtland AFB, NM 87117

MAJOR AIR COMMANDS

1	AFSC, Andrews AFB, Wash, DC 20331
1	AFLC (MCSW), Wright-Patterson AFB, Ohio 45433
1	ADC (Ops Anlys), Ent AFB, Colorado Springs, Colo 80912
1	AUL, Maxwell AFB, Ala 36112
1	USAFIT, Wright-Patterson AFB, Ohio 45433
1	USAF, Colo 80840

AFSC ORGANIZATIONS

1	AFSC Scientific and Technical Liaison Office, Research and Technology Division (AFUPO), Los Angeles, Calif 90045
1	FTD (TDBTL), Wright-Patterson AFB, Ohio 45433
1	AF Materials Laboratory, Wright-Patterson AFB, Ohio 45433
1	ASD, Wright-Patterson AFB, Ohio 45433
	RTD, Bolling AFB, Wash, DC 20332
1	(RTN-W, Lt Col Munyon)
1	(RTS)
1	BSD, Norton AFB, Calif 92409
1	SSD (SSSD), AF Unit Post Office, Los Angeles, Calif 90045
1	ESD (ESTI), L. G. Hanscom Fld, Bedford, Mass 01731
1	AF Msl Dev Cen (RRRT), Holloman AFB, NM 88330

DISTRIBUTION (cont'd)

No. cys

1	AFMTC (MU-135, Tech Library), Patrick AFB, Fla 32925
1	RADC (Document Library), Griffiss AFB, NY 13442

KIRTLAND AFB ORGANIZATIONS

1	AFSWC (SWEH), Kirtland AFB, NM 87117
	AFWL, Kirtland AFB, NM 87117
20	(WLIL)
1	(WLR)
1	(WLRC)
75	(WLRB)
1	(WLRJ)
1	(WLRP)
1	(WLRM)
1	(WLA)
1	(WLAV)
1	(WLAX)
1	(WLAS)
1	(WLD)
1	(WLDW)
1	(WLDN)
1	(WLDC)

OTHER AIR FORCE AGENCIES

1	Director, USAF Project RAND, via: Air Force Liaison Office, The RAND Corporation, 1700 Main Street, Santa Monica, Calif 90406
5	School of Aerospace Medicine, Aerospace Med Cen (AFSC), Chief, Bionucleonics Div, Brooks AFB, Tex
1	Medical Service School (Radiobiology Br), USAF (ATC), Gunter AFB, Ala 36114
1	AFOAR, Bldg T-D, Wash, DC 20333
1	AFOSR, Bldg T-D, Wash, DC 20333
1	AFCRL, L. G. Hanscom Fld, Bedford, Mass 01731

DISTRIBUTION (cont'd)

No. cys

ARMY ACTIVITIES

- 1 Chief of Research and Development, Department of the Army
(Special Weapons and Air Defense Division), Wash, DC 20310
- 1 Director, Walter Reed Army Institute of Research, Walter Reed
Army Medical Center, ATTN: Adjutant, Wash 12, DC
- 2 Director, US Army Engineer Research and Development Laboratories,
ATTN: STINFO Branch, Ft Belvoir, Va
- 1 Commanding General, White Sands Missile Range (Technical
Library), White Sands, NM 88002

NAVY ACTIVITIES

- 1 Office of the Chief of Naval Operations, Department of the Navy,
Wash, DC 20350
- 1 Chief of Naval Research, Department of the Navy, Wash, DC 20390
- 2 Commanding Officer and Director, US Naval Radiological Defense
Laboratory, San Francisco, Calif 94135
- 1 Office of Naval Research, Wash, DC 20360

OTHER DOD ACTIVITIES

- 2 Director, Defense Atomic Support Agency (Document Library Branch),
Wash, DC 20301
- 1 Commander, Field Command, Defense Atomic Support Agency (FCAG3,
Special Weapons Publication Distribution), Sandia Base, NM 87115
- 1 Director, Weapon Systems Evaluation Group, Room 1D-847, The
Pentagon, Wash, DC 20330
- 1 Director, Advanced Research Projects Agency, Department of
Defense, The Pentagon, Wash, DC 20301
- 1 Office of Director of Defense Research and Engineering, ATTN:
John E. Jackson, Office of Atomic Programs, Room 3E 1071, The
Pentagon, Wash, DC 20330
- 20 Hq Defense Documentation Center for Scientific and Technical
Information (DDC), Bldg 5, Cameron Sta, Alexandria, Va 22314

AEC ACTIVITIES

- 1 US Atomic Energy Commission (Headquarters Library, Reports
Section), Mail Station G-017, Wash, DC 20545
- 1 Sandia Corporation (Technical Library), P. O. Box 969, Livermore,
Calif 94551

DISTRIBUTION (cont'd)

No. cys

- 1 Chief, Division of Technical Information Extension, US Atomic Energy Commission, Box 62, Oak Ridge, Tenn 37831
- 1 University of California Lawrence Radiation Laboratory (Technical Information Division), P. O. Box 808, Livermore, Calif 94551
- 1 Director, Los Alamos Scientific Laboratory (Helen Redman, Report Library), P. O. Box 1663, Los Alamos, NM 87554
- 1 Brookhaven National Laboratory, Upton, Long Island, NY
- 1 Oak Ridge National Laboratory (Tech Library), Oak Ridge, Tenn 37831
- 1 Argonne National Laboratory (Tech Library), 9700 S. Cass Ave, Argonne, Ill 60440

OTHER

- 1 Langley Research Center (NASA), ATTN: Assoc. Director, Langley Station, Hampton, Va
- 1 National Bureau of Standards, Radiological Equipment Section, Wash 25, DC
- 1 Central Intelligence Agency, 2430 E Street NW, Wash, DC 20505
- 1 National Aeronautics and Space Administration, Manned Spacecraft Center, ATTN: Chief, Technical Info Div, Houston 1, Tex
- 1 OTS, Department of Commerce, Wash 25, DC
- 1 Institute for Defense Analysis, Room 2B257, The Pentagon, Wash 25, DC THRU: ARPA
- 1 Massachusetts Institute of Technology, Lincoln Laboratory (Document Library), P. O. Box 73, Lexington, Mass 02173
- 2 Aerospace Corporation, P. O. Box 95085, Los Angeles 45, Calif
- 1 The Dikewood Corporation, 4805 Menaul Blvd NE, Albuquerque, NM
- 1 Union Carbide Research Institute, ATTN: Dr. Clay Zerby, P. O. Box 278, Tarrytown, NY
- 10 Boeing Aircraft Company, ATTN: Dr. Bryan Mar, P. O. Box 3707, Seattle 24, Wash
- 1 General Dynamics, ATTN: Richard A. Miller, P. O. Box 748, Fort Worth 1, Texas
- 1 General Dynamics Corp, Nuclear Instrumentation Division (NARF), ATTN: Dr. Kelley R. Spearman, Fort Worth 1, Texas
- 1 S & ID, ATTN: E. C. Olivares, Dept 093, Downey, Calif

DISTRIBUTION (cont'd)

No. cys

1	ASD, ATTN: Mr. Loren Pittman, Wright-Patterson AFB, Ohio 45433
1	US Naval School of Aviation Medicine, ATTN: Dr. H. J. Schaefer, Pensacola, Fla
1	SSD (SSTA, Lt Col E. D. Harney), AFUPO, Los Angeles, Calif 90045
1	McDonnell Aircraft Corp, ATTN: Tom Galbraith, Dept 401, St Louis, Mo
1	Ames Research Center, ATTN: Dr. Rudolf A. Hoffman, Biosatellite Project, Moffett Field, Mountain View, Calif
1	Hughes Research Laboratories, ATTN: Dr. Norman Bailey, 3011 Malibu Canyon Road, Malibu, Calif
1	Hq, NASA, ATTN: Mr. Warren Keller, 1520 H Street NW, Wash 25, DC
1	AVCO Corporation, ATTN: Mr. Kay Hoalst, P. O. Drawer N, Admiral Station, Tulsa 15, Okla
1	S & ID, North American Aviation, ATTN: Mr. Fred Raymes, Dept 695/224, 12214 Lakewood Blvd, Downey, Calif
1	Bendix Corp, Bendix Systems Div, ATTN: Mr. Lynn Lewis, 3300 Plymouth Road, Ann Arbor, Mich
1	Iowa State University, ATTN: Dr. James Van Allen, Dept of Physics & Astronomy, Ames, Ia
1	Hq AFSC (SCT, Maj R. E. Linkous), Andrews AFB, Wash, DC 20331
1	Bell Laboratories, ATTN: Dr. Walter L. Brown, Murray Hill, NJ
1	AFOAR (RROSE, Lt Col Howard), Bldg T-D, Wash, DC 20333
1	AFSC (SCGS, Col S. E. Lifton), Andrews AFB, Wash, DC 20331
1	Northrup Space Laboratory, ATTN: Mr. Robert Fortney, Nuclear Sciences Laboratory, 1111 E. Broadway, Hawthorne, Calif
1	Aerospace Corp, ATTN: Dr. Stan Freden, Space Physics Laboratory, El Segundo, Calif
1	Aerospace Corp, ATTN: Bob Pruett, Los Angeles, Calif
1	USAFSAM (SMBN, Lt Col Ed Ballinger), Brooks AFB Texas 78235
1	Lockheed Missiles & Space Co., ATTN: Mr. Bill Imhof, Phys Sciences Lab, Palo Alto, Calif
1	SSD (SSTRS, Maj Don Evans), AFUPO, Los Angeles, Calif 90045
1	NASA Manned Space Flight Center, ATTN: Mr. Jerry Modisette, Houston 1, Texas
1	AFOSR (SRPN, Lt Col Ralph Allen), Bldg T-D, Wash, DC 20333
1	General Dynamics/Astronautics, ATTN: A. W. McReynolds, Space Science Lab (596-0), San Diego, Calif

DISTRIBUTION (cont'd)

No. cys

1	Dept of Defense (DDR & E, Lt Col Lou Allen), Wash 25, DC
1	General Dynamics/Astronautics, ATTN: Edward L. Noon (528-40), 5001 Kearny Villa Road, San Diego, Calif
1	Hq USAF (AFRST, Col Jack Bollerud), Wash, DC 20330
1	LASL, ATTN: Dr. Wright Langham, Los Alamos, NM
1	General Electric Co, ATTN: Dr. R. T. Frost, Mgr, Space Physics, Rm ML316, VF STC, P. O. Box 8555, Philadelphia 1, Pa
1	Lovelace Clinic, ATTN: Dr. William R. Lovelace, Albuquerque, NM
1	UCLA, ATTN: Dr. Jerry McDonald, Los Angeles, Calif
1	Lovelace Clinic, ATTN: Dr. Clayton S. White, Albuquerque, NM
1	LASL, ATTN: Dr. Payne Harris, Los Alamos, NM
1	University of California Lawrence Radiation Laboratory, ATTN: Dr. Harry West, Livermore, Calif
1	ORNL, ATTN: Mr. Evverett Blizzard, Oak Ridge, Tenn
1	University of California, ATTN: Dr. C. H. Sondhaus, Donner Lab, Livermore, Calif
1	LLOAR (Col Hill), AFUPO, Los Angeles 45, Calif
1	University of California, ATTN: Dr. Cornelius A. Tobias, Donner Lab, Livermore, Calif
1	SSD (SSZB, Lt Col T. Martin), AFUPO, Los Angeles, Calif 90045
1	Goddard Space Flight Center, ATTN: Dr. Wilmot Hess, Green Belt, Md
1	AMD (AMR, Col John Pickering), Brooks AFB, Tex 78235
1	AFCRL (CRZI, Mr. Lou Katz), Hanscom Fld, Bedford, Mass 01731
1	AFCRL, ATTN: Mr. Charles Reynolds, Hanscom Fld, Bedford, Mass 01731
1	Hq NASA, ATTN: Art Reetz, 1520 H Street, NW, Wash 25, DC
1	Lovelace Clinic, ATTN: Dr. A. H. Schwichtenberg, Albuquerque, NM
	General Atomic, A Division of General Dynamics Corp, P. O. Box 608, San Diego 12, Calif
1	(Mr. Roger Jurgovan)
1	(Dr. Clyde Jupiter)
	NASA, 1520 H Street NW, Wash, DC 20546
1	(Dr. Fred Casal, Code MT)
1	(Dr. Leo Fox, Code RBH)

DISTRIBUTION (cont'd)

No. cys

	NASA, Marshall Space Flight Center, Huntsville, Ala
1	(Dr. R. D. Shelton, Code M-RP-N)
1	(Dr. Nat Edmonson)
1	(Mr. Henry Stearn)
1	(Mr. Martin Burrell)
1	(Mr. Gus Whiton)
1	NASA, Goddard Space Flight Center, ATTN: Dr. George F. Pieper, Greenbelt, Md
	Langley Research Center, Langley Station, Hampton, Va
1	(Dr. Trutz Foelsche)
1	(Mr. Harry Heyson)
1	(Dr. John Duberg)
1	(Mr. Raymond Hansen)
1	(Mr. Wayne Scott)
1	(Mr. William Hulten)
1	NASA Manned Spacecraft Center, ATTN: Mr. Lou Vosteen, Houston, Tex
	Lewis Research Center, Cleveland, Ohio
1	(Mr. Irving Karp)
1	(Mr. Robert Hildebrand)
1	(Mr. R. V. Brown)
	Jet Propulsion Laboratory, Pasadena, Calif
1	(Mr. Dwain F. Spencer)
1	(Dr. Robert Mackin)
1	Official Record Copy (Lt D. A. Adams, WLRB-1)